Influence of Amyloid Deposition and Neuroinflammation on Brain Connectivity and Cognition in Alzheimer's Disease Spectrum: a Multimodal Imaging Study

Fangda Leng

PhD thesis

2021

Imperial College London, Department of Brain Science

Copyright declaration

Declaration of originality

The work that I have described in this thesis was performed by me. Work done by other colleagues has been clearly stated and appropriately referenced.

Acknowledgments

I am extremely grateful to my supervisor Dr Paul Edison who provided me the opportunity to work on this project and provided intellectual and practical guidance throughout my PhD training. I appreciate his help to keep my project on track even during the COVID-19 crisis, and his encouragement to constantly explore the frontier of neuroimaging research. Without his help I couldn't have learned the knowledge and practical skills with regard to clinical research.

I am very grateful to my supervisor Dr Rainer Hinz, who provided vital guidance on PET analysis. His scientific rigorousness has inspired me to always (try to) understand the bases of methodologies and has encouraged me to explore disciplines I am not familiar with.

I am also very grateful to my co-supervisor Professor Steve Gentleman who has provided vital supervision to keep my project on track and offered me the chance to learn more about histopathology research.

I am very thankful to my co-supervisor Dr Adam Hampshire, who has inspired me on key statistical and analytical methods.

I thank Dr Melanie Dani who has worked on the "Amyloid and neuroinflammation" project, which has provided me the data to work on. I am also very grateful to Dr Valeria Calsolaro and Dr Daniela Femminella for their help on data analysis and management when my project started.

My PhD training is funded by the China Scholarship Council and I am extremely grateful for the CSC for providing me the opportunity to study here.

I would also like to thank my family and my fiancé for their support throughout the years, without their support I would not have been able to make it through today.

Table of Contents

Abstract

Influence of Amyloid Deposition and Neuroinflammation on Brain Connectivity and Cognition in Alzheimer's Disease Spectrum: A Multimodal Imaging Study

A thesis submitted to Imperial College London for Doctor of Philosophy degree (PhD) by Fangda Leng, May 2021.

Background: Neuroinflammation has been recognised as an important factor in the pathogenesis of Alzheimer's disease (AD). In neurodegeneration, preclinical evidence has suggested that activated microglia, the main cells in neuroinflammation, could damage neuronal circuit structures and disrupt neuronal activity. β-amyloid (Aβ) deposition is one of the hallmarks of AD and is associated with neuroinflammation. However, there is limited clinical evidence on whether neuroinflammation and amyloid deposition influence brain connectivity and cognition. Therefore, this project interrogated the relationship between neuroinflammation, Aβ deposition and brain connectivity/cognition in Alzheimer's spectrum, which covers preclinical, mild cognitive impairment and dementia stage of the AD.

Methods: Cross-sectional multimodal imaging data at baseline and neuropsychological assessments at both baseline and follow-up visits were obtained from the 'Amyloid and Neuroinflammation' study, including 18 healthy volunteers, 54 MCI and 21 AD patients. ^{11}C-PBR28, ^{18}F-Flutemetamol and ^{18}F-AV1451 PET were used to quantify neuroinflammation, amyloid and tau pathology, respectively; T1-weighted MRI, diffusion tensor imaging, resting state functional MRI, and arterial spin labelling MRI measured the grey matter structure, structural connectivity, functional connectivity and cerebral blood prefusion status. Linear models, including principal component analysis, linear regression, and sparse canonical correlation analysis were then applied to interrogate the association between PET markers of Alzheimer's pathology, MRI markers of brain connectivity and cognitive impairment.

Results: ^{11}C-PBR28 uptake was negatively associated with fractional anisotropy of white matter tracts in Aβ positive cohort (standardised β=-0.51, p=0.014, in multiple regression), independent of ^{18}F-Flutemetamol uptake and cortical thickness. ^{11}C-PBR28 uptake was associated with increased amplitude of low frequency fluctuation of BOLD signal in multiple regions including medial prefrontal cortex (MPFC), while ^{11}C-PBR28 in MPFC was associated with decreased MPFC connectivity with posterior cingulate and precuneus (suggesting impaired communication within default mode network). MPFC ^{18}F-Flutemetamol uptake was associated with local connectivity alterations mainly within frontal lobe. Global measure of ^{11}C-PBR28 uptake was associated with decreased local efficiency of brain's functional organisation (standardised β=-0.38, p=0.001), while ^{18}F-Flutemetamol was not. ^{11}C-PBR28 uptake was also negatively associated with cerebral blood perfusion in multiple regions including precuneus and posterior cingulate. MRI measures of neuronal damage performed better in predicting baseline cognitive performance, while PET markers of amyloid, tau pathologies and neuroinflammation outperformed MRI measures in predicting future cognitive decline in patients.

Conclusions: (1) neuroinflammation is associated with both structural and functional connectivity disruption in Alzheimer's spectrum, which is independent of the amount of amyloid deposition; (2) neuroinflammation, amyloid deposition and tau pathology markers together have been found to predict longitudinal cognitive decline in MCI and AD patients, underlining their independent contributions; (3) neuroinflammation is associated with abnormal neuronal hyperactivity and impaired neurovascular coupling in AD.

Frequently used abbreviations

Aβ	β-amyloid
AD	Alzheimer's disease
AIF	Arterial input function
ALFF	Amplitude of low-frequency fluctuations
APP	Amyloid precursor protein
ASL	Arterial spin labelling
BBB	Blood-brain barrier
BOLD	Blood oxygen level dependent
CBF	Cerebral blood flow
CCA	Canonical correlation analysis
CCB	Corpus callosum body
CCG	Corpus callosum genu
CCS	Corpus callosum splenium
DA	Axial diffusivity
DTI	Diffusion tensor imaging
DMN	Default mode network
DR	Radial diffusivity
DVR	Volume of distribution ratio
EPI	Echo-planar imaging
FA	Fractional anisotropy
fMRI	functional MRI
HC	Healthy controls
IRF	Impulse response function
ICA	Independent component analysis
ILF	Inferior longitudinal fasciculus
IFOF	Inferior fronto-occipital fasciculus
MCI	Mild cognitive impairment
MD	Mean diffusivity
MMSE	Mini mental state examination
MPFC	Medial prefrontal cortex
MRI	Magnetic resonance imaging

MTL	Medial temporal lobe
NFT	Neurofibrillary tangles
PC	Principal component
PCA	Principal component analysis
PCC	Posterior cingulate cortex
PET	Positron emission tomography
ROI	Region of interest
SA	Spectral analysis
SLF	Superior longitudinal fasciculus
SFOF	Superior fronto-occipital fasciculus
SUVR	Standard uptake value ratio
TREM2	Triggering receptor expressed on myeloid cells 2
TSPO	18kDa translocator protein
UF	Uncinate fasciculus
V_T	Tissue distribution volume

Chapter 1. Introduction

1.1 Alzheimer's Disease

Alzheimer's disease (AD) is the most prevalent form of senile dementia and accounts for ~60% of all clinical diagnosed dementia. It is estimated that ~10% people above 65 years old have AD, and ~40% for those aged above 85 years("2018 Alzheimer's disease facts and figures," 2018). Typical AD present with gradual memory impairment, and loss of other cognitive functions in language, visuospatial, executive function, complex attention, perceptual-motor, social cognition domains emerge at later stages of the disease (G. M. McKhann et al., 2011). Extracellular amyloid-β (Aβ) plaques, intracellular neurofibrillary tangles (NFT) and neuronal loss are typical pathological hallmarks of AD. Current understanding of AD has established a specific spatial-temporal pattern of amyloid deposition, starting from the neocortex, and extending sequentially to the allocortex, subcortical nuclei, brain stem and cerebellum (Thal, Rub, Orantes, & Braak, 2002). Within the telencephalon, it has been observed that the basal frontal and temporal regions are involved earliest, followed by other association neocortices, hippocampus and lastly primary motor and sensory cortices (Braak & Braak, 1997). Similarly, tau pathology follows a stereotypical pattern of emergence, starting from locus coeruleus, migrating sequentially to transentorhinal cortex, entorhinal cortex, CA1 and CA4 sector of hippocampus, association isocortex and eventually precentral/postcentral gyri (Alafuzoff et al., 2008; Braak & Braak, 1991). Along disease trajectory, it has been suggested that Aβ deposition is the earliest event in the pathogenesis of AD, followed by formation of tau pathologies and neuronal losses in telencephalon (Jack et al., 2013), though emerging evidence suggests that tau pathology may start at mid-30s in locus coeruleus, decades before disease onset (Braak & Del Tredici, 2011). The original observations lead to the amyloid cascade hypothesis, which suggests that the

initial accumulation of amyloid toxicity leads to subsequent events including hyperphosphorylation of tau, NFT formation and neuronal damage (Hardy & Selkoe, 2002). While the central role of Aβ deposition in AD is not questionable based on the facts that dominantly inherited familial AD (FAD) is caused by either mutation on amyloid precursor protein (APP) itself or on genes of amyloid processing proteins (presenilin 1 and presenilin 2), it is acknowledged that amyloid deposition alone is not sufficient for full clinical presentation of AD syndrome (Jack et al., 2013). For instance, in late disease stages, the amount of amyloid deposition plateaus while there are still ongoing neuronal damage and cognitive decline. Further, recent clinical trials of amyloid clearance strategies in AD patients has proved largely disappointing, in that while the amyloid deposition was successfully reduced, it did not significantly slow down disease progression (Lannfelt, Relkin, & Siemers, 2014) (Small & Duff, 2008). Moreover, the large variance of individual resilience to amyloid deposition and propagation of tau pathology indicates other vital processes bridging the two pathologies and driving neuronal dysfunction in AD pathogenesis. Indeed, recent advances in the field have highlighted the important role of neuroinflammation and neurovascular pathways in AD pathogenesis (Leng & Edison, 2021; Zlokovic, 2011b).

Following the 1984 NINCDS-ADRDA consensus on Alzheimer's Disease diagnosis criteria (G. McKhann et al., 1984), in 2011, the National Institute on Aging-Alzheimer's Association (NIA-AA) have updated clinical and research guidelines for diagnosis of dementia due to Alzheimer's disease, mild cognitive decline (MCI) due to Alzheimer's disease, and preclinical stages of Alzheimer's disease, based on the hypothetical model of Alzheimer's spectrum/continuum (patients considered to fall within the preclinical phase—MCI—dementia due to AD are referred to as patients within **Alzheimer's spectrum** in the current thesis) (Albert et al., 2011; G. M. McKhann et al., 2011; Sperling et al., 2011). International Working Group (IWG) for New Research Criteria for the Diagnosis of Alzheimer's Disease

also recommended the classification of clinical phenotypes into typical AD and atypical AD, with the former having predominant episodic memory impairment and the latter including the posterior variant, logopenic variant, frontal variant and Down's syndrome variant (Dubois et al., 2014). While imaging and fluid biomarkers have been incorporated into the NIA-AA (2011) research guidelines as evidence of Alzheimer's pathophysiology, the core clinical criteria for diagnosing MCI and AD rely purely on clinical information and neuropsychological assessments, and still serve as the standard for clinical practice. Nevertheless, with the constant advances of understanding on AD, the research criteria (IWG and NIA-AA) have rapidly evolved over the past decades (Dubois et al., 2021). In 2018, NIA-AA proposed the A/T/N framework for a better biological definition of AD, with A referring to evidence of Aβ deposition, T reflecting evidence of tau pathology, and N standing for evidence of neuronal damage (Jack et al., 2018). The A/T/N framework is well received by the research community, as it facilitates clinical investigation into the highly heterogenous MCI/dementia population by providing an unbiased classification scheme, however, its generalisation to clinical practice is not recommended to date (Dubois et al., 2021).

1.2 Neuroinflammation: concept and components

Various pathological conditions, including infection, ischemia, haemorrhage, trauma and protein aggregation can initiate an inflammatory response in the CNS, which is generally termed neuroinflammation. The major players in the inflammatory process are activated microglia and astrocytes, but other cells such as infiltrating macrophages and vascular endothelial cells also contribute to neuroinflammation. The activated cells usually lose their homeostatic functions (Liddelow et al., 2017), and could further cause damage to neuronal structures directly or via various pro-inflammatory cytokines, chemokines and other messengers including IL-1β, IL-6, IL-18, TNF, CCL1, CXCL1, NO and prostaglandins

(DiSabato, Quan, & Godbout, 2016; Heneka, Kummer, & Latz, 2014; S. Hong et al., 2016). These pro-inflammatory molecules could further cause damage to neuronal cells and inhibit neurogenesis (Lyman, Lloyd, Ji, Vizcaychipi, & Ma, 2014; Micheau & Tschopp, 2003; Mishra, Kim, Shin, & Thayer, 2012). Meanwhile, in normal circumstances anti-inflammatory cytokines, such as IL-10 and IL-11, are also produced as negative feedback to the pro-inflammatory pathways (Calsolaro & Edison, 2016). However, in neurodegenerative disease, chronic stimuli from abnormal protein aggregations could break the balance and cause persistent neuroinflammation, which is considered to facilitate the disease process (Heneka et al., 2015).

1.2.1 Microglia

Microglia are resident myeloid lineage immune cells in the CNS, which originate from the yolk sac and later migrate to the CNS during embryonic development (Ginhoux et al., 2010; Kierdorf et al., 2013). Under normal physiological conditions, microglia take a highly ramified form and survey the surrounding environment constantly with their fine processes (Nimmerjahn, Kirchhoff, & Helmchen, 2005). Microglia express various surface receptors for damage-associated molecular patterns (DAMPs) and pathogen-associated molecular patterns (PAMPs), which could recognise endogenous and exogenous pathological factors including Aβ and tau species and induce microglial activation (Heneka et al., 2015). Activated microglia lose the ramified morphology but gain the capability to internalise the pathogenic particles via endocytosis, phagocytosis or pinocytosis, degrade them by endocytic pathways and activate inflammatory associated genes including the those for cytokines and chemokines, which play central role in neuroinflammation (Sole-Domenech, Cruz, Capetillo-Zarate, & Maxfield, 2016) (Owens, Khorooshi, Wlodarczyk, & Asgari, 2014). Under temporary stimuli, microglial activation could resolve by itself via negative feedback, while in the context of aging and neurodegeneration where there are constant stimuli from the

protein deposits, microglia are prone to sustained activation which is now considered to be a vital part of neurodegeneration (Leng & Edison, 2021; Spittau, 2017).

Traditional histopathology method relied on cell morphology and immunohistochemistry markers such as CD68, HLA-DR, Iba-1 and arginase 1 (ARG1) to probe the function of microglia and it was proposed that activated microglia could fall in M1-M2 phenotypes, as macrophages do (Heneka et al., 2015; Hopperton, Mohammad, Trepanier, Giuliano, & Bazinet, 2018; Minett et al., 2016). With the M1-M2 dichotomy, the M1 type was supposed to be a pro-inflammatory phenotype while M2 type was anti-inflammatory(Varnum & Ikezu, 2012). However, emerging evidence from recent transcriptomic studies has challenged the over-simplified model, arguing that activated microglia do not follow the binary path at all (Ransohoff, 2016). Moreover, there have been suspicions that the traditional immunohistochemistry markers such as CD68 and HLA-DR lack the specificity to identify pro-inflammatory and ant-inflammatory microglia (Walker & Lue, 2015),(Kim, Nakamura, & Hsieh, 2016). Despite the ongoing debate, the pro- and anti-inflammatory framework is still in wide use, reflecting the hypothesis that activated microglia could be over all either harmful (M1) or protective (M2) to the brain tissue.

With rapid advance in transcriptomic studies, the transition from homeostatic microglia to disease-associated microglia (DAM) has been depicted at transcription level, with homeostatic genes downregulated while others upregulated, including apolipoprotein E (APOE), triggering receptor expressed on myeloid cells 2 (TREM2) and TYRO protein tyrosine kinase-binding protein (TYROBP), which are AD-related risk alleles (Keren-Shaul et al., 2017). The process of DAM activation has also been elucidated, where microglia undergo an initial TREM2-independent step and following TREM2-dependent activation, which explained the strong genomic association between TREM2 alleles and AD risk (Jay, von Saucken, & Landreth, 2017). In ageing brains, microglia have shifted transcriptomic

profile with decreased gene transcription of cytoskeleton-associated proteins, cell surface receptors and adhesion molecules, and upregulation of inflammation-associated genes including IL-15, CXCR4, VEGF4 and RUNX3 (Galatro et al., 2017). Further, in a mouse model of AD (CK-p25 mouse), a temporal shift of microglial transcriptomic/phenotypic profile has been found, with early response marked by proliferation genes expression and late response associated with immune-related genes (Mathys et al., 2017). However, it should be noted that significant heterogeneity of transcriptomes exists in late-response microglia (sub-clusters), which is consistent with histopathology findings of diverse microglial morphology and immunology profiles (Mathys et al., 2017). Interestingly, analysis on microglial transcriptomics in different animal models including amyloid and tauopathy models revealed more diverse phenotypes, suggesting amyloid and tau may induce different microglial response at gene and molecular level (Friedman et al., 2018). Furthermore, spatial microglial transcriptomic heterogeneity has been observed in the brain, which might be related to the regional resilience to amyloid and tau pathology propagation (Masuda et al., 2019; Prokop et al., 2019).

The advance of transcriptomic studies has encouraged investigation into strategies manipulating microglial phenotypes via key upstream molecules, such as TREM2, which however, led to conflicting outcomes. For example, while Lee et al. reported that enhancing microglial TREM2 expression upregulated phagocytosis genes and mitigated inflammation associated genes, conferring a neuroprotective effect(C. Y. D. Lee et al., 2018), others observed that microglial TREM2 activation induced APOE-dependent pathway toward loss of homeostatic function and expression of inflammatory molecules, which was proved to be detrimental for neuronal survival (Krasemann et al., 2017). Knockout of TREM2 gene has also led to conflicting results with regard to plaque clearance and neuroprotection (Jay et al., 2015; Y. Wang et al., 2016).

The rapid advance of single cell transcriptomics and proteomics has greatly challenged our perception of cells in health and disease. There is an ongoing debate whether we should understand the states of microglia as continuous between two extremes or discontinuous. However, the relationship between the two theories could be just like that between Newtonian mechanics and quantum mechanics, with a continuous law that apply to macroscopic world driven by discontinuous events happening in microcosms. Thus, it might be a practical way to understand the function of microglia with the continuous model, though it is not reasonable to infer the role of a cell with a handful of microscopic markers. In summary, while the exact point of microglia phenotypic conversion and its impact on disease progression is still in debate, the spatial and temporal diversity of microglia should be considered in clinical and preclinical studies (Figure 1.1).

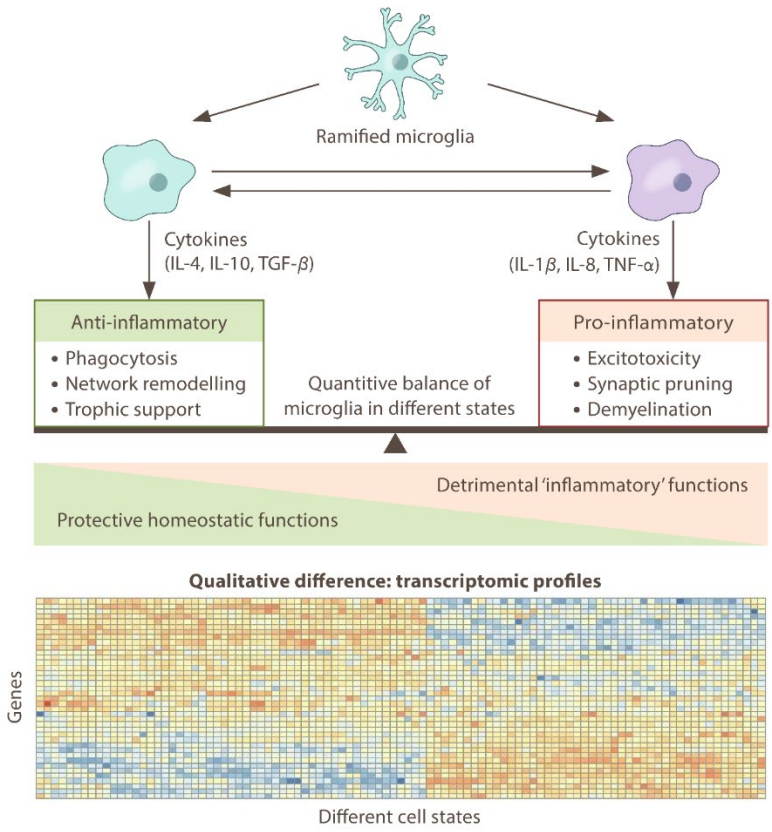

Figure 1.1 The multifaceted role of microglia in neurological diseases.

Under certain conditions microglia play a protective role by secreting anti-inflammatory cytokines, performing phagocytosis, and supporting network remodelling, while under other conditions microglia contribute to neuroinflammation. It is believed that the phenotypic change to microglia underlies this phenomenon, and a pro-inflammatory/anti-inflammatory scheme has been proposed to categorize microglial phenotype.

1.2.2 Astrocyte

Astrocytes generally take protoplasmic form in grey matter and fibrous form in white matter of the brain. Structurally, the astrocyte end feet form the outer layer of the blood-brain barrier (BBB) and envelope synapses. Physiologically, they regulate cerebral blood flow, induce synaptic formation, provide metabolic and neurotrophic support for neurons, and regulate fluid and neurotransmitter homeostasis (Attwell et al., 2010; Eroglu & Barres, 2010; Pekny et al., 2016). Recent advances have also suggested they are involved in the glymphatic clearance of amyloid and tau species (Jessen, Munk, Lundgaard, & Nedergaard, 2015; Tarasoff-Conway et al., 2015). Under pathological conditions, astrocytes respond by reactive gliosis, which is a vital part of neuroinflammation, and is marked by upregulation of GFAP expression (Pekny, Wilhelmsson, & Pekna, 2014). However, diverse phenotypes have been observed in the activated astrocyte population, with A1 phenotype activated via NF-κB and A2 phenotype induced by Signal Transducers and Activators of Transcription 3 (STAT3) pathway (Liddelow & Barres, 2017). It has been suggested that A1 phenotype of astrocytes lose homeostatic functions, express pro-inflammatory molecules, and could induce neuronal apoptosis, while A2 astrocytes express various neurotrophic molecules and are ‘protective’ (Liddelow et al., 2017). However, this binary scheme of astrocyte activation is still debatable (Martinez & Gordon, 2014).

Preclinical studies have observed that reactive astrocytes could migrate to amyloid plaques and degrade Aβ polymers (Wyss-Coray et al., 2003), and Aβ containing granules are found in human brains with AD, suggesting an effort of Aβ clearance by astrocytes (Thal et al., 2000). On the other hand, majority of activated astrocytes in post-mortem AD brains have been identified as A1 astrocytes which is supposed to be toxic to neurons (Wyss-Coray et al., 2003). In animal models of AD, A1 astrocytes have been found to induce neuronal excitotoxicity via excessive release of GABA and glutamate, disrupt cerebral microcirculation and BBB integrity(Jo et al., 2014; Kisler, Nelson, Montagne, & Zlokovic, 2017; E. A. Winkler et al., 2015). The crosstalk between astrocytes and microglia in inflammatory milieu may also exaggerate the toxic effect of each cell type (Liddelow et al., 2017) (Figure 1.2A and 1.2B).

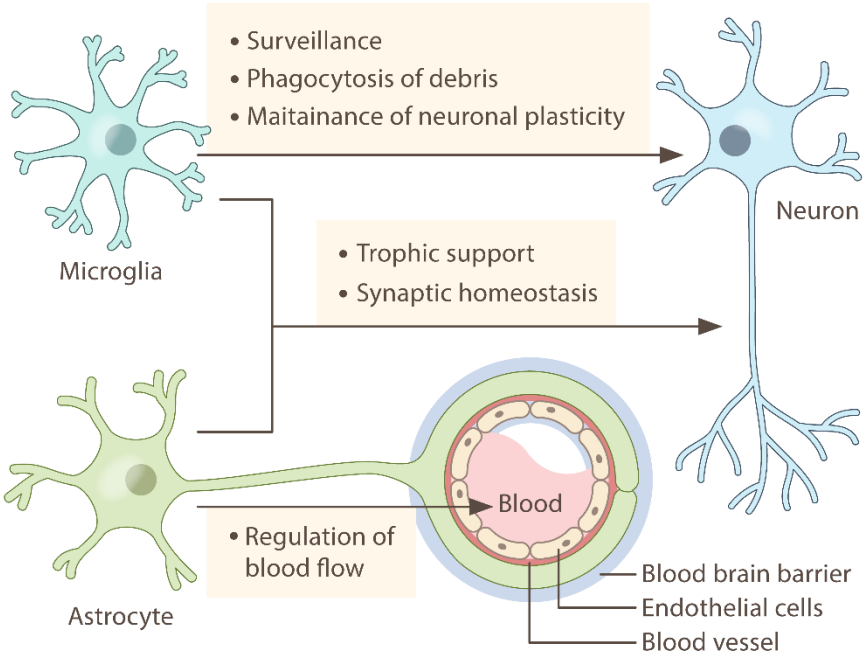

Figure 1.2A Physiological function of glial cells

Under physiological condition, ramified microglia survey the brain microenvironment and sense damage signals, make transient contact with neuronal network structures, including synapses and axons. These dynamic ramifired cells provide immune surveillance and trophic support to the CNS, remove pathogen or debris and are involved in maintenance of synaptic homeostasis and neuronal plasticity. The processes of astrocytes form the last layer of the blood-brain barrier and closely envelope synapses. Physiological roles of astrocytes include regulation of cerebral blood flow, maintenance of synaptic homeostasis, and neurotrophic support.

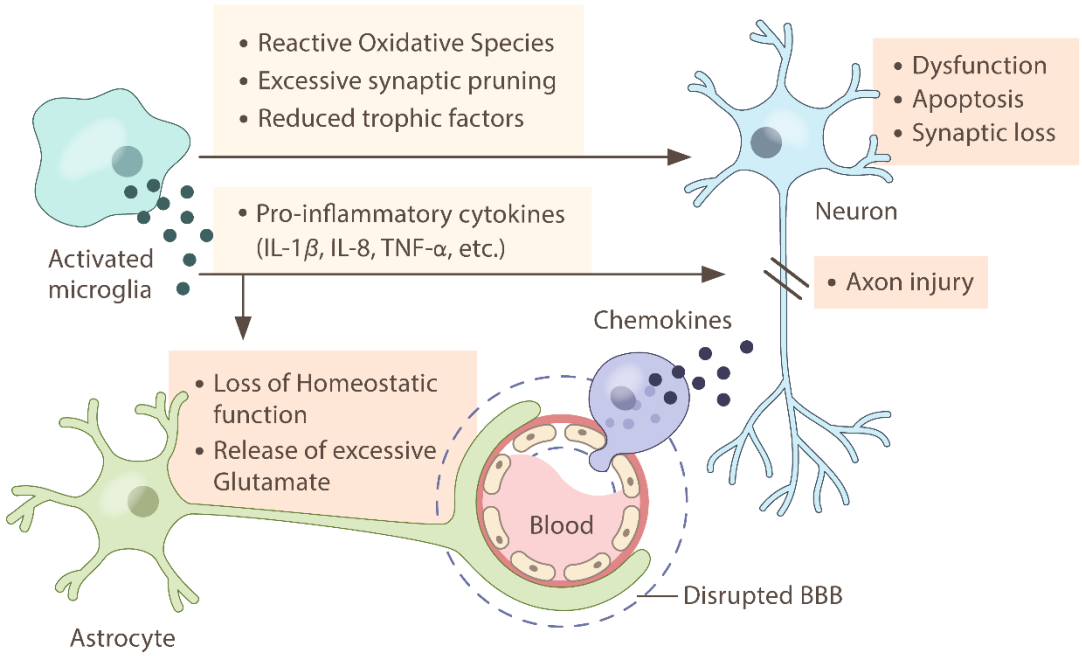

Figure 1.2B Inflammatory response of glia cells

Under pathological challenge, activated microglia, astrocytes as well as macrophages migrating through damaged BBB contribute to neuroinflammation. These activated cells lose homeostatic functions, secrete less neurotrophic factor and more pro-inflammatory

cytokine/chemokines, which could help pathogen/toxin clearance but also lead to neuronal dysfunction and damage. Activated microglia have been found to directly eliminate synaptic structures.

1.3 Evaluation of neuroinflammation in AD in vivo

To facilitate the investigation on the role of neuroinflammation in diseases, especially longitudinally, biomarkers have been developed to evaluate the level of neuroinflammation in vivo. These biomarkers can be classified as fluid (blood and CSF) and imaging-based markers.

1.3.1 Fluid Biomarkers

Traditional fluid biomarkers of neuroinflammation encompass various cytokines, including IL-1β, IL-2, IL-6, IL-8, IL-10, IL-12, IL-18, interferon-γ (IFN-γ), TNF-γ and transforming growth factor-β (TGF-β). While several studies reported that in AD patients there was an overall increase of IL-1β, IL-6, IL-12, IL-18, TNF-γ and TGF-β, significant discrepancies between the studies questioned the specificity of these traditional inflammatory markers (Swardfager et al., 2010). More importantly, the production of the aforementioned cytokines is associated with various non-specific inflammatory events, which undermines their potential as biomarkers of neuroinflammation. Novel glial activation markers include chitinase-3-like protein 1 (known as YKL-40) and monocyte chemotactic protein 1 (MCP1) (El Kadmiri, Said, Slassi, El Moutawakil, & Nadifi, 2018). A recent meta-analysis has confirmed that YKL-40 is moderately associated with AD, while the change of MCP-1 or GFAP was concluded as nonsignificant. Activated astrocytes and microglia have been found to be the primary source of YKL -40 in AD (Baldacci, Lista, Cavedo, Bonuccelli, & Hampel, 2017), which is elevated from preclinical stage and increases as disease progress (Alcolea et al., 2015; Sutphen et al.,

2015). More recently, soluble TREM2 (sTREM2) have been the frontier of investigation. sTREM2 is produced by cleavage of TREM2 receptor on microglial membrane, and has been proposed as a specific marker of microglial activation and TREM2 signalling (Wunderlich et al., 2013). Increased concentration of sTREM2 has been reported in the CSF of AD patients, which further rises as disease progresses (Henjum et al., 2016) (Suarez-Calvet et al., 2016). More recently, studies have reported that CSF sTREM2 is positively associated with tau pathology (Suarez-Calvet et al., 2019), and that interestingly, higher sTREM2 level is associated with better cognitive outcome in patients along AD continuum (Ewers et al., 2019; Franzmeier, Suarez-Calvet, et al., 2020). These findings warrant further investigation into how sTREM2 is produced and may imply novel therapeutic targets.

1.3.2 TSPO imaging of neuroinflammation

The 18kDa translocator protein (TSPO), also known as peripheral benzodiazepine receptor (PBR) is an inner mitochondrial membrane protein expressed in various types of cells including microglia, astrocytes, endothelial cells, monocytes and macrophages (Edison & Brooks, 2018). TSPO forms part of the mitochondrial permeability transition pore, which is involved in mitochondrial permeability regulation, steroid synthesis and inflammatory response regulation (Edison & Brooks, 2018). It has been demonstrated that activated microglia upregulate the expression of TSPO protein under various pathological conditions, including ischemia, trauma and exposure to abnormal protein aggregates including Aβ plaques and NFT (Venneti, Lopresti, & Wiley, 2006)·(Diorio, Welner, Butterworth, Meaney, & Suranyi-Cadotte, 1991).However, in vivo imaging using TSPO tracers could not distinguish different microglia phenotypes, nor could it differentiate signals from other cells in the CNS. Activated astrocytes also overexpress TSPO protein (Ji et al., 2008) (Rojas et al., 2007), and albeit autoradiography studies suggest ^{3}H-PK11195 binding correlated better with immunohistochemical markers of microglia as compared to astrocyte markers in vitro

(Venneti, Wang, Nguyen, & Wiley, 2008), there is an ongoing debate on how specific TSPO tracers are in terms of evaluating microglial activation in vivo. Nevertheless, as microglial activation and astrocyte reaction accompany each other in neurodegenerative conditions, TSPO is still a valuable target to probe neuroinflammation in vivo in neurodegeneration (Varrone & Nordberg, 2015).

Currently TSPO ligands are the most commonly used tracers in neuroinflammation imaging studies, with multiple generations developed. The first generation TSPO ligand developed include Ro5-4864 and PK11195, with the latter outperformed the former and saw wide applications (Junck et al., 1989). However, ^{11}C-PK11195 still suffers from high nonspecific bindings and low signal to noise ratio (SNR). Therefore, the second-generation TSPO tracers were developed which encompass ^{11}C-PBR28, ^{11}C-DAA1106, ^{11}C-DPA713, and ^{18}F-PBR06 (Alam, Lee, & Lee, 2017). The second-generation tracers have better BBB permeability and higher affinity to TSPO, which however, is influenced by the rs6971 single-nucleotide polymorphism (147 Ala/Thr) of the TSPO gene, with the Ala/Ala carriers being high affinity binders (HAB), Ala/Thr carriers being mixed affinity binders (MAB) and Thr/Thr variant being low affinity binders (LAB) (D. R. Owen et al., 2012) (Kreisl, Jenko, Hines, Lyoo, Corona, Morse, Zoghbi, Hyde, Kleinman, Pike, McMahon, Innis, & Biomarkers Consortium, 2013). For ^{11}C-PBR28, LABs have approximately 50-fold lower affinity compared to HABs, resulting in negligible PET signals and therefore not suitable for participating imaging studies (D. R. J. Owen et al., 2011). Further, the affinity difference between HABs and MABs makes controlling for the effect of TSPO genotype essential in imaging analysis (Kreisl, Jenko, Hines, Lyoo, Corona, Morse, Zoghbi, Hyde, Kleinman, Pike, McMahon, Innis, & Radiolig, 2013).

1.4 Interaction between neuroinflammation and Alzheimer's pathologies

Pathology studies have established that activated ameboid form microglia collocate with amyloid plaques and NFT in post-mortem AD brains (Hayes, Thaker, Iwatsubo, Pickering-Brown, & Mann, 2002; Mcgeer, Itagaki, Tago, & Mcgeer, 1987; Tooyama, Kimura, Akiyama, & Mcgeer, 1990). The temporal emergence of Aβ plaques, microglial activation and NFT has given rise to the 'amyloid cascade-inflammation hypothesis', positioning microglial activation between amyloid deposition and further tau pathology propagation and neuroinflammation (Hayes et al., 2002; Kitazawa, Yamasaki, & LaFerla, 2004; McGeer & McGeer, 2013).

It has been well acknowledged that Aβ oligomers can activated glia cells which in turn produce neurotoxic proinflammatory cytokines, chemokines and reactive oxygen species (ROS) (Akiyama et al., 2000; Delbo, Angeretti, Lucca, Desimoni, & Forloni, 1995; Hanisch, 2002). Microglia recognise Aβ species via various pattern recognition receptors (PRRs), including Toll-like receptors (TLR1, TLR2, TLR4, TLR6, etc.), CD14, CD47, α6β1 integrin, scavenger receptors (SR-As and SA-Bs, including CD36), which then activate downstream pathways and induce phagocytic change or expression of the pro-inflammatory modules (Alawieyah Syed Mortadza, Sim, Neubrand, & Jiang, 2018; S. Liu et al., 2012; Murgas, Godoy, & von Bernhardi, 2012; Venegas & Heneka, 2017). As examples, activation of TLR2 can lead to IL-8 and TNF-α expression(S. Liu et al., 2012), activation of SRs upregulates IL-1β and NO production through NF-κB, c-Jun N-terminal kinase (JNK) and mitogen-activated protein kinase (MAPK) pathways (Murgas et al., 2012), while CD36-CD47-α6β1 integrin complex mediates phagocytic change of microglia (Koenigsknecht & Landreth, 2004). More recent research has revealed the pyrin domain-containing 3 (NLRP3) inflammasome recruitment as an important event in microglial pro-inflammatory response, which is

followed by subsequent expression of caspase-1 and maturation of IL-1β(Heneka et al., 2013; Strowig, Henao-Mejia, Elinav, & Flavell, 2012).

The phagocytic function of microglia has also been well established, with *in vitro* experiments demonstrating that microglia could phagocytose and degrade amyloid fibrils via autophagy pathways (Cho et al., 2014; Paresce, Chung, & Maxfield, 1997; Plaza-Zabala, Sierra-Torre, & Sierra, 2017). However, the capability of microglia to handle amyloid species in actual AD brains is still debatable, as it has been demonstrated that more toxic Aβ oligomers could induce pro-inflammatory phenotype of microglia, which produce inflammatory cytokines but are inefficient at phagocytosing fibrillary amyloid (Pan et al., 2011). Further, microglia in late stage of AD are often found in a morphologically dystrophic state, implying loss of surveillance functions (Navarro et al., 2018; Streit, Braak, Xue, & Bechmann, 2009). Further, only limited proportion of TREM2- and CD68-positive microglia were found in microglia population around amyloid plaques in AD and Down syndrome patients' brains, suggesting an incompetence of phagocytic function in majority of activated microglia (Raha-Chowdhury et al., 2018). It has also been suggested that the loss of microglial phagocytic functions is associated with ageing, which may explain the reduced resilience to AD pathology in the aged population (Streit, 2006; Streit, Sammons, Kuhns, & Sparks, 2004).

Recently, there has been emerging evidence that activated microglia could further exaggerate Aβ pathology by promoting Aβ genesis and facilitate Aβ cross seeding in AD. It has been reported that the pro-inflammatory cytokines produced by microglia, such as IL-1β, IL-6, and TNF, could activate NF-κB pathway and promote beta secretase (BACE1) expression in neurons, which acts to cleave APP into pathogenic Aβ monomers (Chen et al., 2012; Hawcroft, Gardner, & Hull, 2003). More recently, Heneka and colleagues have demonstrated that the NLRP3 inflammasome pathway in activated microglia could lead to assembly and

release of apoptosis-associated speck-like protein containing a CARD (ASC) specks, which in extracellular space could bind to soluble Aβ species and form the core of amyloid plaques (Venegas et al., 2017). While the process could also be protective as the soluble Aβ species have been proved to be more neurotoxic compared to fibril Aβ, the same experiment showed an overall detrimental effect of NLRP3 pathway by showing the benefits of ASC knockout.

Hyperphosphorylated tau oligomers and fibrils have also been proven to be potent stimuli for microglial activation in vitro and in vivo, marked by DAM genes' upregulation, among which the CD68 and TYROBP genes are found as hubs of gene association network (Morales, Jimenez, Mancilla, & Maccioni, 2013; Wes et al., 2014). The classical and alternative complement pathways have been suggested to be critical pathways in tau induced microglial activation (Wes et al., 2014), and it has been observed that activated microglia in cell culture and healthy mice are capable of phagocytosing tau fibrils (Bolos et al., 2016). However, pathology studies on late-stage AD human brains have observed morphologically degenerated microglia to be closely associated with tau pathology, questioning the ability of microglial defence against tau species (Sanchez-Mejias et al., 2016; Streit et al., 2009). Based on the observation that the emergence of dystrophic microglia is chronologically ahead of tau pathology, it has been further proposed that ageing and chronic exposure to Aβ may undermine microglial function and pave the way for spreading of tau pathology (Streit et al., 2018). Indeed, previous literature have suggested that the phagocytosis and exosome secretion of tau species by microglia may provide an intraneuronal propagation pathway in conjunction with trans-synaptic seeding of tau pathology (Asai et al., 2015). With coexisting amyloid pathology, microglia have been shown to exacerbate tau pathology in synergy with Aβ, with microglial NLRP3 pathway being a possible bridge between amyloid and tau pathologies (Felsky et al., 2019; Ising et al., 2019).

Efforts have been made to untangle the complex relationship among neuroinflammation, amyloid deposition and tau pathology. The TREM2/TYROBP pathway has been identified as a common pathway in both Aβ-42 and tau-induced microglial activation, with over >50% overlap among Aβ/TREM2 and tau/TREM2 induced gene expression, which suggest microglial activation as a common factor in both amyloid and tau toxicity (Sekiya et al., 2018). Intriguingly, the same study has observed that TREM2 signalling can suppress half of the gene modules activated by Aβ-42 alone, with presumably protective effects, while tau and TREM2 induced pathways could exaggerate neuronal damage synergically. These findings underline the differential position of neuroinflammation in context of amyloid and tau pathology. Indeed, other studies manipulating microglial activation through progranulin, CX3CL/CXC3R pathways have reported opposing effects on development of amyloid and tau pathologies (Bolos et al., 2017; S. Lee et al., 2014; Takahashi et al., 2017). The different interactions among neuroinflammation, Aβ and tau pathologies also highlight the need to consider the stage of disease when interpreting the role of neuroinflammation in AD, as the dominant pathology might be different at early and late stages (amyloid and tau, respectively) (Dani et al., 2018a; Fan, Brooks, Okello, & Edison, 2017; L. Hamelin et al., 2016; Parbo et al., 2018).

1.5 Impact of neuroinflammation on AD progression: current evidence

Epidemiological studies have observed that mid-life systemic inflammatory factors such as diabetes and smoking, as well as CNS injury are associated with increased risk of AD (Dunn, Mullee, Perry, & Holmes, 2005; Johnson et al., 2013). Further, several studies have suggested a possible protective effect of NSAIDs against AD in the elderly, which have provided first evidence that neuroinflammation might be involved in initiation of AD (Corrada, Stewart, & Kawas, 1996; Etminan, Gill, & Samii, 2003). The systemic inflammation factors could induce neuroinflammation by cytokines which could enter the

CNS via circumventricular organs or disrupted BBB, and through vagal nerve transport system (Calsolaro & Edison, 2016), which have been supported by the observation of activated microglia in young patients who suffered from systemic inflammation premortem (Tischer et al., 2016).

It has been reported that microglial activation starts even at pre-plaque stage in animal models and MCI patients, indicating the involvement of inflammation from the earliest stage of AD (Dani et al., 2019; Femminella et al., 2019; L Hamelin et al., 2016; Kreisl, Henter, & Innis, 2018; Kreisl et al., 2016a; Okello et al., 2009). More intriguingly, in non-human primates it has been observed that co-injection of LPS and Aβ, or injection of Aβ in brains with chronic inflammation conditioning, but not injection of Aβ alone, could lead to the formation of Aβ plaques (Philippens et al., 2017). Human post-mortem study has also observed microglial activation in all asymptomatic subjects with evidence of amyloidosis, which strongly suggest neuroinflammation as a necessary condition for AD pathogenesis (Streit et al., 2009). Recent genome wide association studies have further substantiated the position of neuroinflammation in AD pathogenesis, with the finding that mutations in microglial/innate immune genes are strongly associated with increased risk of AD, including CD33, TREM2, complement receptor type 1 (Hollingworth et al., 2011; Jonsson et al., 2013; Lambert et al., 2013).

Clinical PET/MRI studies using TSPO tracers have reported negative associations between microglial activation and hippocampal volume/metabolism in patients with AD dementia (Fan, Aman, et al., 2015; Femminella et al., 2016). More recent imaging studies have also observed that microglial activation correlates with disruption of brain's functional connectivity (Passamonti et al., 2019; Yokoi et al., 2018). More importantly, negative relationship between neuroinflammation and cognitive performance has been reported in AD dementia patients (Edison et al., 2008; Kreisl, Lyoo, et al., 2013; Yokokura et al., 2011). The

evidence that neuroinflammation has a detrimental role in late disease trajectory is further supported by preclinical findings. It has been established that the proinflammatory cytokines secreted by activated microglia, such as IL-6, IL-1β and TNF can cause functional disruption and structural damage to neurons (Combs, Karlo, Kao, & Landreth, 2001; Floden, Li, & Combs, 2005; Martin, Boucher, Fontaine, & Delarasse, 2017; Spangenberg & Green, 2017). More recent studies have demonstrated the excessive synaptic pruning by microglia in animal models of AD, which leads to synaptic loss and impaired long-term potentiation (S. Hong et al., 2016; Neniskyte, Neher, & Brown, 2011). The complement system seems to play a key role in the excessive synaptic elimination process, as complement C3 knockout seems to protect against the process in APP/PS1 mice, with the presence of activated microglia and pro-inflammatory cytokines (Shi et al., 2017). More interestingly, there has been evidence that microglia may have a circuit-specific preference of pathological synaptic pruning, which might be related to the stereotypical pattern of neurodegeneration and NFT formation in AD (Braak & Del Tredici, 2015; Raj, Kuceyeski, & Weiner, 2012).

More recent efforts have been made on investigating the dynamic of neuroinflammation along disease trajectory and its impact on disease progression. Previously, our group have observed a longitudinal increase of microglial activation in 6 out of 8 AD patients using ^{11}C-PK11195, but with a dynamic change of 'hot spot' of inflammation, which correlated with metabolic decline (Fan, Okello, Brooks, & Edison, 2015). Interestingly, 2 patients showed a longitudinal decline of neuroinflammation, which might be caused by the 'burn out' of microglia at the terminal stage (Sanchez-Mejias et al., 2016). Kreisl and colleagues have also reported a progressive increase of ^{11}C-PBR28 uptake in a combined AD and MCI cohort (Kreisl et al., 2016a).

Interestingly, in early stage of the disease (MCI) patients, there has been conflicting evidence on dynamic change of microglial activation. Hamline and colleagues have reported that there

was comparable longitudinal increase of microglial activation in both prodromal and demented AD patients, using the tracer ^{18}F-DPA. They have further observed distinct dynamic patterns of neuroinflammation (lower initial level and rapid rise vs high baseline level and slow progression), with the latter pattern associated with better outcome (Hamelin et al., 2018). On the other hand, our group have found different dynamic change of neuroinflammation in AD and MCI patients, with MCI cohort showing a longitudinal decrease of ^{11}C-PK11195 uptake and AD patients showing an increase (Fan et al., 2017). However, the power of evidence from both cohorts are limited by their sample sizes and coverage of disease spectrum. Recently, a meta-analysis has been performed to provide better understanding of the spatial and temporal change of neuroinflammation, and have suggested a longitudinal increase of microglial activation along the AD trajectory based on current evidence (Bradburn, Murgatroyd, & Ray, 2019). Furthermore, the meta-analysis has also confirmed a negative relationship between parietal neuroinflammation and cognitive performance in AD patients, supporting a detrimental effect of microglial activation in AD dementia. The study has also suggested a spatial development of neuroinflammation in AD, starting from the neocortex in the MCI stage and spread ventrally throughout the brain, with temporal regions most heavily involved AD (Bradburn et al., 2019). There is still ongoing controversy on whether neuroinflammation is protective or harmful in MCI patients, with conflicting evidence emerging (Fan et al., 2017; Femminella et al., 2019; Malpetti et al., 2020). It should be noted however, that caution should be taken when interpreting the PET imaging studies across research centres, as various tracers and analytical methodologies (Leng & Edison, 2021) (Figure 1.3).

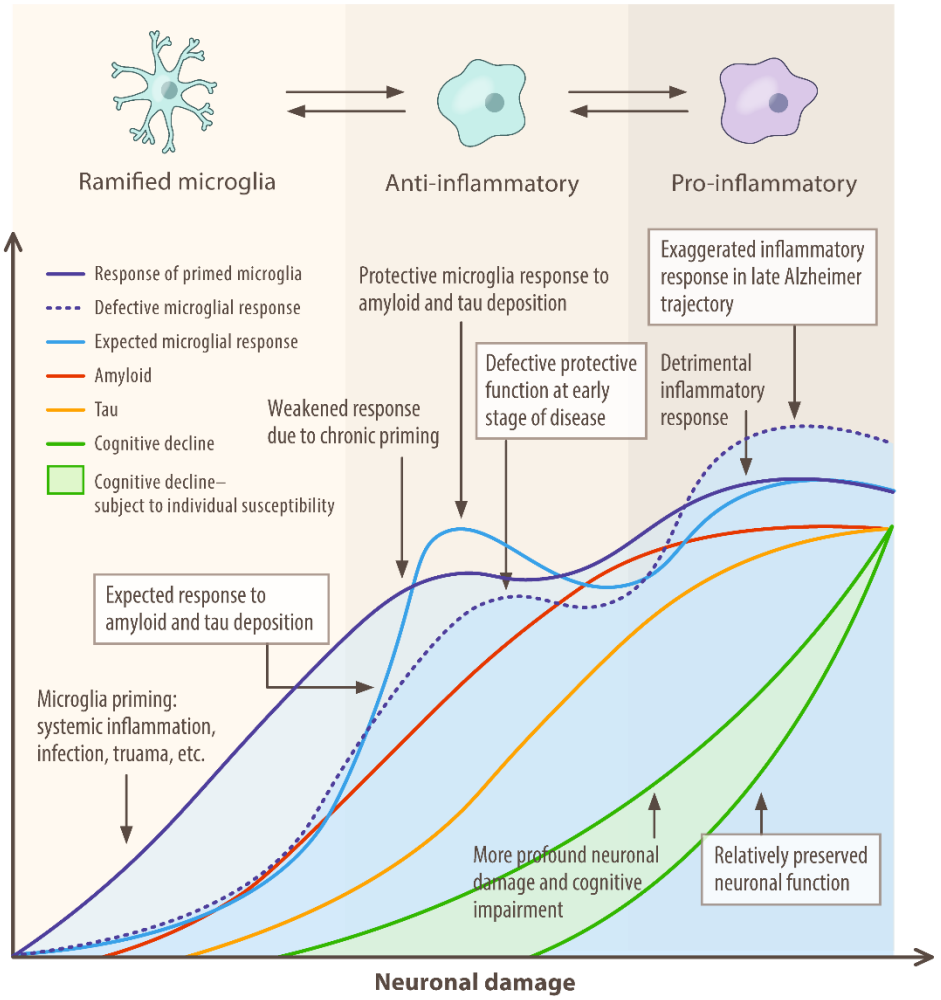

Figure 1.3 Dynamic of microglial activation and its impact on disease progression

Patients with defective microglial protection (phenotype) may present with cognitive decline at an early pathological stage (marked by amyloid and tau load) compared to those with normal microglial function. Priming of microglia due to chronic systemic inflammation, infection or brain trauma may cause a weakened primary protective response of microglia under degenerative challenge. Microglial functions vary individually, and those with defective protective functions due to genetic or acquired factors may present with increased susceptibility to Alzheimer's disease.

To summarise, while there has been evidence of a detrimental influence from neuroinflammation in late AD stage, its role in the broader AD spectrum, especially towards

the earlier stages still remains to be explored and established. Further, the mechanism by which neuroinflammation may influence disease progression in humans still awaits to be clarified before novel disease modifying strategies could be developed with precision.

1.6 Functional and Structural Connectivity Impairment in AD

With the advance of cognitive neuroscience, the brain is now considered as a network organ, the functioning of which depends on information flow across local and distal functionally associated brain regions (Horwitz, 2003). It has been well established that in various neurological disorders, including stroke, multiple sclerosis and neurodegeneration, focal neuronal deficit could not completely explain the clinical presentations, which could result from disruption of brain network with regard to cortical hub or white matter connections (van den Heuvel & Hulshoff Pol, 2010). Over the past two decades, AD is increasingly understood as a network disconnection syndrome. The first line of evidence came from functional MRI (fMRI) studies, which have consistently observed an impairment of the default mode network (DMN) during resting state in AD and preclinical AD patients (Lustig et al., 2003; Seeley, Crawford, Zhou, Miller, & Greicius, 2009; Sorg et al., 2007). Spontaneous activity has been found in the DMN, which consists of the posterior cingulate, precuneus, medial prefrontal, lateral parietal cortices and putatively hippocampi (Buckner, Andrews-Hanna, & Schacter, 2008). The DMN is believed to be associated with emotional processing, memory recollection, self-referential mental activities (M. E. Raichle, 2015). It has been further established that the functional connectivity within DMN is associated with the cognitive performance in cognitively impaired patients (Verfaillie et al., 2018). Interestingly, regions with increased functional association within prefrontal, parietal, occipital and temporal lobe have also been observed in parallel with those with decreased communication, possibly reflecting a compensatory mechanism (Qi et al., 2010; K. Wang et al., 2007). This compensating mechanism is a reminder that dementia is based on the dysfunction of the brain

as a functional system but not based purely on structural impairment. In light of this, it is interesting to consider the well observed fluctuation of cognitive status in AD patients, which could be rather better explained by the functional disruption of the neuronal circuit than the permanent structural changes of the brain (Palop, Chin, & Mucke, 2006). Thus, investigating the underlying pathophysiology of circuit impairment as well as compensation mechanism might offer a new perspective of intervention.

Apart from the individual functional networks, the organisation of functional network at whole brain level has also been investigated using graph theory (details in chapter 3). It has been established that human brain has a small-world organisation to obtain a balance between local and global efficiency in information processing (Achard, Salvador, Whitcher, Suckling, & Bullmore, 2006). In AD, the topological organisation of brain's functional network has been found to be disrupted compared to healthy brain (delEtoile & Adeli, 2017): reduced small-worldness, as well as altered local and global efficiency have been reported.

This functional network failure could be at least partly attributed to structural connectivity impairment, as diffusion tensor imaging (DTI) studies have found an early degeneration of susceptible white matter tracts along Alzheimer trajectory, many of which, intriguingly, are connected to the impaired functional hubs (Hahn et al., 2013). The white matter impairment has been further found to correlate with cognitive decline (Bosch et al., 2012) in AD patients. White matter damage has also been reported early in disease trajectory. Several studies have found white matter damage in MCI patients and even middle-aged asymptomatic subjects with family history, including the posterior cingulum bundle, uncinate fasciculus and centrum semiovale (Mito et al., 2018) (Douaud et al., 2011), suggesting WM damage as an early event in Alzheimer trajectory (Bendlin et al., 2010) and even before grey matter atrophy becomes evident (Y. J. Hong et al., 2016).

Although lesions in WM tracts have been previously presumed as secondary change due to grey matter atrophy or cerebrovascular diseases, accumulating evidence suggests it as an independent feature associated with Alzheimer's pathology. Early pathology studies have found disproportionate damage of white matter tracts and corresponding grey matter atrophy, which could not be explained by concurrent vascular disease (Caso, Agosta, & Filippi, 2016; Sjobeck, Haglund, & Englund, 2006a). Further, recent imaging studies have reported positive correlations between impaired WM integrity and amyloid load, as well as NFT stages (Kantarci et al., 2017; Racine et al., 2014), suggesting a specific WM damage relating to Alzheimer's pathology. More interestingly, the imaging evidence of white matter predilection falls in line with the retrogenesis theory of AD, which derives from pathological observation that damage of axons and oligodendrocytes in reverse sequence to myelin formation and proposes that the process independently contributes to Alzheimer pathology (Benitez et al., 2014) (Braak & Del Tredici, 2015). This hypothesis has been further supported by the observation that cerebrospinal fluid AD markers correlate with WM damage in healthy subjects with family history of AD (Bendlin et al., 2012).

More intriguingly, recent studies on brain connectivity and AD have suggested an important role of brain's functional and structural network in the dissemination and propagation of amyloid and tau pathologies. In particular, the key hubs of functional brain network, especially within the DMN, where neuronal activities are supposed to be most frequent, are shown to be the earliest regions of amyloid deposition (Palmqvist et al., 2017). This phenomenon might be associated with the activity-dependent production of Aβ (Kamenetz et al., 2003b), though Iturria-Medina and colleagues have suggested that the emergence of Aβ deposition may also be related to brain's structural connectome (Iturria-Medina, Sotero, Toussaint, Evans, & Alzheimer's Disease Neuroimaging, 2014). With regard to tau pathology, early preclinical studies have established the prion-like properties of

hyperphosphorylated misfolded tau species (Frost & Diamond, 2010), and it has been proposed that trans-neuronal seeding of tau species underlies stereotypical spatial-temporal pattern of NFT pathology (Iba et al., 2013; L. Liu et al., 2012). With the recent wide application of tau PET imaging, studies have found a striking overlap between cross-regional covariance of tau tracer uptake and structural/functional connectivity pattern (Ossenkoppele et al., 2019). Further epidemiological modelling has suggested that structural connectivity best explained tau tracer-positivity covariance pattern across population (Vogel et al., 2020). More specifically, structural impairment of the hippocampal cingulum has been found to be able predict future tau deposition in the posterior cingulate cortex, strongly supporting the hypothesis that tau species propagates through the brain's connectome (Jacobs et al., 2018).

Given the evidence that connectivity disruption is not only associated with cognitive reserve in Alzheimer's disease, but is also involved in the propagation of amyloid and tau pathologies, understanding the factors associated with network disruption in AD is of paramount importance.

1.7 Microglia and brain connectivity

Microglia progenitors arise from primitive haematopoiesis early in the embryonic development. Primitive myeloid precursors arise from yolk sac. and then migrate into the developing brain from embryonic day 8.5 in mice (Ginhoux et al., 2010) (Kierdorf et al., 2013). During brain development, it has been demonstrated that microglia contribute to neurogenesis, migration and differentiation of neuron precursor cells (C. L. Cunningham, Martinez-Cerdeno, & Noctor, 2013) (Antony, Paquin, Nutt, Kaplan, & Miller, 2011), outgrowth of axons and positioning of interneurons (Squarzoni et al., 2014), as well as induction and remodelling of synapses (Lim et al., 2013) (Miyamoto et al., 2016) (Parkhurst

et al., 2013). Further, microglia have been suggested to be involved in myelination in development by providing cues for oligodendrocytes (Nave & Werner, 2014).

Accumulating evidence suggests microglia continue to maintain effective neuronal network in adulthood. It has been reported that microglia play a vital role in experience-driven plastic change of neuronal network, as seen in hippocampal long term potentiation and ocular dominance plasticity (Sipe et al., 2016) (Pascual, Ben Achour, Rostaing, Triller, & Bessis, 2012) (Pfeiffer, Avignone, & Nagerl, 2016). This process is believed to be mediated by activity-dependent dynamic and direct contact between microglia processes and synaptic structures (Posfai, Cserep, Orsolits, & Denes, 2019) and axon initial segments (AIS), where action potential is generated (Baalman et al., 2015). In white matter, evidence suggests a vital role of microglia in maintenance and repair of myelin under physiological conditions (Michell-Robinson et al., 2015) (Peferoen, Kipp, van der Valk, van Noort, & Amor, 2014).

However, the morphological and immunological profile of microglia change drastically in condition of aging and systemic inflammation, marked by spheroidal swelling, fragmentation of microglia processes, decreased intracellular contact and upregulated expression of CD68 (Streit et al., 2004) (Streit, 2006). This process is considered as microglial senescence, which is believed to reflect impaired homeostatic competence of microglia and indulge initiation of degeneration of neuronal networks (Streit et al., 2009) (Streit et al., 2018). It has been further demonstrated that under pathological conditions microglia undergo activation, adopting various phenotypes with different gene expression profiles, and consequently perform protective or destructive roles in diseases (Mathys et al., 2017) (Friedman et al., 2018) (Z. R. Yin et al., 2017).

1.8 Neuroinflammation may Influence Brain Connectivity in AD

Clinical observations that elevated CSF markers of microglia activation correlate with white matter microstructure damage (Melah et al., 2016) suggest a role of microglia in network damage in AD. Indeed, increased density of activated CD45+ microglia have been found in white matter of AD brains (Shah et al., 2010), where they co-localise with toxic amyloid plaques and dystrophic axons (Masliah et al., 1991). It is also interesting to consider that chronic activation of microglia and ongoing white matter damage observed after traumatic brain injury, one of the strongest epidemiological factors associated with AD, suggesting a role of microglia and white matter damage in the initiation of Alzheimer's pathology (Johnson et al., 2013).

Base on knowledge from preclinical studies, microglia might lead to brain network impairment in AD include loss of supportive functions, causing direct structural damage and mediating abnormal neuronal activity. The morphological changes of activated microglia in AD have been well documented, which include decreased cell surface area, number of branches, total branch length and ramification index (defined as actual cell surface area divided by surface area of a hypothetical sphere which have the same volume as the cell) (Plescher et al., 2018) (Davies, Ma, Jegathees, & Goldsbury, 2017), which limit the capability of microglia to perform homeostatic functions. For example, the contact of microglia with AIS is dramatically decreased during brain injury (Baalman et al., 2015). Moreover, microglia activated through complement pathway can engulf synapses inappropriately, leading to early synaptic loss and defect in long-term potentiation (S. Hong et al., 2016) (Neniskyte et al., 2011). Microglia mediated circuit-specific synaptic pruning has been reported as the major driver of familial frontotemporal dementia, which is also a common neurodegenerative disease (Lui et al., 2016). Consistently in AD subjects, neuroimaging studies found a negative relationship between cognitive function and

microglial activation, but not amyloid load (Edison et al., 2008) (Yokokura et al., 2011). With regard to white matter tracts, it has been suggested that microglia can cause direct damage to oligodendrocytes and axons through production of reactive oxygen species, matrix metalloproteinases, and pro-inflammatory cytokines (Peferoen et al., 2014). These pro-inflammatory cytokines, including IL-1b, TNF-alpha and IL-6, could further cause excitotoxicity to the neurons, leading to dysregulation of the functional network (Vezzani & Viviani, 2015). Given the role of microglia in adult network plasticity, one could also suppose that they may be involved in compensating mechanisms in diseased brains.

1.9 Hypothesis

Given current preclinical and clinical evidence, it could be hypothesised that:

Neuroinflammation in Alzheimer's disease can actively and independently contribute to the microstructural damage of neuronal circuits and disrupt normal neuronal activity functionally, the consequence of which are global impairment of the brain's macroscopic structural and functional network, and ultimately cognitive impairment.

Based on the prior hypothesis, the following predictions have been tested in the study:

(1) Neuroinflammation in Alzheimer's disease trajectory is associated with both functional and structural connectivity disruption, independent of amyloid pathology.
(2) Neuroinflammation in Alzheimer's disease trajectory can independently predict cognitive decline in the patients.

1.10 Approach of the Project

The current project aimed to test the hypothesis using PET and MRI imaging data **(already collected) form the 'amyloid and neuroinflammation' study by Dr Dani and Dr Edison**. ^{18}F-Flutemetamol, ^{18}F-AV1451, ^{11}C-PBR28 PET imaging were used to quantify amyloid, tau

pathologies and neuroinflammation, respectively. Resting-state fMRI and diffusion tensor MRI were used to evaluate the functional and structural networks of brain. Neuropsychological assessment records were reviewed to assess the relationship between imaging markers of AD and cross-sectional/longitudinal cognitive impairment.

The aim of the project is to test the hypotheses by analysing the multimodality imaging data, provide evidence on whether neuroinflammation is influencing cognitive deterioration in Alzheimer's disease, and investigate possible mechanisms. The challenges of the project reside in its multimodality nature, as robust inference relies on appropriate processing of imaging data and using multivariate statistical models, especially with each imaging modality providing high-dimensional data itself.

Therefore, the focus of the current project is to extract biological information from neuroimaging data using appropriate analytical procedures, to further analyse the high-dimensional data with appropriate statistical models to make inferences on the relations of pathological processes in disease, and finally to provide better understanding of neuroinflammation's role in Alzheimer's disease.

The study cohort recruitment and data availability of MCI study (regarding T1-weighted MRI and PET scans are summarised in Figure 1.4.

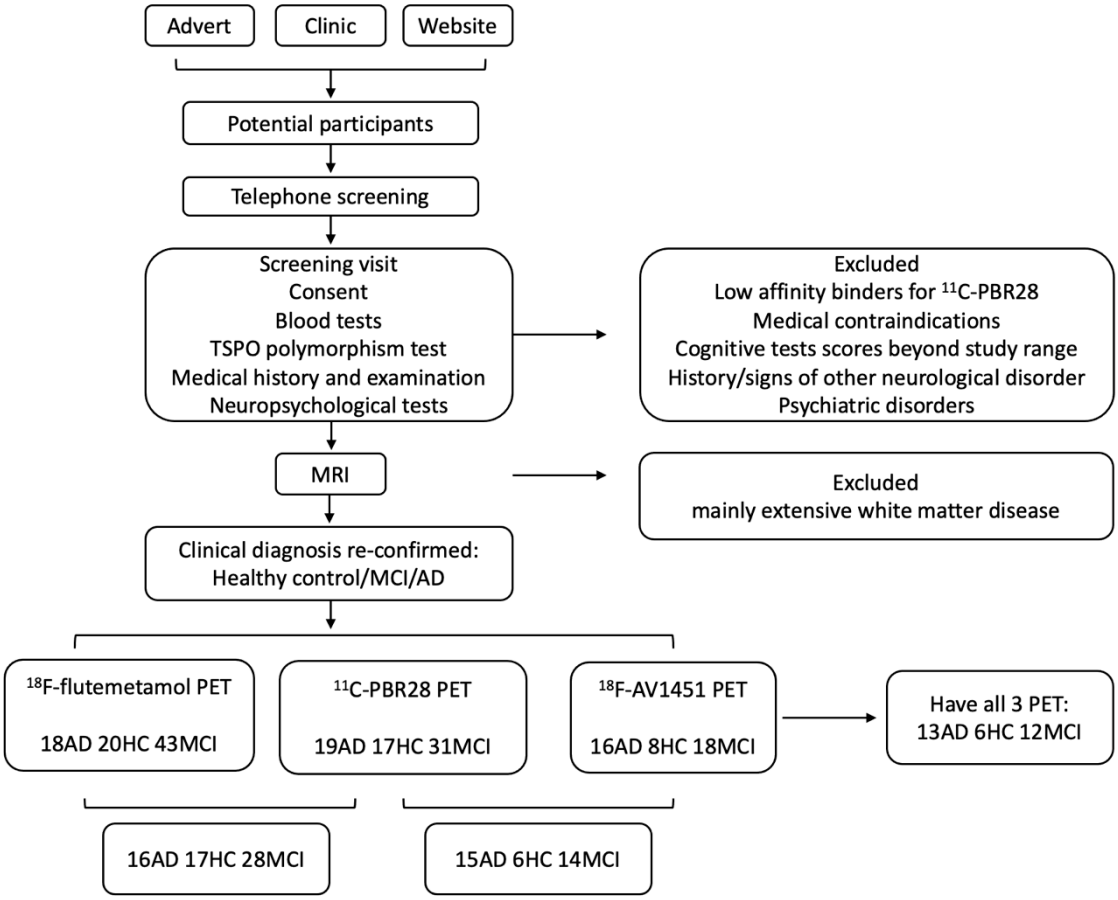

Figure 1.4 Participant recruitment, consents, inclusion and exclusion criteria

This study was approved by the London Riverside Research Ethics Committee, National Health Research Services, Health Research Authority, UK. Administration of PET tracers was approved by Administration of Radioactive Substances Advisory Committee (ARSAC). Written informed consent was obtained from all participants in the study.

Potential participants in the study were recruited via the following ways: 1- referral from memory clinics in UK, 2-through "Join dementia research" website and 3-through General Practitioner's surgery and through advertisement. Interested participants undertook a telephone pre-screening, and eligible participants were invited to Hammersmith Hospital for a screening visit, where medical history and examination, blood tests, cognitive tests were performed, and written consent was obtained. Participants were then invited to have an MRI

scan, and patients with MRI findings of any significant vascular (above Fasika score >2) disease were excluded. The clinical diagnosis was re-confirmed before the participants were invited to have PET scans. The PET scans were obtained within a year from the first PET scan.

Clinical diagnosis of Alzheimer's dementia or mild cognitive impairment was made based on the 2011 NIA-AA (National Institute of Aging and Alzheimer's Association) recommendations(Albert et al., 2011; G. M. McKhann et al., 2011). Other inclusion criteria include: 50-85 years-old at study entry; Mini-Mental State Examination (MMSE) score >24 for MCI patients and > 15 for Alzheimer's disease patients; at least 8 years of education; ability to give informed consent.

Patients with (1) history or signs of other neurological diseases, including significant brain MRI findings; (2) contraindications for MRI scanning; (3) malignancy within the last 5 years; (4) major depression; (5) homozygous 147 Thr/Thr single nucleotide polymorphism of the 18kDa translocator protein (TSPO) gene (low affinity binders of ^{11}C-PBR28) were excluded from the study.

Chapter 2. PET Analysis and Comparison of ^{11}C-PBR28 Quantification methods

2.1 Introduction

2.1.1 A Brief overview of PET quantification methods

PET tracer binding quantification methods could be generally summarized into several categories, with increasing precision on tracer kinetic behaviour but model complexity as well: semiquantitative standard uptake value (SUV), graphical analysis, spectral analysis and compartment modelling (Bertoldo, Rizzo, & Veronese, 2014).

Compartment modelling is the very basis of PET quantification, as it explicitly describes the dynamic parameters of tracers inside the tissue, based on a predefined model of the physiological system. For a tracer that can reversibly bind to its receptor, the most commonly kinetic model is the 2-tissue compartment model (Figure 2.1).

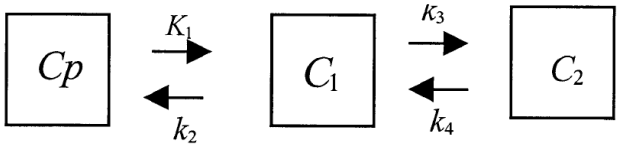

Figure 2.1. 2-tissue compartment model

Where C_p, C_1 and C_2 are the concentration of parent tracer in plasma and tissue compartments, respectively and K_1~k_4 are the transport constant between blood and tissue/between tissue compartments. The relationship of tracer concentration in plasma and tissue compartments is given by following equations:

$$\frac{dC_1}{dt} = K_1 C_p(t) - (k_2 + k_3)C_1 + k_4 C_2 \qquad (2.1)$$

$$\frac{dC_2}{dt} = k_3 C_1 - k_4 C_2 \qquad (2.2)$$

With dynamic PET and arterial plasma samples, the model micro-parameters (K1~k4) could then be estimated. The macro-parameters such as tissue distribution volume (V_T) and non-displaceable binding potential (BP_{ND}) could then be calculated:

$$V_T = \frac{K_1}{k_2}(1 + \frac{k_3}{k_4}) \quad (2.3)$$

$$BP_{ND} = \frac{k_3}{k_4} \quad (2.4)$$

Because it can explicitly describe the mathematical details of tracers' kinetic inside the system, compartment modelling is considered as the 'gold-standard' for PET analysis. However, it also requires precise understanding of the tracers' kinetic behaviour inside the physiological system, reliable arterial input and dynamic PET acquisition. Further, because the estimation of microparameters involves non-linear least square method, compartment modelling is less suitable for calculating voxel-wise parametric maps due to issues such as high noise level at single voxel and computational costs (Bertoldo et al., 2014; Slifstein & Laruelle, 2001).

In spectral analysis, the radioactivity in tissue is regarded as the convolution product of the input of system (AIF) and the impulse response function (IRF). Whereas compartment modelling requires explicit kinetic description of the system, spectral analysis (SA) decomposes the IRF into a sum of exponential functions:

$$C_t(t) = \sum_{j=0}^{M} \alpha_j \cdot C_p(t) \otimes e^{-\beta_j t} \ (\alpha_j > 0, 0 < \beta_1 < \beta_2 < \cdots < \beta_M) \quad (2.5)$$

$$IRF(t) = \sum_{j=0}^{M} \alpha_j \cdot e^{-\beta_j t} \quad (2.6)$$

In analysis of decaying data, the high frequency β component (β = 1 s^{-1}, log (β) = 0) corresponds to the rapid flow of tracer in blood flow within the vasculature, the intermediate

frequency component(s) reflect the extravascular kinetic behaviour of the tracer, while the lowest frequency component (β close to the decay constant of used isotope) correspond to the irreversible trapping of the tracer in tissue (V. J. Cunningham & Jones, 1993).

For reversible tracers V_T can be calculated as the integral of IRF(t):

$$V_T = \int_0^\infty IRF(\tau)d\tau = \sum_{j=1}^{M} \frac{\alpha_j}{\beta_j} \qquad (2.7)$$

Spectral analysis is a model-free method and could be used for model development of new tracers, as the components estimated is suggestive of a range of models associated with the kinetic spectrum. Spectral analysis is applicable for both voxel-wise and ROI level analysis, though it has been suggested to be sensitive to noise (F. Turkheimer et al., 1998), and an appropriate β grid needs to be defined (Veronese, Rizzo, Bertoldo, & Turkheimer, 2016). In regional analysis, the β range could be set between the decay constant of radioactive isotope to 1 s^{-1} for analysis of decaying data, as it covers the slowest and most rapid possible change of signal in tissue, which correspond to signal loss due to decay of the radioactive isotope and transient delivery of blood from vessels (V. J. Cunningham & Jones, 1993).

Graphical analysis transforms AIF and ROI tracer uptake data points into a linear plot, the slope of which reflects the kinetics of tracer binding. For a 2-tissue compartment model with reversible binding (Logan graphical analysis), equation (1) and (2) could be rearranged to:

$$\frac{\int_0^t ROI(t')dt'}{ROI(t)} = \left[\frac{K_1}{k_2}\left(1+\frac{k_3}{k_4}\right)+V_p\right]\frac{\int_0^t C_p(t')dt'}{ROI(t)} + intercept \qquad (2.8)$$

$$intercept = -\frac{1}{k_2}\left[1+\frac{k_3}{k_4}\right] - \frac{C_2(t)}{k_4[C_1(t)+C_2(t)]} \;\; (V_p \; neglected) \qquad (2.9)$$

Therefore, if the intercept holds constant, there is linear relationship between $\frac{\int_0^t ROI(t')dt'}{ROI(t)}$ and $\frac{\int_0^t C_p(t')dt'}{ROI(t)}$, which could be obtained from imaging frames. That the intercept is (approximately) constant holds true after a steady-state condition is met certain time post-injection of the tracer, that is, the tracer concentration in compartment 1 (C_1) and C_2 both follow the plasma concentration C_p, i.e., $C_1(t) \propto C_p(t); C_2(t) \propto C_p(t), t > T^*$. Where T^* is the time after which the system reaches the steady state. After time T, $\frac{C_2(t)}{C_1(t)+C_2(t)}$ cancels the function $C_p(t)$, thus the intercept is a constant determined by k_2~k_4, and the slope is the tissue distribution volume (V_T) (Logan, 2000).

Graphical analysis is less computational demanding and can be applied to both voxel-wise and ROI level analysis. It should be noted that a good estimation depends on the appropriate choice of T^*. Also, noise in PET data tend to lead to underestimation of V_T in Logan analysis, especially at voxel-level when signals are not averaged to cancel zero-mean noise (as at ROI level) (Slifstein & Laruelle, 2000).

SUV is the most used measurement in clinical practice, which is calculated by dividing tracer uptake by the injection dose and a normalizing factor. The most common normalizing factors are body weight, body surface area or lean body mass. SUV does not provide kinetic information of the tracers, but its simplicity and non-invasiveness (no arterial sampling required) make it ideal for clinical settings (Bertoldo et al., 2014).

Due to the invasiveness of the methods that require arterial sampling, reference region methods have been developed to derive arterial input function from time-activity data from a reference region. An ideal reference region should have similar non-specific tracer bindings as target ROIs but have little/no specific binding sites (Zanderigo, Ogden, & Parsey, 2013). Reference regions are also used to calculate distribution volume ratios (DVR) and standard

uptake value ratios (SUVR) to normalize individual variability of PET scans (J. M. Rasmussen et al., 2012). To date, many of the most widely used tracers in clinical and scientific settings are analysed using the SUVR methods, such as ^{18}F-Flutemetamol, ^{11}C-PIB and ^{18}F-AV1451, because of its simplicity and the effectiveness.

2.1.2 Challenges in ^{11}C-PBR28 quantification

The quantification of ^{11}C-PBR28 PET scans have been proved to be challenging, due to its high within-subject and more importantly, inter-subject binding variability. Test-retest stability analysis have found an absolute within subject VT variability of 18.3±12.7% using the 2-tissue compartment model in healthy volunteers. However, the coefficient of variation at inter-subject level was substantially higher, at 49% after accounting for TSPO genotypes (Collste et al., 2016). Further studies have demonstrated that the circadian rhythm, physiological and psychological factors such as age, gender, BMI, anxiety, could all influence TSPO expression, which lead to high inter and intra-subject variability (Gavish et al., 1999) (Tuisku et al., 2019) (Collste et al., 2016). It has been also suggested that introducing a vascular compartment in the kinetic model could improve the model fit (Rizzo et al., 2014; Veronese et al., 2018). Since V_T accounts for both specific bindings and non-specific bindings of PBR in tissues, which add up to the noise in data, efforts have also been made to estimate specific bindings in analysis (Guo, Owen, Rabiner, Turkheimer, & Gunn, 2014; Schain, Zanderigo, Ogden, & Kreisl, 2018).

Although accounting for numerous demographic factors and specifying more precise kinetic models could improve model fit, the complexity undermines its practicality, and the relatively small sample sizes in human brain imaging studies often limit the number of nuisances in regression. Further, from statistical point of view, too high a variance could not

only undermine the statistical power, but also cause high data skewness and render further analysis unreliable. Therefore, many clinical studies have decided to use the ratio method (DVR and SUVR) with reference region to ameliorate the inter-subject variability issue, because it could cancel most of the individual-specific physiological and psychological factors (Lyoo et al., 2015b). However, because there is no region in the brain that is devoid of TSPO expression, a pseudo-reference region could be delegated as best (F. E. Turkheimer et al., 2007). The choice of pseudo-reference region is often based on the knowledge of disease in question, for example, in epilepsy studies often the region contralateral to the lesion is selected (Dickstein et al., 2019), while in motor neuron diseases the cortical brain grey matter is selected because the diseases mainly involve primary motor cortex (Paganoni et al., 2018) (Alshikho et al., 2016). In Alzheimer's disease, the whole neocortex could be involved depending on the pathological stage, but the cerebellum has only minimal Alzheimer's pathology until the very terminal stage, which is usually beyond the scope of imaging studies (Braak & Braak, 1991). It has also been reported that the TSPO expression patterns in cerebellum is significant different compared to that found around amyloid plaques in the neocortex (Slifstein & Laruelle, 2001). Based on the reasoning, Kreisl and colleagues have tested the possibility of quantifying ^{11}C-PBR28 uptake using SUVR with cerebellum grey matter as pseudo-reference region, and have reported that the method is reliable and might be more sensitive for detecting neuroinflammation in AD compared to compartment modelling (Lyoo et al., 2015b). Further test-retest stability analysis has also suggested better stability of SUVR over 12 weeks of time in ^{11}C-PBR28 quantification (Nair et al., 2016). Several studies have since adopted the method and reported further progress with regards to the influence of neuroinflammation on cognition and disease progression in AD (Kreisl et al., 2016b) (Zou et al., 2020) (Kreisl et al., 2017). On the other hand, the SUVR method is also criticized in that SUVR does not correlate very well with V_T values estimated by the gold standard (Albrecht

et al., 2018) (Matheson et al., 2017). However, as the variance introduced by individual factors which have significant effect on absolute quantification is normalized by ratio methods, one may reasonably expect the ratios to be different from V_T. Of note, to date there has not been study investigating whether ^{11}C-PBR28 SUVR is associated with amyloid and tau pathologies in vivo. One would expect that if ratio method is valid for quantification of neuroinflammation, the SUVR would correlate well with Alzheimer's pathologies in vivo according to established pathological knowledge.

Based on the consideration that the SUVR method could ameliorate the inter-subject variability issue and improve the statistical power/robustness of further analysis of my project, I have adopted SUVR method as the primary method of my analysis, but I also compared SUVR results with the output from Logan analysis, spectral analysis, and DVR values based on V_T values. Because the imaging data for my project is already acquired, a test-retest stability analysis of different methods is not possible. As we have prior knowledge that neuroinflammation accompanies amyloid and tau pathologies in pathological examination, and that increased ^{11}C-PK11195 uptake is found in the medial temporal lobe, inferior/middle temporal gyri, I hypothesized that if SUVR is a suitable method for detecting neuroinflammation in AD, I should be able to replicate the previous imaging findings, and the SUVR values should correlate with imaging markers of amyloid and tau pathologies.

2.2 Methods

2.2.1 ^{11}C-PBR28 PET scan acquisition

^{11}C-PBR28 was synthesized at London Imanova Centre for Imaging Sciences. ^{11}C-PBR28 PET scans were acquired with a Siemens Truepoint PET/CT scanner at the same site with the following parameter: axial field of view 218mm, 111 axial planes, spatial resolution

2.056mm × 2.056mm × 2mm. Radial artery cannulation was performed prior to scanning to draw arterial blood samples. ^{11}C-PBR28 was dissolved in 20ml normal saline and a mean dose of 330.9 (±30) MBq was injected for imaging. 8 × 15s, 3 × 60s, 5 × 120s, 5 × 300s and 5 × 600s frames were acquired using 3D list mode acquisition over 90 minutes. Images were reconstructed using filtered backward projection with 2.6× zoom and 5mm Gaussian filter.

Arterial blood was sampled continuously for the first 15 minutes after injection and discrete samples were drawn at 5, 10, 20, 30, 50 ,70 and 90 minutes. Whole blood and plasma radioactivity were measured, and reverse-phase chromatography was performed to separate radioactive metabolites (Dani et al., 2018b).

2.2.2 ^{18}F-Flutemetamol PET scan acquisition

18F-Flutemetamol was provided by GE Healthcare and scans were acquired at Imperial College Clinical Imaging Facility with Siemens Biograph 6 scanner. A mean dose of 183.4 (±5.3) MBq was injected in 8ml normal saline followed by 10 ml saline flush. Scans were acquired from 90-120 minute after injection with following parameters: 15cm field of view, 2.6 × zoom, spatial resolution 1.56mm × 1.56mm × 1.92mm. 6 of 5-minute frames were acquired in 3D list mode. Filtered back projection was performed to reconstruct the images and attenuation was corrected. Post-construction smoothing was performed with 5mm Gaussian kernel.

2.2.3 ^{18}F-AV1451 PET scan acquisition

^{18}F-AV1451 was provided by Imanova Centre for Imaging Sciences, London, where scans were performed with Siemens Truepoint PET/CT scanner. A mean dose of 168.3 (±7.4) MBq of ^{18}F-AV1451 was injected in 20ml normal saline. 8 ×15s, 3 × 60s, 5 × 120s, 5 × 300s,

8 × 600s frames were acquired over 120 minutes in 3D list mode. Images were reconstructed using iterative reconstruction and post-construction smoothing was performed with 5mm Gaussian kernel.

2.2.4 Pre-processing of PET images

Due to the long period of PET scanning, many patients/volunteers made head movements that caused displacement of the frames (as noticed in visual inspection of the frames. Therefore, realignment was performed before further processing. Because the first 15-second frames contained little spatial information, the realignment was performed by aligning the rest of the frames to the third frame and leave the first 2 frames as were. The realignment was performed on statistical parametric mapping 8 package (SPM8, University College London).

A weighted average image (Add-image) of all frames was then created for each subject as it may provide better spatial information compared with parametric maps and was used for further spatial transformation process.

Each subject's T1-weighted MRI image was co-registered to the Add-image, followed by normalization to MNI space with MNI-152 average T1 image as template. Spatial transformation parameters were recorded, and the inverse transformation parameters to MNI space were applied to Hammers Atlas to generate a subject-specific ROI map in PET space. The co-registered MRI image in PET space was segmented, and the ROI map was multiplied by the binarized grey-matter mask (>0.5 probability) using nearest neighbour interpolation to create a grey-matter object map in PET space for each subject respectively.

2.2.5 ^{11}C-PBR28 PET analysis

Arterial input function

Arterial input function (AIF) was calculated using COMIF (in house MATLAB based software) by the following steps:

(1) Background radioactivity correction: the sensor may detect background radiation in the room due to inadequate shielding, so a 15s segment of arterial blood radioactivity readings prior to injection was extracted and the mean value is subtracted for all subsequent measurements (Figure 2.2).

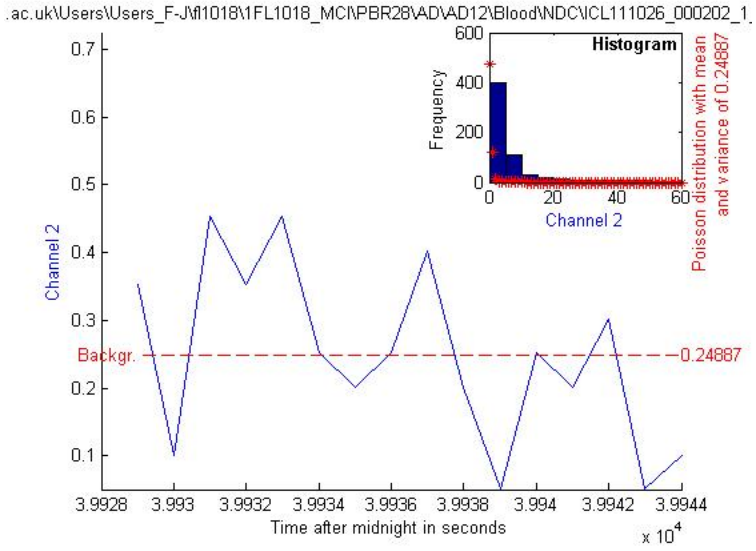

Figure 2.2. Background radioactivity

(2) Blood time-activity curve was created by combining the continuous readings over the first 15 minutes and discrete blood samples' measurements from a well-counter (Figure 2.3).

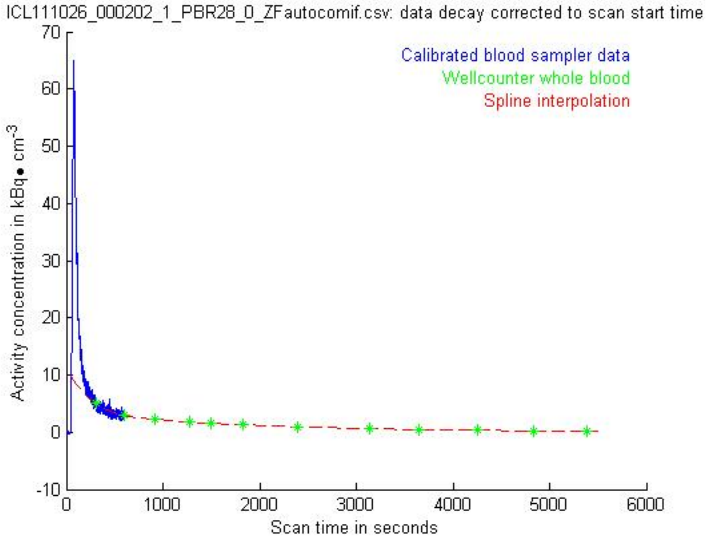

Figure 2.3. Fitted curve of blood radioactivity

(3) Plasma-over-blood correction: plasma over blood concentration ratio line was fitted using data points from discrete samples and a simple linear model was used for ^{11}C-PBR28 (Figure 2.4).

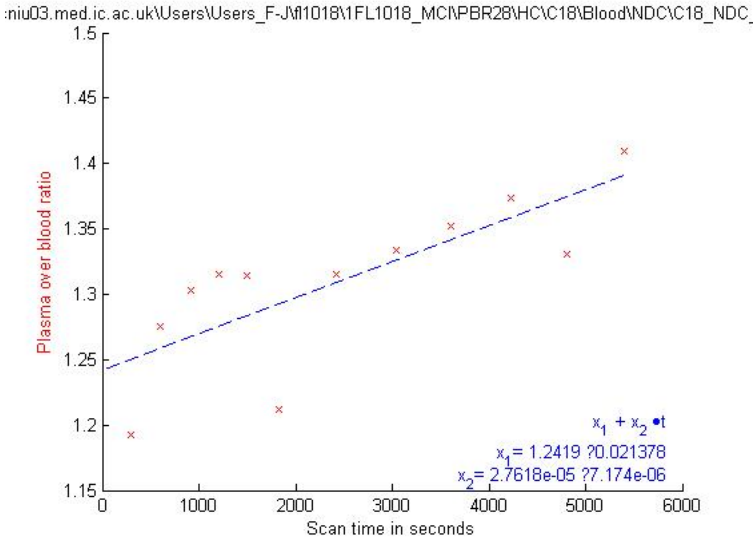

Figure 2.4. Plasma over blood model

The first 15-minute continuous plasma time-activity curves were then obtained by multiplying the blood time-activity curve by the plasma over blood function, and the final total plasma time-activity curves were generated by combining the corrected continuous curve and discrete well-counter readings of the plasma (Figure 2.5).

Figure 2.5. Total plasma time-activity curve

(4) Metabolite correction: Radiolabelled metabolite correction is needed to obtain plasma parent compound time-activity curve. To achieve this, the parent compound (^{11}C-PBR28) fraction in plasma curve is fitted using a sigmoidal function (Figure 2.6).

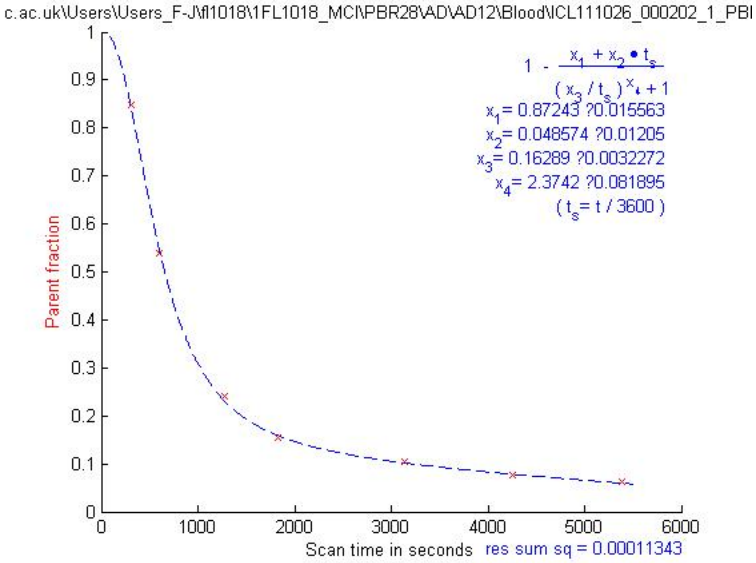

Figure 2.6. Parent compound fraction in plasma

^{11}C-PBR28 plasma input function was calculated by multiplying total plasma time-activity curve by parent compound fraction function and was used for further analysis (Figure 2.7).

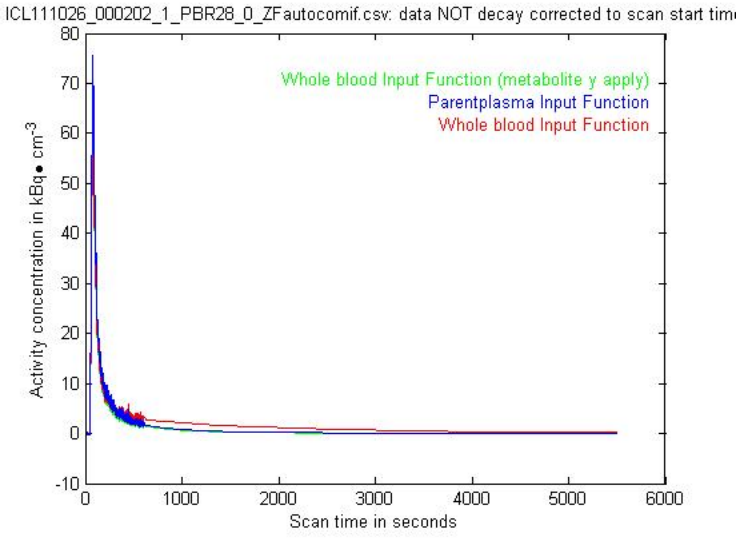

Figure 2.7. Parent plasma input function

Delay correction of ^{11}C-PBR28 arterial input function

Because arterial blood samples are drawn from radial artery, where it takes longer time for blood to travel from left ventricle compared to brain, the measurement of arterial blood radioactivity lags behind perfusion to the brain, and thus delay correction is needed to prevent bias in further analysis. Delay was detected by fitting compartment model to the data iteratively with time-shifted arterial input curves and choosing the time delay that result in best fit between AIF and imaging data (Iida et al., 1988). In the current project the delay detection was performed on MICK program (Dr Rainer Hinz, University of Manchester) using whole-brain grey matter as region of interest (ROI) and a 2-tissue compartment model with variable blood volume (4k-bv). Brain blood volume was estimated in the same process by fitting AIF with imaging data iteratively with a range of blood volumes and approximating the value resulting in best fit. Detected time delay was recorded for each subject and corrected in further analysis where AIF is used.

Standardized uptake value ratio (SUVR) images for ^{11}C-PBR28

As previous studies have reported that SUVR calculated with cerebellar grey matter as a pseudo-reference region and late frames (60-90 minutes) of ^{11}C-PBR28 scan could be a feasible method compared to absolute quantifications (Lyoo et al., 2015a), a 60-90-minute SUVR image was created first for each subject.

The average image of last three 600s frames was create for each subject. The radioactivity concentration in bilateral cerebellar grey matter was sampled and the average image was divided by cerebellar grey matter concentration to obtain the SUVR image for each subject.

Calculation of volume of distribution (V_T) image using graphical analysis (Logan)

Logan-V_T parametric map was created for each voxel using MICK-pm program (Dr Rainer Hinz, University of Manchester) using AIF, corrected for delay time and blood volume. Data points obtained from 2100s were used for estimation (Dani et al., 2018a) (Figure 2.8).

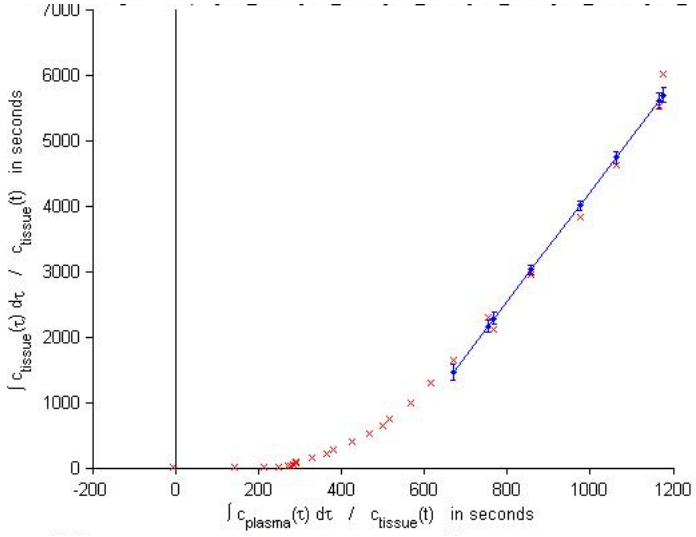

Figure 2.8. Logan graphic analysis at ROI level

Calculation of Impulse Response Function (IRF) Image Using Spectral Analysis

At voxel level the β grid was narrowed to 0.00085-0.1 considering increased statistical noise at voxel level, which resulted in V_T close to that calculated at ROI scale.

Processing of parametric images

The parametric maps of SUVR, Logan-V_T, SA-V_T and IRF were sampled in original PET space using the individualized Hammer's atlas to acquire ROI level metrics. Normalization of the parametric maps to the MNI space was performed with following steps: (1) Each subject's T1 weighted MRI image was co-registered to the Add-image using linear transformation; (2) The co-registered MRI image was then normalized to MNI-152 template using non-linear transformation and the same spatial transformation was applied to the PET parametric maps for each individual, bringing the PET images to standard space. The normalized images were then used in voxel-wise statistical analyses.

2.2.6 Processing of ^{18}F-Flutemetamol and ^{18}F-AV1451 PET images

The weighted average images were created using all 60-90 minutes ^{18}F-Flutemetamol frames and 80-100 minutes ^{18}F-AV1451 frames. Same procedures as ^{11}C-PBR28 SUVR calculation were performed. Cerebellum grey matter was used as reference region for both images.

2.2.7 Statistical analysis

Left and right medial temporal lobe (MTL) and combined middle/inferior temporal gyri were defined *a prior* as primary ROIs in statistical analysis, based on prior findings from in vivo TSPO imaging and post-mortem pathology studies. Analysis of covariance (ANCOVA) was performed to test any difference across AD, MCI and HC cohorts, with TSPO genotype and diagnosis included as fixed factors and age as covariate. Student's T-test was performed to test difference between any two of the diagnostic groups, with false discovery rate (FDR) correction. Post hoc exploratory analyses were performed in larger and more general ROIs including bilateral frontal, temporal, parietal, occipital lobes and cingulate gyri. Correlation between ^{18}F-Flutemetamol and ^{11}C-PBR28, ^{11}C-PBR28 and ^{18}F-AV1451 uptake in these ROIs to examine if neuroinflammation is associated with amyloid and tau deposition *in vivo*. Further, regression analysis was performed with ^{18}F-Flutemetamol and ^{18}F-AV1451 SUVR as independent variables and ^{11}C-PBR28 measurements as dependent variable in AD and combined amyloid positive cohorts. Age and TSPO genotype (where ^{11}C-PBR28 was involved) were included as covariate of no interest in all tests. All statistical analysis at ROI level was performed with R.

Voxel-wise group comparisons were performed on SPM8. Cluster-forming threshold was set at 0.05 at voxel-level and multiple comparison correction as performed at cluster level using random field theory with a threshold of 0.05. Age and TSPO genotype were included as covariate of no interest in the tests.

Further, voxel-wise regression analysis was performed on ^{18}F-Flutemetamol, ^{18}F-AV1451, and ^{11}C-PBR28 SUVR images using the VoxelStat package (Mathotaarachchi et al., 2016). Images were smoothed with a 6mm Gaussian kernel before analysis, and age was included as a covariate. Results were corrected for multiple comparisons using random field theory with a $p<0.01$ cluster forming threshold.

2.3 Results

The study protocol and data availability are summarised in Figure 1.4. The demographic data and scan availability for each participant are summarised in Appendix 3.

2.3.1 ^{18}F-Flutemetamol SUVR

ANCOVA showed significant cross group difference of ^{18}F-Flutemetamol SUVR across frontal, temporal, parietal, occipital and cingulate cortices ($p<0.01$, Bonferroni corrected). AD cohort showed significantly higher ^{18}F-Flutemetamol SUVR across all the regions compared to HC and MCI cohort, while MCI cohort did not show significant increase at ROI level comparison (Figure 2.9).

14 of the clinical diagnosed probable AD subjects and 26 of 55 clinical diagnosed MCI and 2 of 19 HC subjects were defined as amyloid positive (Aβ+) based on increased amyloid deposition (^{18}F-Flutemetamol SUVR>1.46) in composite region defined by Thurfjell et al. (Thurfjell et al., 2014).

Voxel-wise comparison have shown that AD cohort had increased ^{18}F-Flutemetamol uptake across the cortical cortex (Figure 2.10a), while MCI cohort showed clusters of increased ^{18}F-Flutemetamol SUVR in bilateral lateral frontal, temporal, inferior parietal, occipital lobes and cingulate cortices (Figure 2.10b).

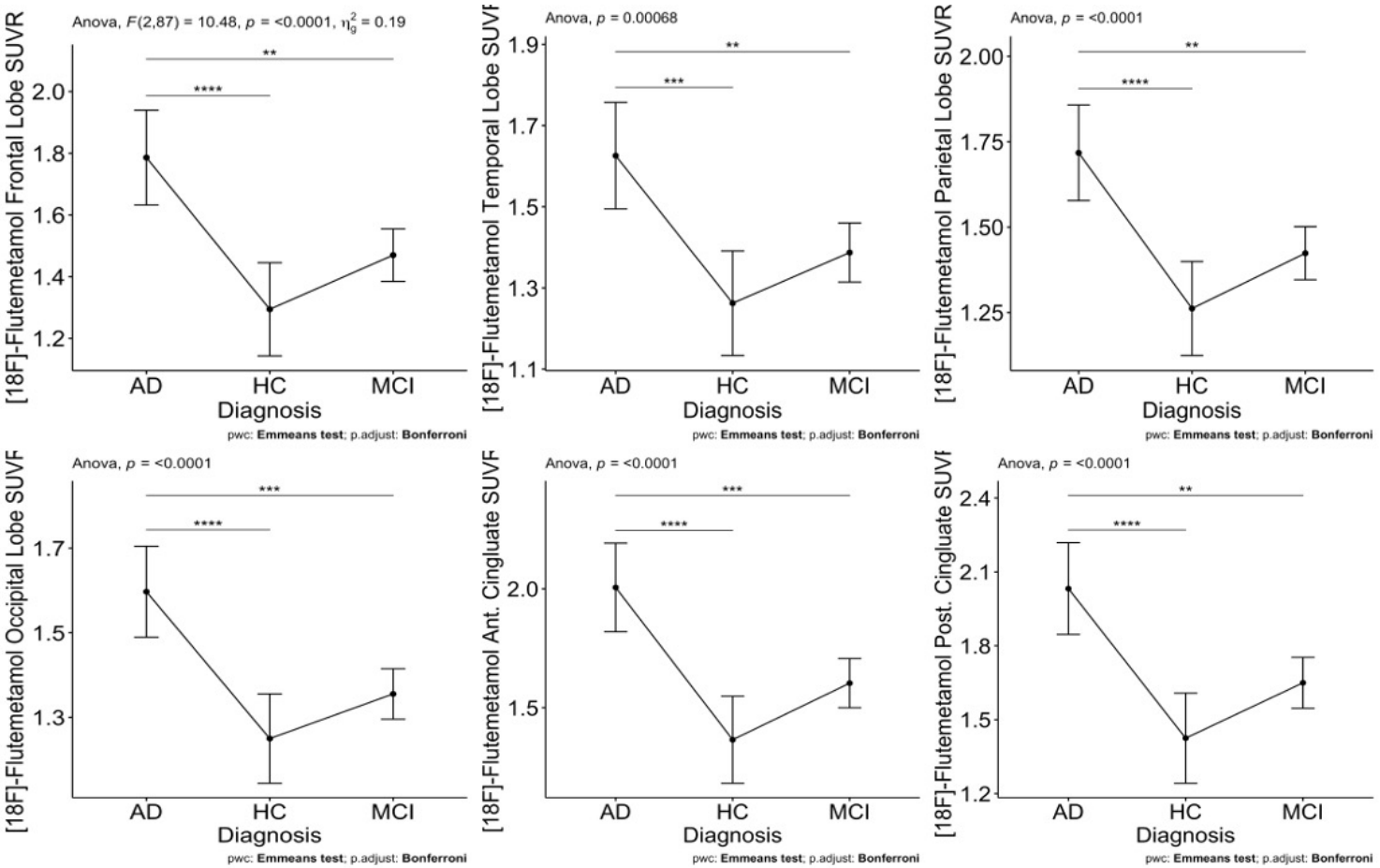

Ant.: Anterior; Post.: Posterior; Corrected for multiple comaprisons using Bonferroni correction.

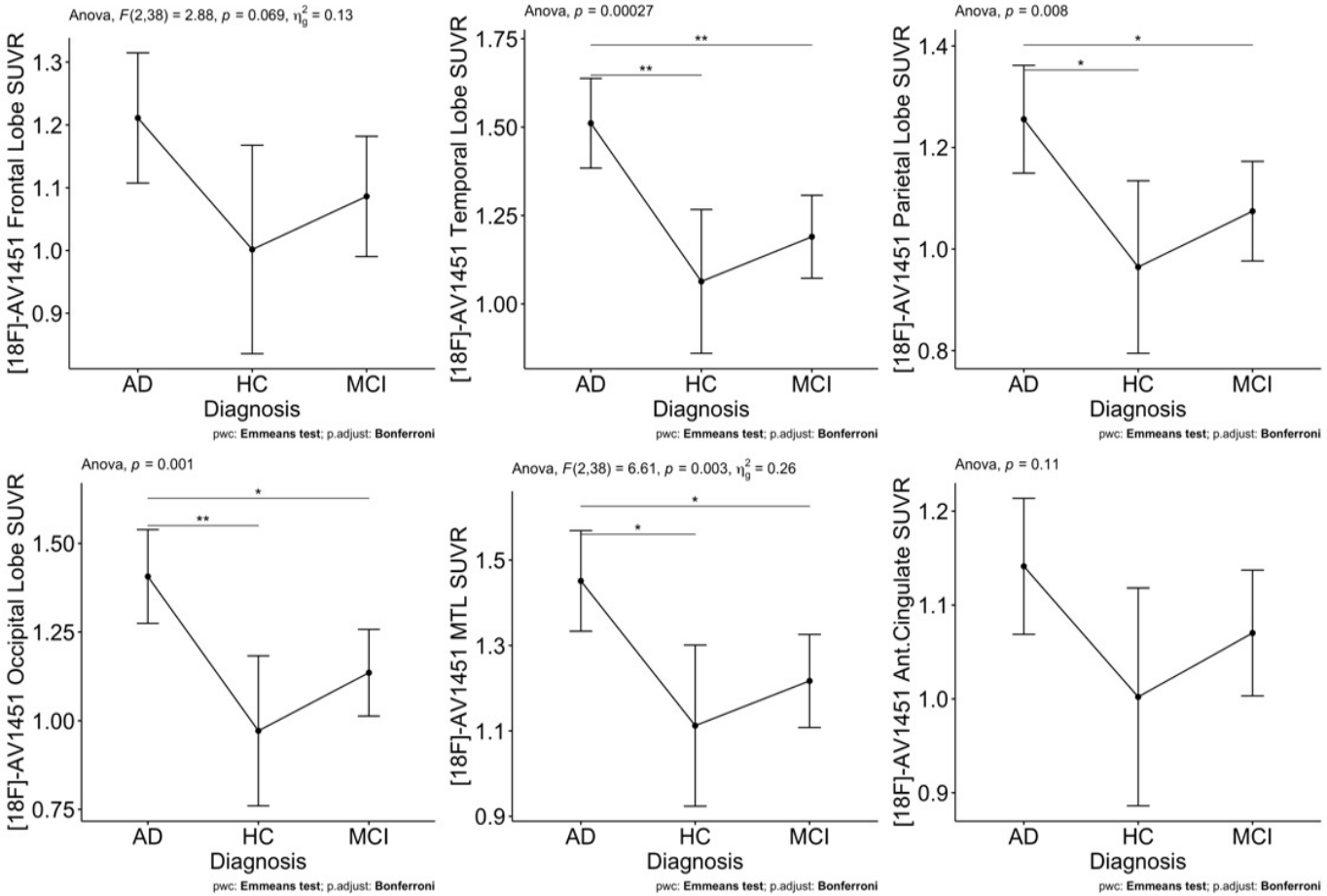

MTL: Medial temporal lobe; Ant.: Anterior; Corrected for multiple comparisons using Bonferroni correction.

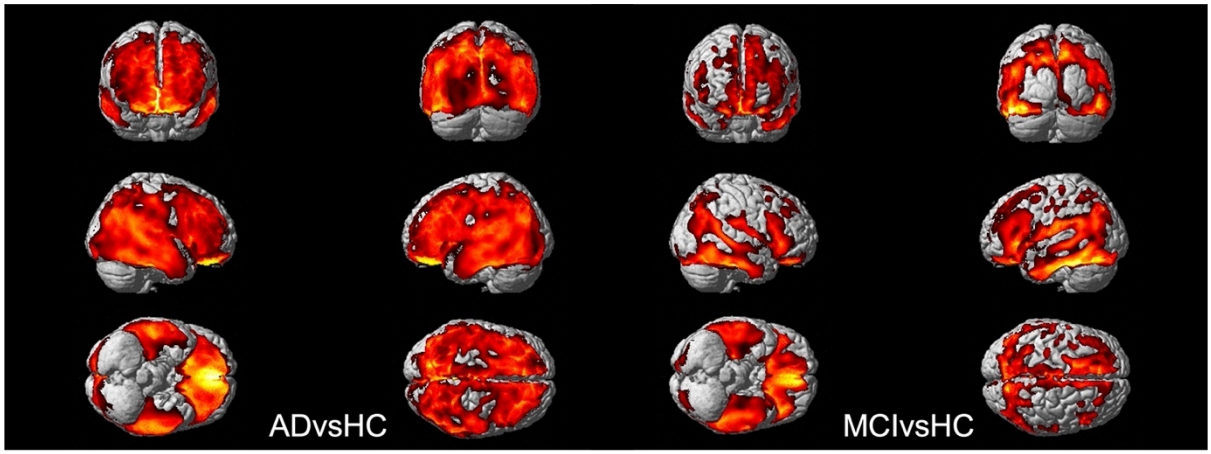

Voxel-wise comparison have shown that AD cohort had increased ^{18}F-Flutemetamol uptake across the cortical cortex (a), while MCI cohort showed clusters of increased ^{18}F-Flutemetamol SUVR in bilateral lateral frontal, temporal, inferior parietal, occipital lobes and cingulate cortices (b).

2.3.2 ^{18}F-AV1451 SUVR

Cross group comparison showed significant difference of ^{18}F-AV1451 SUVR in temporal, parietal, occipital and posterior cingulate cortices. AD cohort showed increased SUVR in temporal, parietal, occipital and posterior cingulate cortices compared to HC ($p<0.05$, Bonferroni corrected), while MCI cohort did not differ significantly from HC cohort in all ROIs (Figure 2.11).

12 of 16 clinical diagnosed AD and 4 of 19 clinical diagnosed MCI subjects were defined as positive for neurofibrillary tangles (NFT+) based on increased ^{18}F-AV1451 SUVR in the middle temporal lobe or at least two of the other 5 major cortical ROIs (frontal, parietal, occipital, anterior and posterior cingulate cortices). None of the HC subjects was found to be NFT+.

Voxel wise comparison found clusters of increased ^{18}F-AV1451 SUVR in bilateral temporal, and inferior frontal cortices in AD subjects, and in bilateral hippocampi, parahippocampal gyri, inferior and posterior temporal gyri and inferior frontal gyri in Aβ+ MCI subjects (Figure 2.12). No significant cluster was found in comparison between MCI and HC cohort.

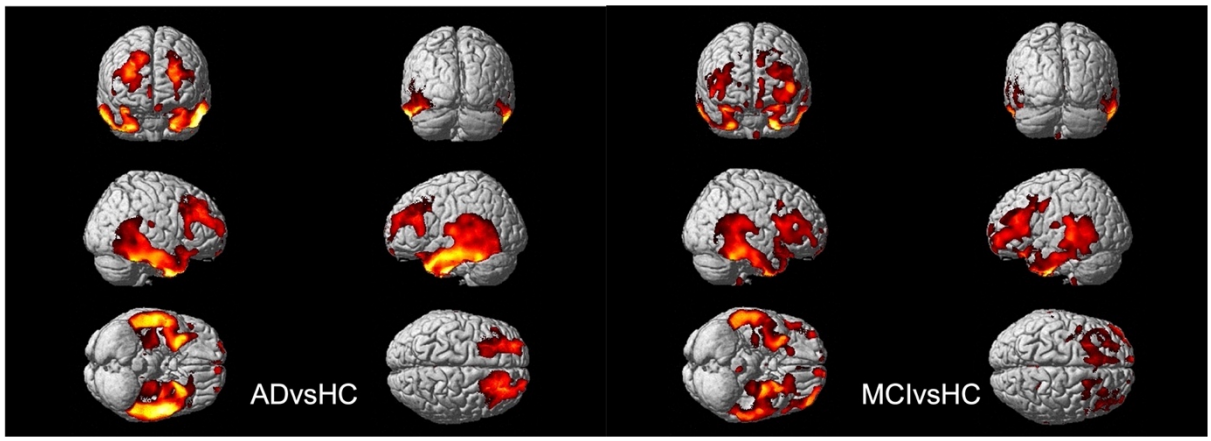

Voxel wise comparison found increased ^{18}F-AV1451 uptake in bilateral temporal, and inferior frontal cortices in AD, and in bilateral hippocampi, parahippocampal gyri, inferior and posterior temporal gyri and inferior frontal gyri in Aβ+ MCI participants

2.3.3 ^{11}C-PBR28 spectral analysis and Logan analysis

The number, TSPO phenotypes and demographics of participants who had analysable dynamic ^{11}C-PBR28 scans (1 AD and 2 MCI patients had apparent abnormal blood data and therefore kinetic modelling could not be performed) are summarised in table 2.1.

Table 2.1. TSPO phenotypes and demographics of participants with ^{11}C-PBR28 PET data

	AD	MCI	HC
Number	18	29	18
HAB	11	16	11
MAB	7	13	7
Age	73.9	72	65.1
Gender(M/F)	11/7	16/13	8/10
MMSE	23.4	27.6	28.9

HAB: high affinity binder; MAB: mixed affinity binder; MMSE: mini mental state examination.

VT and IRF parametric images created using spectral analysis with β-grid from 0.00085 to 0.1 turned out to be more robust to statistical noise compared to Logan graphic method and offered better quality of the images (Figure 2.13).

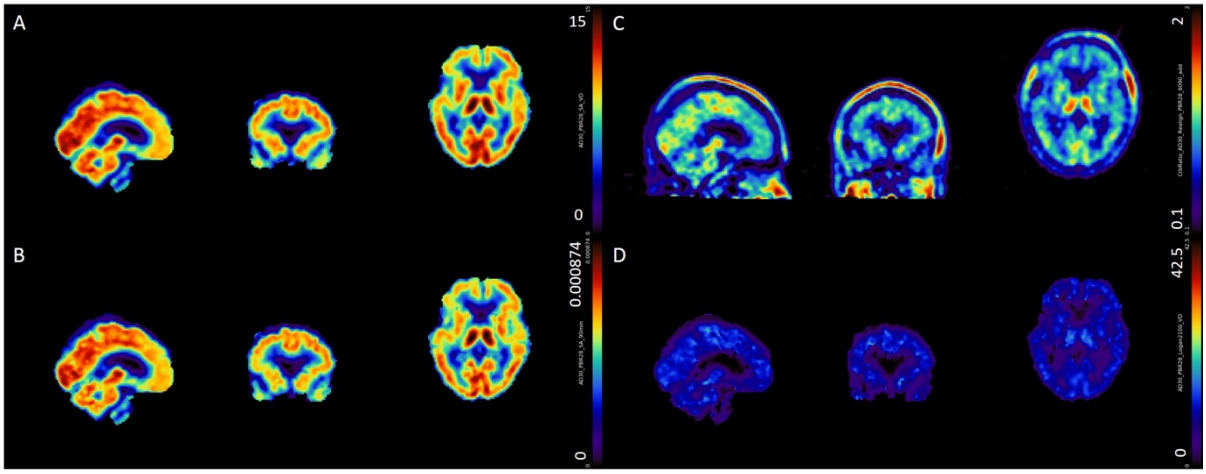

Figure 2.13. Parametric images created by Logan graphic analysis, SUVR method and spectral analysis. A: V_T calculated in spectral analysis; B: IRF at 90 minute in spectral analysis; C: SUVR using cerebellum as reference region and 60-90 minute frames; D: Logan V_T.

Impulse response function at 90-minute (IRF-90min) calculated using spectral analysis showed good agreement with Logan VT values across the ROIs ($r=0.99$, $p<0.001$, Figure 2.14).

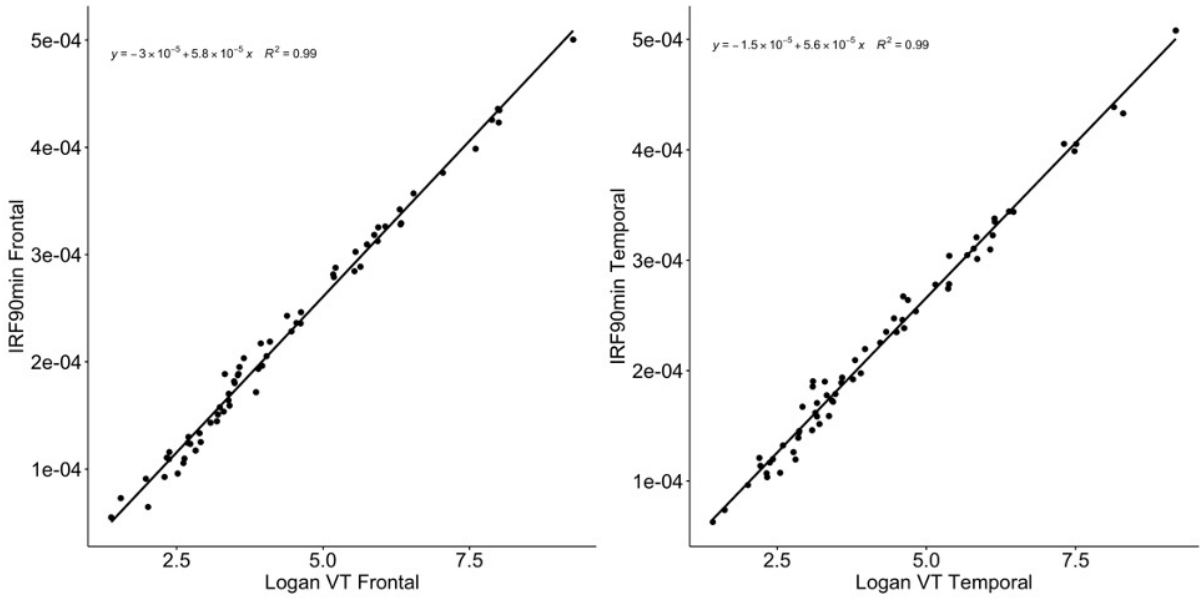

Figure 2.14. Correlation between IRF-90min and Logan V_T

In cross-group 2-way ANCOVA where TSPO genotype and diagnosis were used as grouping variable and age as covariant of no interest, only TSPO genotype was found to have significant effect on V_T and IRF values in MTL and middle/inferior temporal gyri ($p<0.01$, FDR corrected), while diagnostic groups were not.

In pairwise comparisons adjusted for TSPO genotype and controlled for age, AD patients did not show significantly increased Logan-V_T or IRF in MTL or middle/inferior temporal gyri on either side (Figure 2.15. $p>0.05$).

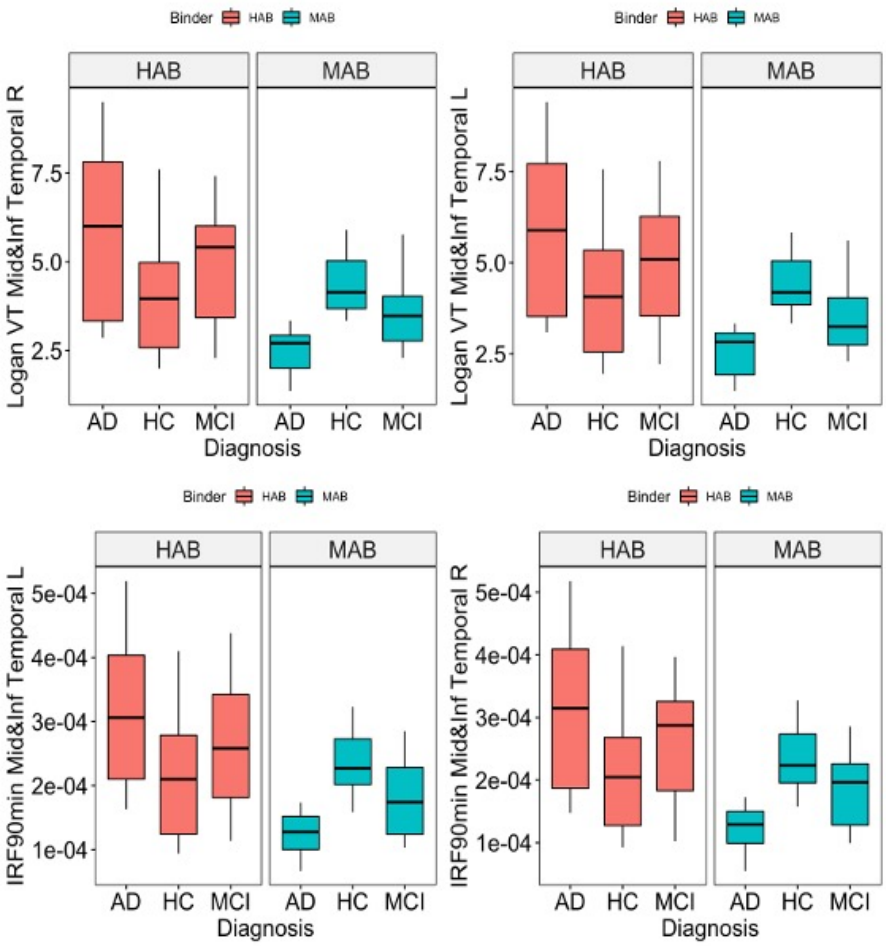

Figure 2.15. Pairwise comparisons of Logan-V_T and IRF values in the middle/inferior temporal gyri, grouped by TSPO genotype.

The Logan V_T values and IRF-90min did not differ across diagnostic groups in cerebellar grey matter (Figure 2.16).

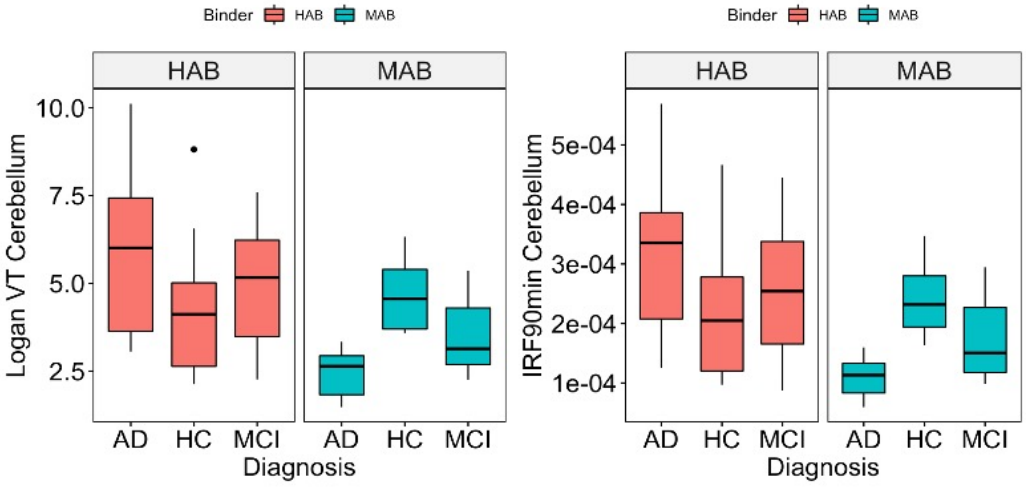

Figure 2.16. Logan V_T and IRF-90min in cerebellar grey matter.

2.3.4 ^{11}C-PBR28 SUVR analysis

AD group showed increased ^{11}C-PBR28 SUVR in left and right middle/inferior temporal gyri compared to HCs (p=0.04 and 0.05, respectively), however, the results did not survive FDR correction (Figure 2.17).

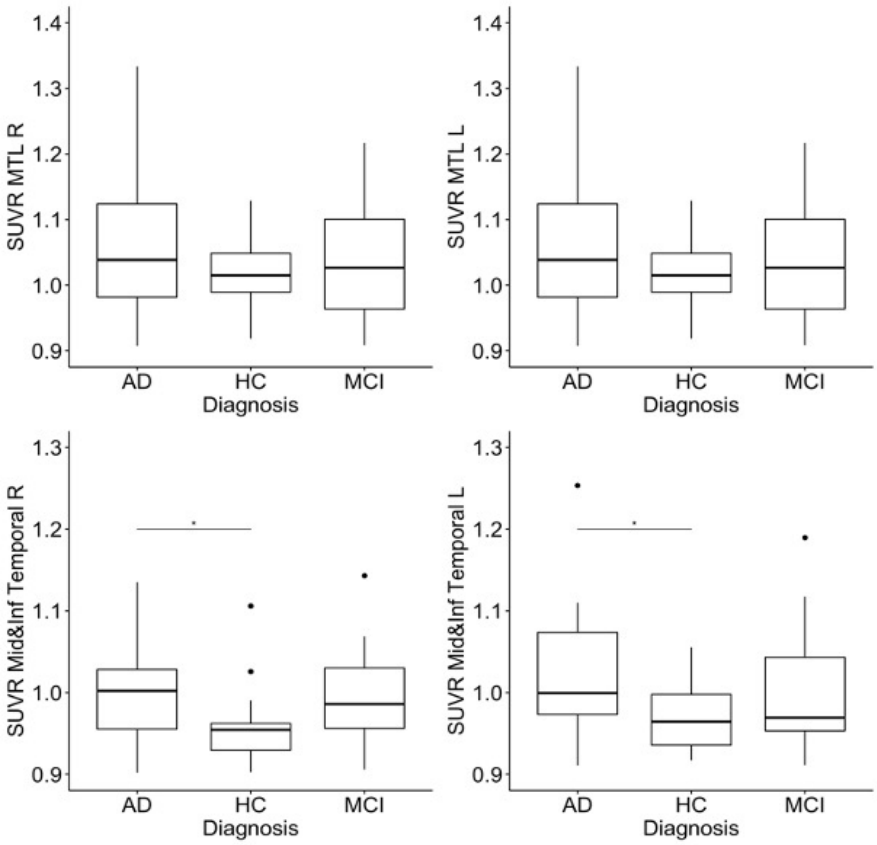

Figure 2.17. ^{11}C-PBR28 SUVR in medial temporal lobe (MTL) and middle/inferior temporal gyri. *: p<0.05 in pairwise t-test.

Post-hoc exploratory analysis did not find significantly increased ^{11}C-PBR28 uptake in other cortical regions using any of the methods.

2.3.5 Comparison between ^{11}C-PBR28 DVR and SUVR

The distribution volume ratio (DVR) calculated using Logan V_T with cerebellum as reference region was compared to SUVR, in order to examine the accordance between ratio methods. The SUVR and DVR showed good agreement with each other, with correlation coefficients of ~0.9 and p-value of Pearson's correlation <0.001 across multiple major ROIs (Figure 2.18). However, the correlations between ratio methods and absolute quantifications were not significant.

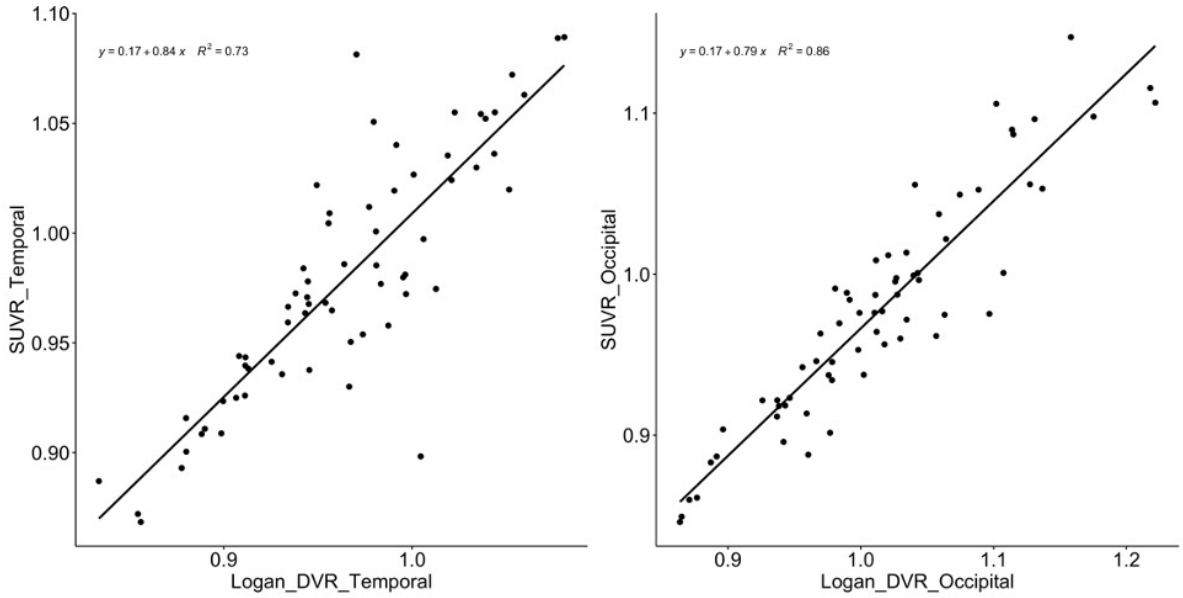

Figure 2.18. Correlation between ^{11}C-PBR28 DVR and SUVR in temporal lobe and occipital lobes.

2.3.6 Voxel-wise analysis of ^{11}C-PBR28 parametric images

In voxel-wise comparisons of Logan-V_T and IRF parametric images there was no significant clusters of difference between AD versus HC or MCI versus HC cohort.

Voxel-wise comparison of SUVR images showed significant clusters of increased SUVR in AD cohort in bilateral superior and middle frontal gyrus, left precentral and postcentral gyrus,

left posterior temporal lobe, and right superior and inferolateral parietal lobe in AD subjects (FDR corrected $p<0.05$ at cluster level, Figure 2.19).

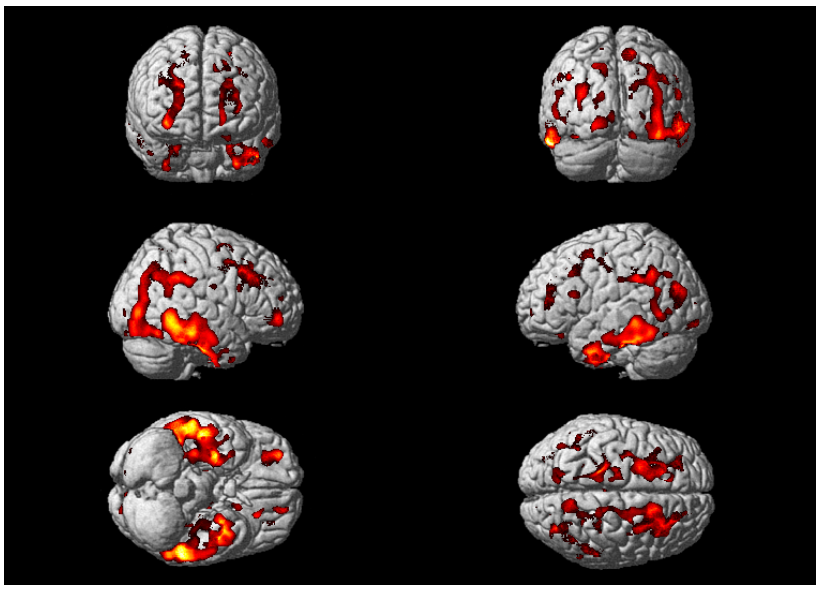

Figure 2.19. Voxel-wise analysis detected increased ^{11}C-PBR28 SUVR in AD subjects compared to HC cohort.

Voxel-wise comparison of SUVR images showed significant clusters of increased SUVR in AD cohort in bilateral superior and middle frontal gyrus, left precentral and postcentral gyrus, left posterior temporal lobe, and right superior and inferolateral parietal lobe in AD subjects

2.3.7 Relationship between ^{11}C-PBR28 and ^{18}F-Flutemetamol/^{18}F-AV1451 measurements

In cognitively impaired subjects (AD and MCI), ^{18}F-Flutemetamol SUVR correlated with ^{11}C-PBR28 SUVR in temporal and occipital regions (β=0.059, 95%CI 0.0086~0.11, p=0.024; β=0.096, 95%CI 0.022~0.17, p=0.013, respectively), while age and TSPO genotypes where not significant predictors. ^{18}F-Flutemetamol SUVR did not have significant relationship with ^{11}C-PBR28 Logan-V_T or IRF90min across the ROIs (Figure 2.20).

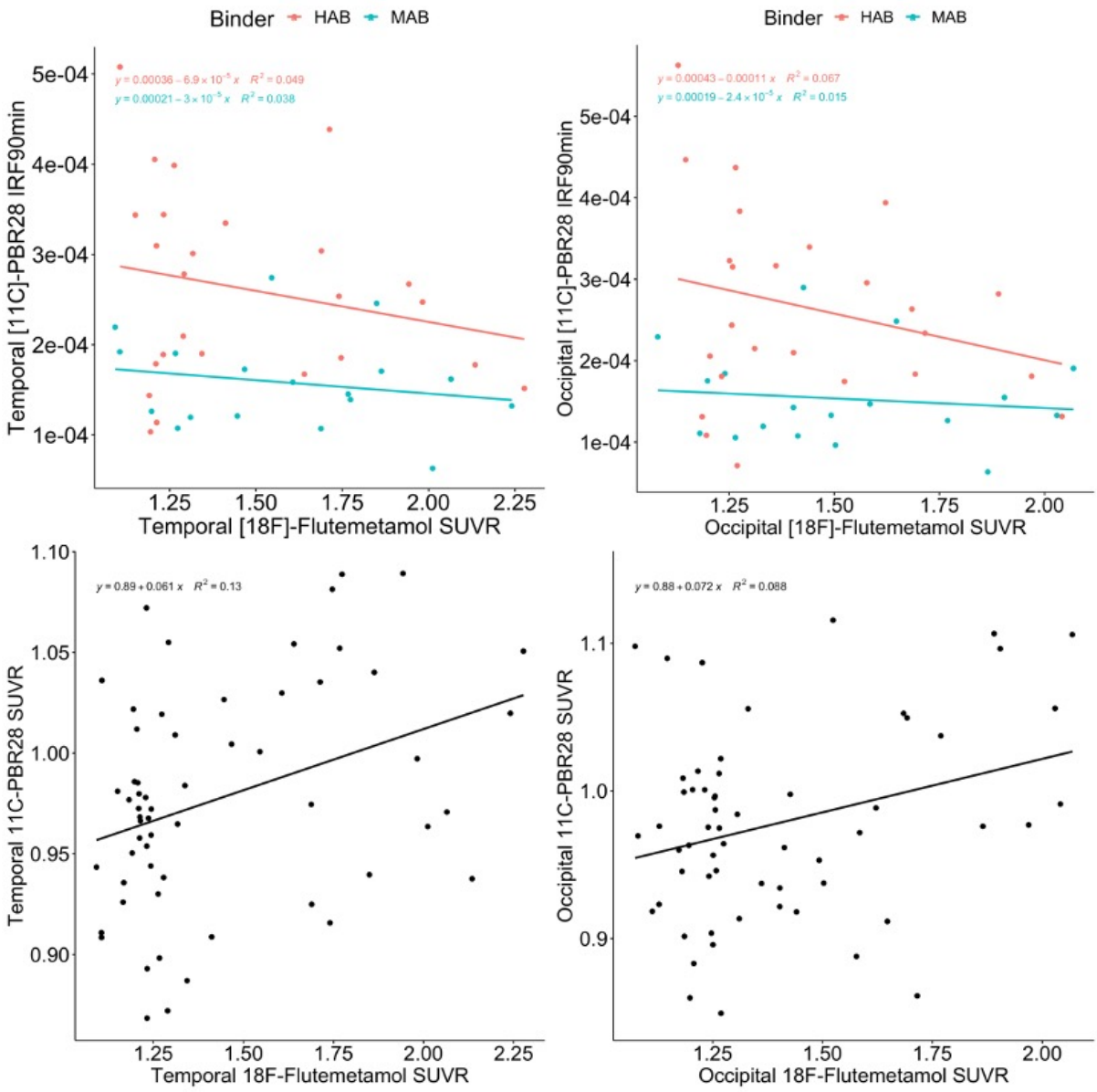

Figure 2.20. Correlation between ^{11}C-PBR28 and ^{18}F-Flutemetamol measurements

In medial temporal lobe and occipital lobe, ^{18}F-AV1451 SUVR significantly correlated with ^{11}C-PBR28 SUVR (β=0.19, 95%CI 0.045~0.33, p=0.015; β=0.11, 95%CI 0.031~0.19, p=0.0099), but not ^{11}C-PBR28 Logan-V_T or IRF90min (Figure 2.21). Age and TSPO genotypes were included in all regression models as independent variables of no interest.

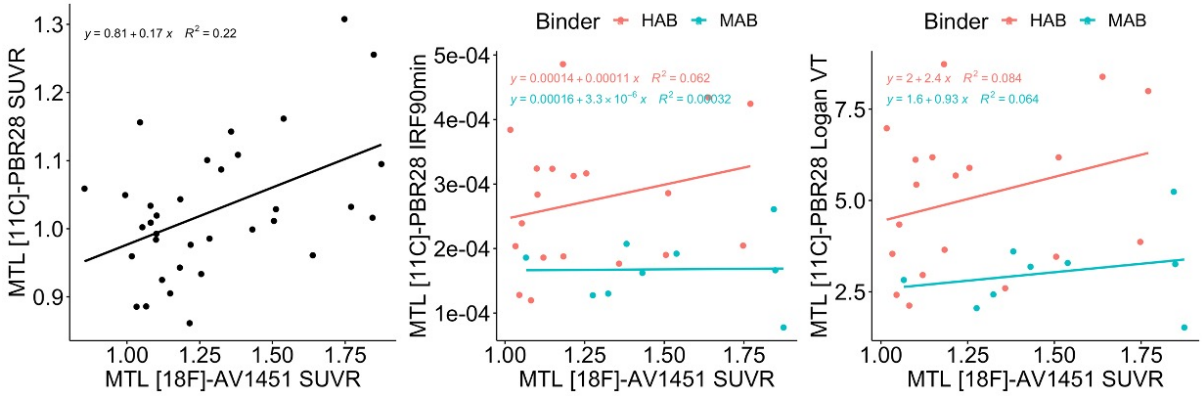

Figure 2.21. Correlation between ^{11}C-PBR28 and ^{18}F-AV1451 measurements in medial temporal lobe.

2.3.8 Voxel-wise regression analysis between ^{18}F-Flutemetamol, ^{18}F-AV1451, and ^{11}C-PBR28 SUVR images

In the regression model, ^{11}C-PBR28 uptake was positively associated^{18}F-Flutemetamol mainly in the posterior part of the brain including bilateral precentral and postcentral gyri, precuneus, occipital pole, lingual gyri, cuneal cortices, parahippocampal gyri and right lateral occipital cortex (Figure 2.22 A). While ^{18}F-AV1451 SUVR was associated with increased ^{11}C-PBR28 uptake in more wide-spread areas covering bilateral hippocampi, parahippocampal gyri, inferior temporal gyri, posterior cingulate gyri, precuneus, superior parietal lobules, occipital pole, lateral occipital cortices, angular gyri, lingual gyri, supramarginal gyri, precentral and postcentral gyri, superior frontal gyri, frontal pole, plus right temporal pole and middle temporal gyrus (Figure 2.22 B).

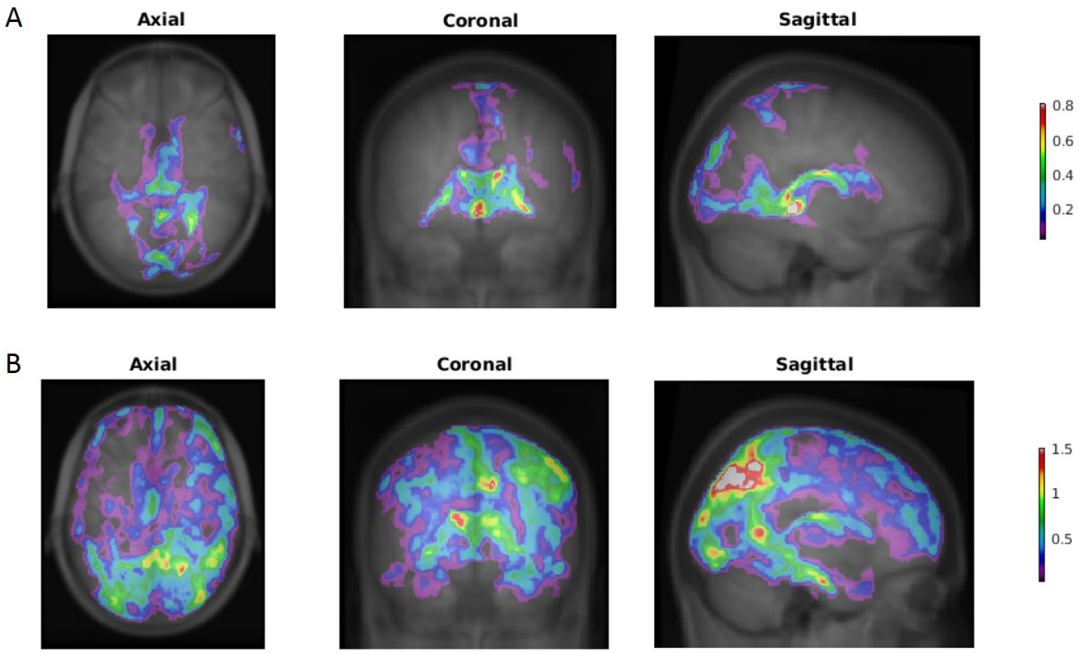

Figure 2.22. Voxel wise correlation between tracer uptakes (age adjusted). A: association between ^{11}C-PBR28 and ^{18}F-Flutemetamol SUVR; B: association between ^{11}C-PBR28 and ^{18}F-AV1451 SUVR

2.4 Discussion and Conclusions

^{11}C-PBR28 has become one of the most widely applied TSPO tracers in neuroinflammation research (Varrone & Nordberg, 2015). One of the major challenges in interpreting ^{11}C-PBR28 data is the high inter-subject variability in absolute quantifications of ^{11}C-PBR28 bindings even after correcting for TSPO genotype and using improved models (Collste et al., 2016). It has been shown that the absolute bindings could be influenced by numerous factors including demographic characteristics, psychological events and even time of the day (diurnal changes). Further, it has been argued that errors in arterial blood measurements may add up to the variation in final quantification results (Lyoo et al., 2015b). In fact, in the current analysis, 3 of the patients (1AD and 2MCI) were excluded because of apparent errors

in the arterial blood data, and it is inevitable that tolerable errors exist in any measurement step. Altogether, the high variability in absolute quantifications may reduce statistical power in analysis and requires more samples to be acquired to detect a difference in populations or to reliably infer an association in clinical studies, which is often costly and not always practical.

Analysis of ^{11}C-PBR28 absolute quantifications (Logan V_T and IRF-90min) has shown a trend of increased ^{11}C-PBR28 binding in AD and MCI patients compared to healthy volunteers in HAB group. However, due to the high variability in the data, the differences did not reach statistical significance. In MAB group, interestingly, AD patients seemed to have lower tracer binding compared to HCs. However, the findings in MAB group should be treated with caution because of limited number of cases (7 AD and 7 HC MABs). These findings also highlight the issue of high inter-subject variability in ^{11}C-PBR28 bindings. And the single nucleotide polymorphism of TSPO gene further complicates the problem, as by splitting research cohorts into different groups would further reduce the available data for analysis in each group, which would undermine the statistical power to detect meaningful signals from noisy data.

One of the approaches to reduce the inter-subject variability is to use the reference region method. An ideal reference region in PET kinetic modelling should have negligible expression of tracer binding sites and therefore an input function could be derived from the time-activity data in the reference region to substitute arterial sampling data (Slifstein & Laruelle, 2001). However, there is no region completely devoid of TSPO expression in human brain, and there have been efforts in extracting 'clusters' of reference tissue for derivation of input function (Zanotti-Fregonara, Kreisl, Innis, & Lyoo, 2019). Alternatively, in clinical research a pseudo-reference region could be putatively defined as a region that has similar physiological properties as the target region but is minimally affected by the disease

in question. For example, the contralateral region versus epileptogenic site in epilepsy (Dickstein et al., 2019), the rest of cerebral cortex versus precentral gyrus in motor neuron disease (Paganoni et al., 2018) (Alshikho et al., 2016), and normal appearing white matter versus lesions in multiple sclerosis (Singhal et al., 2018). This ratio method would control for the demographic, physiological and psychological effect in a specific subject, and reflect the relative change in tracer bindings associated with the disease.

For AD, depending on the pathological stage of the disease, the whole neocortex, including primary motor and sensory cortex, could be affected by Alzheimer's pathology. Although there have been reports that the whole brain or the occipital cortex could be used as a reference region in relatively early AD cohorts (Albrecht et al., 2018) (Nair et al., 2016), our analysis on the current cohort have shown increased ^{18}F-Flutemetamol and ^{18}F-AV1451 bindings in the entire neocortex including the occipital cortex, suggesting that these choices are not suitable for the current cohort. The cerebellum, on the other hand, in minimally involved in AD until the terminal stage (Braak & Braak, 1991), and therefore was more commonly used as reference region in AD research (Kreisl et al., 2017; Kreisl et al., 2016b; Lyoo et al., 2015b; Zou et al., 2020). However, it has been criticized that the ratio methods may lose biological relevant variations compare to the gold standard (Matheson et al., 2017).

To address the argument, I have tested whether I could replicate established findings of TSPO imaging studies using SUVR method with cerebellum as reference region for ^{11}C-PBR28 quantification using an independent dataset, and tested whether the variation in ^{11}C-PBR28 SUVR is associated with biological factors such as amyloid and tau pathologies. I have first validated that there is no difference of tracer bindings in the cerebellum using Logan graphic and spectral analysis, which permitted the use of cerebellum as a pseudo-reference region. Further, using the SUVR method and our independent dataset, we have found increased ^{11}C-PBR28 uptake in the MTL and middle/inferior temporal gyri, which is

consistent with the findings by Lyoo and his colleagues (Lyoo et al., 2015b). Moreover, I have demonstrated that ^{11}C-PBR28 SUVR correlates with amyloid and tau pathologies, as evaluated by ^{18}F-Flutemetamol and ^{18}F-AV1451, in vivo at both ROI and voxel level, which is consistent with prior pathology knowledge and consistent with recent imaging findings using ^{11}C-PK11195 (Ismail et al., 2020). Also, this finding has suggested the although the variance of SUVR is much lower compared to absolute quantifications, the variance remained biologically relevant.

In conclusion, I have shown that the SUVR method using cerebellum as a pseudo-reference region could ameliorate the high inter-subject variability issue in ^{11}C-PBR28 quantification and could produce more consistent findings across independent cohorts in Alzheimer's research. Further, given the stronger association between ^{11}C-PBR28 SUVR and imaging markers of amyloid and tau pathologies in cognitively impaired cohort, we can reasonably believe that by carefully selecting appropriate reference region, the SUVR method not only does not eliminate biological relevant signals, but could improve statistical power by cancelling variations caused by other non-disease-specific factors, which could be very helpful in clinical studies with moderate sample size. The simplicity and relative non-invasiveness of SUVR method could facilitate the use of ^{11}C-PBR28 at larger scale and benefit neuroimaging research of neuroinflammation.

Based on previous reasoning, SUVR method was used in further analysis of my project. Because there is no significant abnormality in PET imaging data of the 3 subjects with failed arterial sampling, these subjects were included in further analysis using SUVR values.

Chapter 3. Influence of neuroinflammation on neuronal activity and functional connectivity

3.1 Introduction

3.1.1 Functional MRI and BOLD signal

Functional MRI (fMRI) utilizes the blood oxygen level dependent (BOLD) contrast. The inversion recovery echo-planar imaging (EPI) sequence fMRI is sensitive to T2* relaxation time, which is influenced by the ratio between oxyhaemoglobin (HbO_2) and deoxygenated haemoglobin (Hb). Hb is paramagnetic and Hb in tissues can cause inhomogeneities of magnetic field in the microenvironment, which will facilitate the desynchronisation process of protons after the excitation sequence, and hence reduce the signal. HbO_2, on the other hand, is diamagnetic and does not interfere with the T2 relaxation process. Therefore, using a T2* sensitive sequence, tissues that has more Hb in its blood vessels will have lower signals, which is the case when there is less neuronal activity in that region (Ogawa, Lee, Nayak, & Glynn, 1990) (Belliveau et al., 1991).

That regions with increased neuronal activity have higher HbO_2 concentration is caused by the haemodynamic response (Figure 3.1). In brain, the blood supply increases in response to neuronal activity to meet the metabolic and oxygen demand, and the amount of compensatory supply after neuronal activity exceeds the initial consumption. As a result, the ratio between HbO2 and Hb increases after neuronal activity in that region, which in turn lead to an increased BOLD signal in fMRI. One should note that there is a 6~7 second delay between neuronal activity and the peak of haemodynamic response, followed by a lower than initial blood supply before returning to normal state (Iadecola, 2004). The haemodynamic response function should be considered in the first-level analysis of task-based fMRI scans; however,

it is less relevant in resting state fMRI (rs-fMRI) since there is no specific event related change to be modelled.

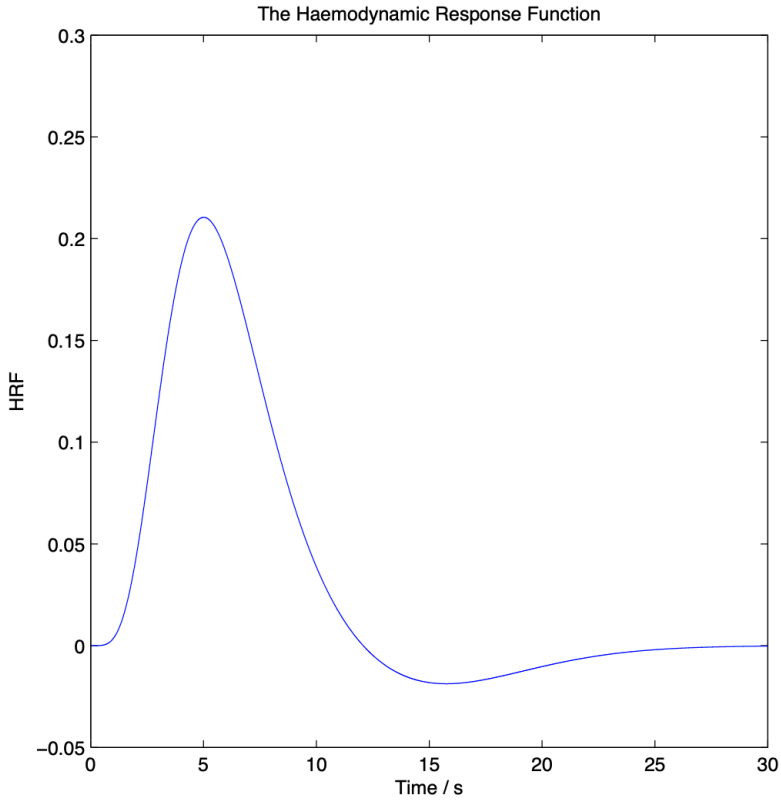

Figure 3.1 Illustration of haemodynamic response function.

The function peaks at 6~7s after the onset of the related event, followed by a lower than initial blood supply before returning to normal state.

The rs-fMRI refers to fMRI acquisition when no specific task or stimulus is present for the brain to process, hence the brain is at "resting state". However, the neurons in living brain are not exactly resting, as simultaneous fluctuations of signals have been well observed at "resting state" by functional brain imaging techniques (Biswal, Van Kylen, & Hyde, 1997). It has been demonstrated that the fluctuations in BOLD signals are related to the simultaneous neuronal activities (Shmuel & Leopold, 2008) (Scholvinck, Maier, Ye, Duyn, & Leopold, 2010). Using the timeseries of rs-fMRI scans, not only the simultaneous neuronal activities at

an individual region can be detected, but the functional relationship between anatomically separated locations can be inferred from the temporal coherence of BOLD signals in these regions.

3.1.2 What can be inferred from resting state fMRI

One of the key targets of interest in neuroscience is the level of neuronal activity itself. As the BOLD signal reflects the haemodynamic response of neuronal activity, the amplitude of BOLD signal fluctuations can serve as a marker of local neuronal activity. The idea has been reinforced by the findings that fluctuations of BOLD signal are well correlated to electrophysiological recordings of neuronal activities (Nir et al., 2008) (Scholvinck et al., 2010). To avoid contamination from noise due to movement or other physiological factors such as cardiac pulses and respiration, only low-frequency signals are of interest for this purpose, hence the amplitude of low-frequency (~0.01-0.1Hz) fluctuations (ALFF) has been proposed as a probe to reflect neuronal activity and assess functional connectivity (Cordes et al., 2001).

Taking one step forward, as the brain relies on cooperation of multiple cortical regions in effective functioning, how well the key regions are functionally linked together is of interest. The term “functional connectivity” is coined to describe this functional association between brain regions. To evaluate functional connectivity between two different regions of the brain, the coherence or corelation between the timeseries of BOLD signal from two regions can be calculated, based on the assumption that if two regions are functionally connected, they will coactivate to work together in order to perform certain task, and therefore their BOLD timeseries will be temporally dependent with each other (Aertsen, Gerstein, Habib, & Palm, 1989).

Using rs-fMRI, a number of resting state brain networks have been observed, including the motor, visual, salient, dorsal attention and default mode network (Damoiseaux et al., 2006; van den Heuvel & Hulshoff Pol, 2010). Among these networks, the most prominent one is the default mode network (DMN), which shows increased activity in resting state and is believed to represent the default state of the brain (Marcus E Raichle et al., 2001). The key hubs of the DMN are posterior cingulate cortex/precuneus (PCC), medial prefrontal cortex and bilateral inferior parietal cortices (M. E. Raichle, 2015). The connectivity within DMN has been found to be associated with cognition and emotion processing, perceiving the outside environment and mind wandering. Because of the stability of DMN across population and the functional importance of DMN, it has become one of the most investigated resting state networks in numerous neurological and psychological disorders (M. E. Raichle, 2015).

3.1.3 Approaches in rs-fMRI analysis

Seed-based analysis

The methodology of analysing connectivity of a region or a network can be generally categorised into the model-dependent and model-free approaches. The model-dependent approach is based on prior knowledge of a network or a ROI, for example, the key hubs of a network and their anatomical positions. By defining a ROI, or seed, the average timeseries form the seed region can be extracted and used to correlate with all voxels inside the brain or the average BOLD signals in other seed regions. The whole brain functional connectivity map of the seed region or the connectivity metrics between the seeds can then be produced for further analysis (Cordes et al., 2000). The advantages of seed-based method are its simplicity and easiness for interpretation, moreover, by using the same seed in analysis, data from different studies can be easily compared and analysed. However, the model-dependent nature of seed-based approach also limits its potential to find unexpected yet meaningful

patterns of brain connectivity that is not considered in model design (van den Heuvel & Hulshoff Pol, 2010).

Independent component analysis

The model-free approaches do not require a pre-defined set of seeds and are data-driven methods. The most successful and commonly used data-driven approach in fMRI analysis is independent component analysis (ICA). ICA functions to decompose mixed signals into separate components that are linearly independent of each other (McKeown & Sejnowski, 1998). The fact that BOLD timeseries in each voxel are mixture of neuronal activities that are from different neuronal circuits (and noise components) makes ICA ideal for analysing the complex fMRI data. As ICA is completely data driven, it can often unveil unexpected components from fMRI data, and is useful in exploring novel patterns of connectivity, breaking known networks into sub-networks and separating noise components. One of the limitations of ICA approach, however, is that the decomposition driven by different data are not exactly comparable across studies, making interpretation of results more difficult compared to model-dependent approaches (Fox & Raichle, 2007). Another issue is that unlike principal component analysis which has single 'correct' solution, the solutions can vary using different algorithms (Risk, Matteson, Ruppert, Eloyan, & Caffo, 2014). Further, the optimal number of independent components find by the algorithm to minimize the cost function can vary a lot depending on input data, and too large/small a number of components can lead to degradation/fusion of networks of interest, adding up to difficulty to interpret the results.

Graph theory

Another way to examine brain connectivity is to treat the entire brain as a network, and to look at the global organisation of the entire network. In practice, the brain can be parcellated

into a number of ROIs, based on prior anatomical or functional knowledge, and each of the ROI is considered as a node of a graphical network (Rubinov & Sporns, 2010). The connectivity between each two of the nodes can then be computed, and if the connectivity between two nodes is strong enough, an edge is considered to exist between the nodes (Bullmore & Sporns, 2009). Therefore, a graph G= (N, E) can be established, with N being the collection of nodes and E being the collection of edges (Figure 3.2). Following the construction of graph G, its key properties can be examined, including its segregation, integration, and small-world property.

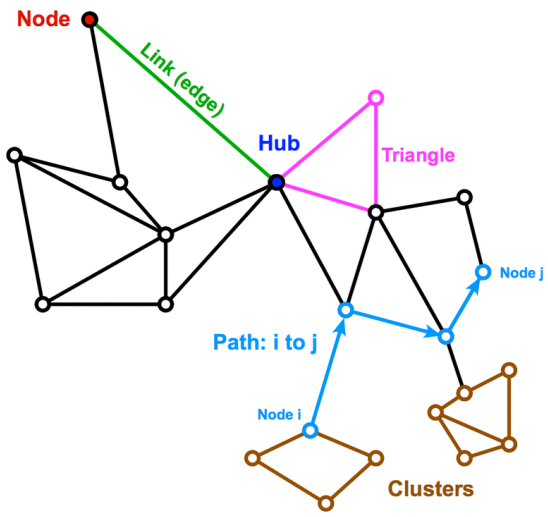

Figure 3.2 Visual illustration of a graph consisting of edges and nodes (image adapted from http://mriquestions.com/networkgraphs.html)

Network segregation refers to the ability of the brain to process information within an interconnected subgroup of regions. These subgroups of nodes may be specialised for certain tasks and with a number of segregated subgroups the brain can process various tasks simultaneously with high efficiency. These clusters of functional connected nodes are presented as triangles in the graph, i.e., the neighbours of a nodes are interconnected as well. Clustering coefficient of a node is defined as the fraction of triangles around that node, in

other words, for node A, clustering coefficient is the number of edges between A's neighbours divided by all possible links between A's neighbours (Watts & Strogatz, 1998). The clustering coefficient of a network is simply the average nodal clustering coefficients. Local efficiency, similarly, is also a measure of network segregation, but with the path length between A's neighbours considered, and provides information about how well neighbouring nodes forms local connections and communicate locally (Latora & Marchiori, 2001).

Network integration, on the other hand, reflects the brain network's ability to summarise or combine information across segregated regions. In other words, it measures how easy it is for information to be passed from a node to any other node in the brain. In graph, this can be represented by the average shortest path length (edges that must be passed) from node A to any other node in the network. For a network, its characteristic path length is defined as the average shortest path length between all pairs of nodes (Watts & Strogatz, 1998). This simple measure, however, has the caveat that it cannot deal with disconnected nodes. To deal with the caveat, the measure global efficiency was proposed, which is related to the inverse of shortest path length, but for disconnected nodes the path length is considered infinite and therefore the global efficiency can be meaningfully computed as zero (Latora & Marchiori, 2001).

One would perceive that organisation of brain network has to balance the need to have both high local efficiency and high global efficiency. This demand cannot be met by two most simple and common network organisations: random network and regular network. For a random network, where the edges randomly connect pairs of nodes, the characteristic path length is low, but the clustering coefficient is also low, and therefore the network will not satisfy the need for local efficiency. On the other hand, a regular network has high clustering coefficient but large characteristic path length as well, so the need for global efficiency is not met. It has been established that the brain uses a small-world organisation to solve the

aforementioned issue (Achard et al., 2006) (Fair et al., 2009). Technically, small-world networks are those which have approximately same characteristic path length as random networks, but still have significantly higher clustering coefficient compared to random networks (Watts & Strogatz, 1998). This is achieved by having highly connected hubs in the network, the edges between which form common pathways for connections between members of different clusters (Figure 3.3). The metric small-worldness is coined to reflect how effective is the network organised in a small-world fashion and is expressed as the ratio between network G's clustering coefficient and clustering coefficient of similar random networks, divided by the ratio between G's characteristic path length and that of similar random networks (Humphries & Gurney, 2008). The exact expressions of the network measures are presented in method session.

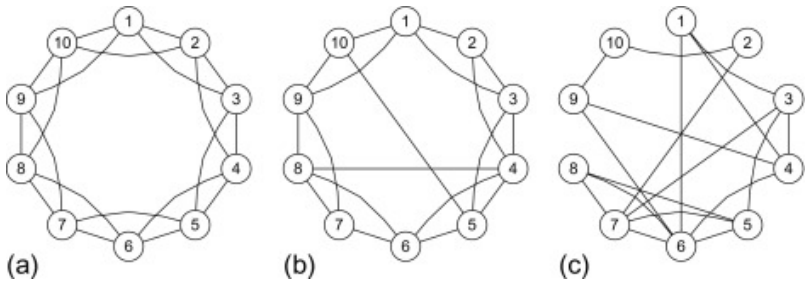

Figure 3.3 Illustration of common network organisations. (a) regular network; (b) small-world network; (c) random network. (image by Arnaboldi et al. (Arnaboldi, Passarella, Conti, & Dunbar, 2015))

In addition, using graph theory, the characters of individual node can be examined by graph metric such as degree and betweenness centrality. The degree of a node refers to the number of edges connected to the node, while betweenness centrality of a node indicates how many shortest paths between other node pairs go through the node in question. One would expect nodes that have high degree and betweenness centrality to take important positions in global

network and facilitate network integration, and thus these nodes are considered as functional hubs.

3.1.4 Rs-fMRI Studies in AD Research

One of the earliest findings of resting state functional network alteration in AD patients is the decreased functional connectivity within the DMN, especially in PCC and hippocampus (Greicius, Srivastava, Reiss, & Menon, 2004) (L. Wang et al., 2006). The disruption of DMN connectivity has been later consistently found in AD, MCI and even healthy cohorts at risk of AD, with an anterior-posterior dissociation being the most prominent feature (Binnewijzend et al., 2012; Lustig et al., 2003; Seeley et al., 2009; Sorg et al., 2007; Y. Wang et al., 2013).

Using graph theory methods, studies have found a disruption of functional brain network organisation in AD patients. Decreased network segregation measures, including clustering coefficient and local efficiency have been found in brain networks of AD patients (Dai et al., 2019; Reijmer et al., 2013; Supekar, Menon, Rubin, Musen, & Greicius, 2008). On the other hand, increased characteristic path length and decreased global efficiency have been reported, indicating impaired network integration (Y. Liu et al., 2014). These changes could be associated with a loss of small-world properties of functional architecture of the brain network. Indeed, studies have suggested that the brain changes towards a random network structure in AD (Supekar et al., 2008). Similar changes have been found in MCI patients, although less prominent (Dai & He, 2014).

The integrity of DMN and network segregation/integration metrics have been further found to be associated with cognitive performance in AD and MCI patients (Dai & He, 2014), and in fact several studies have demonstrated functional connectivity as a good biomarker for classifying Alzheimer's disease (de Vos et al., 2018; Khazaee, Ebrahimzadeh, & Babajani-Feremi, 2015). These findings highlight the importance of functional brain connectivity in

cognition and disease. However, how the changes are associated with pathological factors of AD remains to be elucidated. Several studies have reported that amyloid positive patients or healthy elderly have disrupted functional connectivity compared to amyloid negative patients (Hedden et al., 2009; Sheline et al., 2010) , however, the quantitative influence of amyloid deposition on functional network still remains to be tested. More recently, Passamonti and colleagues reported that an increased load of independent component of ^{11}C-PK11195, which predominately reflected inferior and medial temporal tracer uptake, was associated with decreased DMN intra-network connectivity in a similar combined amyloid positive cohort (Passamonti et al., 2019), but how an inflammation pattern influenced brain scale connectivity remained to be explored, as discussed in chapter 1.

3.2 Hypothesis and aim of the chapter

The hypothesis of current study is that neuroinflammation in Alzheimer's disease can actively and independently contribute to the damage of neuronal circuit and disrupt normal neuronal activity, the consequence of which are global impairment of the brain and ultimately cognitive impairment.

The aim of the current chapter is to test the prediction (based on the hypothesis): neuroinflammation is associated with the disruption of functional connectivity in AD and MCI patients, both at network level and global level, independent of amyloid deposition quantity.

3.3 Methods

The MRI scans were acquired with a 3 Tesla Siemens Verio scanner using a 32-channel head coil at the clinical imaging facility, Hammersmith Campus, Imperial College London.

3.3.1 T1-weighted MRI scan acquisition

The T1-weighted scans were acquired using the MPRAGE sequence for better tissue segmentation performance**:** Sagittal orientation; Anterior to posterior phase encoding direction; FOV 256×240×160mm; 1×1×1mm isotropic voxels; TR=2300ms; TE=2.98ms; TI=900ms; Flip angle=9°; Bandwidth=240Hz/Px; Echo spacing=7.1ms; Interleaved acquisition.

3.3.2 Resting state fMRI scan acquisition

Resting state functional scans (RS-fMRI) were acquired by an EPI sequence over 10 minutes with the following parameters: 35 axial slices, TR=2000ms, TE=30ms, FOV=192×192mm^2, Flip angle=80°, 3×3×3mm voxel size, anterior-posterior phase encoding direction, bandwidth=1906 Hz/Px, echo spacing=0.61ms. A total of 300 volumes were acquired per scan.

3.3.3 Volumetric and surface-based statistics on T1-weighted scans

Distortion corrected T1-weighted scans were processed using the automatic structural image analysis pipeline provided by FreeSurfer (Harvard Medical School; surfer.nmr.mgh.harvard.edu). The T1 images first underwent non-uniform intensity normalization, and then transformed in to Talairach space. Brain extraction was then performed using a watershed/surface deformation procedure (Segonne et al., 2004). Further linear and nonlinear volumetric registration was then performed using the extracted brain. Following that, segmentation of deep grey matter, white matter and ventricles was performed, giving volumetric measurements on subcortical structures including hippocampus, amygdala, basal ganglion and ventricles (Fischl et al., 2004). Then white matter segmentation and tessellation of grey matter/white matter boundary were executed, creating the original surface (Fischl, Liu, & Dale, 2001). The original surface was then smoothed, inflated and underwent

topology correction (Segonne, Pacheco, & Fischl, 2007). The final surfaces were finally inflated to spherical geometry, on which anatomical parcellation was performed and surface-based metrics, including cortical thickness, surface area, surface curvature, cortical grey matter volumes, were measured (Fischl & Dale, 2000).

3.3.4 Pre-processing of fMRI scans

RS-fMRI pre-processing was performed with FEAT and MELODIC tools in FSL (Smith et al., 2004). Briefly, the first 5 volumes of rs-fMRI images were discarded to allow magnetic field stabilization. The rest 295 volumes were first realigned using rigid-body transformation with FSL's FLIRT (FMRIB's Linear Registration Tool) (Jenkinson, Bannister, Brady, & Smith, 2002). Next, slice timing correction was applied to each voxel's using sinc interpolation to shift timeseries by the fraction of TR corresponding to the acquisition order. The aim of the step is to make all voxel in a 3D-volume as if they were all acquired at same time, which is not the case in echo planar imaging. The movement parameters were recorded for use in further denoising step. Volumes with framewise displacement > 0.9mm or global BOLD signal changes above 5 standard deviation were considered as outliers and discarded.

FSL's BET tool was used for brain extraction of the fMRI images. The mean image of all volumes was used as reference and a liberal threshold was used to prevent losing brain voxels.

Following slice timing correction, spatial smoothing was performed with a 4mm full-width half maximum (FWHM) Gaussian kernel. The intention of smoothing is to ameliorate zero-mean noise problem while preserving physiological signal. The 4mm FWHM was chosen to preserve as much spatial resolution as possible. The functional images were registered to the T1-weighted images and transformed to MNI space.

3.3.5 Denoising of rs-fMRI data

High-pass temporal filtering was applied to remove low-frequency fluctuations in the timeseries (<0.01Hz), which is usually caused by the drift of scanner field. To minimise the influence of noise in statistical inference, a combined ICA + nuisance regression approach was used in denoising, with FSL's MELODIC tool (Griffanti et al., 2014). Briefly, ICA decomposition was performed on each individual fMRI scan. The original 4D data are reshaped into a 2D time × space matrix, which is assumed to be the product of the timeseries of independent components and the spatial maps of components (Figure 3.4). The spatial and temporal properties of independent components were then inspected and labelled as noise components or probable valid signals with the help of FSL's FIX toolbox (Salimi-Khorshidi et al., 2014) and according to recommendation "*Hand classification of fMRI ICA noise components*" (Griffanti et al., 2017). The noise components, and the effect of other nuisance factors including white-matter signals, cerebrospinal fluid signals, motion parameters and their first-order temporal derivatives were regressed out.

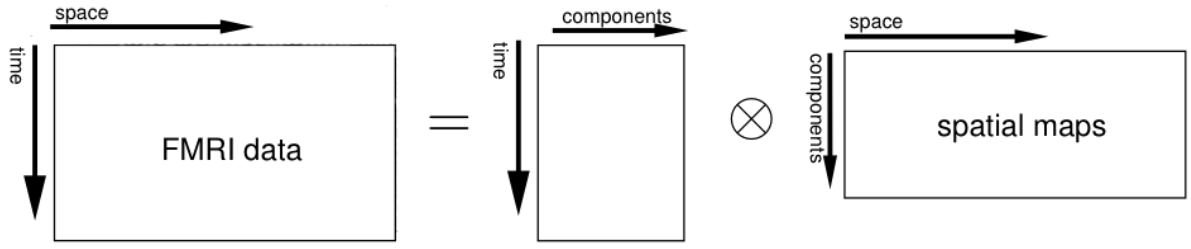

Figure 3.4 Illustration of ICA decomposition of single subject fMRI data

3.3.6 Spatial pre-processing of functional and structural MRI

Spatial pre-processing of fMRI and T1-weighted scans were performed using SPM12 embedded in CONN toolbox (Whitfield-Gabrieli & Nieto-Castanon, 2012). T1-weighted structural scans were segmented and transformed into MNI space using non-linear

transformation, while fMRI scans were first registered to structural scans using linear transformation and normalised to MNI space using same parameters as the structural scans.

3.3.7 Amplitude of low-frequency fluctuation analysis

After denoising, the ALFF parametric map was generated for each fMRI scan using CONN toolbox. Briefly, a fast Fourier transform (FFT) was applied for the timeseries of each voxel, generating a power spectrum. Then, the square root of amplitude at each frequency in the power spectrum was calculated and ALFF was defined as the average square root of amplitude across 0.01~0.1Hz (Cordes et al., 2001). Voxel wise comparison of ALFF was performed between HC, MCI, AD and amyloid positive groups to find any alteration of neuronal activity in patients. Further, in order to explore whether amyloid deposition or neuroinflammation is associated with altered neuronal activity in patients, voxel-to-voxel regression analysis was performed using ALFF image as dependent variable and ^{18}F-Flutemetamol SUVR, ^{11}C-PBR28 SUVR images as independent variables, with age and gender controlled as covariates of no interest. The voxel-to-voxel regression analysis was performed using the 'VoxelStat' package (Mathotaarachchi et al., 2016). Cluster forming threshold was set at $p<0.05$ and random field theory was used for FDR correction at cluster level. Clusters which survived FDR correction at $p<0.05$ were considered significant. The analyses were limited in grey matter regions using a grey matter mask, as one would expect most meaningful ALFF that is associated with neuronal activity to be within the grey matter.

3.3.8 Seed-based connectivity analysis

As previous literature has reported disrupted DMN connectivity consistently in different cohorts, the medial prefrontal cortex (MPFC) and posterior cingulate/precuneus (PCC) were selected as seeds in connectivity analysis. It has been established that MPFC and PCC are the anterior and posterior hub of DMN, respectively. The masks for MPFC and PCC were

provided by CONN toolbox, based on the group ICA analysis of HCP dataset (n=497) (Whitfield-Gabrieli & Nieto-Castanon, 2012). The main reasons for using seed-based analysis predefined ROI masks were to improve reproducibility across studies and avoid cohort specific bias, as compared to defining ROIs based on ICA of the local dataset. Voxel-wise comparisons of MPFC and PCC connectivity maps between different diagnostic cohorts were performed. Further, the effects of local neuroinflammation and amyloid deposition on brain connectivity of MPFC and PCC were analysed using linear regression models. The same masks were transformed into each individual's PET spaces where ^{11}C-PBR28 and ^{18}F-Flutemetamol SUVR were sampled. Age and gender were included in both group comparisons and regression models as covariate of no interest. Cluster forming threshold was set at $p<0.05$ and random field theory was used for FDR correction at cluster level. Clusters which survived FDR correction at $p<0.05$ were considered significant.

3.3.9 Graph theory analysis

Construction of functional connectivity matrices was performed by GRETNA(J. Wang et al., 2015) using the anatomical automatic labelling atlas (AAL-90). For each fMRI scan, the mean timeseries of each ROI was extracted, and the temporal correlations between each pair of ROIs were computed, generating a 90×90 connectivity matrix. The matrices were then Z-transformed and binarized connectivity matrices were created with a network sparsity threshold of 0.2, in order to maintain the connectedness of brain network and remove spurious correlations. A network sparsity threshold was used instead of a Z-threshold or p-threshold was used because the latter approaches would result in different number of edges in different participants and render the networks less comparable across the cohort. The threshold of 0.2 was chosen based on the following reasons: (1) the network metrics trend to stabilise after the network sparsity level of 0.2 has been reached, (2) the network metrics computed under the

threshold of 0.2 could better distinguish different diagnostic groups (especially between Alzheimer's dementia patients and healthy controls, Figure 3.5).

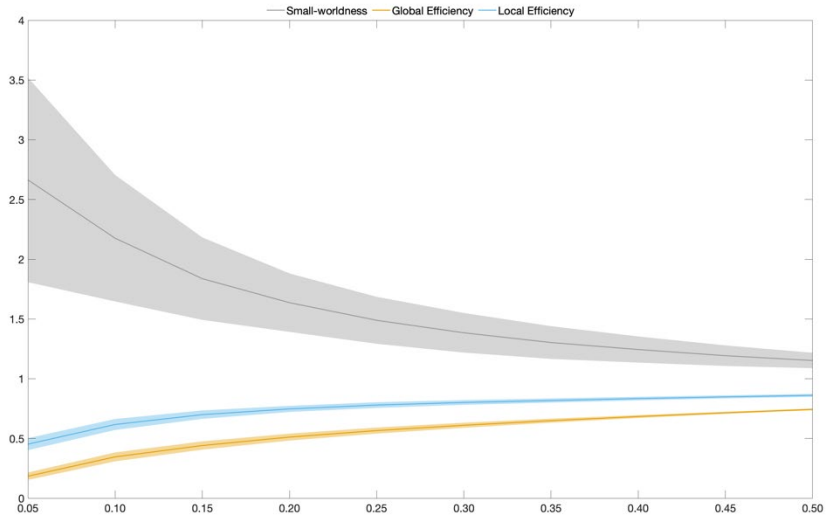

Figure 3.5 Mean values of network topology metrics under different sparsity thresholds of functional connectivity matrix.

Solid lines show the mean value of the whole study cohort and shaded area show the standard deviation of values. X-axis is value of sparsity threshold; Y-axis is the value of network metrics.

To investigate the global functional network organisation, the following measures of the network were computed. These measures can provide information about network segregation, network integration and small-world property:

(1) Network segregation measures: Clustering coefficient and local efficiency; (2) Network integration measures: characteristic path length and global efficiency; (3) Small-worldness. The exact formulae for computation of the metrics are as following:

$$C = \frac{1}{n}\sum_{i\epsilon N} C_i = \frac{1}{n}\sum_{i\epsilon N}\frac{2t_i}{k_i(k_i-1)} \quad (3.1)$$

$$E_{loc} = \frac{1}{n}\sum_{i\epsilon N} E_{loc,i} = \frac{1}{n}\sum_{i\epsilon N}\frac{\sum_{j,h\epsilon N.j\neq i} a_{ij}a_{ih}[d_{jh}(N_i)]^{-1}}{k_i(k_i-1)} \quad (3.2)$$

$$L = \frac{1}{n}\sum_{i\epsilon N} L_i = \frac{1}{n}\sum_{i\epsilon N} \frac{\sum_{j\epsilon N, j\neq i} d_{ij}}{n-1} \quad (3.3)$$

$$E_g = \frac{1}{n}\sum_{i\epsilon N} E_i = \frac{1}{n}\sum_{i\epsilon N} \frac{\sum_{j\epsilon N, j\neq i} d_{ij}^{-1}}{n-1} \quad (3.4)$$

$$SW = \frac{C/C_{rand}}{L/L_{rand}} \quad (3.5)$$

Where C is the clustering coefficient, E_{loc} is the network local efficiency, L is the characteristic path length, E_g is the global efficiency, and SW is the small-worldness. t_i is the number of triangles with node i being one apex, ki is the number of edges connected to node i, E_i is the global efficiency of node i, d_{ij} is the shortest path between node i and j. $E_{loc,i}$ is the local efficiency of node i, $d_{jh(N_i)}$ is the shortest path between two neighbour nodes of i, (j and h), and K_i is the degree of node i, which is the number of edges connected to the node. C and C_{rand} are clustering coefficients, L and L_{rand} are characteristic path lengths of current network and random networks (Rubinov & Sporns, 2010).

These network topology metrics were compared with diagnostic groups, and linear regression analyses were performed using network measures as dependent variable and measures of amyloid deposition, neuroinflammation, as independent variables. As network topology measures are reflecting the organisation of brain overall, global measures of ^{18}F-Flutemetamol and ^{11}C-PBR28 uptake are better fitted for the analysis. To obtain an overall tracer uptake, principal component analysis was performed using the tracer SUVRs in left and right frontal, temporal, parietal and occipital lobes, plus anterior and posterior cingulate cortices. The first principal components for both tracers were used in the analysis. In addition, the average SUVR in the cerebral grey matter was also tested in the regression models. Because the limited number of cases, robust regression method was used to estimate the parameters (βs) and permutation tests were used to determine the significance of the parameters.

According to the NIA-AA consensus on the framework of Alzheimer's disease spectrum(Jack et al., 2018), cognitively impaired participants (AD and MCI patients) who were amyloid-beta positive (Aβ+) in composite brain regions (N=26) were considered to be representative of the disease continuum, and were used as primary cohort for analyses. On the other hand, same analyses were also performed in AD and MCI groups separately in order to explore whether there are disease stage-dependent effects.

3.4 Results

3.4.1 Overview of available data and patient demographics

A total of 93 participants in the cohort had fMRI scans, of whom 21 were AD patients, 54 were MCI patients and 18 were healthy volunteers. Of all participants, 62 had ^{11}C-PBR28 scans, 84 had ^{18}F-Flutemetamol scans, and 40 had ^{18}F-AV1451 scans. The detailed demographic information, amyloid positivity and data overlap are summarized in table 3.1.

Table 3.1 Summary of available data regarding fMRI and DTI analysis on study cohort

Diagnosis	AD			MCI			HC		
Amyloid status	All	Aβ+	Aβ-	All	Aβ+	Aβ-	All	Aβ+	Aβ-
N	21	15	2	54	22	26	18	3	15
Gender (M/F)	12/9	8/7	1/1	34/20	13/9	16/10	10/9	1/2	9/6
Age (Mean±SD)	74±8.0	74±7.4	55, 78	71±8.6	75±7.4	67±9.0	66±9.0	71±12	65±8.3
MMSE (Mean±SD)	23±4.9	23±3.9	19, 27	28±2.0	28±1.8	27±2.4	29±1.8	30±0.6	29±2.0
^{11}C-PBR28$^{\#}$	19	14	1	28	12	13	15	3	12
^{18}F-Flutemetamol$^{\#}$	17	15	2	48	22	26	18	3	15
^{18}F-AV1451$^{\#}$	16	13	1	16	7	7	7	2	5

$^{\#}$: Number of available scans.

The demographics and cognitive performance of the study cohort are summarised in the following table 3.2.

Table 3.2. Demographics of the study cohort

	AD	MCI	HC	ANOVA
Cases	16	25	17	-
Age	72.8±8.64[a]	71.5±8.45[b]	64.3±9.38	0.012*
Gender (Male/Female)	9/7	14/11	8/9	0.82
IQ	113.3±16.35	111.3±13.42	113.4±8.66	0.91
NART	12.4±10.0	12.8±10.1	12.8±7.28	0.99
MMSE	23.0±3.67[a]	27.7±2.01	28.7±1.68	<0.0001**
Rey Copy	27.3±10.5	31.0±4.85	34.5±2.65	0.043*
Rey Imm	5.09±4.40[a]	15.4±6.15	17.5±11.1	0.14
Rey Del	4.71±6.67[a]	11.4±6.00	17.8±7.11	0.0001**
WLM Imm	17.2±10.1[a]	28.7±9.98[b]	44.4±8.67	<0.0001**
WLM Del	5.42±7.74[a]	12.8±6.39[b]	27.6±6.71	<0.0001**
Hopkins Imm	9.82±8.40[a]	20.9±6.39[b]	25.4±8.87	0.00026**
Hopkins Del	1.55±1.80[a]	6.54±6.69[b]	12.7±6.94	0.00015**
Hopkins RI	5.18±3.63[a]	8.33±3.49[b]	11.2±3.11	<0.0001**
LNS	3.64±2.25[a]	7.13±4.18[a]	10.71±3.20	0.001**
Semantic Fluency	11.1±3.11[a]	16.6±4.64[b]	22.8±9.08	<0.0001**
Verbal Fluency	33.8±12.8[a]	40.2±15.3[b]	48.2±12.9	0.046*
HADS Anxiety	6.73±3.58	7.04±4.28	5.14±3.37	0.35
HADS Depression	6.00±4.26	4.74±3.72	3.07±3.50	0.16

SD: standard deviation; NART: National Adult Reading Test; MMSE: Mini Mental State Examination; Rey: Rey–Osterrieth complex figure test, Imm: immediate recall, Del: delayed recall; WLM: Wechsler Memory Scale–Logical Memory test; Hopkins: Hopkins Verbal Learning Test, RI: Recognition Index; LNS: Letter-Number Sequencing; HADS: Hospital Anxiety and Depression Scale.

* p<0.05; ** p<0.001 in ANOVA; [a]: significant difference between Alzheimer's dementia patients and healthy controls in post-hoc comparisons (p<0.05); [b]: significant difference between mild cognitive impairment patients and healthy controls in post-hoc comparisons (p<0.05).

3.4.2 Demographics of Aβ+ cognitively impaired patients

As the Alzheimer's research community have reached the agreement that amyloid positive (and ideally NFT positive) cognitively impaired patients are more likely to fall within Alzheimer's continuum, effort was made to classify the current study cohort into Aβ+ and Aβ- participants according to ^{18}F-Flutemetamol PET scan. Since less than half of participants had ^{18}F-AV1451 scans, it is not feasible to further break the groups with regard to NFT pathology marker status. In the current cohort, a total of 26 (12 AD and 14 MCI) patients

who were classified as Aβ+ also had ^{11}C-PBR28 PET scans. These participants were considered to be representative of Alzheimer's spectrum and because of the limited number of cases, were combined together as the primary cohort to test the hypothesis. The demographics and cognitive performance of Aβ+ patients are briefly summarized in table 3.3.

Table 3.3. Demographic information of Aβ+ cohort

	Aβ+ Patients	Healthy Controls	P (t-test)
Age	74.7±1.5	64.3±2.3	0.001*
Gender(Male/Female)	14/12	8/9	0.66
Education (years)	14.7±0.7	14.8±1.0	0.98
MMSE	25.3±0.7	28.8±0.4	<0.001*
Ray Delayed Recall	6.8±1.4	17.8±2.2	0.001*
Hopkins Recognition	18.4±1.1	22.6±0.9	0.006*
Semantic Fluency	13.3±0.9	22.9±2.4	0.002*
Verbal Fluency	37.3±2.8	48.2±3.5	0.021*

Data are presented as mean ± SE. MMSE: Mini-mental state examination

3.4.3 Cortical thickness and grey matter volume

AD subjects showed significantly reduced cortical thickness in bilateral lateral occipital lobe compared to HC, and decreased thickness of left precuneus, left precentral gyrus, left medial temporal lobe (MTL), left supramarginal cortex and right lateral occipital lobe compared to MCI, while no significant different cortical thickness was found between HC and MCI subjects (Figure 3.6).

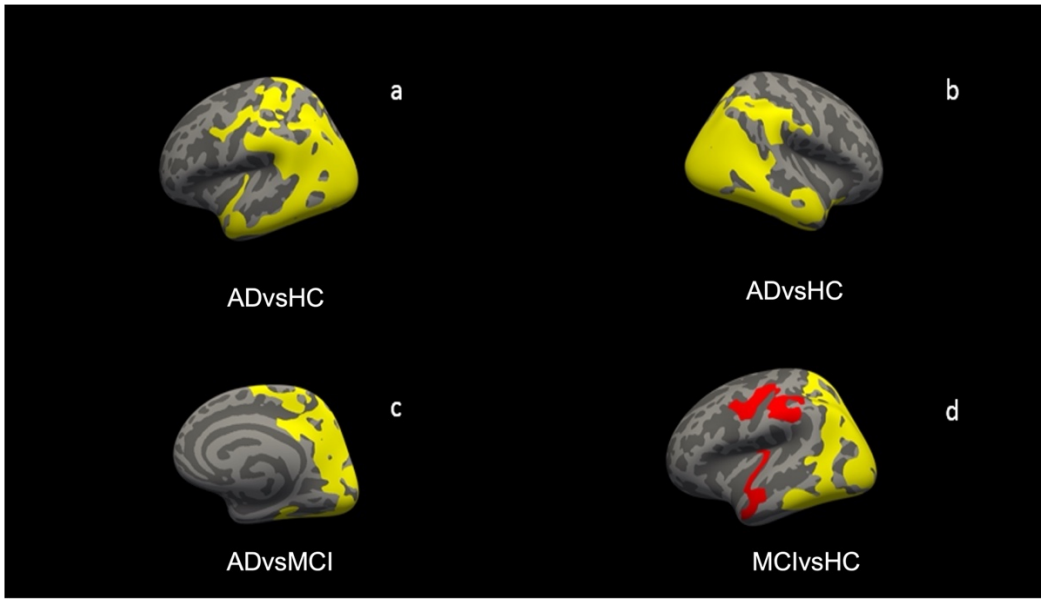

Figure 3.6. Group Comparison of Cortical Thickness

a. HC vs AD, left hemisphere; b. HC vs AD, right hemisphere; c. MCI vs AD, right hemisphere; d. HC vs MCI, left hemisphere; red and yellow denotes vertices that have significant difference between groups.

Decreased GM volume was found in bilateral lateral occipital lobe, right supramarginal cortex, left fusiform and left MTL in AD subjects compared to HC. Same results were found except left MTL in comparison between AD and MCI. Interestingly, MCI group have higher GM volume in right rostral medial frontal lobe compared to HC subjects (Figure 3.7).

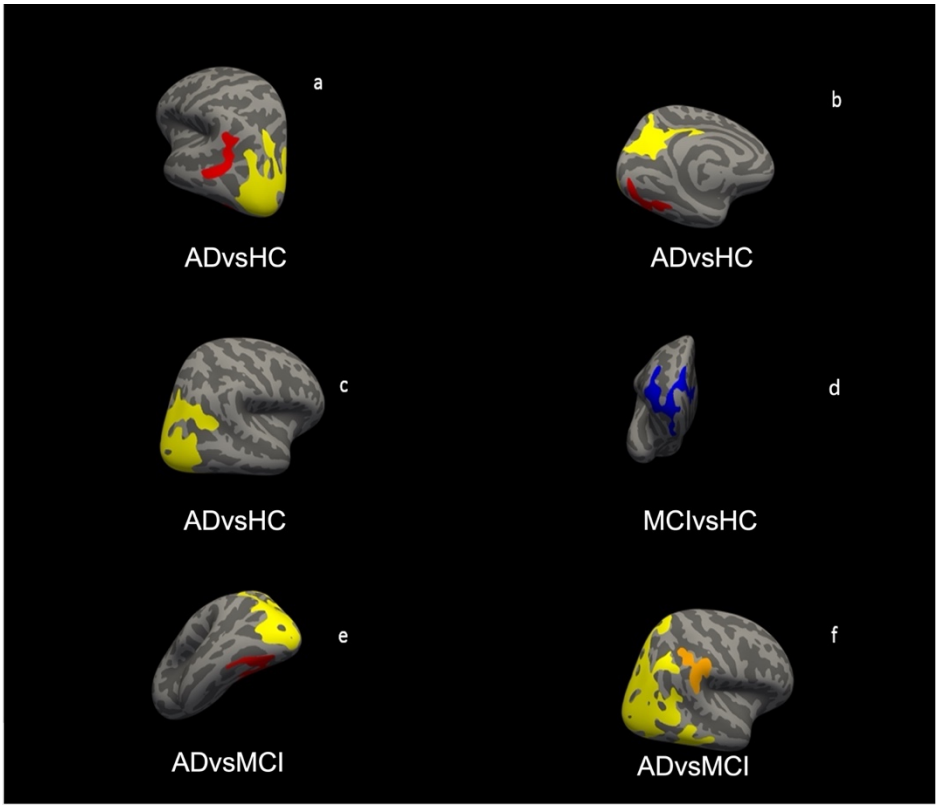

Figure 3.7. Group Comparisons of Grey Matter Volume

a. HC vs AD, left hemisphere; b. HC vs AD, left hemisphere; c. HC vs AD, right hemisphere; d. HC vs MCI, right hemisphere; e. MCI vs AD, left hemisphere; f. MCI vs AD, right hemisphere.

At whole brain level, AD patients had decreased average cortical thickness compared to HC and MCI patients ($p<0.0001$ and $p<0.00001$), and decreased cortex volume compared to HC and MCI ($p=0.0006$ and $p=0.001$). However, MCI patients did not have significant overall

change (Figure 3.8).

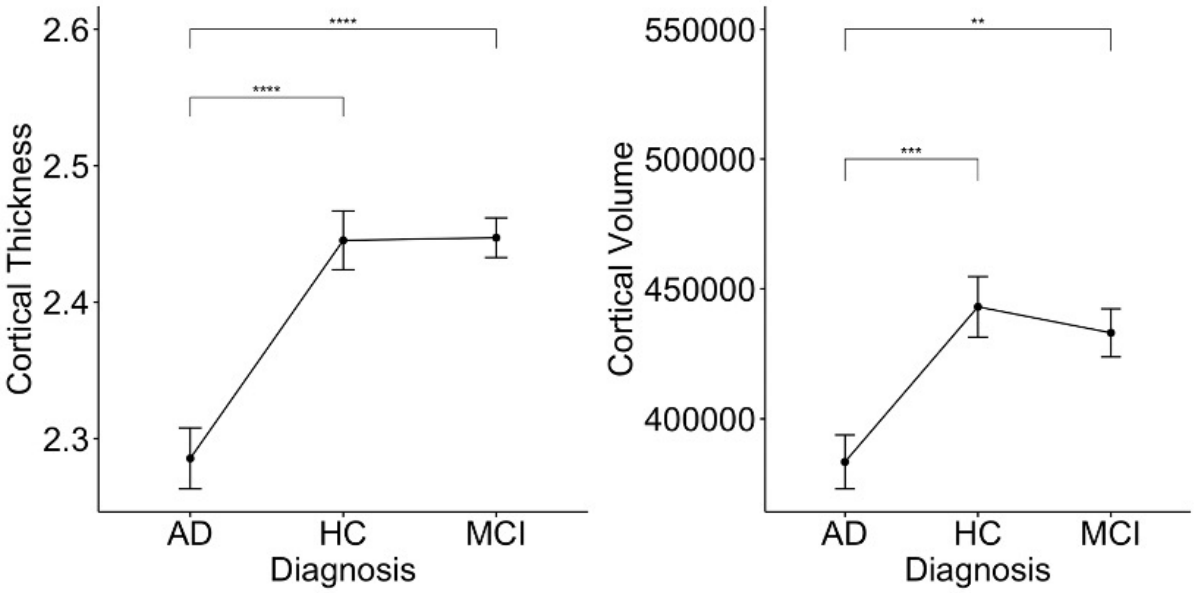

Figure 3.8 Group comparisons of cortical thickness and cortical volume

**: p<0.01; ***: p<0.001; ****: p<0.0001 in t-test.

3.4.4 Using PCC and MPFC as seeds to probe DMN connectivity

The default mode network connectivity pattern has been successfully depicted using either the PCC mask or MPFC mask (Figure 3.9). The most significant regions associated with DMN activity are the medial prefrontal cortex (and frontal pole), posterior cingulate, precuneus, bilateral lateral parietal cortices, and bilateral hippocampi.

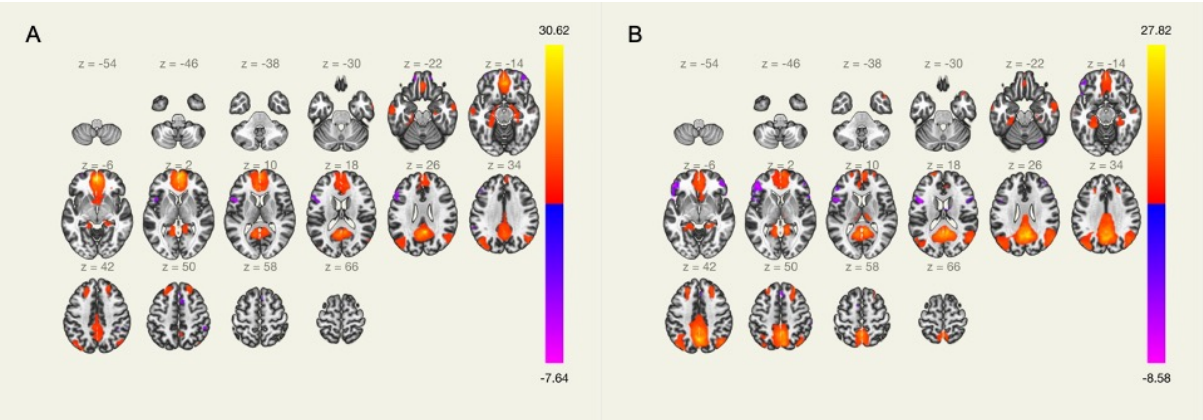

Figure 3.9 Default mode network pattern detected by seed-based connectivity maps. A: DMN detected using MPFC as seed; B: DMN detected using PCC as seed.

3.4.5 Altered neuronal activity in Aβ+ patients

Aβ+ cohort had significantly increased ALFF in the right frontal pole, bilateral cingulate gyri, bilateral paracingluate gyri, bilateral occipital pole, left fusiform gyrus and left lingual gyrus, while ALFF in the right superior, middle and inferior temporal gyri, right fusiform gyrus and parahippocampal gyrus (Figure 3.10A).

As increased functional fluctuation in prefrontal cortex in Aβ+ cohort, a question of particular interest is whether increased neuronal activity in MPFC is associated with functional connectivity change. Interestingly, in Aβ+ cohort, MPFC showed increased regional connectivity with right frontal pole, but decreased distal connectivity with bilateral precuneus, bilateral posterior cingulate gyri, left lingual gyrus and right hippocampus (Figure 3.10B). PCC also showed reduced connectivity with anterior cingulate and frontal pole in 2 sample t-test, however the difference was not significant after correcting for age and gender.

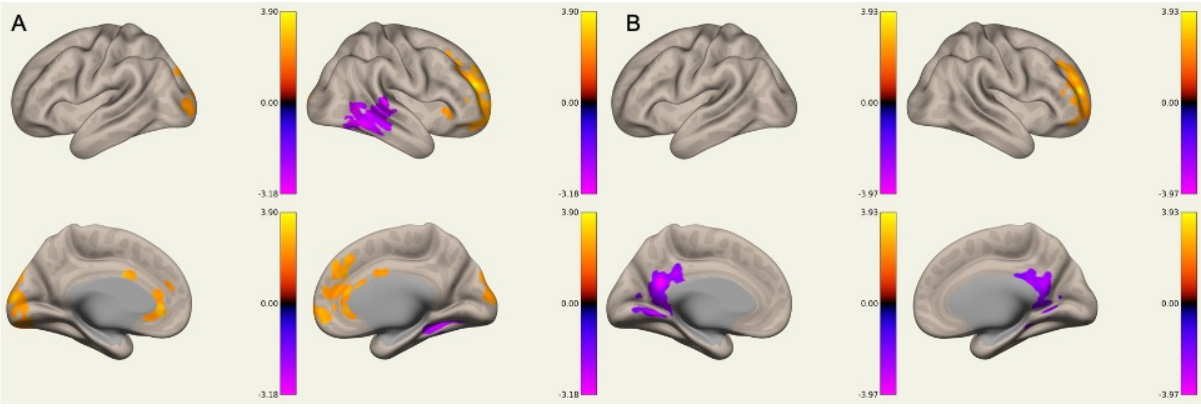

Figure 3.10 A: Altered ALFF in Aβ+ cohort compared to healthy controls; B: Altered MPFC connectivity in Aβ+ cohort compared to healthy controls

3.4.6 Amyloid, neuroinflammation and neuronal activity

Voxel-wise regression analysis showed ^{18}F-Flutemeamol uptake was associated with decreased ALFF in bilateral precentral and postcentral gyri, precuneus, and left lateral occipital gyrus and left frontal pole; while positive association between ^{18}F-Flutemetamol uptake and ALFF was found in bilateral lingual gyri, posterior cingulate cortex, left superior frontal gyrus, and left inferior temporal gyrus (Figure 3.11A). Positive relationship between ^{11}C-PBR28 uptake and ALFF was found in right frontal pole, superior frontal gyrus, paracingulate gyrus, lingual gyrus, posterior cingulate cortex and precuneus (Figure 3.11B).

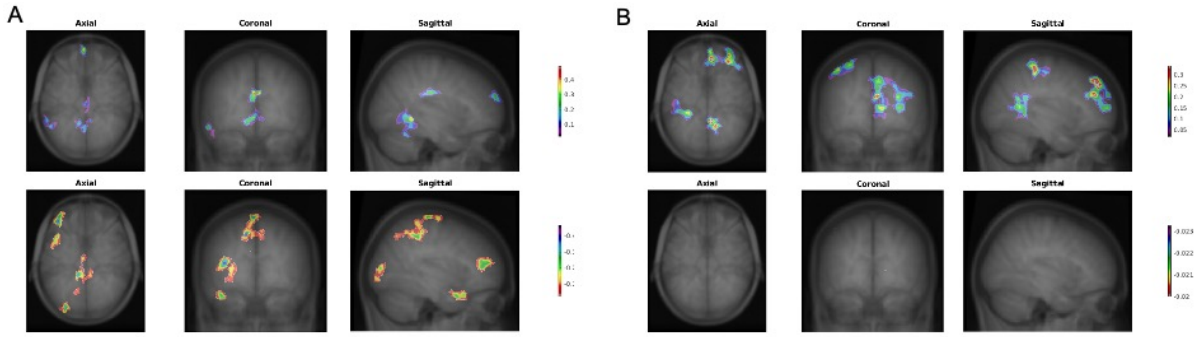

Figure 3.11 Voxel-wise regression analysis using ALFF as dependent variable, ^{18}F-Flutemetamol and ^{11}C-PBR28 uptake as independent variables. A. Effect of 18F-Flutemetamol on ALFF; B. Effect of ^{11}C-PBR28 on ALFF.

3.4.7 Influence of neuroinflammation on brain connectivity

In Aβ+ subjects, multiple regression model showed that ^{11}C-PBR28 uptake in MPFC was found to be associated with decreased connectivity from MPFC to PCC, precuneus, bilateral superior frontal, middle frontal and paracingulate gyri, left planum temporale and superior temporal gyrus (Figure 3.12A). While ^{18}F-Flutemetamol uptake in MPFC was associated with increased MPFC connectivity with anterior cingulate gyrus, bilateral superior frontal gyri, paracingulate gyri, and middle frontal gyri; decreased MPFC connectivity with posterior cingulate gyri and precuneus (Figure 3.12B).

Multiple regression analysis on PCC connectivity showed that ^{11}C-PBR28 uptake in PCC was associated with decreased PCC connectivity with right central opercular, planum temporale, insular cortex, middle temporal gyrus, Heschl's gyrus and frontal operculum cortex; and increased PCC connectivity with precuneus, right lateral occipital cortex and occipital pole (Figure 3.12C). ^{18}F-Flutemetamol uptake in PCC, on the other hand, was associated with increased PCC connectivity with anterior cingulate cortex and decreased PCC connectivity with precuneus, left superior parietal lobule and postcentral gyrus (Figure 3.12D).

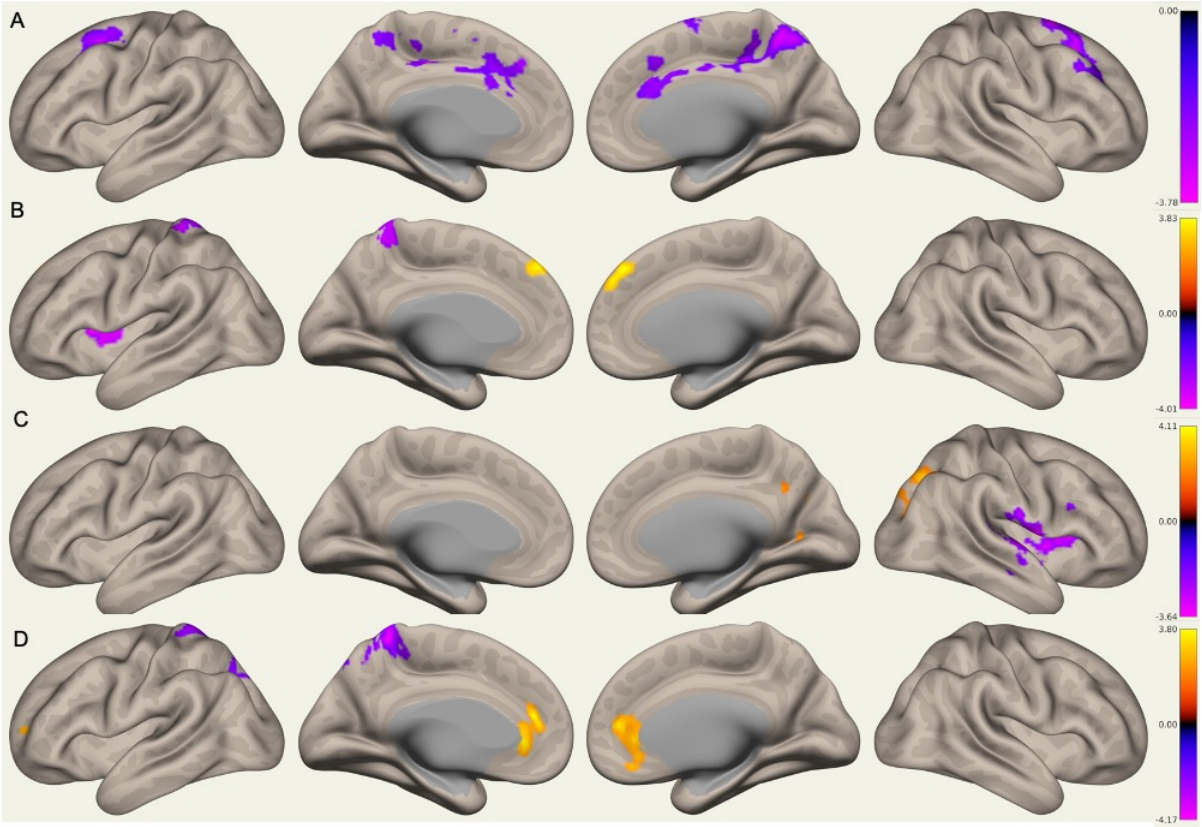

Figure 3.12. Voxel-level regression analysis using regional ^{11}C-PBR28 and ^{18}F-Flutemetamol uptake to predict brain connectivity. A: Effect of MPFC ^{11}C-PBR28 uptake on MPFC connectivity; B: Effect of MPFC ^{18}F-Flutemetamol uptake on MPFC connectivity; C: Effect of PCC ^{11}C-PBR28 uptake on PCC connectivity; D: Effect of PCC ^{18}F-Flutemetamol uptake on PCC connectivity.

3.4.8 Altered simultaneous neuronal activity in AD and MCI patients

AD patients had higher ALFF in anterior cingulate gyrus, right superior frontal gyrus, bilateral frontal pole, paracingulate gyri, occipital pole, occipital fusiform gyri, lingual gyri, intracalcarine cortices, and lateral occipital cortices compared with HC, while decreased ALFF was found in posterior cingulate gyrus, precuneus, right superior, middle and inferior temporal gyri, right hippocampus, right amygdala, right parahippocampal gyrus, and right temporal fusiform cortex (Figure 3.13A).

MCI patients had increased ALFF in medial frontal cortex, anterior cingulate gyrus, right frontal pole, right paracingulate gyrus and right superior frontal gyrus; decreased ALFF was found in medial frontal cortex, left frontal orbital cortex, left inferior frontal gyrus and left putamen (Figure 3.13B). Aβ+ MCI patients had similar results as MCI patients (Figure 3.13C).

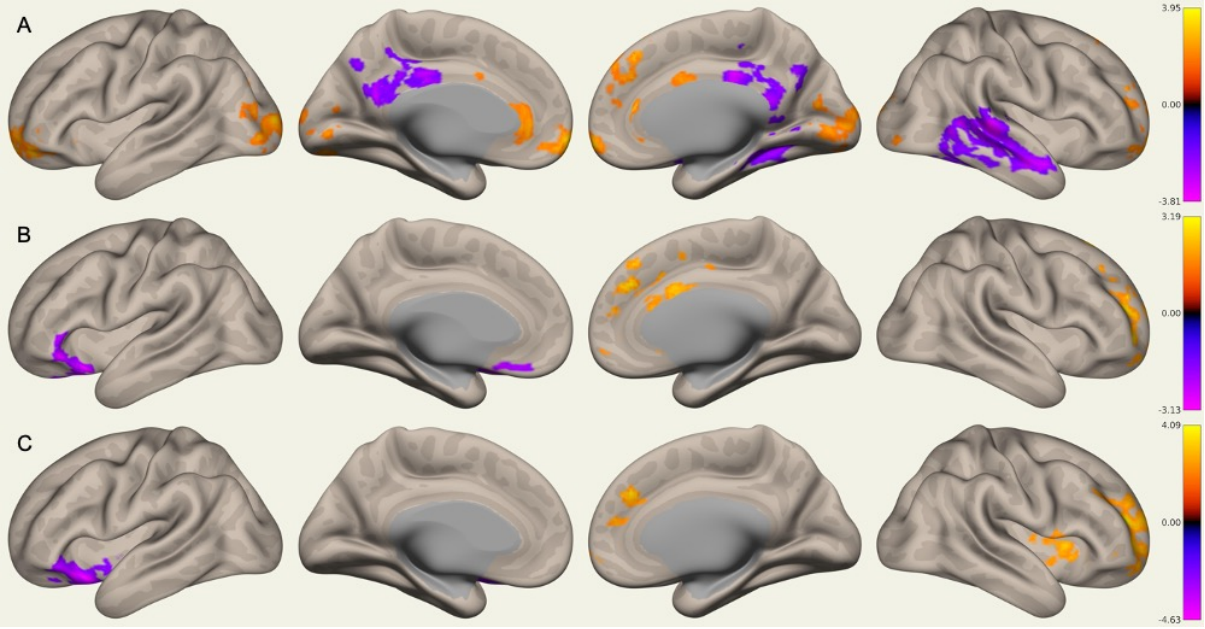

Figure 3.13 Altered ALFF in different diagnostic groups compared to HC. A: Altered ALFF in AD patients; B: Altered ALFF in MCI patients; C: Altered ALFF in Aβ+ MCI patients.

3.4.9 Altered MPFC and PCC connectivity in AD and MCI cohorts

AD patients showed increased MPFC connectivity with local regions including left frontal pole and left orbital cortex, but decreased MPFC connectivity with right supramarginal gyrus, right precentral and postcentral gyrus, right central opercular cortex, right insular cortex, right temporal pole, right parietal operculum cortex, right superior temporal gyrus, as well as anterior and posterior cingulate cortices (Figure 3.14A).

Interestingly, MCI patients had increased MPFC connectivity with bilateral occipital regions including occipital pole, lingual gyri, cuneal gyri and lateral occipital cortices. Decreased MPFC connectivity was found in precuneus cortex, posterior cingulate cortex, left temporal fusiform cortex, bilateral thalami and bilateral hippocampi (Figure 3.14B).

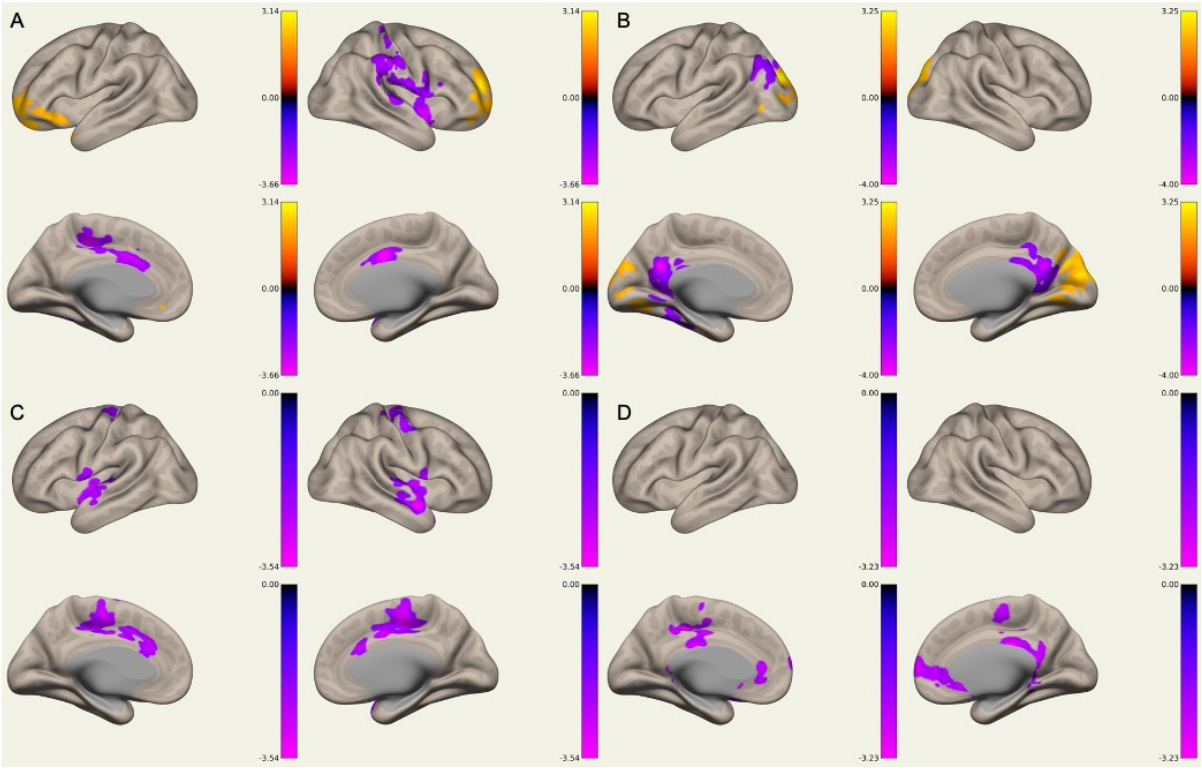

Figure 3.14 Altered MPFC and PCC connectivity in AD and MCI patients. A: Altered MPFC connectivity in AD patients; B: Altered MPFC connectivity in MCI patients; C: Altered PCC connectivity in AD patients; D: Altered PCC connectivity in MCI patients.

Using PCC as seed, AD patients showed decreased PCC connectivity with anterior and posterior cingulate gyrus, bilateral precentral gyri and juxtapositional lobule, left paracingulate gyrus and superior temporal gyrus, right temporal pole, bilateral planum polare, insular cortices, superior temporal gyri, Heschl's Gyri, central opercular cortices, and middle temporal gyri (Figure 3.14C).

MCI patients had decreased PCC connectivity with anterior and posterior cingulate gyrus, subcallosal cortex, left orbital cortex, bilateral frontal pole, paracingulate cortices, juxtapositional lobule, precentral gyri, accumbens, thalami, and hippocampi (Figure 3.14D). Age and gender were controlled in all the comparisons.

3.4.10 Influence of amyloid deposition and neuroinflammation on MPFC and PCC connectivity in AD and MCI cohorts

In MCI cohort, correlation analysis using only ^{18}F-Flutemetamol as independent variable (n=48, with age and gender controlled) showed that ^{18}F-Flutemetamol uptake in MPFC is associated with decreased MPFC connectivity with bilateral frontal pole, inferior frontal gyri, right frontal orbital cortex, right temporal pole and right insular cortex (Figure 3.15A). Correlation analysis using ^{11}C-PBR28 uptake (n=28, age and gender controlled) showed that MPFC ^{11}C-PBR28 uptake was associated with increased MPFC connectivity with bilateral frontal pole, medial frontal cortex and left superior frontal gyrus, and decreased MPFC connectivity with anterior cingulate, bilateral superior frontal gyrus, juxtapositional lobules, left middle frontal gyrus, right parietal operculum cortex, right supramarginal gyrus and right planum temporale (Figure3.14B). Bivariate correlation analysis did not show significant connectivity change associated with ^{11}C-PBR28 or ^{18}F-Flutemetamol uptake in PCC in MCI cohort.

Multiple regression analysis including both ^{11}C-PBR28 and ^{18}F-Flutemetamol uptake (n=24) showed that in MCI patients, MPFC ^{11}C-PBR28 uptake is associated with decreased MPFC

connectivity with bilateral superior frontal gyrus, anterior cingulate gyrus, left middle frontal gyrus, paracingulate cortex and right juxtapositional lobule (Figure 3.15C), while PCC ^{11}C-PBR28 uptake is associate with decrease PCC connectivity with bilateral precentral gyri, juxtapositional lobules, left superior frontal gyrus, and left paracingulate gyrus (Figure 3.15D).

In AD cohort, no significant change in connectivity was found to be associated with ^{11}C-PBR28 or ^{18}F-Flutemetamol uptake in PCC or MPFC in univariate or multivariate regression analyses.

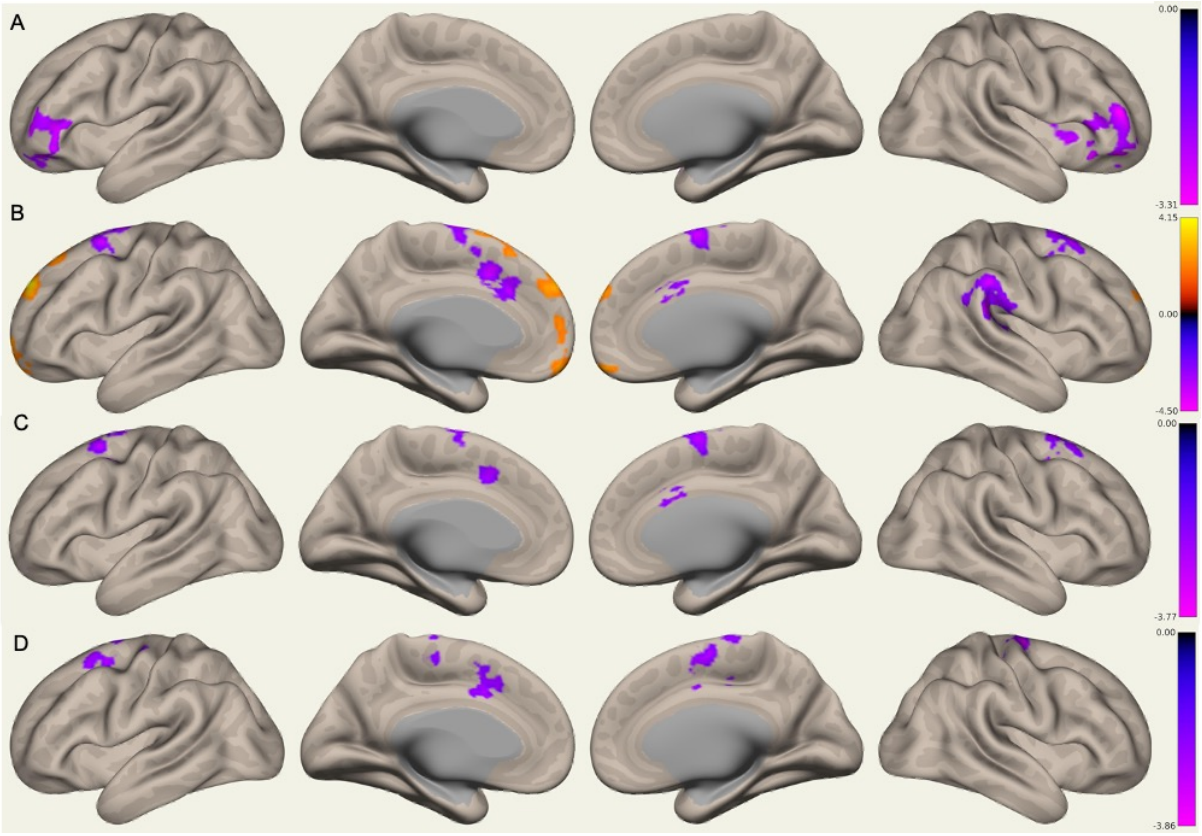

Figure 3.15. Influence of Amyloid Deposition and Neuroinflammation on MPFC and PCC Connectivity in AD and MCI Cohorts. A: bivariate correlation between ^{18}F-Flutemetamol and MPFC connectivity in MCI patients (adjusted for age and gender); B: bivariate correlation between ^{11}C-PBR28 uptake and MPFC connectivity in MCI patients (adjusted for age and gender); C: Effect of ^{11}C-PBR28 uptake on MPFC connectivity in multiple

regression model in MCI patients; D: Effect of ^{11}C-PBR28 on PCC connectivity in multiple regression model in MCI patients.

3.4.11 Connectivity, but not spontaneous neuronal activity is associated with cognition

In MCI subgroup, MMSE scores were positively correlated with connectivity between MPFC and PCC, precuneus, left precentral and postcentral gyri (Figure 3.16), though the association was not significant in the whole Aβ+ cohort. However, ALFF was not found to be associated with MMSE scores in Aβ+ cohort or subgroups.

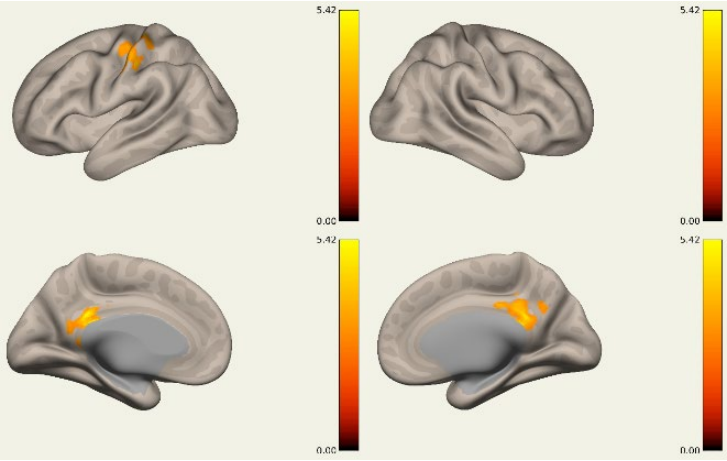

Figure 3.16. Correlation between MMSE score and MPFC connectivity

3.4.12 Network topology changes in disease cohorts

Small-worldness, clustering coefficient and local efficiency of functional network was significantly decreased in AD cohort compared to HC, while global efficiency did not differ ($p = 0.047$, 0.037, 0.017, and 0.31, respectively). No significant difference was seen in the MCI cohort compared to HC (Figure 3.17).

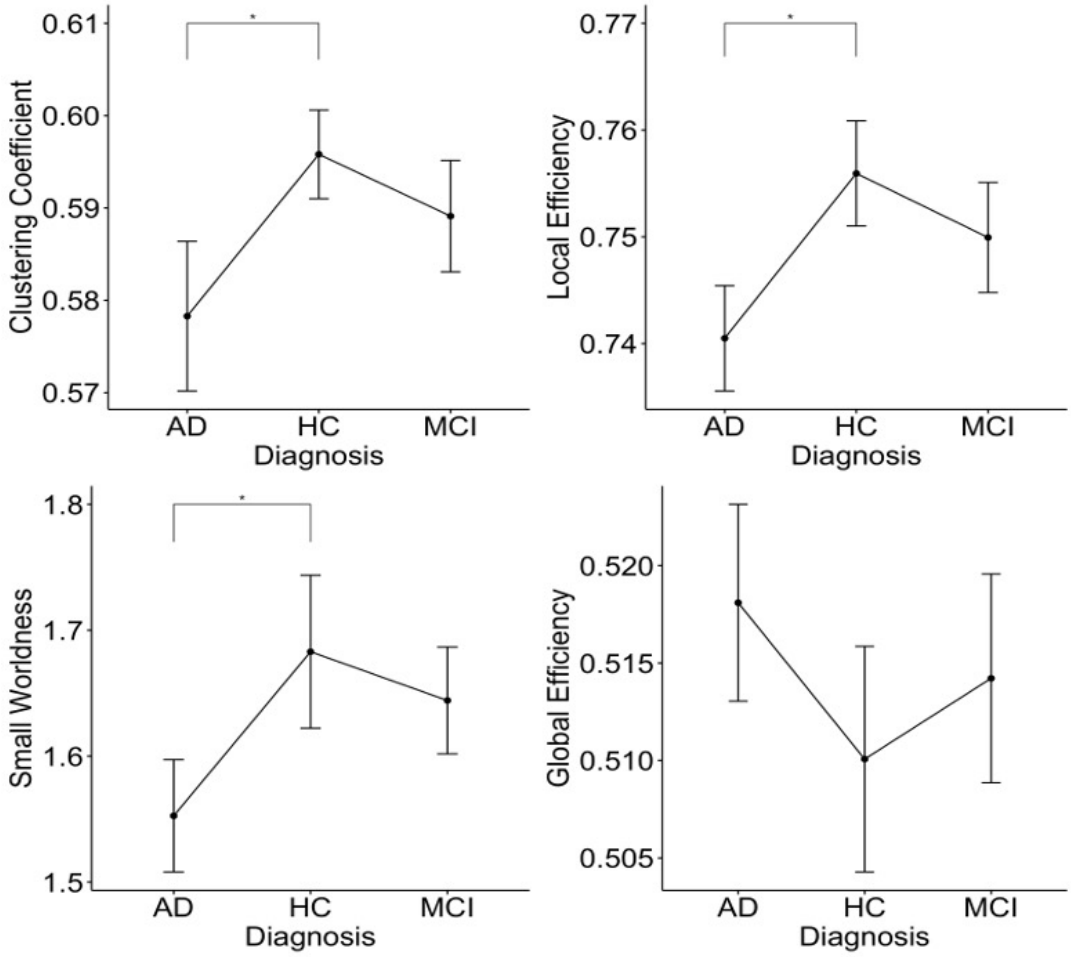

Figure 3.17. Group Comparisons of Network Topology Metrics

*: $p<0.05$ in pairwise comparisons.

3.4.13 Nodal connectivity changes in disease cohorts

With the global organisation change of functional network detected, the changes of nodal network metrics were further tested. In AD patients, decreased nodal clustering coefficient was found in left superior frontal gyrus (p=0.020), left Rolandic operculum (p=0.037), left olfactory blob (p=0.016), right cuneus (p=0.015), left fusiform cortex (p=0.0075), left supramarginal gyrus (p=0.019) and right superior temporal gyrus (p=0.023); decreased betweenness centrality was found in in left superior frontal gyrus (p=0.017), right olfactory bulb (p=0.023), left middle cingulate cortex (p=0.017), and right precuneus (p=0.046).

However, none of the nodes passes the Bonferroni correction for multiple comparisons over 90 regions.

In the MCI patients, decreased nodal clustering coefficient was found in left superior frontal gyrus (p=0.036), left and right olfactory bulbs (p=0.025 and 0.044), bilateral middle cingulate cortex (p=0.047 and 0.0031), left fusiform cortex (p=0.01), left angular gyrus (0.049), right precuneus (p=0.043), while left Rolandic operculum (p=0.029) and left Heschl's gyrus (p=0.036) had increased clustering coefficients; decreased betweenness centrality was found in left anterior cingulate cortex (p=0.038) and left caudate nucleus (p=0.046). These results did not survive the Bonferroni correction for multiple comparisons either.

3.4.14 Relationship between grey matter structural integrity and functional network integrity

In Aβ+ cohort, average cortical thickness was positively associated with network global efficiency (standardised β=0.546, 95%CI: 0.176~0.916, p-perm=0.026, controlled for age), local efficiency (standardised β=0.575, 95%CI: 0.187~0.963, p-perm=0.019, controlled for age), and small-worldness (standardised β=0.602, 95%CI: 0.267~0.937, p-perm=0.006, controlled for age), but not clustering coefficient (standardised β=0.200, 95%CI: -0.269~0.669, p-perm=0.36, controlled for age). Age was included as covariate of no interest in all analysis (Figure 3.18).

In clinical diagnostic groups separately, cortical thickness was positively associated with small-worldness (standardised β=0.556, 95%CI: 0.106~1.01, p-perm=0.037, controlled for age). The associations between cortical thickness and functional network topology measures were not significant in AD and MCI groups.

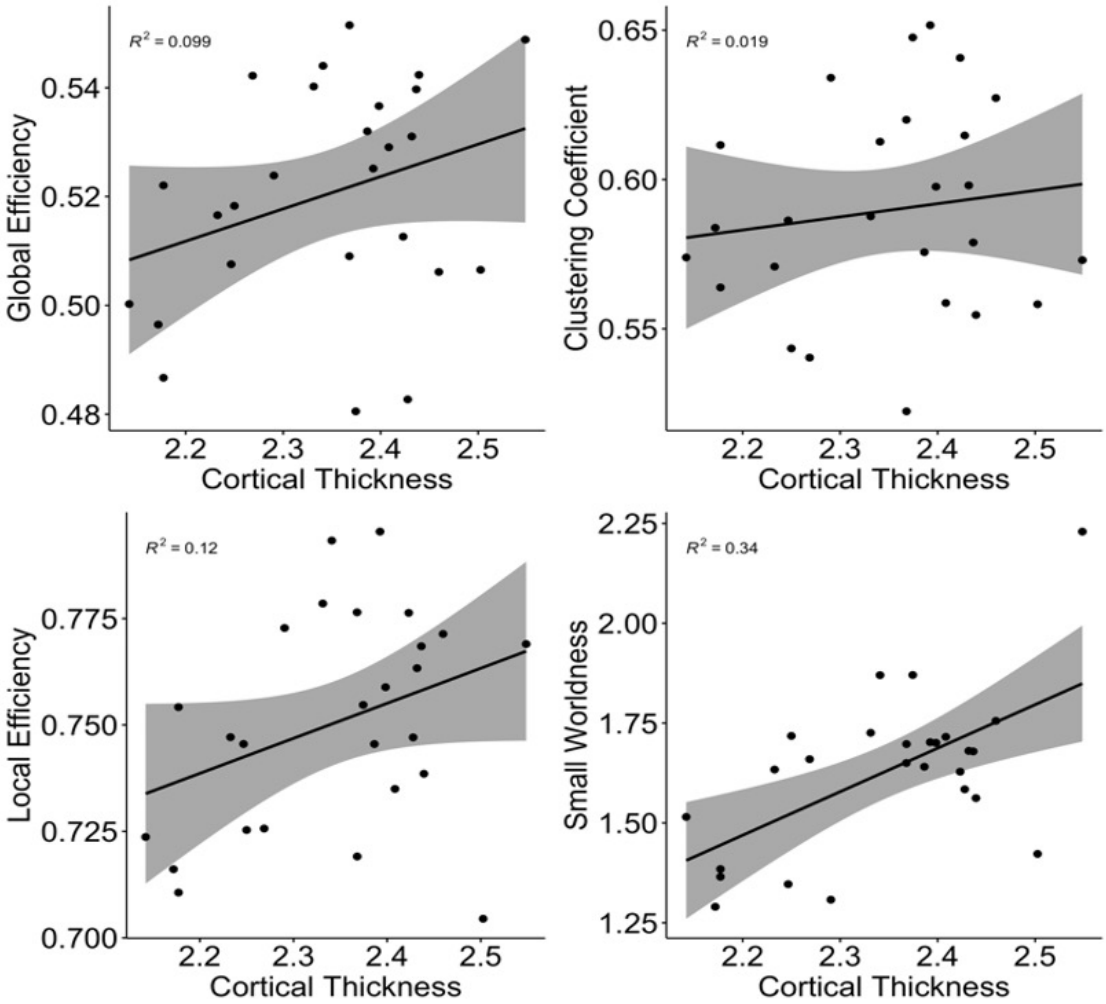

Figure 3.18. Relationship Between Grey Matter Integrity and Functional Network Topology Measures in Aβ+ cohort.

3.4.15 Relationship between functional network organisation and cognition

In Aβ+ cohort, MMSE score was found to be positively associated with network local efficiency (standardised β=0.521, 95%CI: 0.218~0.824, p-perm=0.02) and cortical thickness (standardised β=0.605, 95%CI: 0.294~0.915, p-perm=0.001), but the association with other network topology measures were not significant (Figure 3.19). In separate clinical diagnostic groups, neither cortical thickness nor network topology measures were significantly associated with MMSE.

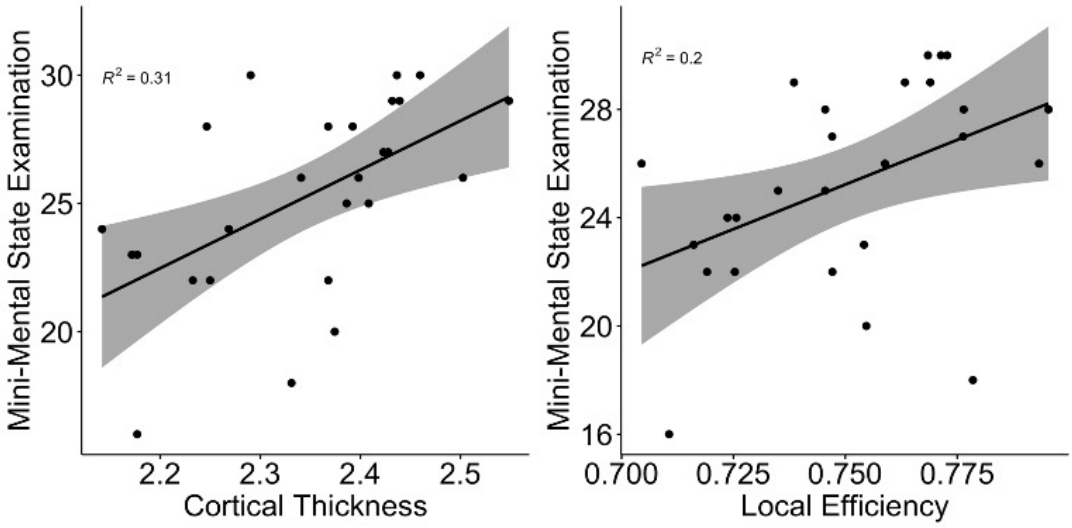

Figure 3.19. Network Organisation and Grey Matter Integrity Are Associated with Cognition in Aβ+ cohort.

3.4.16 Influence of cortical neuroinflammation and amyloid deposition on network functional organisation in Alzheimer's continuum

In Aβ+ cohort, regression analyses considering ^{11}C-PBR28, ^{18}F-Flutematemol, cortical thickness and age showed that ^{11}C-PBR28 SUVR was negatively associated with network local efficiency (standardised β=-0.508, 95%CI: -0.828~-0.188, p-perm=0.001) and clustering coefficient (standardised β=-0.537, 95%CI: -0.863~-0.211, p-perm=0.01), but not global efficiency (standardised β=0.129, 95%CI: -0.244~0.502, p-perm=1)or small-worldness (standardised β=-0.156, 95%CI: -0.488~0.177, p-perm=0.15). ^{18}F-Flutematemol SUVR did not correlate with the network topology metrics (Figure 3.20).

In MCI cohort, interestingly, same linear regression models found that ^{18}F-Flutematemol SUVR was positively associated with clustering coefficient (standardised β=0.495, 95%CI: 0.216~0.774, p-perm=0.002), while ^{11}C-PBR28 SUVR was negatively associated with clustering coefficient (standardised β=-0.565, 95%CI: -0.834~-0.296, p-perm=0.0024) (Figure 3.21). Neither ^{11}C-PBR28 SUVR nor ^{18}F-Flutematemol SUVR was found to be significant predictor for network topology metrics in AD cohort.

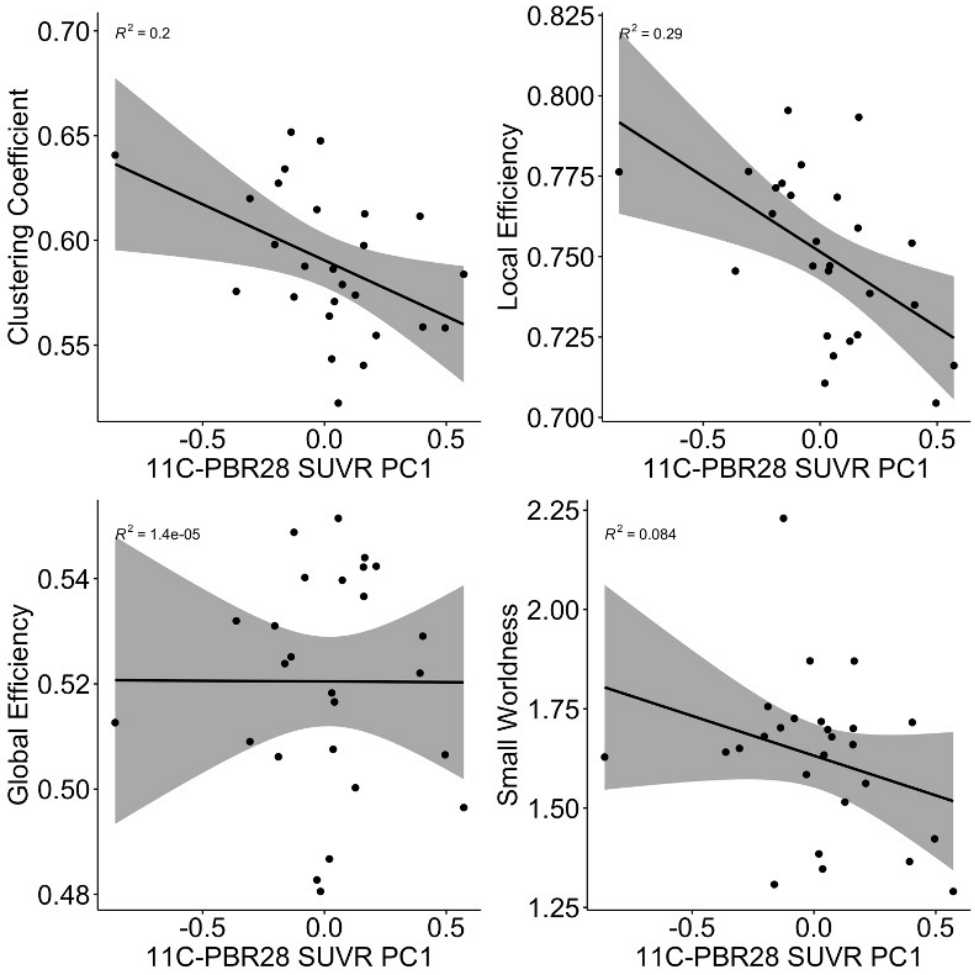

Figure 3.20. Relationship between cortical ^{11}C-PBR28 uptake and functional network topology measures in Aβ+ cohort.

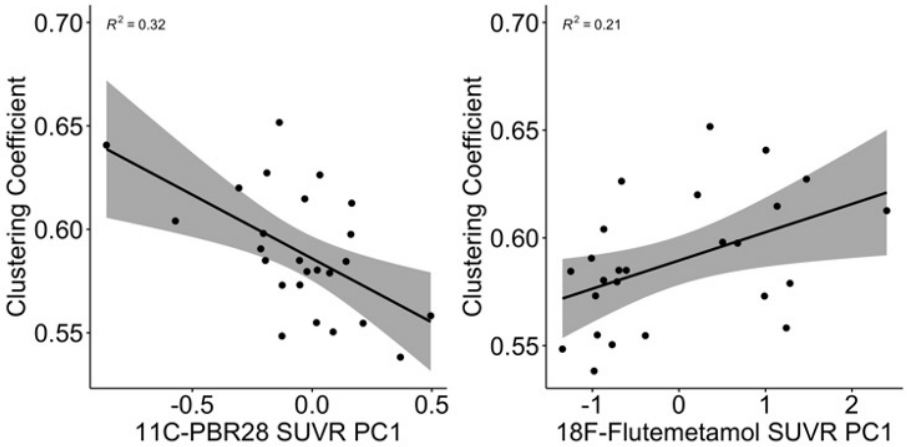

Figure 3.21. Relationship between cortical ^{11}C-PBR28 uptake, ^{18}F-Flutematemol uptake and clustering coefficient in MCI cohort.

3.5 Discussion and Conclusions

In this chapter the functional brain network in AD and MCI patients was examined using resting state fMRI analysis. Seed-based and graph theory analysis were applied in the analysis and independent component analysis was used for denoising. The medial prefrontal cortex and posterior cingulate/precuneus cortices were used as seed region to probe the functional connectivity, as they have been identified as key hubs of the default mode network, which is impaired in AD. Altered MPFC/PCC connectivity was found in both AD and MCI patients, with increased local connectivity within frontal lobe and deceased anterior-posterior connectivity reported. Consistent with previous evidence, a trend of increased connectivity with proximal regions and decreased connectivity with distal areas was found in both AD and MCI patients (K. Wang et al., 2007), leading to the suspicion that the increased connectivity with local areas may be a compensation mechanism in the patients' brains. The most typical findings of the dissociation between anterior hub and posterior hub of the DMN in AD (Broyd et al., 2009), however, came from the Aβ+ cohort, which strongly suggested that the Aβ+ cohort are more representative of Alzheimer's continuum.

The increased connectivity between MPFC and proximal frontal regions including frontal pole is consistent with analysis on amplitude of low-frequency fluctuations of BOLD signals, which revealed increased ALFF within frontal lobe in AD and MCI cohorts. Decreased ALFF, on the other hand, was mainly found in temporal regions and PCC in AD patients. The ALFF is a marker of spontaneous neuronal activity in corresponding regions, considering frontal regions are involved in relatively late stage of the disease while temporal lobe and PCC are hit by NFT and amyloid pathology early on in Alzheimer's trajectory (Braak & Braak, 1991), these findings may be suggestive of excitotoxicity in early involvement of a region, and following formation of NFT and neuronal death (Busche et al., 2019). The excitotoxicity may also explain the increased local connectivity, as the excitotoxicity may

lead to synchronistic and even epileptic activity patterns of neurons, therefore the sophisticated functional compartmentalisation of neuronal network may be lost (Bakker et al., 2012). On the other hand, this increased neuronal activity and local connectivity might also have compensatory effect. However, this phenomenon was not found to be related to cognitive performance in the patients, suggesting that the elevated local neuronal activation is not beneficial, or at least not effective, for preserving cognitive capability of the diseased brains. Indeed, the dissociation between neuronal activity and functional connectivity is also observed in other cohorts (Mascali et al., 2015).

The discrepancy between neuronal hyperactivity and network disruption is consistent with the electrophysiological findings from transgenic AD models where increased but unsynchronised slow-wave oscillations were recorded across multiple cortices (Busche et al., 2015). Together, the current findings and preclinical evidence suggest an ineffective and dysregulated pattern of neuronal activity in AD patients. Interestingly, MMSE scores in our AD cohort were not correlated with MPFC connectivity, which could be due to the pseudo-normalization phenomenon, where there is a U-shape rather than a linear relationship between cognitive performance and network connectivity (Jones et al., 2016)

Taking a step forward to the organisation of entire functional network, the analysis has shown that the functional network in AD patients had decreased local efficiency and small-worldness, but not global efficiency, suggesting that there is a loss of functional segregation of the brain. Functional segregation is important for the brain to use densely connected local clusters to process information in specific domains, the disruption of which could lead to impaired cognitive performance (Bullmore & Sporns, 2009). Indeed, further analysis has shown that in patients group the local efficiency and small-worldness are positively associated with the score in neuropsychological tests. The decreased local efficiency and loss of small-worldness have been well documented by previous studies, however, global

efficiency was not found to be impaired in patients in current analysis, which has been also been observed in several studies (delEtoile & Adeli, 2017). This might be attributed to several factors: firstly, the sample size of current cohort might not have been large enough to detect subtle changes of global efficiency; secondly, a network sparsity threshold was used to create binarized connectivity matrices, under the consideration to make the networks across participants more comparable (same number of nodes and edges), which in hindsight, might have impaired the ability to eliminate weakened links in patients; lastly the patients in current disease cohort were at relatively early stage of the disease (average MMSE in AD and MCI patients were 23.0 and 27.7, respectively), so the global connectivity might be relatively preserved in the patients. If this is the case, it might suggest that the network disruption in AD may first target links within local clusters, before the global network disruption. Considering the second possibility, different thresholding strategies might be tested in further studies to quantify how different approaches may influence the results based on same data.

Given the findings suggesting altered spontaneous neuronal activity, disrupted functional connectivity of key hubs and impaired network organisation in the brains of AD patients, the question to be answered is which pathological factors are responsible for the change. Preclinical studies have suggested that amyloid species to be neurotoxic and could lead to neuronal dysfunction (Meyer-Luehmann et al., 2008). Interestingly, the current analysis has found both positive and negative relationships between Aβ and neuronal activity markers in different sites of the brain. This observation might be explained by the dose-dependent effect of Aβ oligomers on neuronal activity: It has been reported that slightly increased concentration of Aβ oligomers could lead to neuronal hyperactivity by activating presynaptic α7-nAChRs, while high concentration of Aβ oligomers directly inhibits neuronal activity at post-synaptic level (Palop & Mucke, 2010). Although ^{18}F-Flutemetamol can only bind to fibrillary Aβ plaques, the amount of amyloid plaque can be considered to relate to the

progression of amyloid pathogenesis. Another possible explanation for the complex relationship between amyloid deposition is the activity-dependent release of Aβ peptide from neurons (Kamenetz et al., 2003b). As is shown by the analysis, increased neuronal activity can be found in early disease, which might further lead to an increase of Aβ excretion. The initial elevation of Aβ oligomers and monomers could then exaggerate the neuronal hyperactivity, resulting a vicious cycle, until irreversible damage is done to the neurons and negative association emerges (Zott et al., 2019).

Meanwhile, neuroinflammation was found to be associated with only increased neuronal activity in several key regions with regard to brain network, namely frontal pole, posterior cingulate and precuneus. This could be the consequence of excitotoxic pro-inflammatory cytokines released by microglia, or the insufficient recycle of excitatory transmitters (such as glutamate) by glia cells in the neuroinflammatory milieu. Indeed, it was observed that the IL-1β gene rs1143627 polymorphism could modulate ALFF change in MCI patients, suggesting a role of neuroinflammation in neuronal hyperactivity (Zhuang et al., 2012). The pre-inflammatory cytokines such as IL-1β released by activated microglia could perturb neuronal activity, and further activate astrocytes, leading to disturbance of glutamate metabolism and cause glutamate excitotoxicity (Liddelow et al., 2017). Another possibility is that this due to the reorganisation of neuronal circuits and networks by microglia, considering their key role in neuronal plasticity management and synaptic pruning in diseases. As recent advance has suggested that the loss of GABA-ergic inhibitory tones in neuronal circuits (Verret et al., 2012) (Nuriel et al., 2017) (Bi, Wen, Wu, & Shen, 2020). It is worth considering how the excessive pruning of synaptic structures by activated microglia might be involved in the excitatory/inhibitory imbalance of diseased neuronal circuits (S. Hong et al., 2016).

As previous analyses have shown the influence of amyloid deposition and neuroinflammation on spontaneous neuronal activity, their association with functional connectivity have been

further explored. Of note, the MPFC is of special interest in the analysis, as both increased neuronal activity and decreased functional connectivity with PCC was found in MPFC. Interestingly, neuroinflammation in MPFC was found to be associated with decreased MPFC connectivity with distal regions, including PCC and precuneus in Aβ+ cohort, while amyloid deposition was associated with both increased and decreased connectivity with several regions, albeit not functional hubs of DMN. These findings suggest that both neuroinflammation and amyloid pathology are associated with functional connectivity disruption in AD, and that their effects, at least partially, are independent of each other. Further, from the current analysis, neuroinflammation seems to be related to more specific and typical functional connectivity changes in AD. It is possible that both amyloid species and neuroinflammation could cause local abnormal neuronal activities, and further influence connectivity patterns, but neuroinflammation is further involved in more specific circuit remodelling in disease process.

The postulation that neuroinflammation is involved in disease-specific network remodelling and targets key functional connections, is further reinforced by the network level analysis. At the whole network's perspective, neuroinflammation, but not amyloid deposition was found to be associated with decreased clustering coefficient and local efficiency in Aβ+ patients. The decreased network segregation measures suggest that the connectivity within normal clusters is impaired, and the impaired MPFC-PCC connectivity might be an example. The reason why amyloid deposition did not correlate with network topology changes in Aβ+ cohort might be the following: First, the PET measures fibrillary Aβ depositions, but not Aβ oligomer concentration, which is more toxic to neurons; Second, Aβ species may not have a direct quantitative effect on global network disruption in AD, in other words, it might be a upstream event of Alzheimer's pathogenesis, but the damage to brain network is mediated by other processes, for instance neuroinflammation.

Interestingly, in MCI patients, amyloid deposition seemed to be associated with increased clustering coefficient of the functional network, which might be related to network reorganisation of the brain in response to amyloid pathology in early disease. However, neuroinflammation in the same MCI cohort was negatively associated with clustering coefficient, suggesting that neuroinflammation may have hindered the network reorganisation process.

While the current project is going, a parallel study has observed similar findings with regard to neuroinflammation and functional connectivity changes. The parallel study has found one independent component of ^{11}C-PK11195, with the inferior and medial temporal regions having high weight, was associated with decreased DMN within network connectivity in a similar amyloid positive cohort, but how an inflammation pattern influenced brain connectivity in other regions remained to be elucidated (Passamonti et al., 2019). The findings of current study stand in line with the findings from previous study, moreover, it complements the understanding between neuroinflammation and brain connectivity both at local and at global level. More specifically, the current study has illustrated the association between neuroinflammation and local neuronal activity at voxel level, specifically interrogated whether neuroinflammation within a region of interest is associated with connectivity change of the same ROI, and answered the question whether neuroinflammation is related to the disruption of overall organisation of the brain as a network organ.

The current analysis is limited by the number of cases, and therefore the main focus is on the full Aβ positive cohort. If there had been more cases, I would have been able to further analyse the associations at different stages of the disease, for example, Aβ positive subjective cognitive decline, early MCI, late MCI and AD stages, as neuroinflammation may play different roles at these stages. Nevertheless, the association between neuroinflammation and functional connectivity seems to be similar in the current MCI and AD cohort, and the Aβ+

cohort indeed exhibited most typical DMN connectivity disruption. Putatively, it can be assumed that the current Aβ+ cohort is representative of mid-to-late stages of the Alzheimer's continuum, and it could be inferred that neuroinflammation plays a detrimental role in this stage of disease in terms of the brain's functional network.

Given the current and previous evidence of the cognitive implication of brain connectivity, the connectivity disruption associated with neuroinflammation might be of more clinical interest, as it may present as a viable target to preserve cognitive function in AD patients. However, further studies are needed to substantiate this hypothesis, and better understanding of biological basis of circuit organisation needs to be established before intervention strategies can be developed.

Chapter 4. The influence of neuroinflammation on structural connectivity in Alzheimer's spectrum

4.1 Introduction

4.1.1 Diffusion Tensor Imaging

Diffusion MRI utilize the thermal Brownian motion of molecules and aims to quantify the overall diffusion properties in certain environment. Essentially, diffusion MRI exploits the fact that precession frequency has a proportional relationship with magnetic field strength and applies a magnetic gradient field in the first spin echo pulse. Consequently, protons in water molecules at different locations will have different precession frequencies. If a water molecule has moved to another location, its protons will have a phase and frequency difference with those from 'local' molecules. When the second refocusing echo is applied, the 'migrated' protons will fail to synchronize and result in a loss of overall signal in readout. The attenuation effect is dependent on the gyromagnetic ratio, strength of magnetic pulse, duration of the pulse and diffusion coefficient, which was formulated by Stejskal and Tanner (EO Stejskal, 1965). By applying the 'diffusion encoding' gradients, the diffusion properties along different directions could be detected and calculated. Using these principles, diffusion weighted images can be produced in which the signal is attenuated depending on how freely water molecules can diffuse. The diffusion weighted images can be used reflect restrictions on water diffusion caused by cell membranes, fibres and other molecules, and is widely used in clinical practice to detect conditions such as cytotoxic oedema in acute ischemia (Le Bihan et al., 2001) (Lope-Piedrafita, 2018). However, human tissues often have anisotropic diffusion properties, i.e., the tissue structures have different restriction on water diffusion along different directions. Using a single diffusion weighted image or a parametric map of apparent diffusion coefficients (ADC) is not sufficient to reflect the anisotropic properties.

Diffusion tensor imaging takes a step forward and models the water diffusion property in 3-dimensional space using a 'diffusion tensor'. Assuming the diffusion property is the same along opposite directions, the diffusion tensor can take form as a symmetric 3-by-3 matrix. Basser et al. has demonstrated that the linear relationship between that logarithm if echo attenuation and the dot product of diffusion tensor and b factor (depend on acquisition parameters) (Basser, Mattiello, & LeBihan, 1994b) . Therefore, by conducting acquisitions using sufficient number of diffusion gradients, the diffusion tensor can be fitted using linear regression (Basser, Mattiello, & LeBihan, 1994a). The diffusion tensor in the form of matrix inherently contains more information as compared to a single scaler ADC and further analysis take advantage of information to better understand the underlying structures.

In brain white matter, water diffusion is mainly influenced by the axons and surrounding myelin, which restrict water diffusion much more in radial directions compared to axial direction. This tissue structural causes significant anisotropy in diffusion profile and by evaluating the diffusion tensor, the direction of white matter pathways and its microstructural integrity can be inferred (Tournier, Mori, & Leemans, 2011).

4.1.2 Evaluation of human brain structural network: Approaches

On diffusion tensor imaging data, two main streams of analysis can be performed: microstructural analysis and tractography (Soares, Marques, Alves, & Sousa, 2013).

The first approach is microstructural analysis. Under the assumption that there is uniform tissue structure within certain voxel, for each voxel a local orthogonal coordinate system can be constructed, such that its eigenvectors coincide with local principal directions of diffusivity. For each eigenvector, its related eigenvalue quantifies the diffusivity along the direction (Basser et al., 1994b). The first diffusivity coefficient then marks the axial diffusivity (DA), while the last two marks diffusivities in the orthogonal plane. From these

eigenvalues, scaler metrics such as fractional anisotropy (FA), mean diffusivity (MD) and radial diffusivity (DR) can be calculated. These metrics can be further used to evaluate the microstructural integrity of local tissue.

The second approach is tractography. Tractography can be generally categorized into probabilistic and deterministic tractography. Both approaches have 3 main stages in tract construction, namely seeding, propagation and termination. The difference between the two algorithms is that the deterministic approach finds a fixed direction for a streamline in a voxel, while the probabilistic approach estimates a probabilistic distribution of streamline directions within a voxel. It should be noted that single or multiple streamlines can be estimated within a voxel with deterministic approach, but the orientation of each streamline is still fixed. The streamlines are generated linking seed and destination voxels based on the streamline orientation estimated along the way, if certain constraints are satisfied. Using certain seed and termination masks, pathways connecting two distal regions can be constructed, and can be used to evaluate the structural connectivity between the regions. If a number of seeds are provided, tractography can be performed between each pair of them and a connectivity matrix can be obtained (Soares et al., 2013).

4.1.3 Application of Diffusion Tensor Imaging in Alzheimer's Research

White matter damage in AD brains has been well documented previous pathology studies in post-mortem examination. The changes included loss of axons, demyelination and neuroinflammation (Scheltens et al., 1995) (Sjobeck, Haglund, & Englund, 2006b) (Gouw et al., 2008). While previously it was widely presumed that the white matter damage, especially axonal losses is secondary to neuronal death in the cortex, known as Wallerian degeneration (Coleman, 2005), recently more attention has been drawn to the retrogenesis theory, based on the observation that late myelinated fibres are the first to degenerate in the course of disease, highlighting the role of white matter damage in pathogenesis of AD (Reisberg et al., 2002).

With the advance of diffusion tensor imaging in recent years, the structural network damage, or white matter damage, has been well described by a number of studies. In AD patients, increased DA, DR, MD and decreased FA have been found in association fibres including the corpus callosum, fornix, cingulum, inferior and superior longitudinal fasciculi, and uncinate fasciculus (Di Paola et al., 2010; Stricker et al., 2009). Similar changes have been reported in MCI patients, albeit the changes are not as extensive (Wai et al., 2014). More interestingly, the white matter damage can be observed in pre-clinical cases with family history of AD, when grey matter change is not evident (Bendlin et al., 2010) (Y. J. Hong et al., 2016). Importantly, structural network integrity was found to be related to cognition in AD and MCI patients (Bosch et al., 2012). Network topology analyses using tractography have also revealed decreased global network efficiency in AD and MCI patients (Lo et al., 2010; Shu et al., 2012). The early emergence of white matter alterations and its retrogenesis feature highlights the importance of white matter/ structural network damage in the pathogenesis of AD, and therefore efforts to investigate factors associated with the process are needed.

4.2 Aim of the project

The hypothesis of current study is that neuroinflammation in Alzheimer's disease can actively and independently contribute to the damage of neuronal circuit and disrupt normal neuronal activity, the consequence of which are global impairment of the brain and ultimately cognitive impairment.

The aim of current project is to test the prediction originated from the hypothesis: neuroinflammation is associated with structural network disruption in Alzheimer's disease spectrum, independent of amyloid deposition. To evaluate the structural connectivity in our cohort, both microstructural integrity analysis and tractography analysis were used. To assess the global status of brain structural network, the microstructural integrity of major white

matter tracts was evaluated, and the network topology metrics of structural connectivity matrix constructed by tractography were computed. The changes of aforementioned structural network metrics in AD and MCI patients were first analysed, and the relationship between PET measurements of neuroinflammation/amyloid deposition and structural network metrics were analysed using linear regression models.

4.3 Methods

The scans were acquired by a 3 Tesla Siemens Verio scanner using a 32-channel head coil at the clinical imaging facility, Hammersmith Campus, Imperial College London.

4.3.1 T1-weighted MRI scan acquisition

The T1-weighted scans were acquired using the MPRAGE sequence for better tissue segmentation performance**:** Sagittal orientation; Anterior to posterior phase encoding direction; FOV 256×240×160mm; 1×1×1mm isotropic voxels; TR=2300ms; TE=2.98ms; TI=900ms; Flip angle=9°; Bandwidth=240Hz/Px; Echo spacing=7.1ms; Interleaved acquisition.

4.3.2 Diffusion tensor MRI scan acquisition

DTI scans were acquired with the following parameters: Transversal orientation; Anterior to posterior phase encoding direction; FOV 256×256×124mm; 2×2×2mm isotropic voxels; TR=9000ms; TE=99ms; b-value=1000s/mm^2; 64 diffusion directions; Bandwidth=1562Hz/Px; Echo spacing=0.72ms; Interleaved acquisition.

4.3.3 B0 field mapping

B0 field maps were acquired for used of distortion correction of DTI images using the following parameters: Anterior to posterior phase encoding direction; FOV

192×192×105mm; 3×3×3mm isotropic voxels; TR=599ms; TE1=5.19ms; TE2=7.65ms; Bandwidth=260Hz/Px; Interleaved acquisition.

4.3.4 B0 field map processing

In the current study, echo-planar imaging method was used to acquire the DTI images, this method is sensitive to off-resonance fields, especially in the phase-encoding direction. Any non-linearity of the phase-encoding gradient could cause misinterpretation of geometric information, i.e., distortions. The body in scanner, due to different magnetic susceptibilities of various tissue types, will disrupt the homogeneous magnetic field in the scanner and lead to distortions was well (Hutton et al., 2002). To account for the inhomogeneity induced by individual patients, a B0 field maps were acquired with the patient in scanner.

The FSL PRELUDE function was used for preparing a field map image for distortion correction of EPI images. The raw field mapping data from scanner contains a phase difference image and 2 magnitude images (for each TE). The magnitude images were used to provide spatial information and the B0 were inferred from the difference in 2 TEs and phase difference map. The magnitude image was first brain extracted to exclude any voxels outside the brain and a calibrated field map with the unit of rad/s was produced. The undistorted images were then forward warped into a distorted image to better register with distorted EPI images using FUGUE function.

4.3.5 Distortion correction of DTI images

The raw images were first converted from DICOM to NIFTI format using MRIcron tool and the b-vector files b-value files were generated, recording the direction and strength of diffusion gradient field. The first volume of the 4D images without diffusion weighting was extracted for use of spatial reference. Each subject's distorted field map was then registered to the non-diffusion weighted image using rigid body linear transformation and the

transformation matrix was applied to the absolute field map image to bring it to diffusion space.

4.3.6 Eddy current and motion correction of DTI images

Eddy currents are rings of current induced by changing magnetic field in conductors, as described by Faraday's law of induction. The loops of current flow in planes orthogonal to the changing magnetic field and generate an inducted magnetic field that counters the change of the former one. In diffusion tensor imaging, the diffusion encoding gradient is constantly changed to evaluate water diffusion in different directions, which will induce eddy currents in the conducting circuits in the scanner, including the coils. The eddy current induces filed shifts and could cause image shearing and scaling artifacts (Jezzard, Barnett, & Pierpaoli, 1998) (Spees et al., 2011). In addition, head movement of the participant in scanner could cause spatial change of the susceptibility induced field in relation to the eddy current induced field. Therefore, eddy current correction, motion correction and distortion correction were performed in an integrated way using FSL's eddy function, which combines the aforementioned fields together and does the correction in one step (Andersson & Sotiropoulos, 2016).

During the realignment process if a rotation of the head is detected, the difference between the desired and actual diffusion encoding gradient is calculated and recorded. This process generates a corrected b-vector file and was used in further tensor fitting process.

Quality check was performed using FSL's eddy qc function after the eddy correction to ensure satisfactory quality of the images.

4.3.7 Diffusion tensor fitting

Following the image corrections, the diffusion tensors were fitted to individual voxels using FSL's DTIFIT function. Linear regression method was used to extract the first 3 eigenvectors

(V1~V3) and eigenvalues (L1~L3) from diffusion tensor at voxel level. The eigenvalues of principle diffusion directions were then used to compute the diffusion metrics, namely fractional anisotropy (FA), radial diffusivity (RA), axial diffusivity (DA) and mean diffusivity (MD), which are given by (Le Bihan et al., 2001):

$$MD = \frac{L1+L2+L3}{3} \quad (4.1)$$

$$DA = L1 \quad (4.2)$$

$$DR = \frac{L2+L3}{2} \quad (4.3)$$

$$FA = \sqrt{\frac{3[(L1-MD)^2+(L2-MD)^2+(L3-MD)^2]}{2(L1^2+L2^2+L3^2)}} \quad (4.4)$$

At this point the V1 map (reflecting the principal diffusion direction) and FA maps were inspected to ensure the tensor fitting process went correctly.

4.3.8 Tract-based spatial statistics for DTI images

To be able to make statistical inference at group level, the DTI images must be brought to a common or standard space to make voxels from individual maps correspond to comparable structures. However, the standard normalization process as done for T1-weighted scans is not satisfactory for FA images. Therefore, FSL's tract-based spatial statistics (TBSS) pipeline was used for this purpose (Smith et al., 2006).

Briefly, the FA maps were first slightly eroded, and the end slices were zeroed to remove outliers. The pre-processed FA maps were then transformed into the standard MNI152 space using FSL's nonlinear registration function FNIRT with b-spline interpolation, resampled into 1×1×1mm resolution (Rueckert et al., 1999). Next, the mean FA map of the study cohort is calculated, and a threshold of FA>0.2 was applied to only include major tracts that are anatomically stable across subjects. Then a binary white matter skeleton mask was created

based on the mean FA map, and a distance map was computed to project original values onto the group skeleton. Finally, each individual's FA, MD, DA, and DR maps were then projected onto the skeleton for further analysis.

4.3.9 Extraction of DTI Metrics from Tracts of Interest

The Johns-Hopkins University ICBM-DTI-81 white matter labels atlas was used to sample DTI metrics from tracts of interest (Mori et al., 2008).

4.3.10 Tractography

Instead of the diffusion tensor fitting process prior to TBSS, FSL's BEDPOSTX was run in each subject's diffusion space before tractography. BEDPOST is the abbreviation of Bayesian estimation of diffusion parameters obtained using sampling techniques, and the X stands for crossing fibres. The process uses Markov Chain Monte Carlo sampling and Bayes theorem to estimate each voxel's posterior distributions of diffusion parameters based on acquired data. This allows the process to model different numbers of crossing fibres within a voxel and choose the optimal number that fits the data (Behrens et al., 2003).

After the preparation steps, tractography was performed using FSL's PROBTRACKX function, which is a toolbox for probabilistic fibre tracking with crossing fibres. PROBTRACKX tracks streamlines from a seed voxel by drawing distribution parameters form the voxel's posterior distribution function given by BEDPOSTX, stepping along the direction and testing whether the action is feasible according to termination criteria. The step is iterated through all the voxels and parameters and the resulting sample streamlines are produced. Streamline density maps and numbers of streamlines connecting distal seeds could then be produced based on the sample streamlines (Behrens et al., 2003) (Behrens, Berg, Jbabdi, Rushworth, & Woolrich, 2007) .

To evaluate the structural connectivity of entire brain, I aimed to create a ROI-to-ROI structural connectivity matrix for each participant using anatomical parcellation. The white matter surface parcellation given by FreeSurfer was used as seed masks to guide tractography. A total of 148 ROIs were selected for tractography and were listed in Appendix. As tractography is performed in original diffusion space, while the surface parcellation is performed in a conformed space, which is again different from the original T1 structural space, the linear transformation matrices were estimated between DTI space ⇔ Structural space ⇔ FreeSurfer space using FSL's FLIRT tool.

To improve the accuracy of streamline tracking, the CSF segmentation was used as exclusion mask, and the following termination/exclusion criteria were used for streamline tracking: (1) the streamline enters CSF mask; (2) the streamline leaves the brain mask in diffusion space; (3) the streamline have travelled more than 2000 steps with step length at 0.5mm; (4) the curvature associated with a step is too high compared to former step, and the cosine of minimum allowable between two steps was limited at 0.2; (5) the streamline loops back to where it has already gone through.

I should note that the resulting structural connectivity matrix is usually not exactly symmetric, unlike functional connectivity matrix, as starting from opposite ROIs for tractography could end up with different numbers due to difference in tractability. Therefore, the cross-diagonal average was calculated by averaging the original matrix and its transposed matrix. The resulting matrix was used for further analysis.

4.3.11 Graph theory analysis on structural connectivity matrices

The averaged structural connectivity matrix was analysed using the GRETNA toolbox, which is specifically designed for graph theoretical analysis. A sparsity threshold of 10% was used for creating both binarized and weighted connectivity matrices. For the weighted connectivity

matrices, the number of streamlines was used as the weight of an edge, as has been used by previous studies (Sun et al., 2018). Network topology metrics including clustering coefficient, average path length, betweenness-centrality, small-worldness, global efficiency, and local efficiency were computed. Nodal metrics including clustering coefficient, between-centrality and average path length were also computed. The details of the graph theoretical metrics for binarized connectivity matrices have been described in Chapter 3 on functional connectivity analysis. For weighted structural connectivity matrices, the network topology measures are computed as follows:

$$t_i^w = \frac{1}{2}\sum_{j,h\in N, j\neq i}(w_{ij}w_{ih}w_{jh})^{\frac{1}{3}} \quad (4.5)$$

$$d_{ij}^w = \sum_{a_{uv}\in g_{i\to j}} w_{uv}^{-1} \quad (4.6)$$

$$C^w = \frac{1}{n}\sum_{i\epsilon N}\frac{2t_i^w}{k_i(k_i-1)} \quad (4.7)$$

$$E_{loc}^w = \frac{1}{2}\sum_{i\in N}\frac{\sum_{j,h\in N, j\neq i}(w_{ij}w_{ih}\left[d_{jh}^w(N_i)\right]^{-1})^{1/3}}{k_i(k_i-1)} \quad (4.8)$$

$$L^w = \frac{1}{n}\sum_{i\epsilon N}\frac{\sum_{j\in N, j\neq i} d_{ij}^w}{n-1} \quad (4.9)$$

$$E_g^w = \frac{1}{n}\sum_{i\epsilon N}\frac{\sum_{j\in N, j\neq i}(d_{ij}^w)^{-1}}{n-1} \quad (4.10)$$

$$SW = \frac{C^w/C_{rand}^w}{L^w/L_{rand}^w} \quad (4.11)$$

Where the superscript *w* denotes that the measures are weighted; t_i is the number of triangles with node *i* being one apex; w_{ij} is the weight of connection between nodes *i* and *j*; d_{ij} is the shortest path length between node *i* and node *j*; $a_{uv} \in g_{i\to j}$ refers to the edge between nodes *u* and *v* which is part of shortest path between nodes *i* and *j*; *C* is the clustering coefficient; E_{loc} is the network local efficiency; *L* is the characteristic path length; E_g is the global efficiency; and *SW* is the small-worldness. *ki* is the number of edges connected to node *i*; $d_{jh}(N_i)$ is the shortest path between two neighbour nodes of *i*, (*j* and *h),* and K_i is the degree of

node *i*, which is the number of edges connected to the node. C_{rand} is the clustering coefficients of random networks that have same number of nodes and edges as the current network, L_{rand} are characteristic path lengths of random networks comparable to current network (Rubinov & Sporns, 2010).

4.3.12 Statistical analysis

Group wise comparisons between diagnostic groups were first performed on the FA, MD, DR and DA skeletons on a voxel-wise basis using FSL's randomize tool with threshold free cluster enhancement (TFCE) algorithm. The TFCE algorithm takes the raw statistic image (T map) and evaluate the base area of a 3D curve (extent) that surpass different height thresholds. The integral of a function of height that combines extent and height is then calculated and the value assigned to corresponding voxel. This algorithm has its advantage in that it does not require an initial hard cluster-forming threshold as compared to the 'traditional' 2-step approach, and therefore offers better sensitivity and stability (Smith & Nichols, 2009). Following TFCE algorithm, voxel-wise statistical test with multiple comparison correction was carried out. The randomize tool uses a permutational approach that randomly reassign a subject into a different group. The null hypothesis of the permutational approach is that the metric in two groups do not differ, and therefore swapping subjects across groups should not make a difference. The process runs the random swapping for sufficient number of times and compares the observation with the permuted results. The number of more extreme permutation results than the actual observation divided by the total number of permutations is considered as p-value. In other words, the permutation results can be plotted as a histogram, and the tail to the left/right of observation value is used to decide significance (A. M. Winkler, Ridgway, Webster, Smith, & Nichols, 2014). This nonparametric approach does not rely on the hypothesis that the metric in question is normally distributed in both groups and has an advantage over the traditional frequentist

approach in scenarios where the number of participants is limited, and a normal distribution could not be safely assumed. In the current study the p-values in voxel-wise regression on white matter skeletons were defined using TFCE algorithm with 5000 permutations.

Group-wise comparisons at tract of interest (TOI) level is performed using Student's T-test. Uncorrected p-values and FDR corrected P-values were recorded.

As numerous ROIs and TOIs exist in the analysis, dimension reductions were performed for PET and MRI metrics. For ^{11}C-PBR28 and ^{18}F-Flutemetamol, an average of SUVR across the entire cortex (bilateral frontal, temporal, parietal, occipital, anterior and posterior cortices) is calculated first as a simple measure of global inflammation and amyloid deposition, further, principal component analysis was performed using SUVRs in bilateral frontal, temporal, parietal, occipital, as well as anterior and posterior cingulate cortices. Only principal components with eigenvalue greater than on were considered to have sufficient information and were considered in further analysis. Same principle was applied for FA values of all TOIs as a measure of structural network integrity. As there has been concern that white matter damage in Alzheimer's disease is simply a reflection of Wallerian degeneration secondary to cortical atrophy (Coleman, 2005), average cortical thickness was included in the regression analyses as a covariate. The regression analyses were performed both at global level and at voxel level using FA skeleton as dependent variable and other metrics as independent variables. Because of limited number of participants in the study cohort, Because of the relatively small sample size, robust regression method was used to estimate the parameters and permutation tests were performed to confirm the significance of findings at ROI level, as both methods do not presume normal distributions and are robust against possible skewness in data.

Although PCA is a valid method for dimensionality deduction, it captures the principal vector of variance of the input variables and therefore may not be able to capture the 'most interesting' association between two set of variables. In other words, the vectors found using PCA on two set of variables may not be as good correlated as it is possible if different weights are assigned in respective vector space, and therefore we are unable to distinguish which variables contribute most to a correlation, were it to be found. Canonical correlation analysis set in here as it computes latent variates for each set of variables, such that the first two canonical variate are most correlated as possible, and the residuals are used to compute new variates that are linearly orthogonal to previous ones and same maximum correlation rule applies. Each canonical variate is a linear combination of the original variables in the corresponding set, and from the weight of each variable we could infer how important a variable is in terms of the correlation we found. This provides an elegant approach for the analysis in question since it enables us to interpret the pathological process in which brain region matters more in structural network damage in AD.

However, because of the multivariate nature of canonical correlation, there is naturally concern on overfitting current data with the model. Further, as canonical correlation would inevitably assign certain weight to a variable under practical circumstances, it will lead to difficulties in interpreting the model when numerous variables are included. To address the problem, least absolute shrinkage and selection operator (LASSO) regularization was introduced. In linear regression the LASSO method solves the problem to minimize the cost function $L = \|Ax - b\|_2 + \lambda\|x\|_1$, where A is the design matrix, x is the unknown vector of model parameters, b is the observed value of dependent variable, λ is the weight of LASSO penalty (Tibshirani, 1996). In other words, the LASSO method adds a penalty term of the L1 norm of model parameters, weighted by λ, to the ordinary least square (OLS) cost function, which is the L2 norm of difference between observed and predicted outcome (dependent

variable). This penalty term will add up to the cost function whenever a parameter is not zero, and with increasing λ, less relevant independent variables will be effectively excluded from the model to minimize L, therefore leaving us a sparse solution, which avoids overfitting and improves interpretability of the resulting model. The concept could be generalized to CCA and was integrated into R package PMA (Witten, Tibshirani, & Hastie, 2009).

In the current study, I used the PMA package to perform sparse canonical correlation analysis (SCCA) between FA values of variable set of TOIs and variable set of PET ROIs, both for individual tracer and two tracers combined. To determine the statistical significance of the results from SCCA, same permutation method was used as described previously.

4.4 Results

4.4.1 Overview of available data and patient demographics

A total of 93 participants in the cohort had analyzable DTI data, of whom 21 were AD patients, 54 were MCI patients and 18 were healthy volunteers. Of these participants, 62 had ^{11}C-PBR28 scans, 84 had ^{18}F-Flutemetamol scans, and 40 had ^{18}F-AV1451 scans. The detailed demographic information, amyloid positivity and data overlap are summarized in table 3.1.

4.4.2 Group-wise Comparisons of DTI metrics in Tracts of Interest

AD patients showed significantly decreased FA values in the genu and body of corpus callosum (CCG and CCB), the fornix, and bilateral tapetum. Increased MD values in AD cohort were found in the aforementioned regions plus right cingulate bundle and left superior longitudinal fasciculus. Similar differences were found between Aβ+ patients (AD and MCI) and HC. However, significant change of FA and MD was not found in MCI group compared to healthy volunteers. Aβ+MCI patients had lower mean FA and higher mean MD compared to Aβ-MCI and HC participants, but the changes were not statistically significant (Table 4.2).

However, as there were so many of TOIs, the results did not survive Bonferroni correction for multiple comparisons.

Table 4.2 Group comparisons of fractional anisotropy and mean diffusivity across diagnostic groups

		AD (N=21)	MCI (N=54)	HC (N=18)	Aβ+MCI (N=22)	Aβ-MCI (N=26)	Aβ+Patients (N=37)
CCG	FA	0.673±0.055*	0.711±0.055	0.727±0.05	0.709±0.057	0.715±0.056	0.695±0.053*
	MD	8.37E-04±6.47E-05*	7.92E-04±6.71E-05	7.72E-04±7.38E-05	8.01E-04±6.19E-05	7.81E-04±7.10E-05	8.14E-04±6.10E-05*
CCB	FA	0.71±0.034*	0.729±0.039	0.736±0.04	0.722±0.04	0.736±0.038	0.716±0.039
	MD	8.14E-04±4.37E-05*	7.93E-04±5.40E-05	7.76E-04±5.47E-05	8.08E-04±5.06E-05	7.77E-04±5.87E-05	8.11E-04±4.80E-05*
CCS	FA	0.789±0.041	0.805±0.039	0.813±0.022	0.8±0.041	0.809±0.042	0.793±0.043*
	MD	7.03E-04±5.32E-05	6.88E-04±4.73E-05	6.78E-04±3.05E-05	6.99E-04±3.84E-05	6.79E-04±5.51E-05	7.03E-04±4.31E-05*
Fornix	FA	0.311±0.096*	0.364±0.102	0.396±0.095	0.357±0.114	0.382±0.099	0.342±0.102
	MD	2.22E-03±5.15E-04*	2.02E-03±4.35E-04	1.92E-03±3.65E-04	2.03E-03±4.47E-04	1.95E-03±4.44E-04	2.07E-03±4.41E-04
CB_R	FA	0.59±0.049	0.623±0.04	0.632±0.048	0.624±0.037	0.626±0.045	0.608±0.047
	MD	7.18E-04±4.30E-05*	7.11E-04±3.34E-05*	6.92E-04±3.21E-05	7.13E-04±2.74E-05	7.08E-04±3.94E-05	7.16E-04±3.41E-05*
CB_L	FA	0.633±0.047	0.664±0.043	0.669±0.047	0.659±0.042	0.675±0.046	0.647±0.048
	MD	7.25E-04±4.30E-05	7.24E-04±3.15E-05	7.07E-04±4.16E-05	7.30E-04±2.35E-05	7.20E-04±3.67E-05	7.29E-04±3.55E-05*
SLF_R	FA	0.54±0.026	0.559±0.025	0.554±0.032	0.562±0.02	0.556±0.031	0.553±0.026
	MD	7.34E-04±3.88E-05	7.12E-04±3.00E-05	7.10E-04±3.77E-05	7.08E-04±2.57E-05	7.11E-04±3.24E-05	7.18E-04±3.37E-05
SLF_L	FA	0.534±0.025	0.554±0.03	0.552±0.039	0.55±0.023	0.555±0.037	0.544±0.025
	MD	7.38E-04±3.58E-05*	7.17E-04±3.60E-05	7.10E-04±3.67E-05	7.18E-04±2.91E-05	7.15E-04±4.22E-05	7.26E-04±3.25E-05*
SFOF_R	FA	0.597±0.076	0.6±0.052	0.597±0.055	0.606±0.054	0.598±0.053	0.603±0.063
	MD	6.82E-04±6.86E-05	6.67E-04±6.00E-05	6.47E-04±3.62E-05	6.81E-04±7.11E-05	6.57E-04±5.42E-05	6.85E-04±7.15E-05

SFOF_L	FA	0.612±0.059	0.627±0.061	0.626±0.066	0.621±0.057	0.638±0.067	0.618±0.057
	MD	6.50E-04±7.76E-05	6.42E-04±7.97E-05	6.32E-04±5.61E-05	6.70E-04±7.86E-05	6.15E-04±7.93E-05	6.69E-04±7.77E-05
UF_R	FA	0.547±0.061	0.573±0.055	0.564±0.052	0.565±0.055	0.575±0.062	0.559±0.060
	MD	7.06E-04±7.39E-05	6.94E-04±6.02E-05	6.79E-04±4.64E-05	6.99E-04±5.89E-05	6.85E-04±6.33E-05	7.04E-04±6.95E-05
UF_L	FA	0.533±0.065	0.555±0.055	0.547±0.065	0.541±0.057	0.556±0.05	0.538±0.060
	MD	7.17E-04±7.35E-05	7.13E-04±7.28E-05	7.17E-04±2.87E-05	7.35E-04±7.37E-05	7.01E-04±7.37E-05	7.27E-04±7.72E-05
Tap_R	FA	0.469±0.082	0.5±0.092	0.525±0.085	0.501±0.089	0.504±0.096	0.479±0.086
	MD	1.14E-03±1.79E-04*	1.07E-03±1.97E-04*	9.80E-04±1.40E-04	1.06E-03±1.75E-04	1.07E-03±1.82E-04	1.10E-03±1.79E-04*
Tap_L	FA	0.5±0.078	0.549±0.088	0.56±0.074	0.563±0.094	0.538±0.087	0.530±0.091
	MD	1.13E-03±2.25E-04*	1.07E-03±2.02E-04*	9.57E-04±1.29E-04	1.04E-03±2.03E-04	1.10E-03±2.07E-04	1.08E-03±1.99E-04*
CST_R	FA	0.659±0.042	0.652±0.038	0.648±0.033	0.642±0.034	0.665±0.039	0.651±0.038
	MD	5.91E-04±4.77E-05	5.94E-04±4.63E-05	5.99E-04±3.88E-05	5.99E-04±5.28E-05#	5.88E-04±3.91E-05	5.95E-04±5.13E-05
CST_L	FA	0.653±0.04	0.659±0.04	0.664±0.04	0.647±0.038	0.677±0.033	0.652±0.039
	MD	6.08E-04±3.91E-05	6.00E-04±5.03E-05	6.00E-04±3.32E-05	6.14E-04±5.71E-05#	5.82E-04±4.37E-05	6.11E-04±5.10E-05

*: $p<0.05$ in independent samples T-test compared to healthy controls, not corrected; #: $p<0.05$ in independent samples T-test compared to Aβ-MCI cohort, not corrected. Numbers in cells are mean±SD. CCG: corpus callosum genu; CCB: corpus callosum body; CCS: corpus callosum splenium; CB: cingulum bundle; SLF: superior longitudinal fasciculus; SFOF: superior fronto-occipital fasciculus; UF: uncinate fasciculus; Tap: tapetum; CST: corticospinal tract; L: left; R: right; FA: fraction anisotropy; MD: mean diffusivity.

4.4.3 Voxel-wise comparisons of FA, MD, DA and DR skeletons

In voxel-wise comparison on white matter skeletons between AD and HC, significant clusters of deceased FA were found in CCG, CCB, splenium of corpus callosum (CCS), bilateral cingulate part of cingulum, bilateral SLF, bilateral superior fronto-occipital fasciculi (SFOF), bilateral inferior fronto-occipital fasciculi (IFOF), bilateral uncinate fasciculi (UF), left hippocampal part of cingulum and left inferior longitudinal fasciculus (ILF); clusters of increased MD, DA and DR were found CCG, CCB, CCS, bilateral cingulum (both cingulate and hippocampal part), SLF, ILF, IFOF and UF (Figure 4.1).

Figure 4.1 Voxel-wise Comparisons of DTI White Matter Skeletons

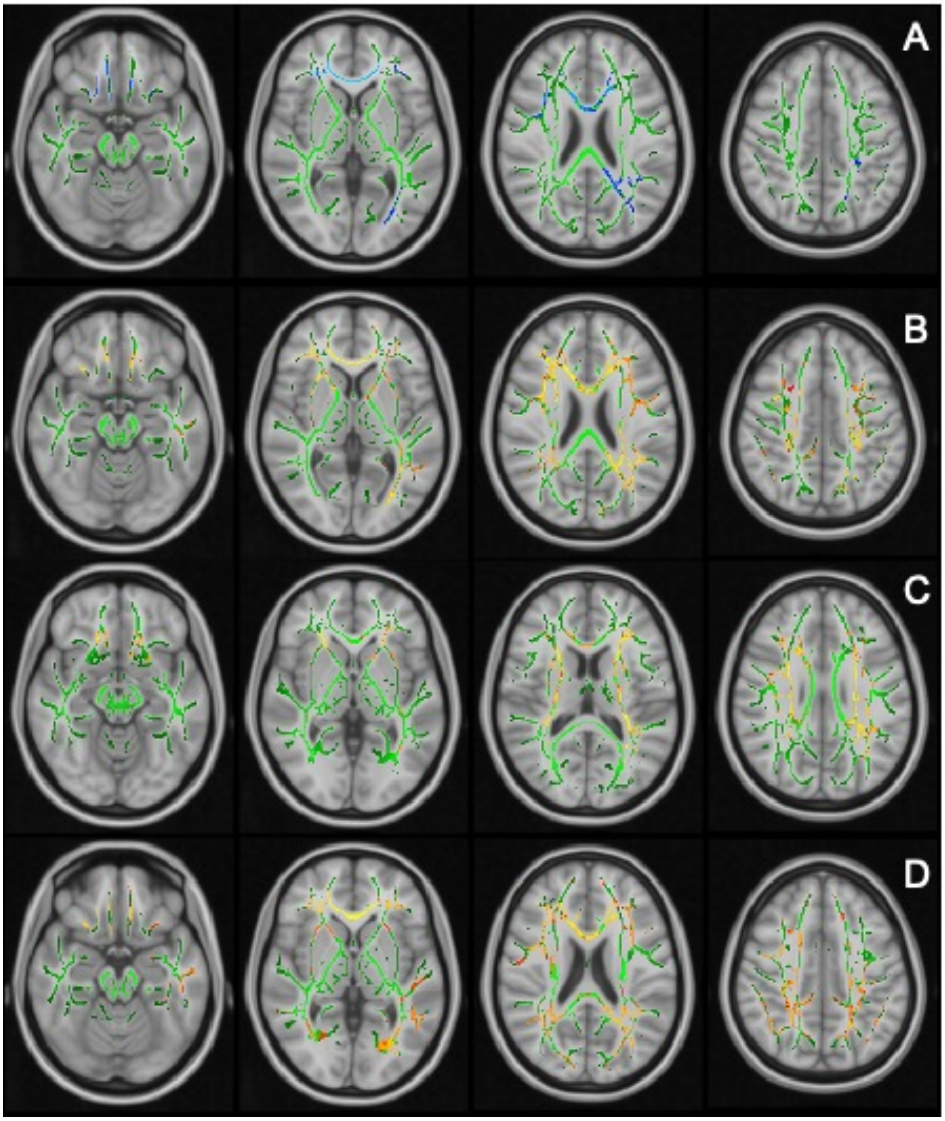

A: Decreased FA values in AD patients compared to HC; B: Increased MD values in AD patients; C: Increased DA in AD cohort; D: Increased DR in AD group. White matter skeletons are shown in green, clusters of increased values are shown in red-yellow scheme, and clusters of decreased values are shown in blue-light blue scheme. Clusters are corrected for multiple comparisons at spatial level using TFCE algorithm ($p<0.05$).

No significant clusters of decreased FA or increased MD/DR/DA were found in MCI group compared to HC. However, in Aβ+MCI patients, increased DA was found in bilateral IFOF, bilateral SLF, left UF and left ILF (Figure 4.1).

4.4.4 Dimensionality reduction: principal component analysis of FA values across TOIs

Principal component analysis was performed using FA values sampled from 48 tracts of interest (from DTI-81 white matter label atlas). The first principal component of FA values (PC1) explained 40.3% variance of data, while PC2 explained 9.7% of variance. Loading weights of TOIs revealed that all TOIs had positive weights on PC1 while there were differential loadings on PC2, with long association fibres having mostly positive weights (Figure 4.2). By plotting data points in 2-dimentional space defined by PC1 and PC2, it can be visually identified that PC2 axis could differentiate AD patients and HC group with good separation, with HCs having positive PC2s and AD patients having negative values (Figure 2). It is probable that the first component represents the overall integrity of white matter structural network, while the second component reflect a process in which association fibres and projection fibres are influenced differently.

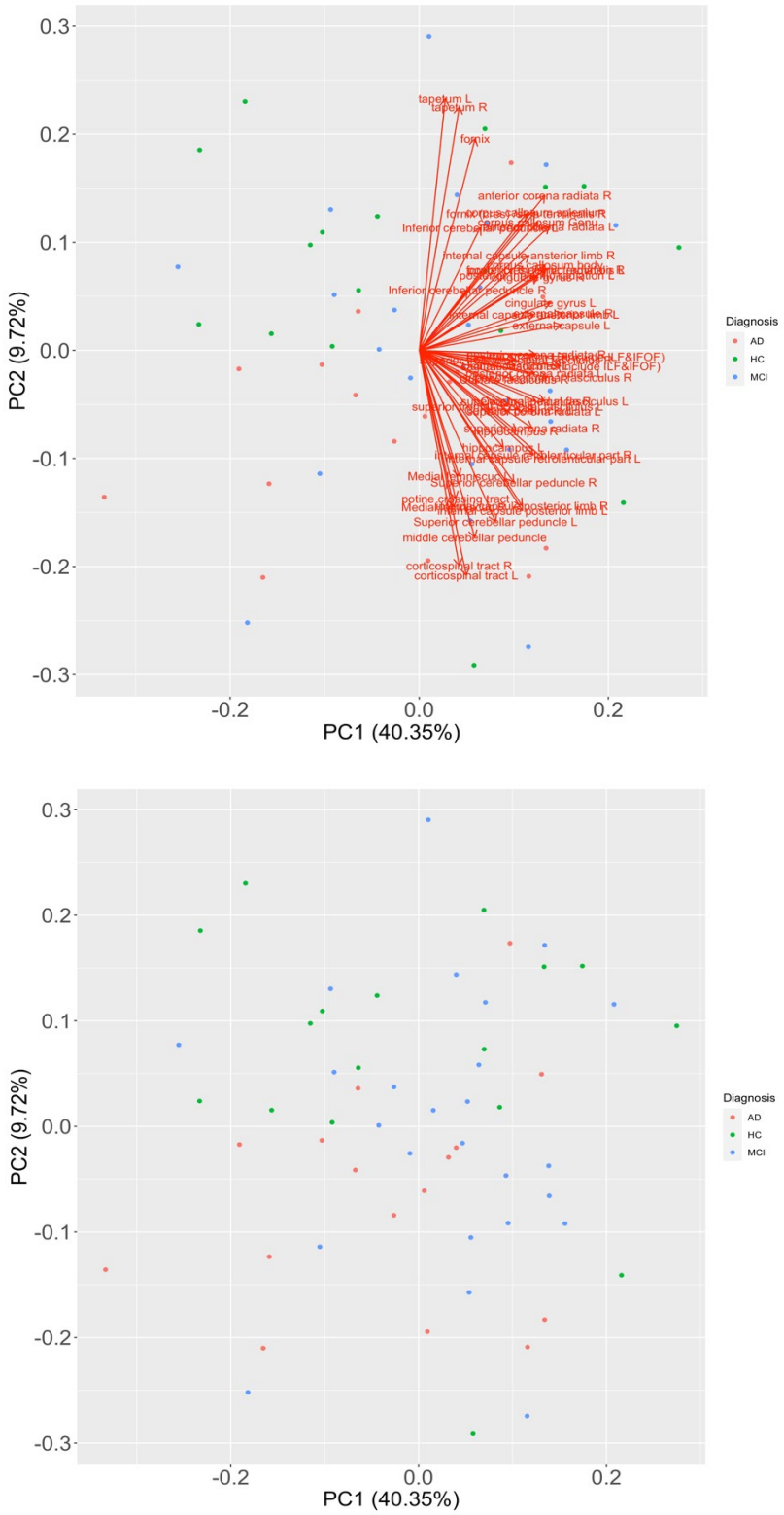

Figure 4.2 Principal Components of FA values in all TOIs

Top: Loadings plot of TOIs; Bottom: Separation of participants in 2D principal component space. Principal component 2 axis distinguishes AD and HC participants with relatively good separation.

4.4.5 Structural connectivity analysis using graph theory

Graph theoretical analysis of structural connectivity matrix constructed by tractography did not show any difference between diagnostic groups. Global network topology metrics including clustering coefficient and local efficiency (network segregation), global efficiency and average path length (network integration), small-worldness, and nodal metrics including nodal betweenness centrality, nodal average path length and nodal clustering coefficient, were tested. Both binary and weighted (weighted by number of streamlines) approach did not detect any topology change in AD or MCI patient group compared to HC participants.

4.4.6 Linking structural network integrity, functional network organisation and cognition

PC2 of FA values had significant positive correlation with network local efficiency (standardised β = 0.437, 95%CI: 0.0814~0.793, p-perm=0.047, age and cortical thickness corrected), while cortical thickness correlated with small-worldness (standardised β = 0.371, 95%CI: 0.001~0.741, p-perm=0.006, age and PC2 corrected).

FA PC2 positively correlated with MMSE scores (standardised β = 0.75, 95%CI: 0.0367~0.836, p-perm=0.019, corrected for age).

4.4.7 Bivariate correlations between FA values and ^{11}C-PBR28 uptake

To explore the relationship between neuroinflammation and white matter network integrity, I first explored the correlation between FA values and ^{11}C-PBR28 uptake across multiple regions. Negative relationship between the two variables was found in multiple ROI-TOI

pairs in both MCI and AD patients. A graphic representation of the correlation in Aβ+ patients is shown in Figure 4.5, where the Pearson correlation coefficients of significant correlations are color-coded in yellow-green scheme. The significance is determined by permutation tests.

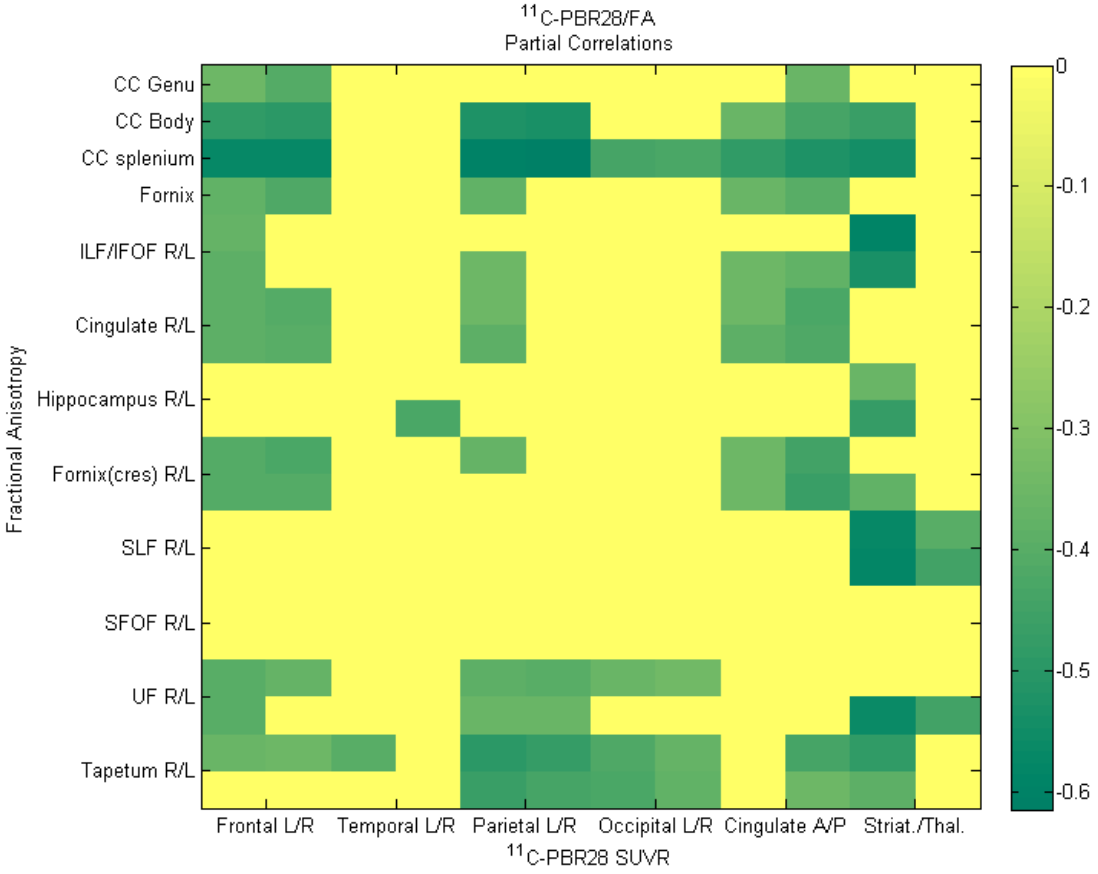

Figure 4.5. Partial correlation matrix between ROIs of ^{11}C-PBR28 and FA values in tracts of interest in the combined Aβ-positive cohort.

Correlation coefficients of non-significant correlations are plotted as zeros.

CC: corpus callosum; ILF: inferior longitudinal fasciculus; IFOF: inferior fronto-occipital fasciculus; SLF: superior longitudinal fasciculus; SFOF: superior fronto-occipital fasciculus; UF: uncinate fasciculus; L: left; R: right; A: anterior; P: posterior; Striat: striatum; Thal: Thalamus.

4.4.8 Network level multiple regressions

To evaluate the brain level relationship between neuroinflammation and structural network integrity, the first principal component of cortical ^{11}C-PBR28 uptake (^{11}C-PBR28 PC1, 78.9% total variance explained) was extracted and its association with FA PCs was analysed.

In MCI cohort, ^{11}C-PBR28 PC1 had negative correlation with FA PC1 (N=25, R=-0.43, 95% CI: -0.71~-0.05, p=0.03) but not FA PC2 (R=-0.20, 95% CI: -0.55~0.21, p=0.34); In AD cohort (N=16), similar trend was found but not statistically significant: ^{11}C-PBR28 PC1& FA PC1(R=-0.43, 95% CI: -0.76~0.08, p=0.10); ^{11}C-PBR28 PC1& FA PC2(R=-0.23, 95% CI: -0.65~0.30, p=0.39).

To fully cover Alzheimer's spectrum and increase statistical power, Aβ+ patients were grouped together (N=26). In Aβ+ patients, ^{11}C-PBR28 PC1 correlated with both FA PC1 and FA PC2 (R=-0.49, 95% CI: -0.74~-0.13, p=0.01; and R=-0.40, 95% CI: -0.68~-0.02, p=0.04, respectively. Figure 4.6). The association remains true after considering the effect of global amyloid load, cortical thickness and age (standardised β=-0.44, 95% CI: -0.848~-0.032, p=0.014; and standardised β=-0.375, 95% CI: -0.749~-0.005, p=0.047, respectively. Parameter were estimated using robust regression and significance were determined using permutation tests).

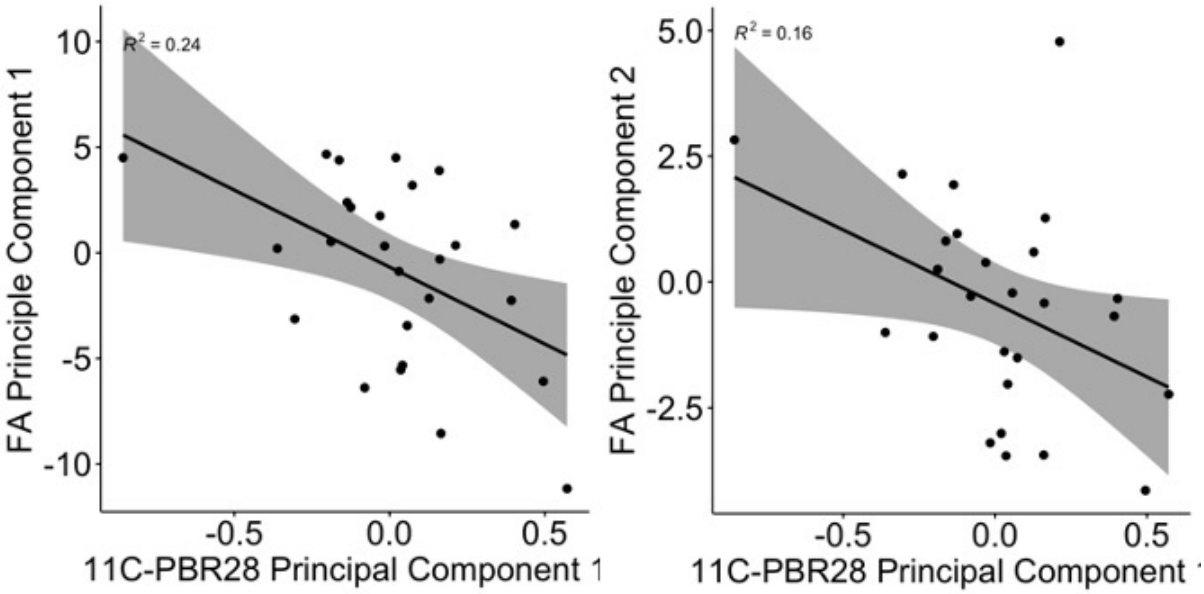

Figure 4.6 Correlation between ^{11}C-PBR28 uptake and FA value principal components

4.4.9 Canonical correlation between FA values and ^{11}C-PBR28/^{18}F-flutematemol SUVR

In the combined Aβ+ cohort, SCCA found a significant negative correlation between ^{11}C-PBR28 and FA (r=0.63, p=0.043, permutation test), with ^{11}C-PBR28 uptake in bilateral frontal, parietal lobe and posterior cingulate having non-zero canonical weights (weights in the table are drawn from SCCA with LASSO penalty term λ=0.7). Canonical correlation between ^{18}F-flutematemol and FA values was not significant (r=0.37, p=0.7). Interestingly, when both ^{11}C-PBR28 and ^{18}F-flutematemol were included, the ^{18}F-flutematemol ROIs were quickly dropped out of the model with increasing λ and when λ was greater than 0.7 none of the ^{18}F-flutematemol ROIs remained in the model (r=0.63, p=0.06 with λ=0.7) (Table 3).

		^{11}C-PBR28/FA		^{11}C-PBR28 & 18F-Flutemametmol/FA		
	PET ROIs	Canonical weights_PET	Canonical weights_FA	Canonical weights_PET	Canonical weights_FA	FA
^{18}F-Flutemametmol	Frontal/L	-	0.16	0	0.06	corpus callosum Genu
	Frontal/R	-	0.51	0	0.58	corpus callosum body
	Temporal/L	-	0.61	0	0.72	corpus callosum splenium
	Temporal/R	-	0.163	0	0.07	fornix
	Parietal/L	-	0.09	0	0	ILF&IFOF R
	Parietal/R	-	0.24	0	0.19	ILF&IFOF L
	Occipital/L	-	0.21	0	0.12	cingulate gyrus R
	Occipital/R	-	0.31	0	0.28	cingulate gyrus L
	Ant. Cingulate	-	0	0	0	hippocampus R
	Post. Cingulate	-	0	0	0	hippocampus L
^{11}C-PBR28	Frontal/L	-0.44	0.12	-0.41	0	fornix (cres) /stria terminalis R
	Frontal/R	-0.42	0.15	-0.41	0.03	fornix (cres) /stria terminalis L
	Temporal/L	0	0.06	0	0	SLF R
	Temporal/R	0	0	0	0	SLF L
	Parietal/L	-0.55	0	-0.56	0	SFOF R
	Parietal/R	-0.34	0	-0.47	0	SFOF L
	Occipital/L	0	0.10	0	0.02	UF R
	Occipital/R	0	0.10	0	0.02	UF L
	Ant. Cingulate	0	0.16	-0.03	0.09	tapetum R
	Post. Cingulate	-0.46	0.15	-0.36	0.07	tapetum L

Table 3. Canonical correlation between PET measurements and FA

ILF: inferior longitudinal fasciculus; IFOF: inferior fronto-occipital fasciculus; SLF: superior longitudinal fasciculus; SFOF: superior fronto-occipital fasciculus; UF: uncinate fasciculus; L: left; R: right; Ant: anterior; Post: posterior.

4.4.10 Voxel-wise regression models

Voxel-wise regression analyses were performed on FA and MD skeletons using the following model: FA/MD ~ ^{11}C-PBR28 uptake + ^{18}F-flutematemol uptake + average cortical thickness + age + gender + intercept. In AD patients, ^{11}C-PBR28 uptake showed significant positive relationship with MD values in bilateral cingulate and hippocampal part of cingulum, genu, body and splenium of corpus callosum, bilateral SLF, ILF, IFOF and UF. however, the association between ^{11}C-PBR28 uptake and FA values was not significant in AD patients. In MCI patients, ^{11}C-PBR28 uptake had negative relationship with FA values in the entire corpus callosum, bilateral cingulum, ILF, ILOF, SLF and UF, and was associated with higher MD values in similar regions. In all Aβ+ patients, same positive relationship between ^{11}C-PBR28 uptake and MD, and negative association between ^{11}C-PBR28 uptake and FA were found in those regions including CC, cingulum, ILF, ILOF, SLF and UF (Figure 4.5).

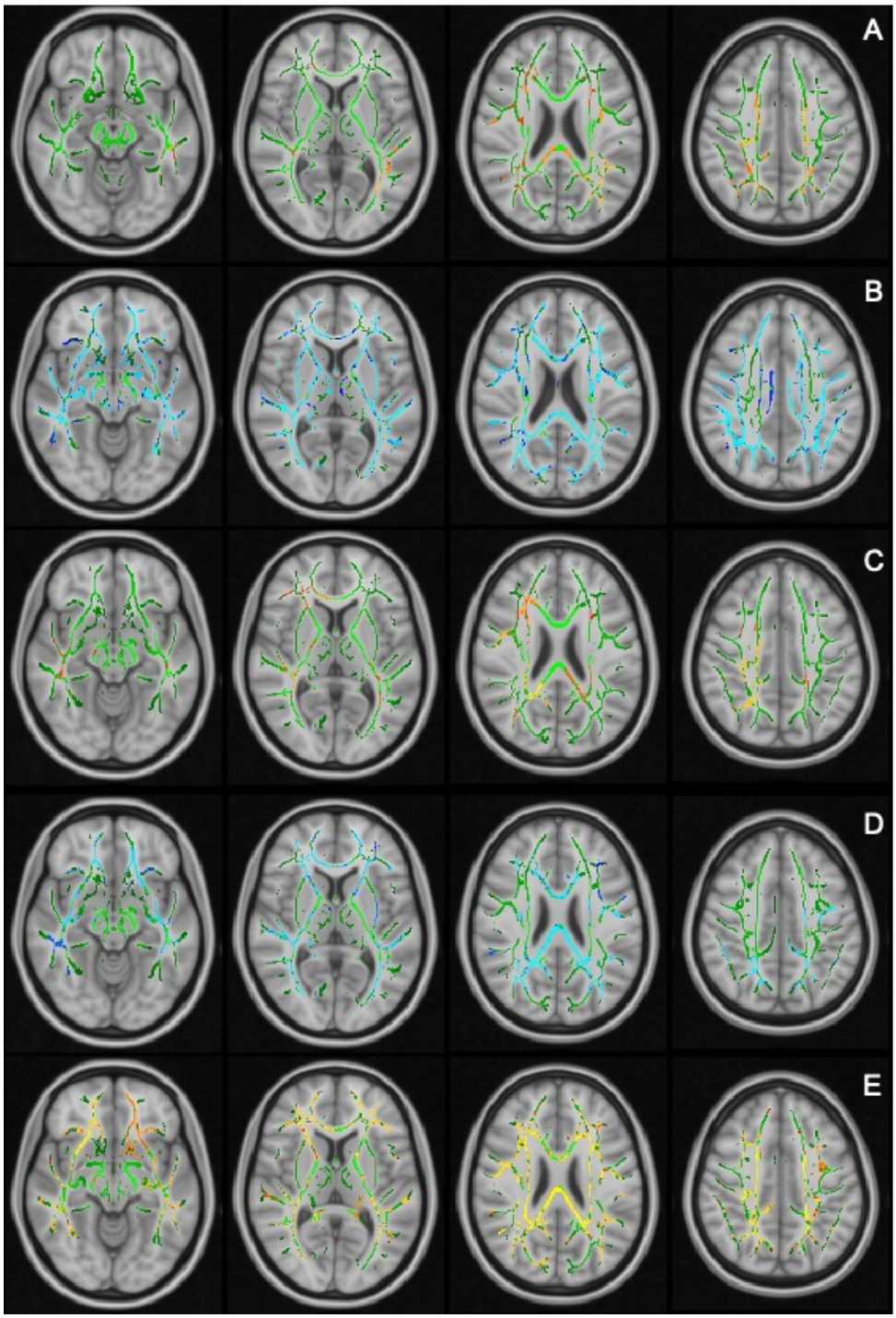

Figure 4.5 Effect of ^{11}C-PBR28 uptake on FA and MD values in voxel-wise regression analysis

A: Effect of ^{11}C-PBR28 cortical uptake (PC1) on MD values in AD patients; B: Effect of ^{11}C-PBR28 PC1 on FA values in MCI patients; C: Effect of ^{11}C-PBR28 PC1 on MD values in MCI patients; D: Effect of ^{11}C-PBR28 PC1 on FA values in Aβ+ patients; E: Effect of ^{11}C-

PBR28 PC1 on MD values in Aβ+ patients. TBSS skeleton is rendered in green, positive effects are shown in red-yellow scheme and negative effects are shown in blue-light blue scheme. Only significant clusters that survived FDR correction at spatial level ($p<0.05$) using TFCE algorithm are shown.

4.4.11 Mediation analysis

Considering that neuroinflammation was associated with both network structural integrity and functional organization, and that structural network is the physical basis of functional organization, we asked whether the effect of neuroinflammation on functional network was mediated by network structural integrity. A linear mediation analysis with ^{11}C-PBR28 and ^{18}F-Flutematemol uptake, PC2 and age as independent variables, local efficiency as dependent variable and PC2 as mediator showed a significant average direct effect of ^{11}C-PBR28 uptake on local efficiency (95% quasi-Bayesian confidence interval -0.25~-0.06, p=0.002) and a marginal average causal mediation effect via PC2 (95% quasi-Bayesian confidence interval -0.12~-0.00, p=0.07).

4.5 Discussion and Conclusions

In the current study, I have first evaluated the structural brain network integrity and structural connectivity in AD and MCI patients using diffusion tensor imaging analysis.

In the current analysis, significant reduced fractional anisotropy and increased diffusion parameters were found mainly in association fibres in AD patients, which is consistent with the literature (Goveas et al., 2015). The increased MD, DA and DR reflect a loss of restriction on water diffusion, and could be caused by demyelination, axonal atrophy and axonal losses. The loss of diffusion restrictions in all directions resulted in a loss of anisotropic feature of white matter structures, and therefore reduced FA (Scheltens et al., 1995) (Sjobeck et al.,

2006b) (Gouw et al., 2008). In MCI patients, we did not find significant changes of FA or diffusion parameters, which has been reported in other cohorts. The number of participants may have limited the statistical power of analysis, as a trend towards decreased FA and increased MD could be seen in our MCI cohort. Further, the MCI patients in the current cohort may be at earlier stage of disease, as the average MMSE was rather high at 28. In Aβ+ MCI patients, increased DA, but not other metrics was found in association fibres compared to HC group. Animal studies have suggested that increase in DA or DR is related more to axonal damage, as opposed to MD which indicates more of demyelination (S. W. Sun et al., 2006) (Harsan et al., 2006). Therefore, the increased DA may reflect the earliest axonal damage among the patients, or it might be related to the disruption of crossing fibres. However, the exact physiological basis of the early increase of axial diffusivity in humans still remains to be elucidated. Nevertheless, the current analysis does support the view that metrics other than FA and MD, such as DA, might be more sensitive for early changes in disease process. Therefore, more detailed examination of diffusion parameters including DA and DR are recommended instead of just focusing on FA and MD whenever possible.

Following up analysis on the relationship between structural network integrity, functional organization and cognition revealed the importance of an intact structural network, as better network integrity metrics were indeed associated with better functional network efficiency and better cognition.

While there has been speculation that white matter damage in AD is simply secondary change of grey matter atrophy, the current analysis revealed altered axial diffusivity in Aβ+ MCI patients, who did not have significant grey matter changes. Moreover, in regression models, cortical thickness was not able to explain all the changes in FA values. These findings highlight structural network damage as an early event in Alzheimer's trajectory, which may even precede overt cortical atrophy. Considering the association between structural network

integrity, functional connectivity and cognition, these early white matter changes should not be overlooked. Therefore, better understanding of the disease and potential treatment strategies may reside on finding the factors contributing to structural network damage.

However, graph theoretical analysis of structural connectivity matrices constructed by tractography failed to detect any difference between AD and HC or MCI and HC groups. Such result was anticipated for the analysis using the binary connectivity matrices, as the major white matter connections of human brain, however healthy or diseased, should exist across the population. Therefore, with a certain sparsity threshold, very similar, if not same binary matrices would be extracted. This is different from functional connectivity matrices, because based on the same structural network, different brain regions could work in a healthy and harmonized way or in a disorganized pattern. In this way, functional connectivity analysis could detect abnormalities with good sensitivity, even when the network structures remain intact, whereas structural connectivity analysis could only answer whether or not two regions are physically connected. As the existence of basic brain 'wiring' is not changed by disease, the structural connectivity topology metrics would not be able to distinguish healthy and disease brains. What was unexpected was that the analysis on streamline density weighted connectivity matrices failed to reveal any change in diseased brains. Several factors may contribute to the failure of this approach:

Firstly, the streamline density may not be a good metric for evaluating the strength of structural connectivity, as they are influenced by the traceability of each scan and does not totally reflect the number of real axons. Indeed, the number of streamlines varied a lot across individuals even within the HC cohort. There have been several studies that used the total number of streamlines to normalize the connectivity matrices before further processing, but this would again result in similar patterns in connectivity matrices that is defined genetically in all humans (Tucholka et al., 2018). A better approach might be to sample the FA or MD

values in each constructed pathway and use them to weight the connectivity matrices, which has been applied by several studies already (Shu et al., 2012). However, due to the high computational cost (performing tractography using each 2 pairs of ROIs in the N-by-N matrices and sampling the FA/MD values), it was not feasible within the time frame and available resources with regard to the current project.

Secondly, the network topology metrics, even if weighted versions were used, were designed to reflect overall network organization, but not structural integrity. Therefore, it may not be as sensitive as the FA/MD values themselves to detect impaired structural network integrity.

Based on the analysis I have performed, I believe the structural network integrity metric which originated from TBSS was better suitable for evaluating the structural brain network impairment in AD. Therefore, in the following analysis on relationship between neuroinflammation and brain structural network, the network integrity metrics were used.

With the new NIA-AA consensus on the ATN framework of Alzheimer's disease (Jack et al., 2018), the current analysis mainly focused on investigating the relationships between neuroinflammation, amyloid deposition and structural network integrity in Aβ+ patients, as I believe they could better represent the Alzheimer's spectrum. Nevertheless, supplementary voxel-wise regression analyses based on clinical diagnostic groups were also performed. While previous studies have reported that Aβ deposition is associated with white matter damage in AD and MCI patients, these studies have mostly relied on clinical diagnosis, and did not specifically interpret the quantitative effect of Aβ deposition on white matter integrity in Aβ+ cohorts (Melah et al., 2016) (Gold et al., 2014). In fact, it is possible that Aβ was a diagnostic marker of AD and the association was mediated by whether or not the patient has Alzheimer's pathology. For example, in the current study increased DA was only found in Aβ+ MCI patients, but not Aβ- MCI or the whole MCI group, however, a direct relationship

between Aβ and white matter alteration could not be readily established, as Aβ is a marker of Alzheimer's disease, which has multifaceted pathologies. In fact, a recent study on longitudinal DMN connectivity have reported that it is APOE genotype but not baseline Aβ status that could predict longitudinal DMN connectivity change (Chiesa et al., 2019). Therefore, I would argue that the quantitative analysis within Aβ+ patients could better identify the factors truly associated with structural network damage in Alzheimer's spectrum.

With that in mind, the current analysis has identified neuroinflammation as an independent factor that is strongly associated with structural network damage in Alzheimer's spectrum, while the amount of Aβ+ plaques is not directly linked with white matter microstructural damage. Similar results have also been found in MCI and AD cohorts separately, while controlling for the effect of Aβ+ deposition and cortical atrophy. The fact that amyloid load, as quantified by ^{18}F-Flutemetamol, did not correlate with structural network impairment in the study cohort, might be attributed to several factors: First, the number of participants may have limited the statistical power of analysis; Secondly, the PET tracers could only bind to fibrillary forms of Aβ species, while current evidence suggest that soluble Aβ monomer and oligomers are more neurotoxic, therefore the tracer uptake may not reflect the amount of toxic Aβ species accurately; Lastly, part of amyloid toxicity might have been mediated by neuroinflammation, and therefore the unique contribution from Aβ in the regression models is limited when neuroinflammation marker is included.

The key finding is the association between neuroinflammation and brain structural network damage across Alzheimer's spectrum, independent of Aβ and cortical thickness. It has been well established that glia cells contribute to the development and maintenance of neuronal network throughout lifespan. During brain development microglia contribute to neurogenesis, axon outgrowth, synapse modelling and myelination(Michell-Robinson et al., 2015). In adulthood, microglia have dynamic and direct interactions with neuronal network

structures(Baalman et al., 2015) and are involved in maintenance and repair of myelin(Michell-Robinson et al., 2015). In AD brains, activated microglia lose their ramified morphology, cease their house-keeping functions, and migrate to Aβ plaques and neurons containing neurofibrillary tangles(Davies et al., 2017). It has been established that the inflammatory cytokines could directly disrupt neuronal activities and induce neuronal death in experimental conditions. Activated microglia can also cause direct damage to oligodendrocytes and axons through production of ROS, matrix metalloproteinases and pro-inflammatory cytokines (Peferoen et al., 2014). Accumulation of activated microglia has also been reported to co-locate with damaged axonal initial segments in a mouse model of AD(Marin, Ziburkus, Jankowsky, & Rasband, 2016). Furthermore, an *ex vivo* experiment has demonstrated that activated microglia can induce neuritic beading of axons, inhibit mitochondrial function and axonal transport through N-methyl-D-aspartate (NMDA) receptor signalling(Takeuchi et al., 2005). The preclinical evidence above suggests that neuroinflammation in AD could be related to structural network breakdown in several ways: (1) disrupting trophic support from glia cells; (2) releasing neurotoxic inflammatory cytokines; (3) direct damage to axons and synapses by cellular interactions.

In the previous analysis, the relationship between neuroinflammation and functional connectivity disruption has been demonstrated (Hahn et al., 2013). Therefore, it is worth exploring whether the influence of neuroinflammation on functional organization is mediated by structural network integrity. Following the line of thought, a linear mediation analysis was performed to find the answer. It was found that while there was a possible path from neuroinflammation to structural network damage and to functional disruption, the direct effect from neuroinflammation to functional disruption was more significant. It could be concluded now that neuroinflammation is directly associated with both functional connectivity disruption and structural network damage in Alzheimer's spectrum. Given the

importance of network organization in brain functioning, neuroinflammation is a potential target for preserving cognitive function in AD patients. However, further investigation is still needed to substantiate the causal relationship and underlying biological mechanisms.

Chapter 5. Cerebral Perfusion, Amyloid and Neuroinflammation

5.1 Introduction

It has been established by autopsy studies that the cerebral vasculature undergoes pathological changes in Alzheimer's disease, including endothelial cell swelling and atrophy, basal membrane thickening and splitting, smooth muscle cells constriction, pericyte atrophy, astrocyte end-feet swelling, BBB breakdown and amyloid deposition in vascular walls (cerebral amyloid angiopathy, CAA) (Farkas & Luiten, 2001; Sweeney, Sagare, & Zlokovic, 2018). Further, epidemiological studies have unveiled that vascular risk factors, such as mid-life hypertension and diabetes, are associated with increased risk for AD (Barnes & Yaffe, 2011). These findings further highlight cerebral perfusion deficits in Alzheimer's disease. Indeed, rather than being a subsequent phenomenon to brain atrophy, cerebral oligaemia and ischemia is now suggested as a potential driving force of AD (Ostergaard et al., 2013; Zlokovic, 2011b).

5.1.1 Using Arterial Spin Labelling to Quantify Brain Perfusion in vivo

Arterial spin labelling (ASL) is a non-invasive MRI technique to measure blood flow *in vivo*. ASL uses a selective radiofrequency (RF) sequence in the selected plane or region to invert the magnetization of water within the region, which will act as endogenous tracer for blood flow. Following the labelling step, a post-label delay (PLD) period is necessary to allow the labelled water molecules to flow through the vasculature and enter tissue compartment. Because the magnetization of labelled water is inverted, they will cancel the net magnetization in tissue when the images are acquired. By comparing the signals in labelled images with control images where the labelling sequence is not applied, the amount of arterial blood perfusion to tissue can be inferred (Grade et al., 2015).

ASL can be categorised into continuous ASL (cASL), pulsed ASL (pASL) and pseudo-continuous ASL (pcASL) according to the labelling schemes. cASL uses a continuous RF field in a thin labelling 'plane' to invert any magnetization that flows across the plane, which is also known as the flow-driven adiabatic inversion; pASL, otherwise, uses a single short RF sequence to invert the magnetization in a 'thick slice' of region, creating a bolus of labelled water. cASL has the desirable features including high labelling efficiency, precise label duration, and possibility to apply long labelling durations, however, clinical scanners are usually not able to apply the continuous RF sequence effectively; pASL is easier to be performed on clinical scanners but has the problems including ill-defined labelling period and low signal-to-noise ratio caused by short label durations. pcASL tries to address the disadvantages of pASL by using a series of short repeating RF pulses to approximate the continuous RF field in cASL. Therefore, pcASL has the advantageous features of cASL, while can still be performed on clinical scanners without specialist hardware. Now pcASL is recommended for research use where possible (Alsop et al., 2015).

5.1.2 Perfusion Deficit in AD

Clinical ASL studies have observed decreased CBF in posterior cingulate, parietal, frontal and temporal cortices in AD patients, which are further related to cognitive performance in the patients (Alsop, Detre, & Grossman, 2000) (Binnewijzend et al., 2014). Recently, a meta-analysis on clinical imaging studies has further summarised that hypoperfusion occurs in precuneus, posterior cingulate and inferior parietal lobule in MCI patients, and further involves frontal and temporal regions in AD patients (Schroeter, Stein, Maslowski, & Neumann, 2009). And it has been suggested that CBF dysregulation starts early in disease trajectory even before brain atrophy in population at high risk of AD (Ruitenberg et al., 2005).

Lines of evidence have suggested that perfusion deficit may take a place in facilitating Alzheimer's pathology. Preclinical study has observed that hypoxia can upregulate BACE1 expression, which is a key enzyme in APP cleavage, and exaggerate amyloid deposition (X. Sun et al., 2006). Apart from amyloid genesis, hypoperfusion may also lead to insufficient clearance of amyloid species via the glymphatic system, as the drainage of the system depends on bulk flow from the vessels (Jessen et al., 2015; M. K. Rasmussen, Mestre, & Nedergaard, 2018). Further, hypoxia has also been found to supress the neprilysin expression, which can degrade Aβ (Z. Wang et al., 2011). Recent evidence has also suggested that hypoxia can induce tau phosphorylation at AD-associated epitope via MAPK pathway (Fang, Zhang, Meng, Du, & Zhou, 2010; Gordon-Krajcer, Kozniewska, Lazarewicz, & Ksiezak-Reding, 2007; Raz et al., 2019). Conversely, Alzheimer's pathology could in turn exaggerate cerebral hypoperfusion and therefore form a downward spiral. Apart from direct deposition on vascular wall in CAA, a recent study has demonstrated that Aβ oligomers can cause capillary constriction by inducing reactive oxygen species and endothelin-1 signalling to pericytes (Nortley et al., 2019).

Notably, inflammatory factors are closely related to the cerebrovascular dysfunctions. It has been observed that brain micro-vessels produce more proinflammatory cytokines and chemokines including TNF, IL-1β, IL-6, CCL2, prostaglandins, and MMPs in brain samples of Alzheimer's disease (Grammas, 2011; Grammas, Moore, & Weigel, 1999). Apart from these cytokines, disrupted blood flow is also associated with production of fibrinogen and thrombin, which can further induce glial activation in brain parenchyma (Davalos & Akassoglou, 2012; X. Yin, Wright, Wall, & Grammas, 2010). Conversely, neuroinflammation could also influence cerebral perfusion. It has been established that astrocytes directly regulate the contractability of arteries in CNS (Takano, Han, Deane, Zlokovic, & Nedergaard, 2007), and astrocyte dysfunction has been suggested to impair

neurovascular coupling in AD (Tarantini, Tran, Gordon, Ungvari, & Csiszar, 2017). Further, the cytokines released by pro-inflammatory microglia and astrocytes could induce inflammatory response of vasculature and disrupt the BBB function (L. R. Liu, Liu, Bao, Bai, & Wang, 2020; Tarantini et al., 2017; Zhao, Nelson, Betsholtz, & Zlokovic, 2015).

5.2 Aim of the project

Based on the previous reasoning, it could be hypothesised that neuroinflammation, as well as amyloid and tau pathologies, are associated with perfusion deficit in Alzheimer's continuum. While there has been reports on association between amyloid deposition and cerebral perfusion in AD patients (Mattsson et al., 2014), there is still a lack of evidence on whether neuroinflammation or tau pathology in AD is associated with perfusion deficit *in vivo*. Therefore, the current analysis investigated on the relationship between PET markers of Alzheimer's disease and CBF in the study cohort.

5.3 Methods

5.3.1 Arterial spin labelling scan acquisition

A Pulsed ASL (pASL) scheme was used for the current study. The pASL scans were acquired using the following settings: 14 axial slices, TR=2500ms, TE=11ms, PICORE Q2T perfusion mode, inversion time of arterial spins (TI1) =700ms, saturation stop time = 1600ms, total transit time of spins (TI2)=1800ms, flow limit= 100cm/s, tag thickness 100mm, gap between tag and proximal slice =29.5mm, FOV=192×192mm^2, Flip angle=90°, 3×3×6mm voxel size, anterior-posterior phase encoding direction, bandwidth=2232 Hz/Px, echo spacing=0.53ms. A total of 101 volumes of 3D-images were acquired for each participant: 50 pairs of tagged and untagged images were acquired, and a water density image acquired prior to these 50 pairs of images as reference image.

5.3.2 Pre-processing of ASL scans

Pre-processing of the ASL scans were performed using FSL's BASIL toolbox (Woolrich et al., 2009). Briefly, the image series were first aligned using rigid body transformation. Next, for each pair of tagged-untagged images, the tagged image was subtracted from the untagged image, and the result is the perfusion-weighted difference image. The mean difference image was used for further modelling and computation of cerebral blood flow (Figure 5.1).

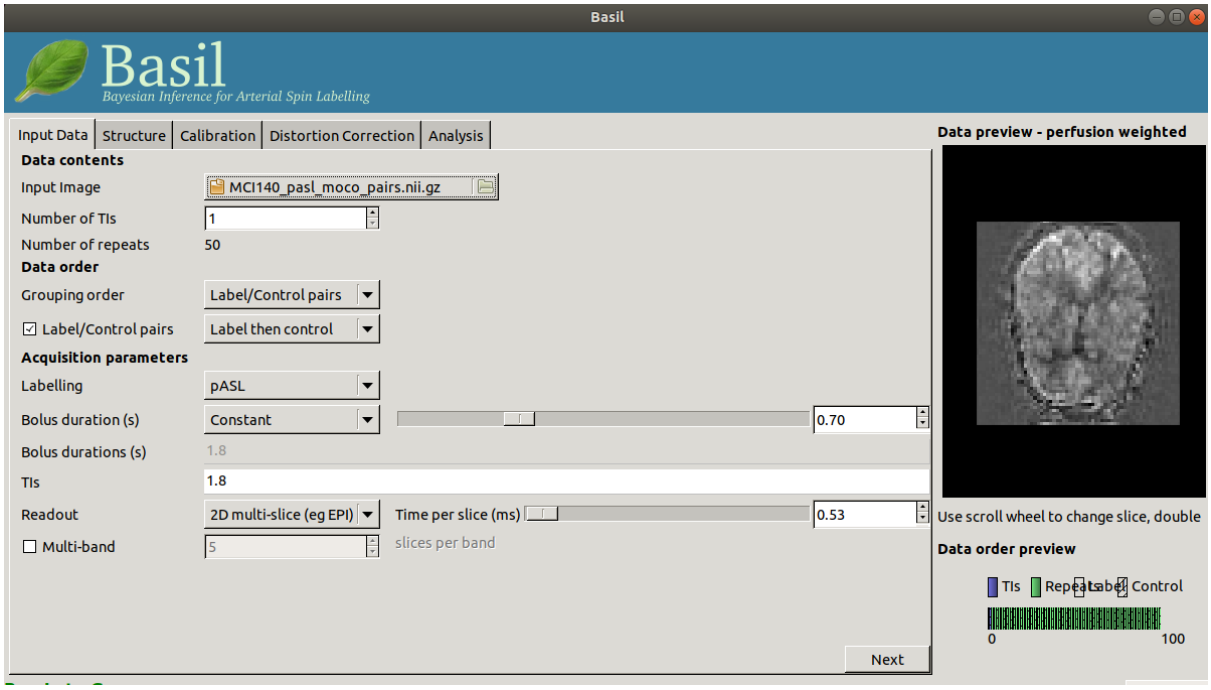

Figure 5.1 Creating difference image from control-label pairs

5.3.3 Spatial transformation

The registration of ASL images to the standard MNI152 space was completed in following steps: first, the reference image was linearly registered to structural T1-weighted image to provide an initial start point. The perfusion-weighted images were then used for finer registration process, as it has better contrast between grey and white matter. The registration of perfusion weighted images to the structural images was performed using the boundary-based registration (BBR) cost function by FSL (Jenkinson & Smith, 2001). The non-linear transformation from structural space to standard space was estimated using FSL_ANAT tool,

which also provided tissue segmentation information for calibration and partial volume effect correction.

5.3.4 Perfusion Modelling and Quantification

The perfusion-weight images are not scaled by absolute values of perfusion (ml/100 g/min). To obtain the cerebral blood flow (CBF) maps in quantitative units, kinetic modelling with Bayesian inference method was performed using BASIL (Chappell, Groves, Whitcher, & Woolrich, 2009). Slice timing was considered as the current study used a 2D acquisition method.

The kinetic of labelled water in brain was described using the following model:

$$C(t) = f \cdot AIF(t) \otimes r(t) = f \cdot \int_0^t AIF(\xi) \cdot r(t-\xi) d\xi \qquad (5.1)$$

Where C(t) is the concentration of tracer in ROI, f is the rate of delivery (perfusion), AIF(t) is the arterial input function, which describes the delivery of tracer to ROI as a function of time, r(t) is the residue function, which describes the behaviour of tracer within ROI after it has arrived.

5.3.5 Calibration

The first image (pre-saturation image) was used to estimate the brain tissue equilibrium magnetization, and the mean CSF magnetization was used for calibration of the image. After this process, the resulting images have the absolute unit of ml/100 g/min.

5.3.6 Partial volume effect correction

The ASL scans acquired in the current study have 3×3×6mm voxel size, which is large compared to the 2~4mm cortical thickness, causing the signals from different tissue types to mix within a voxel. The segmentation of T1 image was down sampled to ASL space and resolution, and the perfusion signal in each voxel was modelled as a linear combination of

signals from grey matter, white matter and CSF. Because the current study used a single delay pASL protocol, it was an underdetermined problem to solve. Therefore, it was assumed that the perfusion varied smoothly across the voxels and the spatial prior information was used to compute the partial volume correct image by BASIL (Chappell et al., 2011) . The resulting PV-corrected CBF images were used in further analysis.

5.3.7 Evaluating early frames of dynamic PET as potential perfusion markers

To test whether it is possible to use early frame PET data to infer cerebral perfusion where ASL data are not available, the IRF at 1 minute after injection was computed using spectral analysis method, as described previously in PET analysis section, and the correlation between IRF 1min and CBF as quantified by ASL was examined. TSPO genotype was included as covariate of no interest in the analysis. Further, the IRF images were normalized using cerebellum grey matter as reference region, and the correlation between CBF and IRF ratios was also examined.

5.3.8 Statistical analysis

The PV-corrected CBF images was sampled using individualized Hammer's Atlas, as described previously in PET analysis. The CBF in frontal, temporal, parietal and occipital lobes, anterior and posterior cingulate cortices and media temporal lobe was compared across diagnostic groups using one-way ANOVA and post-hoc independent samples T-test. Voxel-wise comparisons were performed using SPM12, with cluster-forming threshold at $p<0.05$ and cluster-size FDR correction threshold at $p<0.05$. Because of the small FOV, the voxel-wise comparisons were performed using a mask without cerebellum.

A main concern on the white matter damage seen in AD is whether it is actually related to Alzheimer's pathology or caused by cerebral vascular comorbidities, especially in aged population. To assess whether the white matter microstructural damage in the study cohort is

related to perfusion issues, the relationship was examined between whole brain CBF and principal components of FA values, as metrics for overall brain perfusion and white matter integrity, respectively. Age was included as a covariate of no interest in the analyses.

Correlation analyses were also performed between CBF and PET markers (^{18}F-AV1451, ^{18}F-Flutemetamol and ^{11}C-PBR28) of Alzheimer's disease, in different ROIs.

Voxel-wise correlation analysis was performed between CBF and PET images/ALFF using VOXELSTATS package (Mathotaarachchi et al., 2016). The cluster forming threshold was set at $p<0.01$ and FDR correction was performed using random field theory with a threshold of $p<0.05$.

5.4 Results

5.4.1 Group comparisons of CBF

Group comparisons of CBF showed a trend of decreased CBF in all ROIs in MCI and AD patients, but the change was not statistically significant (Table 5.1). Voxel-wise comparisons of CBF maps did not show significant clusters of CBF change in AD, MCI or Aβ+ patients compared to HC.

Table 5.1 Cerebral Blood Flow in AD, MCI and HC groups

	HC	AD	MCI
N	19	21	59
Frontal Lobe	47.3 (±3.90)	41.7 (±3.14)	43.2 (±1.86)
Temporal Lobe	40.7 (±2.19)	37.9 (±1.58)	40.3 (±1.47)
Parietal Lobe	53.0 (±3.28)	53.4 (±4.44)	53.7 (±2.15)
Occipital Lobe	52.9 (±3.51)	44.8 (±2.76)	44.0 (±2.21)
Ant. Cingulate	52.2 (±5.88)	45.3 (±3.22)	49.8 (±2.55)
Post. Cingulate	65.4 (±4.08)	57.9 (±3.74)	59.7 (±2.55)
MTL	34.5 (±1.86)	31.6 (±1.88)	36.0 (±1.60)
Global CBF	51.9 (±3.26)	46.9 (±2.64)	48.5 (±1.76)

Data are shown in mean (±SE) format.

5.4.2 Comparing ^{11}C-PBR28 IRF-1min to CBF

Correlation analysis showed poor linear relationship between ^{11}C-PBR28 IRF 1min and CBF in the major regions ($p>0.05$). IRF 1min ratios did not have significant relationship with CBF either. Neither of the measures showed group difference between the diagnostic groups.

5.4.3 Relationship between CBF and white matter microstructural integrity

Significant association was not found between global CBF and PC1 or PC2 of FA in AD, MCI or Aβ+ cohorts.

5.4.4 Relationship between CBF and amyloid deposition

In AD cohort, ^{18}F-Flutemetamol uptake was associated with decreased CBF in temporal lobe (N=17, standardized β=-0.55, p=0.022, Figure 5.2A). ^{18}F-AV1451 uptake was associated with decreased CBF in MTL (N=15, standardized β=-0.49, p=0.040, Figure 5.2B). While ^{11}C-PBR28 uptake was not found to be associated with CBF in AD cohort.

In MCI cohort, none of the PET markers was significantly associated with CBF in any ROIs.

In Aβ+ cohort, ^{11}C-PBR28 uptake was found to be associated with decreased CBF in MTL (N=26, standardized β=-0.58, p=0.003, Figure 5.2C). The relationship held true after taking MTL ^{18}F-AV1451 uptake into consideration (N=16, standardized β=-0.56, p=0.018, Figure 5.2D). In other regions there was not association between PET markers (including ^{11}C-PBR28, ^{18}F-AV1451 and ^{18}F-Flutemetamol) and CBF.

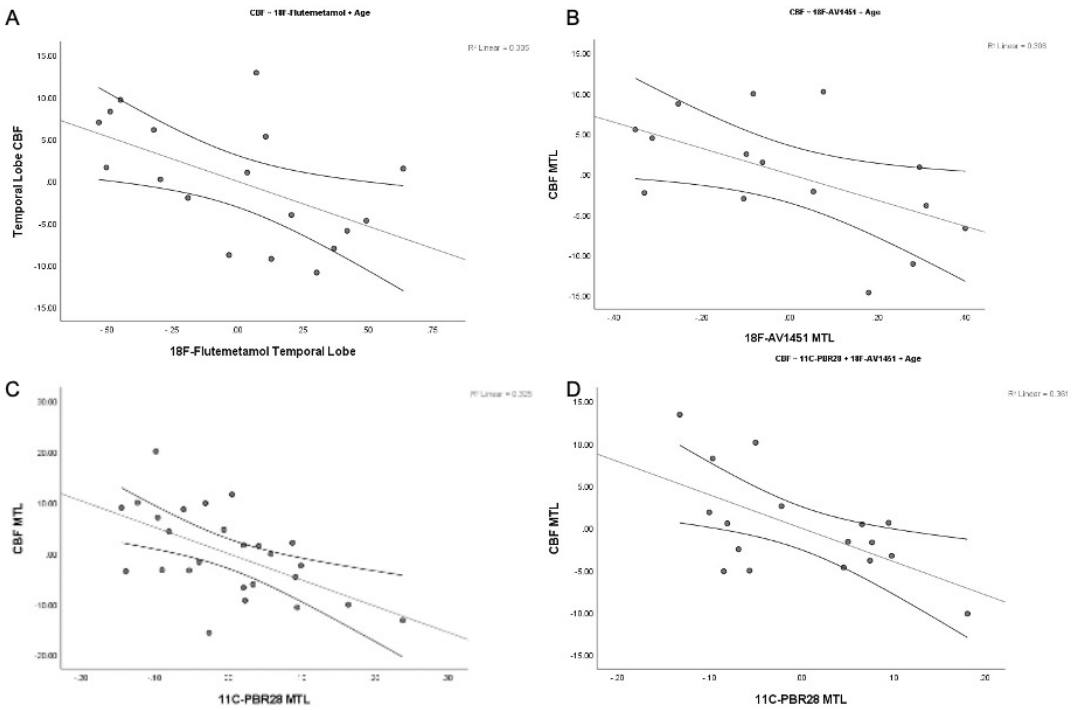

Figure 5.2 Partial correlation between PET markers of AD and CBF

A: correlation between ^{18}F-Flutemetamol and CBF in temporal lobe in AD patients (age controlled, N=17); B: correlation between ^{18}F-AV1451 and CBF in MTL in medial temporal lobe (MTL) in AD patients (age controlled, N=15); C: correlation between ^{11}C-PBR28 uptake and CBF in MTL in Aβ+ cohort (controlled for age, N=26); D: correlation between ^{11}C-PBR28 uptake and CBF in MTL in Aβ+ cohort (controlled for age and ^{18}F-AV1451 uptake, N=16).

5.4.5 Voxel-wise correlation analysis between PET/fMRI markers and CBF in Aβ+ cohort

In Aβ+ cohort, voxel-wise regression analysis detected negative relationship between ^{11}C-PBR28 uptake and cerebral blood flow in widespread regions including left occipital fusiform cortex, left occipital pole, bilateral precuneus cortices, bilateral posterior cingulate gyri, left superior and middle frontal gyri (Figure 5.3A, age controlled). Interestingly, the clusters in MTL regions did not pass the random field theory correction for multiple comparisons. A possible explanation for the observation is that in ROI analysis the individualised GM map

together with partial volume correction may be more robust to regional atrophy, while in voxel-wise analysis certain voxel in standard space may overlap with GM or CSF depending on the atrophy status, which could add noise in statistical inference.

ALFF was positively associated with CBF in widespread areas covering superior frontal gyrus, temporal, parietal, occipital lobe and posterior cingulate cortex (Figure 5.3B, age controlled). However, no significant association was found between ^{18}F-Flutemetamol and CBF.

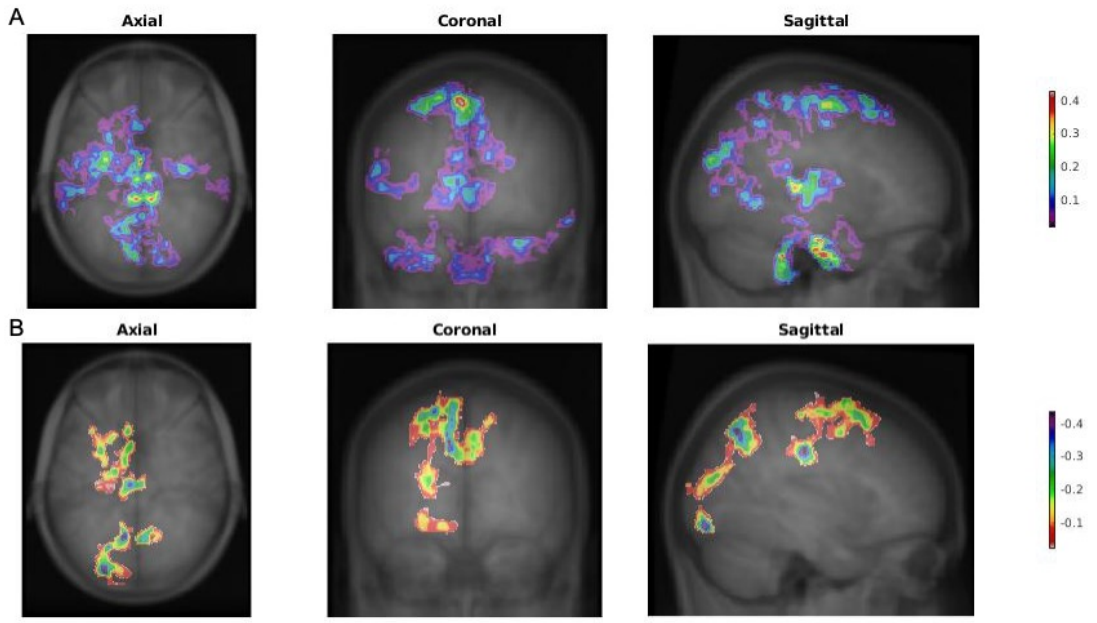

Figure 5.2. Voxel-wise correlation analysis between CBF and PET/fMRI markers

In Aβ+ cohort, voxel-wise regression analysis detected negative relationship between ^{11}C-PBR28 uptake and cerebral blood flow in widespread regions including left occipital fusiform cortex, left occipital pole, bilateral precuneus cortices, bilateral posterior cingulate gyri, left superior and middle frontal gyri (A); ALFF was positively associated with CBF in widespread areas covering superior frontal gyrus, temporal, parietal, occipital lobe and posterior cingulate cortex (B).

5.5 Discussion and Conclusions

In the current chapter, cerebral blood perfusion in AD and MCI patients compared to healthy participants was evaluated using ASL. Further, the relationship between CBF and other markers of Alzheimer's disease was assessed. The primary finding of the current project were that neuroinflammation is associated with decreased CBF in Aβ+ cognitively impaired patients, which suggested that neuroinflammation may be related to perfusion deficit in Alzheimer's disease.

While there has been evidence that neurovascular unit dysfunction is involved in the pathogenesis of AD (Zlokovic, 2011a), and that cerebral perfusion deficit can be found in AD patients (Schroeter et al., 2009), we did not find a significant overt reduction of cerebral blood flow in our AD or MCI cohort. This might be attributed to the following factors: First, the ASL sequence used in the study is single post labelling delay pulsed ASL, with relatively low resolution (3×3×6mm), which may limit the sensitivity of the current analysis; Secondly, the limited number of cases may have undermined the statistical power; more importantly, considering the multifaceted nature of dementia in clinical care, it is possible that certain vascular factors exist in a clinically diagnosed AD patient. However, with the exclusion criteria and evidence of AD pathology indicated by imaging biomarkers, the cognitive impairment in the current cohort may be more specifically caused Alzheimer's pathology.

Nevertheless, I should note that the pASL acquisition parameters used in the current study is far from optimal, and future studies focusing on CBF should consider optimising the acquisition protocol, especially on the following aspects: (1) consider using multi-PLD continuous ASL or pseudo-continuous ASL sequences to obtain more information for kinetic modelling ; (2) use finer resolution; (3) expand the FOV if possible, to cover whole brain

including the cerebellum; (4) use continuous slice readout rather than interleaved readout because it makes more sense to follow the bolus continuously upward (Alsop et al., 2015).

The potential of using early frame dynamic PET data to infer perfusion status has also been tested. However, using the IRF of ^{11}C-PBR28 1 minute after injection, the PET measures did not show significant association with the CBF as quantified by ASL. This is understandable as even though the early tracer uptake is influenced by perfusion, it is also heavily influenced by the tracer dynamics in tissue compartments. More precisely, with early frame PET data, the arterial input function (AIF) in equation (1) is a known variable, but the residual function for a PET tracer (other than $H_2{}^{15}O$) is much more complicated than labelled water, which can be simply modelled by label decay and veinous drainage. Further, unlike water molecules that can simply perfuse through BBB, the tracers' uptake in brain tissues may be influenced by BBB permeability as well. Therefore, the early frames PET data using other tracers (other than H_2O^{15}) may not be optimal for inferring cerebral blood perfusion, and H_2O^{15} PET or ASL is recommended method where it is possible to be obtained. Nevertheless, tests are being performed to evaluate other tracers with more rapid pharmacokinetics to reflect blood perfusion, such as ^{11}C-PIB and ^{18}F-Florbetapir using PET image at ~5 minute post injection (Mittal et al., 2021).

As there is no significant change of perfusion in diseased cohort in this study, it could be assumed that the white matter microstructural damage is unlikely to be caused by cerebral vascular comorbidities. Indeed, in disease cohorts, there was no correlation between CBF and FA values, suggesting that the structural network damage was more probably associated with Alzheimer's disease. This again highlights that importance of investigating structural network damage in Alzheimer's trajectory.

As expected, there was positive correlation between CBF and ALFF in widespread regions. This is likely to be the result of neurovascular coupling, which means blood perfusion will be upregulated where neuronal activity is more frequent (Girouard & Iadecola, 2006). However, the relationship is not observed in prefrontal cortex in current Aβ+ cohort, where increased spontaneous neuronal activity is observed. Indeed, group comparisons did not show an increase of CBF in frontal cortex either, suggesting that the increased neuronal activity in these patients was not accompanied by unregulated blood perfusion, i.e., there was an impaired neurovascular coupling (Kisler et al., 2017). This is an interesting observation, as the mismatch between energy and oxygen demand by neuronal activity and supply by perfusion might lead to further functional hypoxia, oxidative stress and downstream neuronal damage (Zlokovic, 2011b).

Given the evidence of impaired neurovascular coupling in Aβ+ cognitively impaired patients, the relationship between PET markers of AD and CBF was further interrogated, with the aim of finding pathological events that may underly perfusion deficits. Surprisingly, in the current Aβ+ AD and MCI cohort, amyloid load was not found to be associated with CBF change, while neuroinflammation was found to have a negative relationship with CBF. As it is undetermined how well ^{18}F-Flutemetamol can detect amyloid deposition in vascular basal membrane, this observation might be caused by different proportion of amyloid angiopathies in total amyloid load in these patients, which may obscure the negative influence of angiopathies on perfusion. As an example, animal experiment has demonstrated that CBF is associated with cerebral amyloid angiopathy, not related to parenchymal Aβ deposition (Maier et al., 2014).

Another possibility is that there is a complex relationship between amyloid production, clearance, blood perfusion and neuronal activity: as is demonstrated previously,

neurovascular coupling result in increased CBF where there is more neuronal activity, while the production of Aβ is neuronal activity dependent (Kamenetz et al., 2003a), therefore from this perspective, there could be a positive relationship between CBF and amyloid deposition, mediated by neuronal activity. On the other hand, the clearance of Aβ is partly dependent on cerebral perfusion and subsequent glymphatic drainage (Jessen et al., 2015), and amyloid angiopathies could impair blood flow directly, leading to a negative relationship. Indeed, Mattsson and colleagues have observed both positive and negative relationship between CBF and amyloid deposition in a relatively large cohort from ADNI (Mattsson et al., 2014). The complex biological basis of both positive and negative link between amyloid production/clearance and CBF may have obscured the overall observation between amyloid pathology and perfusion in the current Aβ+ cohort. In later stage of the disease (AD group), amyloid and NFT load were associated with decreased CBF in temporal lobe. This may suggest that in later stage of the disease, the negative impact of amyloid and tau pathology on cerebral perfusion are more propound compared to neuroinflammation.

One of the more interesting findings from the current study is that neuroinflammation has a negative relationship with cerebral perfusion, which overlaps with its positive influence on neuronal activity. While the exact causal relationship between neuroinflammation and hypo-perfusion in AD is still debated, it is possible that these two events forms a deleterious spiral (Zlokovic, 2011b) . More specifically, it has been demonstrated that hypoxia can cause neuroinflammation directly via hypoxia-inducible factor-1α (HIF-1α) pathways (Raz, Knoefel, & Bhaskar, 2016). On the other hand, the inflammatory response may influence the endothelial and smooth muscle cells, which may lead to impaired vascular response to physiological demands (Toth, Tarantini, Csiszar, & Ungvari, 2017). Moreover, it has been demonstrated in the previous chapters that neuroinflammation is associated with abnormally increased neuronal activity. This may be suggestive that neuroinflammation bridges the

imbalance between increased demand (neuronal activity) and deficient supply (cerebral blood flow). It is possible that neuroinflammation is introducing a recipe towards further oxidative stress, neuronal dysfunction and degeneration. Therefore, the current study provide evidence that management of cerebrovascular risk factors and intervention targeting neuroinflammation should be considered in new disease modifying strategies on AD prevention and treatment.

Chapter 6. Using Imaging Biomarkers of AD to Predict Cognitive Decline in MCI and AD Patients

6.1 Introduction and aim of the project

In the previous chapters, the complex relationship between amyloid, neuroinflammation and brain's structural and functional biomarkers in AD was explored and discussed. The independent association between neuroinflammation and disruption of brain's connectivity has been demonstrated. It could be therefore postulated, based on our clinical cross-sectional analysis and preclinical evidence, that neuroinflammation may contribute to brain dysfunction and cognitive decline in AD. However, the causal relationship between neuroinflammation and cognitive impairment remains to be established. To interrogate whether the causal relationship does exist, the available longitudinal neuropsychological assessments data were collected, and the baseline imaging markers were used to predict each individual's cognitive trajectory.

In the current chapter, the predictive values of imaging markers of amyloid deposition, NFT pathology, neuronal damage (according to the A/T/N framework), as well as neuroinflammation, were comprehensively analysed. The aim of the current analysis was firstly, evaluate these imaging markers for predicting prognosis in clinical practice; second but more importantly, deepen our understanding of the causal factors of disease thus sheds light on disease modifying avenues.

6.2 Methods

6.2.1 Available Data

8 AD and 24 MCI patients had baseline ^{11}C-PBR28, ^{18}F-Flutemetamol, T1-weight MRI, rs-fMRI, DTI scans and had baseline and at least one follow-up neuropsychological assessments. Of these patients, 5 AD and 19 MCI patients had more than 1 year of follow-up period. Considering only the MCI cohort had reasonable sample size, the MCI cohort was defined as the main cohort for the following analyses. The combined cohort was also used for exploratory purposes.

6.2.2 Neuropsychological Assessments

The neuropsychological tests performed in the current study include: Mini-mental state examination (MMSE), national adult reading test (NART), Rey–Osterrieth complex figure test (Rey), Wechsler memory scale–logical memory (WLM); Hopkins verbal learning test (Hopkins), verbal fluency test, semantic fluency test, trails making test, digit-symbol coding, digit span, letter-number sequencing (LNS), hospital anxiety and depression scale (HADS).

6.2.3 Model the longitudinal cognitive change

Of all neuropsychological tests, MMSE was used as a simple measure of overall cognition assessment across multiple cognitive domains. The other tests were selectively used to generate a composite score of cognition status using PCA. The selection criteria of individual test entry were: (1) they are used to reflect certain domain(s) of cognition; (2) there are less than 5% data missing in the current cohort.

WLM immediate recall, WLM delayed recall, Hopkins immediate recall total score, Hopkins delayed recall, Hopkins recognition index, semantic fluency, verbal fluency, digit span, LNS, trails making test A were selected for computing the composite cognition score. Other than NART and HADS which are not used to evaluate cognition status, the main reason for

excluding entries was missing data. The missing data in selected entries were imputed using factorial analysis which considers its relationship with other entries as well as the individual's score on other entries. The imputation was completed on SPSS.

Following the imputation, a principal component analysis was performed using the complete dataset and the first principal component (cognition-PC1) was used as a composite measure of overall cognition status. In order to improve the interpretability of PCA results, a varimax rotation was applied. This process rotates the coordinate system of PCs to maximise the variance shared among variables. This will eventually simplify the loadings of variables on PCs, forcing them to take either rather high or rather low loading on a PC, thus enabling us to tell upon which PC a variable load on. To make sure the cognition-PC1 was a reasonable measure of cognition, its correlation with MMSE score was examined.

To model the longitudinal change of cognition in the patients, a linear growth model was applied to fit the time points of each participant. Because the follow-up intervals in the current cohort were not uniform, i.e., the participants were revisited at somewhat random intervals, I did not use existing packages for latent growth modelling such as 'lavaan', as they often assume uniform intervals between measures. Instead, for each participant, the time of baseline visit was defined as zero, and the actual interval in years was calculated for each subsequent visit. The resulting time-score series were then used to compute the analytical solution for linear regression, giving the intercept and slope of cognitive change for each participant, which reflect the initial and annual change of cognitive performance. A simple linear growth model was used because there were limited data points for each individual to model, and therefore introducing more terms may cause overfitting.

The intercepts and slopes of MMSE and cognition-PC1were further used as dependent variables in further analysis.

6.2.4 Imaging Biomarkers to Predict Cognitive Change

Imaging markers of β-amyloid deposition, NFT pathology, neuroinflammation, grey matter atrophy, structural network integrity and functional connectivity was included as candidates for predicting current cognitive performance and longitudinal cognitive change in the patients. To represent overall severity of the pathologies, the PET tracers' uptake in left and right frontal, temporal, parietal, occipital lobes plus anterior and posterior cingulate cortices were sampled, and a PCA was performed for dimensionality reduction. For ^{18}F-AV1451 and ^{11}C-PBR28, the first two principal components were used in further analysis, while for ^{18}F-Flutemetamol only the first PC had an eigenvalue greater than one, so only the first PC was included in further analysis.

To evaluate the severity of grey matter atrophy, several metrics were included from volumetric and surface-based analysis on T1-weighted MRI scan using FreeSurfer: the average cortical thickness and cortical grey matter volume as measures of overall grey matter integrity, the hippocampal volume and first 2 principal components of cortical thickness in temporal ROIs as measures of Alzheimer's prone region's grey matter integrity. The temporal ROIs included: left and right superior, middle, and inferior temporal gyri, banks of the superior temporal sulcus, fusiform gyrus, transverse temporal gyrus, entorhinal cortex, temporal pole and parahippocampal gyrus.

Structural network integrity was measured by the first 2 principal components of FA values of association fibres in ICBM-DTI-based white-matter atlas, including the genu, body and splenium of corpus callosum, left and right inferior longitudinal fasciculus, inferior fronto-occipital fasciculus, superior longitudinal fasciculus, superior fronto-occipital fasciculus, uncinate fasciculus, fornix, cingulate and hippocampal part of cingulum bundle, and tapetum.

Functional connectivity measures were computed using graph theory analysis as described previously in chapter 3. The network's clustering coefficient, global efficiency, local efficiency and small-worldness were included as independent variables in further analysis.

6.2.5 Selection of Predictors for Current Cognitive Performance and Longitudinal Cognitive Change

To evaluate the diagnostic and prognostic value of the imaging biomarkers, the imaging measures underwent a 2-step selection procedure.

In the first step, the imaging markers were used as independent variables individually in univariate regression analysis to predict the baseline (intercepts) and longitudinal change (slopes) of cognitive performance measures. Age was controlled for as covariate of no interest in analyses on intercepts and slopes, and intercepts were also controlled in analysis on slopes, as there were significant correlations between slopes and intercepts.

The imaging biomarkers found to be significant predictors of cognitive performance in the first step were further included in further multiple regression analyses (step 2). The aim of step 2 was to select the best imaging biomarkers for predicting the prognosis of a patient. Therefore, a backward selection procedure was applied in the step 2 multiple regression analysis. Briefly, all independent variables were included in the first regression model against the dependent variable. Next, the least significant independent variable was excluded from the model, and a new simpler regression model was evaluated. The adjusted R-squared values (with the number of IVs penalised to prevent overfitting) of the new model was compared against that of the previous model, and if the simpler model had better fit, the newer model would be considered as better model and a new iteration would be initiated. The process would terminate when the adjusted R-squared value of the new model was worse than that of the previous one, indicating the variable should not have been excluded, and the previous model would be the final model of the analysis. The aim of these analytical steps was to

select the most important (significant) markers out of all candidates that could best predict disease progression.

The whole process of analysis is summarised in figure 6.1.

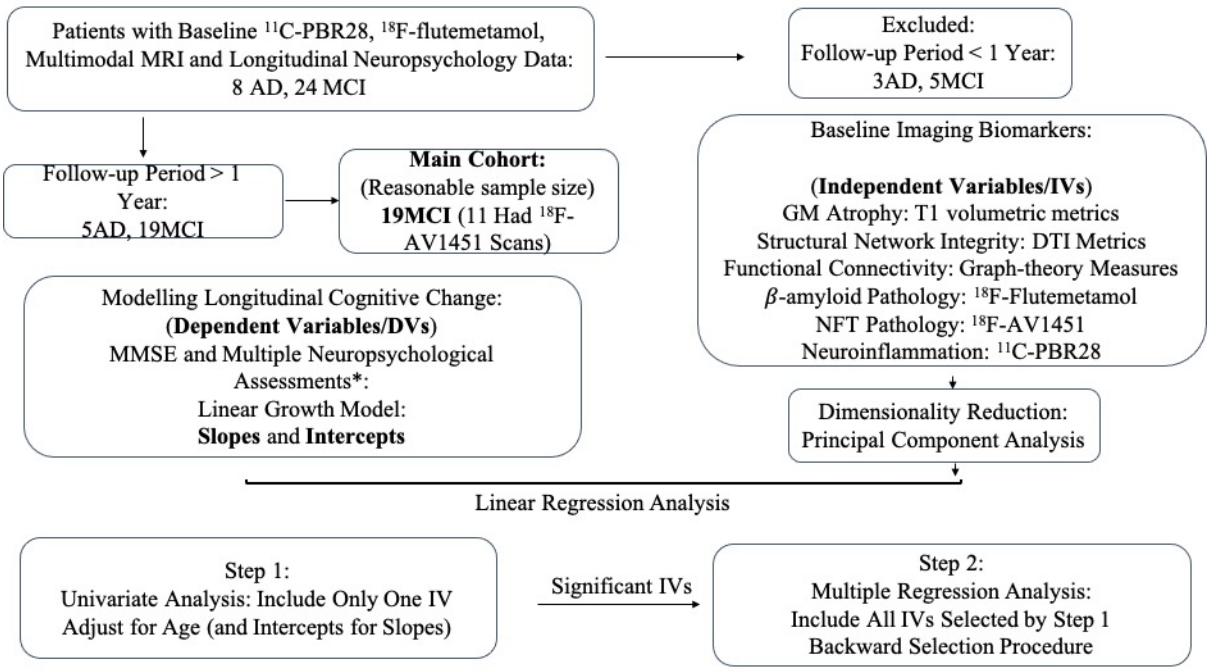

Figure 6.1. Flow diagram of the analysis process.

6.3 Results

6.3.1 Baseline characteristics of patients

The MCI patients had an average age of 70.3 (SD=9.3, minimum=53, maximum=84), baseline MMSE of 28.2 (SD=1.8, minimum=24, maximum=30). The average follow-up duration was 2.8 years (SD=1.3 years, with minimum follow-up duration of 1.1 year, and maximum follow-up period of 4.8 years).

The average age of AD patients was 73.2 (SD=96.2, minimum=65, maximum=79), average baseline MMSE was 23.5 (SD=2.2, minimum=20, maximum=26). The average follow-up

duration was 1.2 years (SD=1.6 year, with minimum follow-up duration of 1.2 year, and maximum follow-up period of 2.5 years).

6.3.2 Principal component analysis of neuropsychological scores

PCA on the selected neuropsychological tests identified two PCs with eigenvalues greater than 1. The first PC is more heavily loaded by memory test scores while the second one has more weights on verbal fluency, letter-number sequencing and digit span (table 6.1 and figure 6.2), suggesting cognition PC1 might be more associated with memory domain. The PC1 explained 39.3% of total variance, while PC2 explained 26.7% of variance.

Table 6.1 Component Loadings of Composite Cognition (Varimax Rotated)

	Loadings on Components	
Test Name	1	2
WLM imm story recall	.854	.312
WLM Del story recall	.888	.242
Hopkins Imm	.658	.475
Hopkins Del	.782	.221
Hopkins RI	.813	.323
Semantic Fluency	.617	.330
Verbal Fluency	.271	.717
Digit span	.160	.872
LNS	.370	.725
Trails A	-.298	-.473

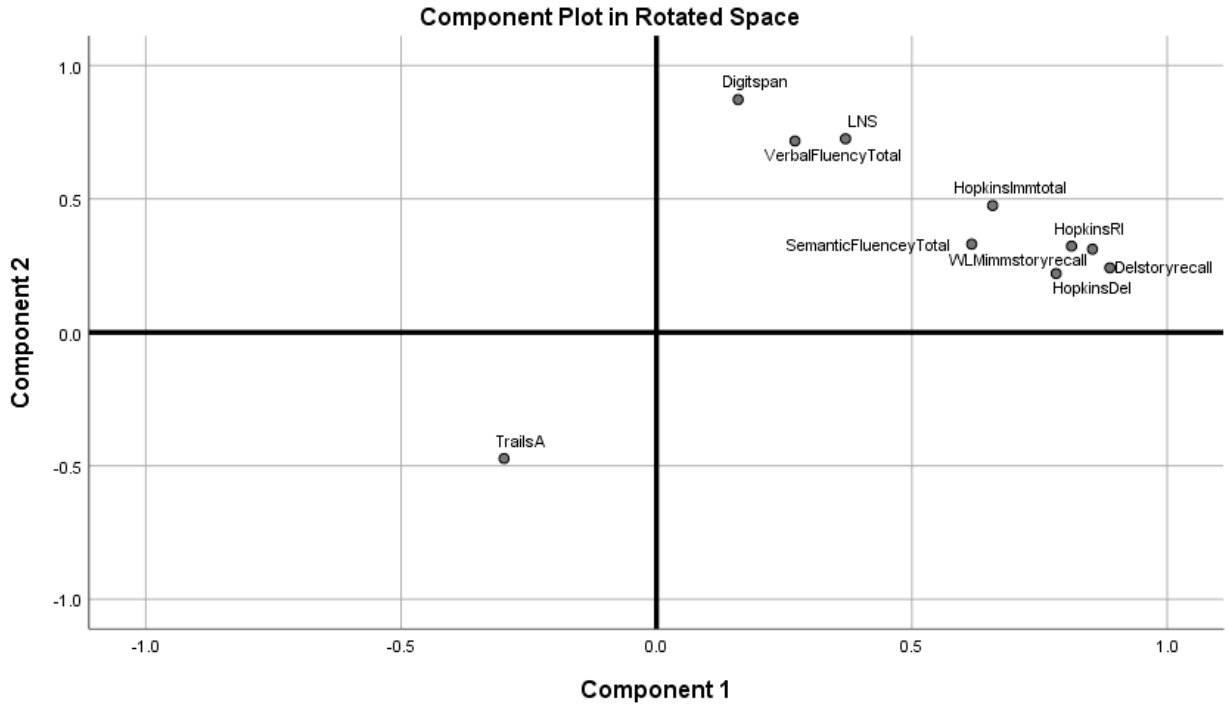

Figure 6.2 Component Plot of PCA on Cognitive Tests

To validate the composite cognitive scores, the correlation between the principal components and MMSE scores was tested. Both PC1 and PC2 had strong correlation with MMSE (Pearson's R=0.561 and 0.495, P=1.8×10^{-13} and 2.2×10^{-10}, Spearman's rho=0.538 and 0.517, P=2.4×10^{-12} and 2.2×10^{-11}, respectively) However, to simplify further analysis, and considering the fact that PC1 is more weighted by memory domain, only PC1 and MMSE were used in further modelling of cognitive trajectory and regression analyses as dependent variables.

6.3.3 Longitudinal cognitive change in patients

The longitudinal cognitive change of AD and MCI patients are demonstrated in figure 6.3.

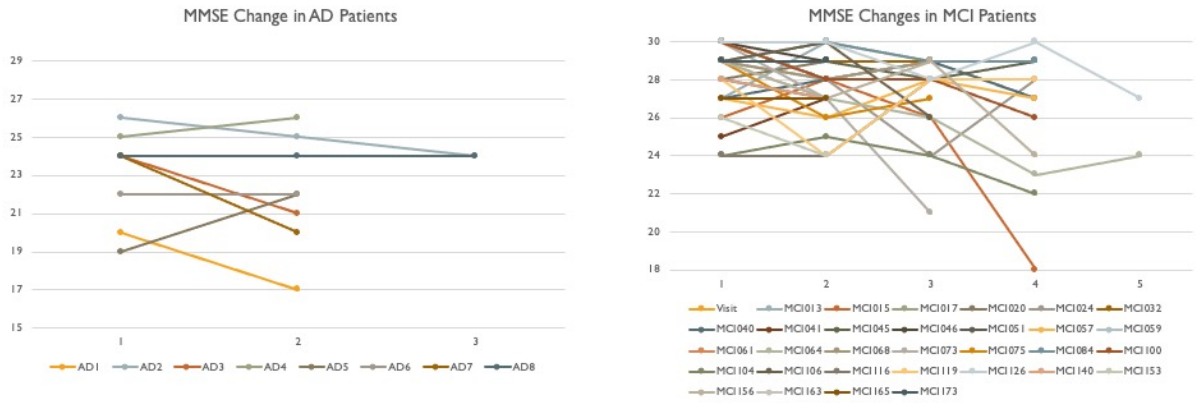

Figure 6.3 Trajectory of cognitive change in cognitively impaired patients

6.3.4 Linear growth model of cognitive change in patients

The mean intercepts of MMSE trajectory were 28.1 in MCI patients and 23.5 in AD patients (mean baseline raw MMSE score were 28.2 and 23.5, respectively), and the mean slopes of MMSE were -0.52 $year^{-1}$ and -0.74 $year^{-1}$ in MCI and AD patients.

The mean intercepts of cognition-PC1 trajectory were 0.11 in MCI patients and -0.88 in AD patients (mean baseline raw cognition-PC1 were 0.10 and -0.88, respectively), and the mean slopes of cognition-PC1 were -0.06 $year^{-1}$ and -0.22 $year^{-1}$ in MCI and AD patients.

There was good correlation between measured baseline cognition scores and fitted intercepts (Pearson's correlation between baseline MMSE and MMSE intercept was R=0.96, P<0.0001, between baseline cognition-PC1 and cognition PC1 intercept was R=0.983, P<0.0001), suggesting a sufficient fit using linear model.

6.3.5 Principal component analysis of ^{11}C-PBR28 uptake

PCA of ^{11}C-PBR28 uptake in main ROIs identified 2 PCs with eigenvalues >1. The first components had more weight on frontal, parietal and cingulate cortices, while the second PC is more weighted by temporal ^{11}C-PBR28 uptake (table 6.2 and figure 6.4). PC1 explained 65.4% of total variance, while PC2 explained 24.2% of variance.

Table 6.2 Component Loadings of ^{11}C-PBR28 Uptake

ROI	Loadings on Components 1	2
Frontal (L)	.912	.282
Frontal (R)	.944	.237
Temporal (L)	.229	.913
Temporal (R)	.114	.951
Parietal (L)	.971	.168
Parietal (R)	.955	.158
Occipital (L)	.760	.510
Occipital (R)	.761	.432
Anterior Cingulate	.900	.200
Posterior Cingulate	.964	.052

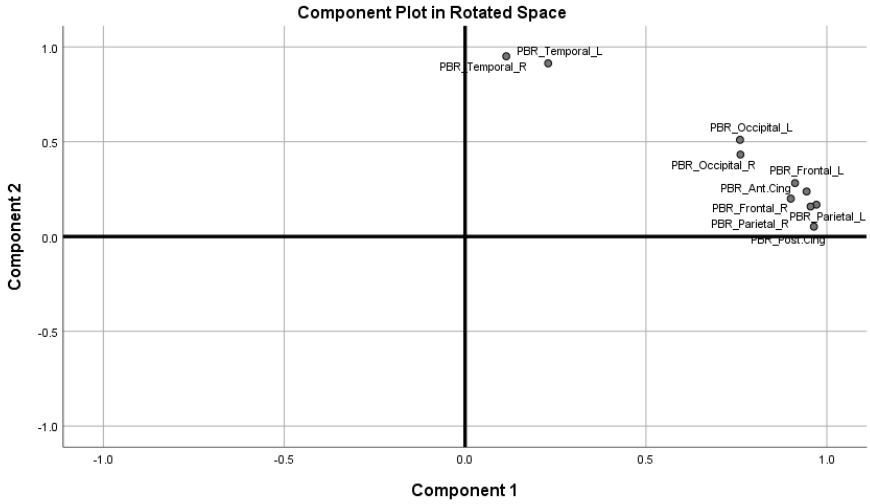

Figure 6.4 Component Plot of PCA on ^{11}C-PBR28 Uptake

6.3.6 Principal component analysis of ^{18}F-AV1451 uptake

PCA of ^{18}F-AV1451 uptake in main ROIs identified 2 PCs with eigenvalues >1. The first components had more loadings from frontal, parietal and occipital and posterior cingulate

tracer uptake, while the second PC is more weighted by temporal and anterior cingulate cortices (table 6.3 and figure 6.5). PC1 explained 56.9% of total variance, while PC2 explained 34.0% of variance.

Table 6.3 Component Loadings of ^{18}F-AV1451 Uptake

	Loadings on Components	
ROI	1	2
Frontal (L)	.783	.568
Frontal (R)	.704	.633
Temporal (L)	.527	.766
Temporal (R)	.541	.751
Parietal (L)	.856	.488
Parietal (R)	.920	.328
Occipital (L)	.912	.292
Occipital (R)	.915	.215
Anterior Cingulate	.125	.962
Posterior Cingulate	.865	.345

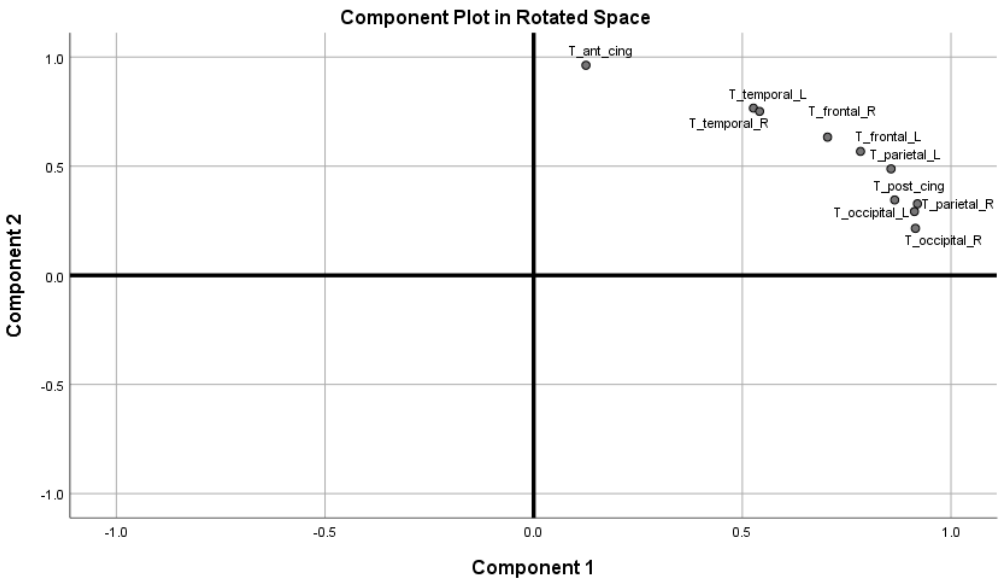

Figure 6.5 Component Plot of PCA on ^{18}F-AV1451 Uptake

6.3.7 Principal component analysis of ^{18}F-Flutemetamol uptake

PCA of ^{18}F-Flutemetamol uptake in main ROIs identified only one PC with eigenvalue >1, which is rather equally weighted by tracer uptake in all ROIs (table 6.4). This could be due to the global deposition pattern of amyloid in human cortex. This PC explained 96.3% of total variance.

Table 6.4 Component Loadings of ^{18}F-Flutemetamol Uptake

ROI	Loadings on Component
Frontal (L)	.986
Frontal (R)	.991
Temporal (L)	.976
Temporal (R)	.978
Parietal (L)	.995
Parietal (R)	.991
Occipital (L)	.955
Occipital (R)	.986
Anterior Cingulate	.967
Posterior Cingulate	.991

6.3.8 Principal component analysis of FA values

PCA of FA values in main association fibres identified 2 PCs with eigenvalues >1. The first components had more loadings from tapetum, cingulum, and fornix, while the second PC is more weighted by uncinate fasciculi and superior longitudinal fasciculi (table 6.5 and figure 6.6). PC1 explained 28.7% of total variance, while PC2 explained 24.5% of variance.

Table 6.5 Component Loadings of Tract FA Values

TOIs	Loadings on Components 1	2
corpus callosum Genu	.619	.541
corpus callosum body	.422	.542
corpus callosum splenium	.615	.512
fornix	.748	.066
cingulate gyrus R	.695	.406
cingulate gyrus L	.711	.511
superior longitudinal fasciculus R	.048	.687
superior longitudinal fasciculus L	.080	.753
superior frontal-occipital fasciculus R	.272	-.112
superior frontal-occipital fasciculus L	.134	.400
Uncinate fasciculus R	-.012	.799
Uncinate fasciculus L	-.051	.804
tapetum R	.663	.019
tapetum L	.758	-.061
fornix (cres) /stria terminalis R	.755	.136
fornix (cres) /stria terminalis L	.647	.338

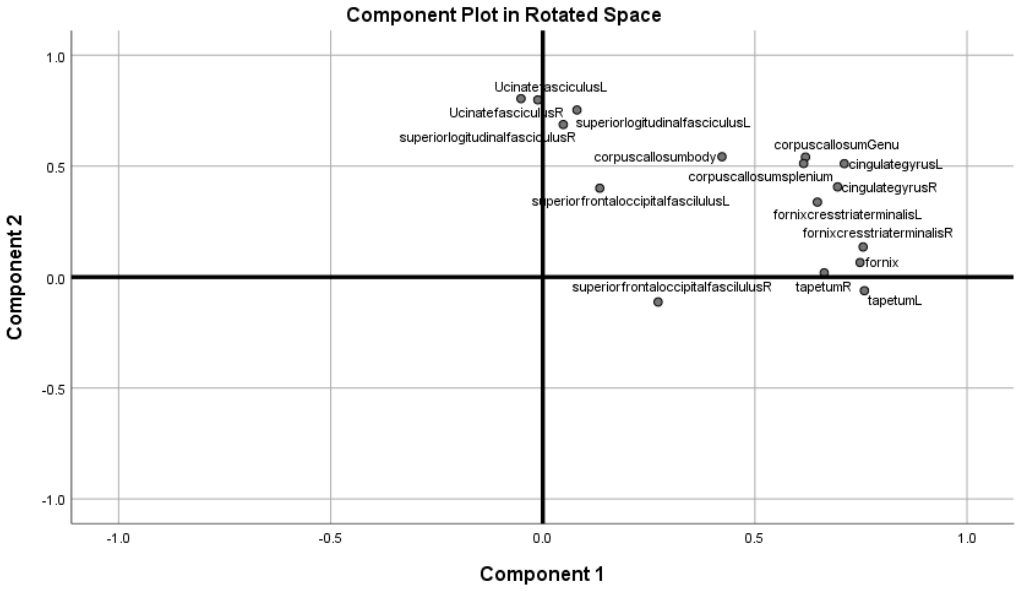

Figure 6.6 Component Plot of PCA on Tract FA Values

6.3.9 Principal analysis of T1 surface-based measures

PCA of cortical thickness in temporal ROIs identified 2 PCs with eigenvalues >1. The first components had more loadings from entorhinal cortex, parahippocampal, inferior temporal, and middle temporal gyri, while the second PC is more weighted by superior temporal regions (table 6.6 and figure 6.7). PC1 explained 38.3% of total variance, while PC2 explained 19.8% of variance.

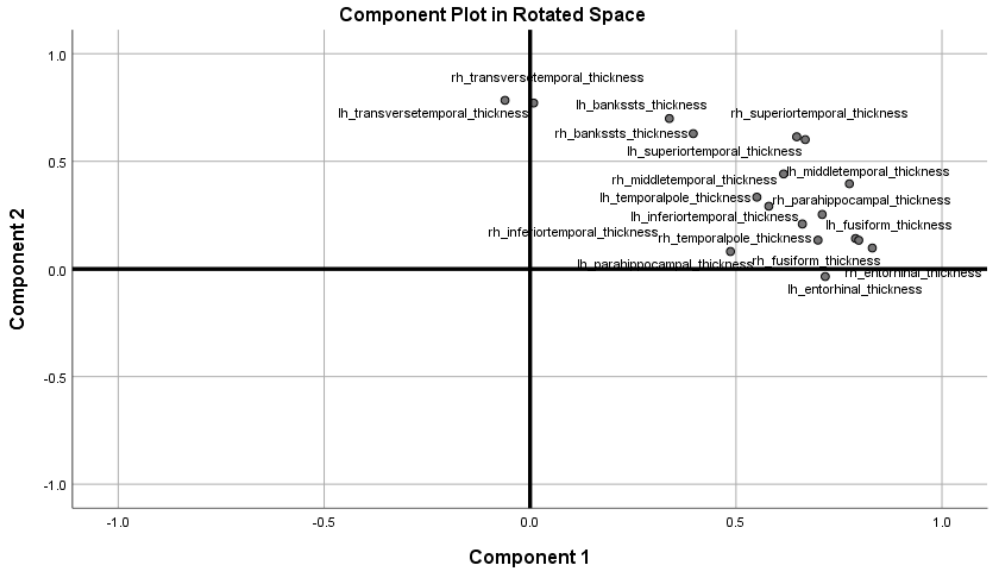

Figure 6.7 Component Plot of PCA on Temporal cortical Thickness measures

Table 6.6 Component Loadings of Temporal Cortical Thickness Measures

	Loadings on Components	
	1	2
lh_bankssts_thickness	.338	.699
lh_entorhinal_thickness	.717	-.035
lh_fusiform_thickness	.790	.141
lh_inferior temporal_thickness	.709	.253
lh_middle temporal_thickness	.616	.441
lh_parahippocampal_thickness	.486	.081
lh_superior temporal_thickness	.647	.614
lh_temporal pole_thickness	.551	.333
lh_transverse-temporal_thickness	-.061	.783
rh_bankssts_thickness	.396	.629
rh_entorhinal_thickness	.831	.097
rh_fusiform_thickness	.798	.133
rh_inferior temporal_thickness	.661	.209
rh_middle temporal_thickness	.775	.396
rh_parahippocampal_thickness	.580	.292
rh_superior temporal_thickness	.668	.601
rh_temporal pole_thickness	.699	.134
rh_transverse-temporal_thickness	.009	.771

6.3.10 Predicting baseline cognitive performance in MCI cohort

Univariate analysis (controlling for age) showed that in MCI cohort, only FA PC2 had positive association with the MMSE intercept (standardised β=0.49, P=0.016), while the association between FA PC1 and MMSE intercept was marginal (standardised β=0.42, P=0.055, table 6.7). Backward model selection using multiple linear regression method confirmed that FA PC2 was the only and best predictor of MMSE intercept (table 6.11).

Using cognition-PC1 as independent variable, univariate analysis (controlling for age) in MCI cohort found ^{18}F-AV1451 PC2 was significantly associated with lower cognition PC score (N=11, standardised β=-0.67, P=0.014, table 6.8), while ^{11}C-PBR28 PC2 and FA PC1 were marginally associated with cognition-PC1 intercept (standardised β=-0.42, P=0.067 and

standardised β=-0.41, P=0.064, respectively, table 6.8). Backward model selection from age, ^{11}C-PBR28 PC2 and FA PC1 (N=19) found ^{11}C-PBR28 PC2 to be the only and best predictor for cognition-PC1. Adding ^{18}F-AV1451 PC2 to the selection (N=11), both ^{11}C-PBR28 PC2 and ^{18}F-AV1451 PC2 were selected in the best prediction model for cognition-PC1.

6.3.11 Predicting longitudinal cognitive decline in MCI cohort

In MCI cohort, univariate regression analysis (controlled for age and intercept) found that ^{18}F-AV1451 PC1 (N=11, standardised β=-0.40, P=0.049), ^{11}C-PBR28 PC2 (standardised β=-0.48, P=0.01), ^{11}C-PBR28 MTL (standardised β=-0.50, P=0.005), ^{18}F-Flutemetamol PC1 (standardised β=-0.56, P=0.001, table 6.9) were individually associated with annual decline of MMSE (slope). Model selection with age, MMSE intercept, ^{11}C-PBR28 PC2, ^{11}C-PBR28 MTL and ^{18}F-Flutemetamol identified ^{11}C-PBR28 MTL and ^{18}F-Flutemetamol PC1 in the best prediction model. Adding ^{18}F-AV1451 PC1 into the selection (N=11) result in the final model containing only ^{11}C-PBR28 PC2 (table 6.12).

Using the cognition-PC1 as dependent variable, univariate regression analysis (controlled for age and intercept) showed that ^{18}F-AV1451 PC1 (N=11, standardised β=-0.972, P=0.026), ^{11}C-PBR28 PC2 (standardised β=-0.48, P=0.008) and ^{11}C-PBR28 MTL (standardised β=-0.50, P=0.004, table 6.10) were individually associated with annual decline of cognition-PC1 (slope). Model selection with age, cognition-PC1 intercept, ^{11}C-PBR28 PC2 and ^{11}C-PBR28 MTL identified ^{11}C-PBR28 PC2 in the best prediction model. Adding ^{18}F-AV1451 PC1 into the selection (N=11), the final model contained both ^{11}C-PBR28 PC2 and ^{18}F-AV1451 PC1 (table 6.12).

Table 6.7 Univariate Regression Analysis on Baseline MMSE and Imaging Biomarkers

MCI Cohort

			Independent Variable		
Dependent Variable	Covariate(s)	Marker Category	Name	Standardized β	P
MMSE Intercept	Age	Amyloid	^{18}F-Flutemetamol_PC1	0.173	0.44
		NFT	^{18}F-AV1451_PC1	0.257	0.41
			^{18}F-AV1451_PC2	0.31	0.33
			^{18}F-AV1451_MTL	0.275	0.41
		Neuroinflammation	^{11}C-PBR28 PC1	-0.346	0.14
			^{11}C-PBR28 PC2	-0.076	0.75
			^{11}C-PBR28 MTL	0.219	0.36
		Grey Matter Atrophy	Hippocampal Volume	0.083	0.7
			Cortical GM volume	0.051	0.8
			Average Cortical Thickness	0.077	0.71
			Temporal Thickness PC1	-0.131	0.53
			Temporal Thickness PC2	0.241	0.24
		Structural Network	***FA Values PC1***	0.422	0.055#
			FA Values PC2	0.488	0.016*
		Functional Connectivity	Global Efficiency	-0.357	0.093
			Local Efficiency	0.039	0.86
			Small-worldness	-0.27	0.19

Table 6.8 Univariate Regression Analysis on Baseline Composite Cognition Score and Imaging Biomarkers

MCI Cohort

			Independent Variable		
Dependent Variable	Covariate(s)	Marker Category	Name	Standardized β	P
Cognition PC1 Intercept	Age	Amyloid	^{18}F-Flutemetamol_PC1	-0.185	0.41
		NFT	**^{18}F-AV1451_PC1**	-0.61	0.014*
			^{18}F-AV1451_PC2	-0.416	0.12
			^{18}F-AV1451_MTL	-0.195	0.51
		Neuroinflammation	***^{11}C-PBR28 PC1***	-0.422	0.067#
			^{11}C-PBR28 PC2	-0.301	0.2
			^{11}C-PBR28 MTL	-0.321	0.17
		Grey Matter Atrophy	Hippocampal Volume	0.226	0.29
			Cortical GM volume	0.153	0.46
			Average Cortical Thickness	-0.008	0.97
			Temporal Thickness PC1	-0.069	0.74
			Temporal Thickness PC2	0.324	0.11
		Structural Network	***FA Values PC1***	0.411	0.064#
			FA Values PC2	0.309	0.15
		Functional Connectivity	Global Efficiency	-0.225	0.3
			Local Efficiency	0.169	0.43
			Small-worldness	0.102	0.64

Table 6.9 Univariate Regression Analysis on MMSE Annual Change and Imaging Biomarkers

MCI Cohort

			Independent Variable		
Dependent Variable	Covariate(s)	Marker Category	Name	Standardized β	P
MMSE Slope	Age	Baseline cognition	MMSE Intercept	-0.567	0.002*
	Age, MMSE Intercept	Amyloid	**^{18}F-Flutemetamol_PC1**	-0.555	0.001*
		NFT	**^{18}F-AV1451_PC1**	-0.395	0.049*
			^{18}F-AV1451_PC2	-0.35	0.089
			^{18}F-AV1451_MTL	-0.29	0.192
		Neuroinflammation	^{11}C-PBR28 PC1	-0.02	0.92
			^{11}C-PBR28 PC2	-0.476	0.011*
			^{11}C-PBR28 MTL	-0.503	0.005*
		Grey Matter Atrophy	Hippocampal Volume	0.173	0.34
			Cortical GM volume	0.135	0.43
			Average Cortical Thickness	0.254	0.13
			Temporal Thickness PC1	0.138	0.43
			Temporal Thickness PC2	0.273	0.12
		Structural Network	FA Values PC1	0.037	0.86
			FA Values PC2	0.278	0.17
		Functional Connectivity	Global Efficiency	-0.109	0.58
			Local Efficiency	-0.261	0.14
			Small-worldness	-0.181	0.33

Table 6.10 Univariate Regression Analysis on Composite Cognition Score Annual Change and Imaging Biomarkers

MCI Cohort

			Independent Variable		
Dependent Variable	Covariate(s)	Marker Category	Name	Standardized β	P
Cognition PC1 slope	Age	Baseline cognition	Cognition_PC1_Intercept	-0.44	0.024*
	Age, PC1 Intercept	Amyloid	^{18}F-Flutemetamol_PC1	-0.102	0.62
		NFT	**^{18}F-AV1451_PC1**	-0.972	0.026*
			^{18}F-AV1451_PC2	-0.062	0.88
			^{18}F-AV1451_MTL	-0.144	0.71
		Neuroinflammation	^{11}C-PBR28 PC1	-0.308	0.14
			^{11}C-PBR28 PC2	-0.511	0.004*
			^{11}C-PBR28 MTL	-0.495	0.008*
		Grey Matter Atrophy	Hippocampal Volume	0.026	0.9
			Cortical GM volume	-0.022	0.91
			Average Cortical Thickness	0.166	0.37
			Temporal Thickness PC1	0.09	0.64
			Temporal Thickness PC2	0.169	0.4
		Structural Network	FA Values PC1	-0.352	0.104
			FA Values PC2	0.072	0.72
		Functional Connectivity	Global Efficiency	0.02	0.92
			Local Efficiency	-0.173	0.37
			Small-worldness	-0.07	0.72

Table 6.11 Multiple Regression on Baseline Cognition and Model Selection

MCI Cohort

Dependent Variable	Name	Independent Variable Standardized β	P
MMSE Intercept	Age	-	-
	FA Values PC2	0.457	0.022*
Cognition PC1 Intercept	Age	-	-
	FA Values PC1	-	-
	^{11}C-PBR28 PC1	-0.474	0.041*
Cognition PC1 Intercept	Age	-	-
	FA Values PC1	-	-
	^{11}C-PBR28 PC1	-0.686	0.005*
	^{18}F-AV1451_PC1	-0.773	0.003*

Table 6.12 Multiple Regression on Longitudinal Cognition Change and Model Selection

MCI Cohort

		Independent Variable	
Dependent Variable	Name	Standardized β	P
MMSE Slope	MMSE Intercept	-0.373	0.022*
	Age	-	-
	^{18}F-Flutemetamol_PC1	-0.44	0.009*
	^{11}C-PBR28 MTL	-0.385	0.02*
	^{11}C-PBR28 PC2	-	-
MMSE Slope	MMSE Intercept	-0.809	0.001*
	Age	-	-
	^{18}F-Flutemetamol_PC1	-	-
	^{11}C-PBR28 MTL	-	-
	^{11}C-PBR28 PC2	-0.362	0.024*
	^{18}F-AV1451_PC1	-	-
Cognition_PC1_slope	Cognition_PC1_Intercept	-0.762	0.001*
	Age	-	-
	^{11}C-PBR28 MTL	-	-
	^{11}C-PBR28 PC2	-0.517	0.003*
Cognition_PC1_slope	Cognition_PC1_Intercept	-1.11	0.002*
	Age	-	-
	^{11}C-PBR28 MTL	-	-
	^{11}C-PBR28 PC2	-0.523	0.019*
	^{18}F-AV1451_PC1	-0.854	0.002*

Table 6.13 Univariate Regression Analysis on Baseline MMSE and Imaging Biomarkers

Combined Cohort

			Independent Variable		
Dependent Variable	Covariate(s)	Marker Category	Name	Standardized β	P
MMSE Intercept	Age, Diagnosis	Amyloid	^{18}F-Flutemetamol_PC1	0.081	0.62
		NFT	^{18}F-AV1451_PC1	0.297	0.2
			^{18}F-AV1451_PC2	-0.103	0.68
			^{18}F-AV1451_MTL	0.069	0.81
		Neuroinflammation	^{11}C-PBR28 PC1	-0.143	0.34
			^{11}C-PBR28 PC2	-0.002	0.99
			^{11}C-PBR28 MTL	0.014	0.34
		Grey Matter Atrophy	Hippocampal Volume	0.155	0.38
			Cortical GM volume	0.13	0.4
			Average Cortical Thickness	0.03	0.86
			Temporal Thickness PC1	-0.173	0.23
			Temporal Thickness PC2	0.27	0.08#
		Structural Network	FA Values PC1	0.26	0.075#
			FA Values PC2	0.25	0.065#
		Functional Connectivity	Global Efficiency	-0.2	0.13
			Local Efficiency	-0.095	0.52
			Small-worldness	-0.139	0.46

Table 6.14 Univariate Regression Analysis on Baseline Composite Cognition Score and Imaging Biomarkers

Combined Cohort

			Independent Variable		
Dependent Variable	Covariate(s)	Marker Category	Name	Standardized β	P
Cognition PC1 Intercept	Age, Diagnosis	Amyloid	^{18}F-Flutemetamol_PC1	-0.16	0.45
		NFT	^{18}F-AV1451_PC1	-0.238	0.25
			^{18}F-AV1451_PC2	-0.349	0.11
			^{18}F-AV1451_MTL	-0.234	0.35
		Neuroinflammation	^{11}C-PBR28 PC1	-0.283	0.13
			^{11}C-PBR28 PC2	-0.12	0.57
			^{11}C-PBR28 MTL	-0.243	0.22
		Grey Matter Atrophy	Hippocampal Volume	0.353	0.103
			Cortical GM volume	0.205	0.31
			Average Cortical Thickness	0.105	0.62
			Temporal Thickness PC1	-0.019	0.91
			Temporal Thickness PC2	0.346	0.073#
		Structural Network	**FA Values PC1**	0.396	0.03*
			FA Values PC2	0.203	0.25
		Functional Connectivity	Global Efficiency	-0.182	0.29
			Local Efficiency	-0.128	0.49
			Small-worldness	0.055	0.75

Table 6.15 Univariate Regression Analysis on MMSE Annual Change and Imaging Biomarkers

MCI Cohort

			Independent Variable		
Dependent Variable	Covariate(s)	Marker Category	Name	Standardized β	P
MMSE Slope	Age, Diagnosis	Baseline cognition	MMSE Intercept	-0.465	0.07#
	Age, MMSE Intercept, Diagnosis	Amyloid	**^{18}F-Flutemetamol_PC1**	-0.607	0.005*
		NFT	^{18}F-AV1451_PC1	-0.363	0.2
			^{18}F-AV1451_PC2	-0.35	0.23
			^{18}F-AV1451_MTL	-0.58	0.06#
		Neuroinflammation	^{11}C-PBR28 PC1	-0.25	0.26
			^{11}C-PBR28 PC2	-0.462	0.046*
			^{11}C-PBR28 MTL	-0.736	<0.001*
		Grey Matter Atrophy	Hippocampal Volume	0.374	0.11
			Cortical GM volume	0.144	0.51
			Average Cortical Thickness	0.234	0.3
			Temporal Thickness PC1	0.209	0.29
			Temporal Thickness PC2	0.196	0.39
		Structural Network	FA Values PC1	0.077	0.73
			FA Values PC2	0.153	0.45
		Functional Connectivity	Global Efficiency	0.227	0.25
			Local Efficiency	-0.287	0.16
			Small-worldness	-0.098	0.62

Table 6.16 Univariate Regression Analysis on Composite Cognition Score Annual Change and Imaging Biomarkers

Combined Cohort

			Independent Variable		
Dependent Variable	Covariate(s)	Marker Category	Name	Standardized β	P
Cognition PC1 slope	Age, Diagnosis	Baseline cognition	Cognition_PC1_Intercept	-0.491	0.013*
	Age, Cognition PC1 Intercept Diagnosis	Amyloid	^{18}F-Flutemetamol_PC1	0.029	0.89
		NFT	**^{18}F-AV1451_PC1**	-0.642	0.022*
			^{18}F-AV1451_PC2	-0.442	0.2
			^{18}F-AV1451_MTL	-0.293	0.43
		Neuroinflammation	***^{11}C-PBR28 PC1***	-0.31	0.083#
			^{11}C-PBR28 PC2	-0.419	0.023*
			^{11}C-PBR28 MTL	-0.506	0.004*
		Grey Matter Atrophy	Hippocampal Volume	0.116	0.62
			Cortical GM volume	0.06	0.78
			Average Cortical Thickness	0.186	0.38
			Temporal Thickness PC1	0.143	0.43
			Temporal Thickness PC2	0.127	0.55
		Structural Network	FA Values PC1	-0.25	0.22
			FA Values PC2	0.139	0.45
		Functional Connectivity	Global Efficiency	0.145	0.42
			Local Efficiency	-0.14	0.46
			Small-worldness	-0.036	0.83

Table 6.17 Multiple Regression on Baseline Cognition and Model Selection

Combined Cohort

	Independent Variable		
Dependent Variable	Name	Standardized β	P
MMSE Intercept	Age	-	-
	FA Values PC1	0.219	0.08#
	FA Values PC2	0.207	0.09#
	Temporal Thickness PC2	0.242	0.09#
	Diagnosis (AD)	-0.566	<0.001*
Cognition_PC1_Intercept	Age	-	-
	FA Values PC1	0.353	0.029*
	Temporal Thickness PC2	0.425	0.01*
	Diagnosis (AD)	-	-

Table 6.18 Multiple Regression on Longitudinal Cognition Change and Model Selection

Combined Cohort

	Independent Variable		
Dependent Variable	Name	Standardized β	P
MMSE Slope	MMSE Intercept	-	-
	Age	-	-
	^{18}F-Flutemetamol_PC1	-0.488	0.01*
	^{11}C-PBR28 MTL	-0.645	0.001*
	^{11}C-PBR28 PC2	-	-
	Diagnosis (AD)	0.53	0.006*
MMSE Slope	MMSE Intercept	-0.426	0.012*
	age	-	-
	^{18}F-Flutemetamol_PC1	-	-
	^{11}C-PBR28 MTL	-0.89	<0.001*
	^{11}C-PBR28 PC2	-	-
	^{18}F-AV1451_MTL	-	-
Cognition_PC1_slope	Cognition PC1 Intercept	-0.719	<0.001*
	Age	-	-
	^{11}C-PBR28 MTL	-0.521	0.002*
	^{11}C-PBR28 PC2	-	-
	Diagnosis	-0.5	0.005*
Cognition_PC1_slope	Cognition PC1 Intercept	-	-
	age	-	-
	^{11}C-PBR28 MTL	-0.578	0.024*
	^{11}C-PBR28 PC2	-	-
	Diagnosis	-	-
	^{18}F-AV1451_PC1	-	-

6.3.12 Predicting baseline cognitive performance in combined AD and MCI cohort

Univariate analysis (controlled for age and diagnosis) showed that in combined AD and MCI cohort, there was marginal association between MMSE intercept and temporal cortical thickness PC2(standardised β=0.27, P=0.08), FA PC1 (standardised β=0.26, P=0.065) and FA PC2 (standardised β=0.25, P=0.075, table 6.13). Backward model selection using multiple linear regression method selected all the aforementioned variables in the best model for predicting MMSE intercept, but all the variables individually had marginal significance in the final model (table 6.17).

Using cognition-PC1 as independent variable, univariate analysis (controlled for age and diagnosis) in combined cohort found cognition-PC1 intercept was associated with FA PC1 (standardised β=-0.40, P=0.03), while temporal cortical thickness PC2 weas marginally associated with cognition-PC1 intercept (standardised β=0.35, P=0.07, table 6.14). Backward model selection from age, T1 PC2 and FA PC1 and diagnosis resulted in the final model containing both T1 PC2 and FA PC1 but without age and diagnosis (table 6.17)

6.3.13 Predicting longitudinal cognitive decline in combined AD and MCI cohort

In combined AD and MCI cohort, univariate regression analysis (controlled for age, intercept and diagnosis) found that ^{18}F-AV1451 MTL (standardised β=-0.58, P=0.06), ^{11}C-PBR28 PC2 (standardised β=-0.46, P=0.05), ^{11}C-PBR28 MTL (standardised β=-0.74, P<0.001), ^{18}F-Flutemetamol PC1 (standardised β=-0.61, P=0.005, table 6.15) were individually associated with annual decline of MMSE (slope). Model selection with age, MMSE intercept, diagnosis, ^{11}C-PBR28 PC2, ^{11}C-PBR28 MTL and ^{18}F-Flutemetamol identified diagnosis, ^{11}C-PBR28 MTL and ^{18}F-Flutemetamol PC1 in the best prediction model. Adding ^{18}F-AV1451 MTL into the selection result in the final model containing only ^{11}C-PBR28 MTL (table 6.18).

Using the cognition-PC1 as dependent variable, univariate regression analysis (controlled for age, intercept and diagnosis) showed that ^{18}F-AV1451 PC1 (standardised β=-0.64, P=0.022), ^{11}C-PBR28 PC2 (standardised β=-0.42, P=0.02) and ^{11}C-PBR28 MTL (standardised β=-0.51, P=0.004, table 6.16) were individually associated with annual decline of cognition-PC1 (slope). Model selection with age, cognition-PC1 intercept, diagnosis, ^{11}C-PBR28 PC2 and ^{11}C-PBR28 MTL identified ^{11}C-PBR28 MTL in the best prediction model. Adding ^{18}F-AV1451 PC1 into the selection, the final model contained only ^{11}C-PBR28 MTL (table 6.18).

Overall, the results in both cohorts showed that baseline cognitive performance was most strongly associated with MRI biomarkers of neuronal damage, while the PET biomarkers of amyloid deposition, tau pathology and neuroinflammation together outperformed MRI markers to predict longitudinal cognitive decline.

6.4 Discussion and Conclusions

There has been extensive effort on identifying biomarkers that can predict cognitive decline in AD, MCI and population at risk of AD (Franzmeier, Koutsouleris, et al., 2020) (Betthauser et al., 2020). Various fluid and imaging markers of neuronal damage (including structural and functional markers), amyloid and tau pathologies have been reported to relate to current and longitudinal cognitive performance (Dickerson, Wolk, & Alzheimer's Disease Neuroimaging, 2013; Olsson et al., 2016). However, there is still limited evidence on neuroinflammation and cognitive decline in AD (L. Hamelin et al., 2016; Kreisl et al., 2016a; Malpetti et al., 2020). Further, few studies have comprehensively evaluated the variety of imaging biomarkers head-by-head to evaluate their performance competitively.

In the current chapter, the predictive values of imaging biomarkers for cognitive trajectory in MCI and AD patients were interrogated using linear models. The primary findings have suggested that MRI markers of grey matter and structural network integrity (measured by T1-

weighted and DTI scans) are better associated with cognitive performance at the time point of evaluation, while PET markers of amyloid deposition, tau pathology and neuroinflammation have better predictive value for future cognitive decline. These findings further indicate that current cognitive performance is best explained by the current level of neuronal damage (which is detected by MRI markers), and to an extent irrelevant of specific underlying pathologies. Conversely, it is the underlying pathology that can cause further neuronal damage, but the current level of neuronal damage is not good indicator of future progression, and therefore biomarkers of underlying pathologies are best at predicting disease progression. Indeed, it has been reported that MRI markers of neuronal injury is only predictive of short-term cognition, but long-term cognitive decline is otherwise predicted by amyloid and tau markers (Dickerson et al., 2013).

Interestingly, the DTI marker on white matter microstructural integrity (or structural network integrity) performed better in predicting current cognitive status compared to grey matter measures in MCI cohort (and at least as good as grey matter markers in combined cohort), suggesting that DTI measures might be more sensitive to subtle changes of brain structural network especially at early stage of the disease. This observation is supported by the findings that damage can be detected by DTI at early preclinical stage when grey matter atrophy is not yet obvious (Bendlin et al., 2010) (Y. J. Hong et al., 2016). While functional topology measures were associated with MMSE scores in previous Aβ positive cohort, they did not show good predictive value for current and future cognitive decline in the current analysis, suggesting that functional connectivity measures may not as a stable metric for predicting cognition as structural measures. Indeed, functional connectivity may be more heavily influenced by subject-dependent factors such as movement in scanner even with advanced denoising techniques. Therefore, while functional connectivity remains an interesting target for understanding the brain under physiological and pathological conditions, caution should

be taken when it is considered as single diagnostic marker without accompanying assessments such as structural connectivity and volumetric measures.

The current study has reinforced the predictive value of amyloid and tau markers in AD and MCI patients. In addition to markers of amyloid deposition and NFT pathology, neuroinflammation marker remained most consistently in predictive models for longitudinal decline, which strongly suggest neuroinflammation as an active driver of the disease, rather than a bystander or subsequent (ineffective) response to amyloid deposition and NFT formation. In terms of the spatial properties of neuroinflammation marker, it has been demonstrated that in experiments, ^{11}C-PBR28 uptake in MTL or PC2 was selected in the final model. Considering the fact that PC2 is specifically weighted by temporal uptake (figure 6.3), it can be concluded that neuroinflammation in temporal regions that have the strongest influence on disease progression in AD. In contrast, ^{18}F-AV1451 PC1, which is more equally weighted by tracer uptake across multiple cortices, seemed to perform better compared to ^{18}F-AV1451 MTL uptake in regression models. This may have indicated that the emergence of NFT pathology in the neocortex is better predictor of rapid progression of the disease. This is interesting considering that NFT pathology can be found propagating from locus coeruleus to entorhinal cortex and limbic system in normal aging, but only in neurodegenerative diseases does it emerge in the neocortex (Kaufman, Del Tredici, Thomas, Braak, & Diamond, 2018). It should be therefore noted that NFT PET imaging has the advantage of providing spatial information as compared to fluid markers, which is important in staging of the disease and stratifying patients.

There has been limited evidence on predictive values of neuroinflammation on cognitive trajectory in Alzheimer's continuum, with only few longitudinal studies with TSPO PET reported (L. Hamelin et al., 2016) (Fan et al., 2017) (Hamelin et al., 2018) (Malpetti et al., 2020). While it has been recently reported that CSF sTREM2, a marker of microglial TREM2

signalling, is associated with slower cognitive decline in MCI and AD patients (Ewers et al., 2019), our result together with Malpetti and colleagues (Malpetti et al., 2020) point to a negative impact of neuroinflammation on cognitive decline in AD and MCI patients using PET imaging with ^{11}C-PBR28 and ^{11}C-PK11195 respectively. The reason for the discrepancy between studies using PET imaging and CSF markers might be due to the fact that TREM2 pathway could modulate pro-inflammatory response of microglia and upregulate phagocytosis (Gratuze, Leyns, & Holtzman, 2018). In other words, while PET imaging with TSPO tracers cannot differentiate the phenotypes of microglia, TREM2 activation markers may reflect the balance between anti-inflammatory and pro-inflammatory phenotypes of microglia in the spectrum of microglial activation. The inability of TSPO tracers to distinguish microglial phenotypes (and even between activated microglia, astrocytes and macrophages), may have also led to conflicting findings of imaging studies on different cohorts (Fan et al., 2017) (Hamelin et al., 2018): while in symptomatic stage of AD the majority of activated microglia are on the pro-inflammatory side of cell fate, and the overall quantification by TSPO tracers may well reflect neuroinflammation, at early stages of pathogenesis where the population of proinflammatory phenotypes is not overwhelming, the PET quantification may be difficult to interpret. In light of this, CSF markers of sTREM2 and PET may supplement each other and form a good pair of biomarkers for comprehensive evaluation of microglial activation/neuroinflammation. Therefore, further studies with regard to the relationship between sTREM2 and TSPO markers at different stages of the disease, and whether a weighted measure of sTREM2 and TSPO can better predict cognition/neuronal injury are strongly encouraged. On the other hand, based on current evidence, the approach of intervention targeting neuroinflammation should be carefully considered as inappropriate manipulation of glial phenotypes may cause more destruction than protection.

To summarise, the current analysis has identified MRI imaging markers on neuronal damage to be most closely related to cognition at the point of assessment, while PET markers of amyloid deposition, NFT pathology and neuroinflammation are strongly predictive for disease deterioration in clinical diagnosed AD and MCI patients. The current study highlighted the value of PET markers in disease diagnosis and evaluating the risk of disease progression and provide evidence that neuroinflammation is indeed a causal factor of disease progression.

Chapter 7. Conclusions and Future Directions

The current project has firstly interrogated the feasibility of using SUVR in ^{11}C-PBR28 quantification and more importantly, investigated: (1) the association between neuroinflammation and brain connectivity; (2) the association between neuroinflammation and cerebral blood perfusion; (3) the predictive value of imaging biomarkers regarding longitudinal cognitive decline in AD and MCI patients.

I should note that the current project is based on the data from "Amyloid and Neuroinflammation" study, and I acknowledge Dr Dani and Dr Edison for their effort in patient recruitment and clinical/imaging data acquisition. The focus of current project is to provide biological insights into the role of neuroinflammation and amyloid deposition in AD by analysing multimodality imaging data. While previous studies have discovered brain connectivity disruption and neuroinflammation in AD patients, there is limited evidence on their relationship. Further, whether neuroinflammation actively contribute to disease progression is still under debate because of limited observations from longitudinal studies. The current project aimed to bridge the gap of current knowledge by multimodal imaging analysis. Apart from imaging processing, the current project tried to manage high-dimensional data both at single modality level and across multiple imaging modalities using multivariate statistical methods such as principal component analysis, independent component analysis, graph theory and canonical correlation analysis with regularisation. By this approach, the current project has provided novel evidence suggesting that neuroinflammation plays an active role in cognitive impairment and that one of the possible mechanism is by causing brain connectivity disruption.

The quantification of second generation TSPO tracers, in particular ^{11}C-PBR28 has always been challenging in clinical imaging studies, mainly due to its high inter-subject variability

even after accounting for the TSPO 147 Ala/Thr polymorphism (Collste et al., 2016). This problem has undermined the statistical power of clinical imaging studies, which generally have limited number of participants due to cost and recruitment issues, and has led to practice of using relative measures (DVR and SUVR) to control for variability due to individual factors (Dickstein et al., 2019) (Paganoni et al., 2018). In Alzheimer's research, Kreisl and colleagues have recently proposed to use cerebellum grey matter as a pseudo-reference region to calculate ^{11}C-PBR28 SUVR (Lyoo et al., 2015b), based on the fact that cerebellum is generally not involved in tau pathology and only have amyloid deposition towards terminal stages of the disease. However, there has been criticism that the ratio methods can drastically reduce the variance, that they may eliminate much of the biological relevant signals (Albrecht et al., 2018; Matheson et al., 2017). The current study has compared the voxel-wise analytical methods to (semi-)quantify ^{11}C-PBR28, including spectral analysis, Logan graphic analysis, distribution volume ratio, and standard uptake value ratio methods. I found that there were very good correlations between absolute quantification, i.e., IRF (spectral analysis) and VT (Logan analysis), and between reference region approaches, i.e., DVR and SUVR, but not between absolute measures and reference region methods. This finding is consistent with previous studies and in fact could be anticipated since a lot of individual variability due to age, BMI, circadian rhythms, systemic inflammation etc., has been eliminated by using reference region (Lyoo et al., 2015b). However, the current analysis found that ^{11}C-PBR28 SUVR was associated with both ^{18}F-Flutemetamol and ^{18}F-AV1451 uptake at both regional and voxel levels, which is consistent with prior pathology and imaging knowledge that neuroinflammation accompanies amyloid and tau pathologies. This finding suggests that while the ratio method has eliminated much inter-subject variability, the resultant SUVR still remains biologically relevant signals. Further, the SUVR measure was able to identify increased level of neuroinflammation in the inferior temporal gyri and medial temporal lobe

in AD patients, which is consistent with previous literature, while absolute quantifications only found a trend but not statistically significant, due to the high standard deviation associated with inter-subject variability. This suggests that SUVR may be indeed a more sensitive method considering the large inter-subject variability of ^{11}C-PBR28 uptake.

I should note, however, the analysis in current project is not stringent for evaluation of PET quantification method, which requires either test-retest stability analysis in vivo or direct comparison to autoradiography results in preclinical settings, which is beyond the scope of the current project. However, based on available data, the results from SUVR analysis were more consistent with our current understanding of neuroinflammation in Alzheimer's disease, and therefore SUVR seemed to be a more viable measure for further analysis. Again, I should note that the current project mainly aimed to evaluate the association between neuroinflammation and brain connectivity, but not the correlation between neuroinflammation and amyloid/tau pathology, and I did the correlation tests only because this was the only way I could indirectly evaluate which quantification method may be more robust against random noise, based on prior knowledge in the field. And I should stress that the SUVR method had been chosen before the primary analysis on brain connectivity was conducted, and it was chosen based on the rationale, but not to present better correlations regarding amyloid and tau PET.

Nevertheless, the current analysis provide evidence on the feasibility of using cerebellum as a reference region in ^{11}C-PBR28 using an independent cohort form that recruited by Kreisl and colleagues, which add up the strength of the argument. Apart from the robustness against inter-subject variability, the SUVR method also have the advantage of being minimally invasive and cost-effective (arterial sampling not required), and our evidence may facilitate wider use of TSPO tracers or ^{11}C-PBR28 in particular in larger scale clinical imaging studies, which deserves consideration considering accumulating evidence on the important role of

neuroinflammation in AD. Further test-retest stability studies and imaging-autoradiography studies should also be considered to substantiate the SUVR method in ^{11}C-PBR28 quantification.

The key contribution of the project is that it has provided novel evidence that neuroinflammation in Alzheimer's spectrum is associated with disruption of both structural and functional brain network. Previous studies have highlighted the key role of neuroinflammation in AD, the importance of intact brain connectome in cognition, and possible involvement if connectome in propagation of Alzheimer's pathology. However, till now there is limited evidence on whether neuroinflammation is associated with connectivity disruption in AD (Melah et al., 2016). While a parallel study has reported the relationship between inflammation pattern and within/between network functional connectivity (Passamonti et al., 2019), the current study has further investigated their relationship at both regional connectivity and whole brain topology level. Further, the current project has interrogated the relationship between neuroinflammation and structural network integrity using multivariate analyses, and has established a link between neuroinflammation and structural network microstructural damage in AD, which to my knowledge is a novel finding in the field of AD research. Moreover, by investigating the Aβ+ cognitively impairment cohort and including both amyloid deposition and neuroinflammation in the model, the current study has suggested neuroinflammation is more directly associated with network failure in AD compared to Aβ. These findings have deepened our understanding of the mechanisms underlying cognitive decline in AD spectrum, and suggested the neuroinflammation is a potential therapeutic target for AD treatment.

The current project has also provided novel evidence that neuroinflammation is associated with disrupted cerebral perfusion, more specifically neurovascular coupling, in Alzheimer's spectrum. This novel finding has suggested neuroinflammation as a common factor in both

classical Alzheimer's pathology cascade and emerging neurovascular pathways that contributes to clinical presentation of AD. This finding again suggests a key position taken by neuroinflammation in the multifaceted pathogenetic pathways towards Alzheimer's disease dementia, again highlighting the therapeutic potential of neuroinflammation management.

Lastly, the current project has evaluated the imaging biomarkers (PET and MRI) with regard to predicting longitudinal cognitive decline in MCI and AD patients. Limited by available data, the current analysis has mainly focused on MCI patients. Using a 2-step selection process, MRI markers of structural network integrity and cortical atrophy have been found to be more closely associated with cognitive status at the same time point, but PET markers of Aβ, tau pathology and neuroinflammation have been found to be predictive of future cognitive decline. While there have been reports on predictive values of individual biomarker or a few of them on cognition, few studies have comprehensively evaluated these image markers in a head-by-head manner (Zou et al., 2020) (L. Hamelin et al., 2016; Kreisl et al., 2016a; Malpetti et al., 2020). The current findings underline the heterogeneity of the MCI population, and have suggested that neurodegeneration markers rather than AD-specific markers could better explain the cognitive impairment in these patients. Furthermore, the findings highlight the predictive value of molecular imaging markers, as they could specifically identify underlying pathologies. Most importantly, neuroinflammation marker has consistently remained in the best multiple regression models to predict cognitive decline in MCI or AD/MCI cohorts, together with amyloid and tau markers. This finding has stressed neuroinflammation as an independent factor that could drive cognitive decline in these patients, rather than just being associated with cognition due to its collinearity with amyloid and tau pathologies. To summarise, the current project has provided further evidence that neuroinflammation is an independent pathogenic factor in AD, and suggested that neuroinflammation markers to be taken more seriously in AD research and management.

The current findings together with previous evidence have suggested a framework of the systemic brain damage in Alzheimer's spectrum: while Aβ deposition can initiate the downstream cascade of AD pathogenesis, the downstream events are not linearly dependent on the quantity of Aβ deposition; neuroinflammation is likely a key factor that mediates the neurotoxicity of various pathological events. In AD, Aβ is undoubtably the primary initial insult, but various other factors, including systemic inflammation, cerebral microcirculation impairment, traumatic brain injury and genetic background could modulate the inflammatory response in early disease, thus increase the risk of AD. Neuroinflammation could further lead to structural and functional brain network damage, and as suggested by other evidence, hyperphosphorylated tau formation and propagation. The tau pathology in turn is associated with network damage as well as cortical atrophy (Strain et al., 2018) (La Joie et al., 2020). Structural network and functional network disruption, as well as cortical atrophy, i.e., neuronal damage and disruption, eventually lead to global multi-domain cognitive impairment in AD (Figure 7.1).

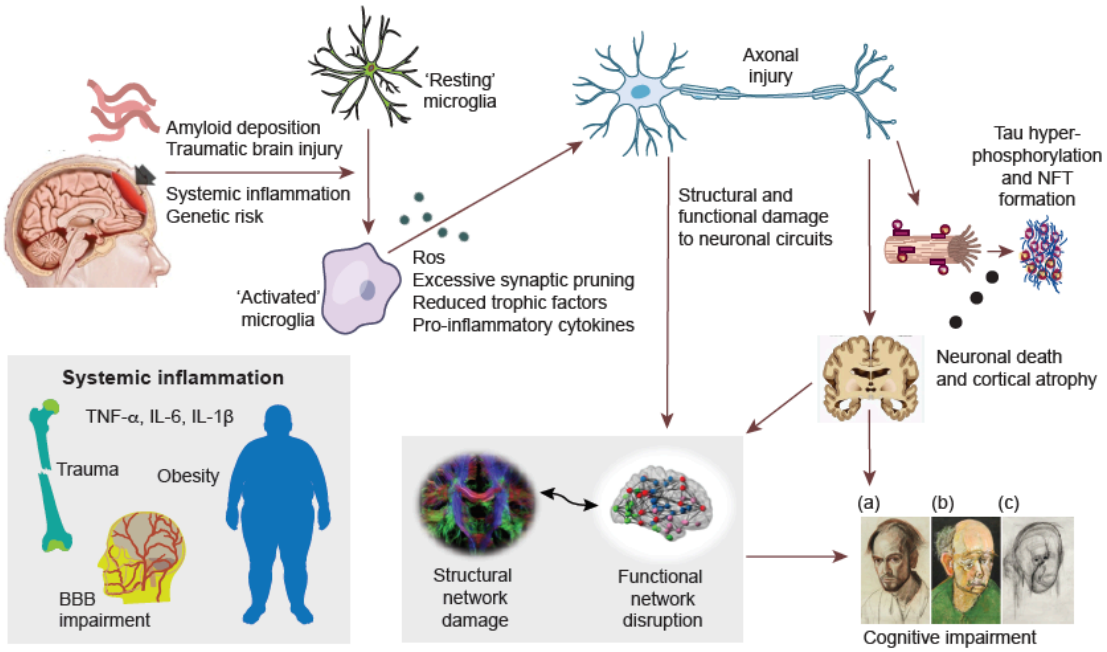

Figure 7.1 A hypothetical framework of pathways leading to cognitive impairment in AD

The hypothetical framework derived from the current project may provide insight to future AD research and management, while leaves open questions to be answered:

(1) Given the evidence that tau species propagate though the brain connectome, and that neuroinflammation is associated with damage of structural connectivity, disruption of functional connectivity and neuronal hyperactivity, how neuroinflammation may influence tau propagation locally and distally? Is the white matter damage a collateral damage by an inflammation response to cut the trans-axonal propagation of tau species? How local neuroinflammation is influencing the local seeding of tau pathology? Structural equation modelling using cross-sectional data may provide some insight into the question, but larger dataset is needed to make a robust inference. Ultimately, to answer these questions, future longitudinal studies with baseline and follow-up tau biomarkers are encouraged.

(2) Given the evidence of microglial phenotypical change, is it possible to combine PET imaging with fluid biomarkers of microglial phenotypes to gain not only spatial information from PET scans, but expand the information dimension on cellular phenotypes from fluid biomarkers such as sTREM2 and YKL-40? Further efforts are needed to explore the feasibility of the approach and may offer better understanding on neuroinflammation in AD.

The current study is also limited by following factors: (1) the cross-sectional nature (only baseline images are available for association analyses among the imaging markers) have limited the ability of the project to infer causal relationships; (2) the data completeness, especially with regard to clinical/neuropsychological follow-up records, have led to loss of participants eligible for analysis, which should be avoided in future studies; (3) the lack of test-retest data to validate the SUVR method for ^{11}C-PBR28 analysis in our centre (which at the time was a relatively new tracer), though evidence from other studies have suggested the

method to be feasible; (4) the ASL acquisition parameters could have been optimised in hindsight, which might have a negative influence on the accuracy and power (more noise in data) of the analysis.

To summarise, although the current project has the limitations, I believe the project has still provided vital evidence to advance our understanding of neuroinflammation in Alzheimer's disease, and has opened avenues for future studies on disease mechanism and interventions.

Reference

2018 Alzheimer's disease facts and figures. (2018). *Alzheimer's & Dementia, 14*(3), 367-429. doi:10.1016/j.jalz.2018.02.001

Achard, S., Salvador, R., Whitcher, B., Suckling, J., & Bullmore, E. (2006). A resilient, low-frequency, small-world human brain functional network with highly connected association cortical hubs. *J Neurosci, 26*(1), 63-72. doi:10.1523/JNEUROSCI.3874-05.2006

Aertsen, A. M., Gerstein, G. L., Habib, M. K., & Palm, G. (1989). Dynamics of neuronal firing correlation: modulation of "effective connectivity". *J Neurophysiol, 61*(5), 900-917. doi:10.1152/jn.1989.61.5.900

Akiyama, H., Barger, S., Barnum, S., Bradt, B., Bauer, J., Cole, G. M., . . . Grp, N. W. (2000). Inflammation and Alzheimer's disease. *Neurobiology of Aging, 21*(3), 383-421. doi:Doi 10.1016/S0197-4580(00)00124-X

Alafuzoff, I., Arzberger, T., Al-Sarraj, S., Bodi, I., Bogdanovic, N., Braak, H., . . . Kretzschmar, H. (2008). Staging of neurofibrillary pathology in Alzheimer's disease: a study of the BrainNet Europe Consortium. *Brain Pathol, 18*(4), 484-496. doi:10.1111/j.1750-3639.2008.00147.x

Alam, M. M., Lee, J., & Lee, S. Y. (2017). Recent Progress in the Development of TSPO PET Ligands for Neuroinflammation Imaging in Neurological Diseases. *Nucl Med Mol Imaging, 51*(4), 283-296. doi:10.1007/s13139-017-0475-8

Alawieyah Syed Mortadza, S., Sim, J. A., Neubrand, V. E., & Jiang, L. H. (2018). A critical role of TRPM2 channel in Abeta42 -induced microglial activation and generation of tumor necrosis factor-alpha. *Glia, 66*(3), 562-575. doi:10.1002/glia.23265

Albert, M. S., DeKosky, S. T., Dickson, D., Dubois, B., Feldman, H. H., Fox, N. C., . . . Phelps, C. H. (2011). The diagnosis of mild cognitive impairment due to Alzheimer's disease: recommendations from the National Institute on Aging-Alzheimer's Association workgroups on diagnostic guidelines for Alzheimer's disease. *Alzheimers Dement, 7*(3), 270-279. doi:10.1016/j.jalz.2011.03.008

Albrecht, D. S., Normandin, M. D., Shcherbinin, S., Wooten, D. W., Schwarz, A. J., Zurcher, N. R., . . . Loggia, M. L. (2018). Pseudoreference Regions for Glial Imaging with C-11-PBR28: Investigation in 2 Clinical Cohorts. *Journal of Nuclear Medicine, 59*(1), 107-114. doi:10.2967/jnumed.116.178335

Alcolea, D., Martinez-Lage, P., Sanchez-Juan, P., Olazaran, J., Antunez, C., Izagirre, A., . . . Lleo, A. (2015). Amyloid precursor protein metabolism and inflammation markers in preclinical Alzheimer disease. *Neurology, 85*(7), 626-633. doi:10.1212/Wnl.0000000000001859

Alshikho, M. J., Zurcher, N. R., Loggia, M. L., Cernasov, P., Chonde, D. B., Garcia, D. I., . . . Atassi, N. (2016). Glial activation colocalizes with structural abnormalities in amyotrophic lateral sclerosis. *Neurology, 87*(24), 2554-2561. doi:10.1212/wnl.0000000000003427

Alsop, D. C., Detre, J. A., Golay, X., Gunther, M., Hendrikse, J., Hernandez-Garcia, L., . . . Zaharchuk, G. (2015). Recommended implementation of arterial spin-labeled perfusion MRI for clinical applications: A consensus of the ISMRM perfusion study group and the European consortium for ASL in dementia. *Magn Reson Med, 73*(1), 102-116. doi:10.1002/mrm.25197

Alsop, D. C., Detre, J. A., & Grossman, M. (2000). Assessment of cerebral blood flow in Alzheimer's disease by spin-labeled magnetic resonance imaging. *Annals of Neurology, 47*(1), 93-100. Retrieved from https://www.ncbi.nlm.nih.gov/pubmed/10632106

Andersson, J. L. R., & Sotiropoulos, S. N. (2016). An integrated approach to correction for off-resonance effects and subject movement in diffusion MR imaging. *Neuroimage, 125*, 1063-1078. doi:10.1016/j.neuroimage.2015.10.019

Antony, J. M., Paquin, A., Nutt, S. L., Kaplan, D. R., & Miller, F. D. (2011). Endogenous Microglia Regulate Development of Embryonic Cortical Precursor Cells. *Journal of Neuroscience Research, 89*(3), 286-298. doi:10.1002/jnr.22533

Arnaboldi, V., Passarella, A., Conti, M., & Dunbar, R. I. M. (2015). *Online social networks : human cognitive constraints in Facebook and Twitter personal graphs*. Amsterdam, Netherlands ; Boston: Elsevier.

Asai, H., Ikezu, S., Tsunoda, S., Medalla, M., Luebke, J., Haydar, T., . . . Ikezu, T. (2015). Depletion of microglia and inhibition of exosome synthesis halt tau propagation. *Nature Neuroscience, 18*(11), 1584-1593. doi:10.1038/nn.4132

Attwell, D., Buchan, A. M., Charpak, S., Lauritzen, M., MacVicar, B. A., & Newman, E. A. (2010). Glial and neuronal control of brain blood flow. *Nature, 468*(7321), 232-243. doi:10.1038/nature09613

Baalman, K., Marin, M. A., Ho, T. S., Godoy, M., Cherian, L., Robertson, C., & Rasband, M. N. (2015). Axon initial segment-associated microglia. *J Neurosci, 35*(5), 2283-2292. doi:10.1523/JNEUROSCI.3751-14.2015

Bakker, A., Krauss, G. L., Albert, M. S., Speck, C. L., Jones, L. R., Stark, C. E., . . . Gallagher, M. (2012). Reduction of hippocampal hyperactivity improves cognition in amnestic mild cognitive impairment. *Neuron, 74*(3), 467-474. doi:10.1016/j.neuron.2012.03.023

Baldacci, F., Lista, S., Cavedo, E., Bonuccelli, U., & Hampel, H. (2017). Diagnostic function of the neuroinflammatory biomarker YKL-40 in Alzheimer's disease and other neurodegenerative diseases. *Expert Rev Proteomics, 14*(4), 285-299. doi:10.1080/14789450.2017.1304217

Barnes, D. E., & Yaffe, K. (2011). The projected effect of risk factor reduction on Alzheimer's disease prevalence. *Lancet Neurol, 10*(9), 819-828. doi:10.1016/S1474-4422(11)70072-2

Basser, P. J., Mattiello, J., & LeBihan, D. (1994a). Estimation of the effective self-diffusion tensor from the NMR spin echo. *J Magn Reson B, 103*(3), 247-254. doi:10.1006/jmrb.1994.1037

Basser, P. J., Mattiello, J., & LeBihan, D. (1994b). MR diffusion tensor spectroscopy and imaging. *Biophys J, 66*(1), 259-267. doi:10.1016/S0006-3495(94)80775-1

Behrens, T. E., Berg, H. J., Jbabdi, S., Rushworth, M. F., & Woolrich, M. W. (2007). Probabilistic diffusion tractography with multiple fibre orientations: What can we gain? *Neuroimage, 34*(1), 144-155. doi:10.1016/j.neuroimage.2006.09.018

Behrens, T. E., Woolrich, M. W., Jenkinson, M., Johansen-Berg, H., Nunes, R. G., Clare, S., . . . Smith, S. M. (2003). Characterization and propagation of uncertainty in diffusion-weighted MR imaging. *Magn Reson Med, 50*(5), 1077-1088. doi:10.1002/mrm.10609

Belliveau, J. W., Kennedy, D. N., Jr., McKinstry, R. C., Buchbinder, B. R., Weisskoff, R. M., Cohen, M. S., . . . Rosen, B. R. (1991). Functional mapping of the human visual cortex by magnetic resonance imaging. *Science, 254*(5032), 716-719. doi:10.1126/science.1948051

Bendlin, B. B., Carlsson, C. M., Johnson, S. C., Zetterberg, H., Blennow, K., Willette, A. A., . . . Sager, M. A. (2012). CSF T-Tau/Abeta42 predicts white matter microstructure in healthy adults at risk for Alzheimer's disease. *PLoS One, 7*(6), e37720. doi:10.1371/journal.pone.0037720

Bendlin, B. B., Ries, M. L., Canu, E., Sodhi, A., Lazar, M., Alexander, A. L., . . . Johnson, S. C. (2010). White matter is altered with parental family history of Alzheimer's disease. *Alzheimers Dement, 6*(5), 394-403. doi:10.1016/j.jalz.2009.11.003

Benitez, A., Fieremans, E., Jensen, J. H., Falangola, M. F., Tabesh, A., Ferris, S. H., & Helpern, J. A. (2014). White matter tract integrity metrics reflect the vulnerability of late-myelinating tracts in Alzheimer's disease. *Neuroimage Clin, 4*, 64-71. doi:10.1016/j.nicl.2013.11.001

Bertoldo, A., Rizzo, G., & Veronese, M. (2014). Deriving physiological information from PET images: from SUV to compartmental modelling. *Clinical and Translational Imaging, 2*(3), 239-251. doi:10.1007/s40336-014-0067-x

Betthauser, T. J., Koscik, R. L., Jonaitis, E. M., Allison, S. L., Cody, K. A., Erickson, C. M., . . . Johnson, S. C. (2020). Amyloid and tau imaging biomarkers explain cognitive decline from late middle-age. *Brain, 143*(1), 320-335. doi:10.1093/brain/awz378

Bi, D., Wen, L., Wu, Z., & Shen, Y. (2020). GABAergic dysfunction in excitatory and inhibitory (E/I) imbalance drives the pathogenesis of Alzheimer's disease. *Alzheimers Dement, 16*(9), 1312-1329. doi:10.1002/alz.12088

Binnewijzend, M. A., Kuijer, J. P., van der Flier, W. M., Benedictus, M. R., Moller, C. M., Pijnenburg, Y. A., . . . Barkhof, F. (2014). Distinct perfusion patterns in Alzheimer's disease, frontotemporal dementia and dementia with Lewy bodies. *Eur Radiol, 24*(9), 2326-2333. doi:10.1007/s00330-014-3172-3

Binnewijzend, M. A., Schoonheim, M. M., Sanz-Arigita, E., Wink, A. M., van der Flier, W. M., Tolboom, N., . . . Barkhof, F. (2012). Resting-state fMRI changes in Alzheimer's disease and mild cognitive impairment. *Neurobiol Aging, 33*(9), 2018-2028. doi:10.1016/j.neurobiolaging.2011.07.003

Biswal, B. B., Van Kylen, J., & Hyde, J. S. (1997). Simultaneous assessment of flow and BOLD signals in resting-state functional connectivity maps. *NMR Biomed, 10*(4-5), 165-170. doi:10.1002/(sici)1099-1492(199706/08)10:4/5<165::aid-nbm454>3.0.co;2-7

Bolos, M., Llorens-Martin, M., Jurado-Arjona, J., Hernandez, F., Rabano, A., & Avila, J. (2016). Direct Evidence of Internalization of Tau by Microglia In Vitro and In Vivo. *J Alzheimers Dis, 50*(1), 77-87. doi:10.3233/jad-150704

Bolos, M., Llorens-Martin, M., Perea, J. R., Jurado-Arjona, J., Rabano, A., Hernandez, F., & Avila, J. (2017). Absence of CX3CR1 impairs the internalization of Tau by microglia. *Molecular Neurodegeneration, 12*. doi:10.1186/s13024-017-0200-1

Bosch, B., Arenaza-Urquijo, E. M., Rami, L., Sala-Llonch, R., Junque, C., Sole-Padulles, C., . . . Bartres-Faz, D. (2012). Multiple DTI index analysis in normal aging, amnestic MCI and AD. Relationship with neuropsychological performance. *Neurobiol Aging, 33*(1), 61-74. doi:10.1016/j.neurobiolaging.2010.02.004

Braak, H., & Braak, E. (1991). Neuropathological stageing of Alzheimer-related changes. *Acta Neuropathol, 82*(4), 239-259. doi:10.1007/BF00308809

Braak, H., & Braak, E. (1997). Frequency of stages of Alzheimer-related lesions in different age categories. *Neurobiol Aging, 18*(4), 351-357. doi:10.1016/s0197-4580(97)00056-0

Braak, H., & Del Tredici, K. (2011). The pathological process underlying Alzheimer's disease in individuals under thirty. *Acta Neuropathol, 121*(2), 171-181. doi:10.1007/s00401-010-0789-4

Braak, H., & Del Tredici, K. (2015). The preclinical phase of the pathological process underlying sporadic Alzheimer's disease. *Brain, 138*, 2814-2833. doi:10.1093/brain/awv236

Bradburn, S., Murgatroyd, C., & Ray, N. (2019). Neuroinflammation in mild cognitive impairment and Alzheimer's disease: A meta-analysis. *Ageing Research Reviews, 50*, 1-8. doi:10.1016/j.arr.2019.01.002

Broyd, S. J., Demanuele, C., Debener, S., Helps, S. K., James, C. J., & Sonuga-Barke, E. J. (2009). Default-mode brain dysfunction in mental disorders: a systematic review. *Neurosci Biobehav Rev, 33*(3), 279-296. doi:10.1016/j.neubiorev.2008.09.002

Buckner, R. L., Andrews-Hanna, J. R., & Schacter, D. L. (2008). The brain's default network: anatomy, function, and relevance to disease. *Ann N Y Acad Sci, 1124*, 1-38. doi:10.1196/annals.1440.011

Bullmore, E., & Sporns, O. (2009). Complex brain networks: graph theoretical analysis of structural and functional systems. *Nat Rev Neurosci, 10*(3), 186-198. doi:10.1038/nrn2575

Busche, M. A., Kekus, M., Adelsberger, H., Noda, T., Forstl, H., Nelken, I., & Konnerth, A. (2015). Rescue of long-range circuit dysfunction in Alzheimer's disease models. *Nature Neuroscience, 18*(11), 1623-1630. doi:10.1038/nn.4137

Busche, M. A., Wegmann, S., Dujardin, S., Commins, C., Schiantarelli, J., Klickstein, N., . . . Hyman, B. T. (2019). Tau impairs neural circuits, dominating amyloid-beta effects, in Alzheimer models in vivo. *Nature Neuroscience, 22*(1), 57-64. doi:10.1038/s41593-018-0289-8

Calsolaro, V., & Edison, P. (2016). Neuroinflammation in Alzheimer's disease: Current evidence and future directions. *Alzheimers Dement, 12*(6), 719-732. doi:10.1016/j.jalz.2016.02.010

Caso, F., Agosta, F., & Filippi, M. (2016). Insights into White Matter Damage in Alzheimer's Disease: From Postmortem to in vivo Diffusion Tensor MRI Studies. *Neurodegener Dis, 16*(1-2), 26-33. doi:10.1159/000441422

Chappell, M. A., Groves, A. R., MacIntosh, B. J., Donahue, M. J., Jezzard, P., & Woolrich, M. W. (2011). Partial volume correction of multiple inversion time arterial spin labeling MRI data. *Magn Reson Med, 65*(4), 1173-1183. doi:10.1002/mrm.22641

Chappell, M. A., Groves, A. R., Whitcher, B., & Woolrich, M. W. (2009). Variational Bayesian Inference for a Nonlinear Forward Model. *Ieee Transactions on Signal Processing, 57*(1), 223-236. doi:10.1109/tsp.2008.2005752

Chen, C. H., Zhou, W., Liu, S., Deng, Y., Cai, F., Tone, M., . . . Song, W. (2012). Increased NF-kappaB signalling up-regulates BACE1 expression and its therapeutic potential in Alzheimer's disease. *Int J Neuropsychopharmacol, 15*(1), 77-90. doi:10.1017/S1461145711000149

Chiesa, P. A., Cavedo, E., Vergallo, A., Lista, S., Potier, M. C., Habert, M. O., . . . Alzheimer Precision Medicine, I. (2019). Differential default mode network trajectories in asymptomatic individuals at risk for Alzheimer's disease. *Alzheimers Dement, 15*(7), 940-950. doi:10.1016/j.jalz.2019.03.006

Cho, M. H., Cho, K., Kang, H. J., Jeon, E. Y., Kim, H. S., Kwon, H. J., . . . Yoon, S. Y. (2014). Autophagy in microglia degrades extracellular beta-amyloid fibrils and regulates the NLRP3 inflammasome. *Autophagy, 10*(10), 1761-1775. doi:10.4161/auto.29647

Coleman, M. (2005). Axon degeneration mechanisms: commonality amid diversity. *Nat Rev Neurosci, 6*(11), 889-898. doi:10.1038/nrn1788

Collste, K., Forsberg, A., Varrone, A., Amini, N., Aeinehband, S., Yakushev, I., . . . Cervenka, S. (2016). Test-retest reproducibility of C-11 PBR28 binding to TSPO in healthy control subjects. *Eur J Nucl Med Mol Imaging, 43*(1), 173-183. doi:10.1007/s00259-015-3149-8

Combs, C. K., Karlo, J. C., Kao, S. C., & Landreth, G. E. (2001). beta-Amyloid stimulation of microglia and monocytes results in TNFalpha-dependent expression of inducible nitric oxide synthase and neuronal apoptosis. *J Neurosci, 21*(4), 1179-1188.

Cordes, D., Haughton, V. M., Arfanakis, K., Carew, J. D., Turski, P. A., Moritz, C. H., . . . Meyerand, M. E. (2001). Frequencies contributing to functional connectivity in the cerebral cortex in "resting-state" data. *AJNR Am J Neuroradiol, 22*(7), 1326-1333. Retrieved from https://www.ncbi.nlm.nih.gov/pubmed/11498421

Cordes, D., Haughton, V. M., Arfanakis, K., Wendt, G. J., Turski, P. A., Moritz, C. H., . . . Meyerand, M. E. (2000). Mapping functionally related regions of brain with functional connectivity MR imaging. *AJNR Am J Neuroradiol, 21*(9), 1636-1644. Retrieved from https://www.ncbi.nlm.nih.gov/pubmed/11039342

Corrada, M., Stewart, W., & Kawas, C. (1996). Nonsteroidal anti-inflammatory drugs and the risk of Alzheimer's disease. *Neurology, 46*(2), 6015-6015. Retrieved from <Go to ISI>://WOS:A1996UA47601059

Cunningham, C. L., Martinez-Cerdeno, V., & Noctor, S. C. (2013). Microglia Regulate the Number of Neural Precursor Cells in the Developing Cerebral Cortex. *Journal of Neuroscience, 33*(10), 4216-4233. doi:10.1523/Jneurosci.3441-12.2013

Cunningham, V. J., & Jones, T. (1993). Spectral analysis of dynamic PET studies. *J Cereb Blood Flow Metab, 13*(1), 15-23. doi:10.1038/jcbfm.1993.5

Dai, Z., & He, Y. (2014). Disrupted structural and functional brain connectomes in mild cognitive impairment and Alzheimer's disease. *Neurosci Bull, 30*(2), 217-232. doi:10.1007/s12264-013-1421-0

Dai, Z., Lin, Q., Li, T., Wang, X., Yuan, H., Yu, X., . . . Wang, H. (2019). Disrupted structural and functional brain networks in Alzheimer's disease. *Neurobiol Aging, 75*, 71-82. doi:10.1016/j.neurobiolaging.2018.11.005

Damoiseaux, J. S., Rombouts, S. A., Barkhof, F., Scheltens, P., Stam, C. J., Smith, S. M., & Beckmann, C. F. (2006). Consistent resting-state networks across healthy subjects. *Proc Natl Acad Sci U S A, 103*(37), 13848-13853. doi:10.1073/pnas.0601417103

Dani, M., Wood, M., Mizoguchi, R., Fan, Z., Edginton, T., Hinz, R., . . . Edison, P. (2019). Tau Aggregation Correlates with Amyloid Deposition in Both Mild Cognitive Impairment and Alzheimer's Disease Subjects. *J Alzheimers Dis, 70*(2), 455-465. doi:10.3233/JAD-181168

Dani, M., Wood, M., Mizoguchi, R., Fan, Z., Walker, Z., Morgan, R., . . . Edison, P. (2018a). Microglial activation correlates in vivo with both tau and amyloid in Alzheimer's disease. *Brain, 141*(9), 2740-2754. doi:10.1093/brain/awy188

Dani, M., Wood, M., Mizoguchi, R., Fan, Z., Walker, Z., Morgan, R., . . . Edison, P. (2018b). Microglial activation correlates in vivo with both tau and amyloid in Alzheimer's disease. *Brain, 141*, 2740-2754. doi:10.1093/brain/awy188

Davalos, D., & Akassoglou, K. (2012). Fibrinogen as a key regulator of inflammation in disease. *Semin Immunopathol, 34*(1), 43-62. doi:10.1007/s00281-011-0290-8

Davies, D. S., Ma, J., Jegathees, T., & Goldsbury, C. (2017). Microglia show altered morphology and reduced arborization in human brain during aging and Alzheimer's disease. *Brain Pathol, 27*(6), 795-808. doi:10.1111/bpa.12456

de Vos, F., Koini, M., Schouten, T. M., Seiler, S., van der Grond, J., Lechner, A., . . . Rombouts, S. (2018). A comprehensive analysis of resting state fMRI measures to classify individual patients with Alzheimer's disease. *Neuroimage, 167*, 62-72. doi:10.1016/j.neuroimage.2017.11.025

Delbo, R., Angeretti, N., Lucca, E., Desimoni, M. G., & Forloni, G. (1995). Reciprocal Control of Inflammatory Cytokines, Il-1 and Il-6, and Beta-Amyloid Production in Cultures. *Neuroscience Letters, 188*(1), 70-74. doi:Doi 10.1016/0304-3940(95)11384-9

delEtoile, J., & Adeli, H. (2017). Graph Theory and Brain Connectivity in Alzheimer's Disease. *Neuroscientist, 23*(6), 616-626. doi:10.1177/1073858417702621

Di Paola, M., Di Iulio, F., Cherubini, A., Blundo, C., Casini, A. R., Sancesario, G., . . . Spalletta, G. (2010). When, where, and how the corpus callosum changes in MCI and AD: a multimodal MRI study. *Neurology, 74*(14), 1136-1142. doi:10.1212/WNL.0b013e3181d7d8cb

Dickerson, B. C., Wolk, D. A., & Alzheimer's Disease Neuroimaging, I. (2013). Biomarker-based prediction of progression in MCI: Comparison of AD signature and hippocampal volume with spinal fluid amyloid-beta and tau. *Front Aging Neurosci, 5*, 55. doi:10.3389/fnagi.2013.00055

Dickstein, L. P., Liow, J. S., Austermuehle, A., Zoghbi, S., Inati, S. K., Zaghloul, K., . . . Theodore, W. H. (2019). Neuroinflammation in neocortical epilepsy measured by PET imaging of translocator protein. *Epilepsia, 60*(6), 1248-1254. doi:10.1111/epi.15967

Diorio, D., Welner, S. A., Butterworth, R. F., Meaney, M. J., & Suranyi-Cadotte, B. E. (1991). Peripheral benzodiazepine binding sites in Alzheimer's disease frontal and temporal cortex. *Neurobiol Aging, 12*(3), 255-258. Retrieved from https://www.ncbi.nlm.nih.gov/pubmed/1652108

DiSabato, D. J., Quan, N., & Godbout, J. P. (2016). Neuroinflammation: the devil is in the details. *J Neurochem, 139 Suppl 2*, 136-153. doi:10.1111/jnc.13607

Douaud, G., Jbabdi, S., Behrens, T. E., Menke, R. A., Gass, A., Monsch, A. U., . . . Smith, S. (2011). DTI measures in crossing-fibre areas: increased diffusion anisotropy reveals early white matter alteration in MCI and mild Alzheimer's disease. *Neuroimage, 55*(3), 880-890. doi:10.1016/j.neuroimage.2010.12.008

Dubois, B., Feldman, H. H., Jacova, C., Hampel, H., Molinuevo, J. L., Blennow, K., . . . Cummings, J. L. (2014). Advancing research diagnostic criteria for Alzheimer's disease: the IWG-2 criteria. *Lancet Neurol, 13*(6), 614-629. doi:10.1016/S1474-4422(14)70090-0

Dubois, B., Villain, N., Frisoni, G. B., Rabinovici, G. D., Sabbagh, M., Cappa, S., . . . Feldman, H. H. (2021). Clinical diagnosis of Alzheimer's disease: recommendations of the International Working Group. *Lancet Neurol*. doi:10.1016/S1474-4422(21)00066-1

Dunn, N., Mullee, M., Perry, V. H., & Holmes, C. (2005). Association between dementia and infectious disease - Evidence from a case-control study. *Alzheimer Disease & Associated Disorders, 19*(2), 91-94. doi:DOI 10.1097/01.wad.0000165511.52746.1f

Edison, P., Archer, H. A., Gerhard, A., Hinz, R., Pavese, N., Turkheimer, F. E., . . . Brooks, D. J. (2008). Microglia, amyloid, and cognition in Alzheimer's disease: An

[11C](R)PK11195-PET and [11C]PIB-PET study. *Neurobiol Dis, 32*(3), 412-419. doi:10.1016/j.nbd.2008.08.001

Edison, P., & Brooks, D. J. (2018). Role of Neuroinflammation in the Trajectory of Alzheimer's Disease and in vivo Quantification Using PET. *J Alzheimers Dis, 64*(s1), S339-S351. doi:10.3233/JAD-179929

El Kadmiri, N., Said, N., Slassi, I., El Moutawakil, B., & Nadifi, S. (2018). Biomarkers for Alzheimer Disease: Classical and Novel Candidates' Review. *Neuroscience, 370*, 181-190. doi:10.1016/j.neuroscience.2017.07.017

EO Stejskal, J. T. (1965). Spin diffusion measurements: Spin echoes in the presence of a time-dependent field gradient. *The journal of chemical physics, 42*(1), 288-292.

Eroglu, C., & Barres, B. A. (2010). Regulation of synaptic connectivity by glia. *Nature, 468*(7321), 223-231. doi:10.1038/nature09612

Etminan, M., Gill, S., & Samii, A. (2003). Effect of non-steroidal anti-inflammatory drugs on risk of Alzheimer's disease: systematic review and meta-analysis of observational studies. *Bmj-British Medical Journal, 327*(7407), 128-+. doi:DOI 10.1136/bmj.327.7407.128

Ewers, M., Franzmeier, N., Suarez-Calvet, M., Morenas-Rodriguez, E., Caballero, M. A. A., Kleinberger, G., . . . Alzheimer's Disease Neuroimaging, I. (2019). Increased soluble TREM2 in cerebrospinal fluid is associated with reduced cognitive and clinical decline in Alzheimer's disease. *Sci Transl Med, 11*(507). doi:10.1126/scitranslmed.aav6221

Fair, D. A., Cohen, A. L., Power, J. D., Dosenbach, N. U., Church, J. A., Miezin, F. M., . . . Petersen, S. E. (2009). Functional brain networks develop from a "local to distributed" organization. *PLoS Comput Biol, 5*(5), e1000381. doi:10.1371/journal.pcbi.1000381

Fan, Z., Aman, Y., Ahmed, I., Chetelat, G., Landeau, B., Ray Chaudhuri, K., . . . Edison, P. (2015). Influence of microglial activation on neuronal function in Alzheimer's and Parkinson's disease dementia. *Alzheimers Dement, 11*(6), 608-621 e607. doi:10.1016/j.jalz.2014.06.016

Fan, Z., Brooks, D. J., Okello, A., & Edison, P. (2017). An early and late peak in microglial activation in Alzheimer's disease trajectory. *Brain, 140*(3), 792-803. doi:10.1093/brain/aww349

Fan, Z., Okello, A. A., Brooks, D. J., & Edison, P. (2015). Longitudinal influence of microglial activation and amyloid on neuronal function in Alzheimer's disease. *Brain, 138*(Pt 12), 3685-3698. doi:10.1093/brain/awv288

Fang, H., Zhang, L. F., Meng, F. T., Du, X., & Zhou, J. N. (2010). Acute hypoxia promote the phosphorylation of tau via ERK pathway. *Neurosci Lett, 474*(3), 173-177. doi:10.1016/j.neulet.2010.03.037

Farkas, E., & Luiten, P. G. (2001). Cerebral microvascular pathology in aging and Alzheimer's disease. *Prog Neurobiol, 64*(6), 575-611. doi:10.1016/s0301-0082(00)00068-x

Felsky, D., Roostaei, T., Nho, K., Risacher, S. L., Bradshaw, E. M., Petyuk, V., . . . De Jager, P. L. (2019). Neuropathological correlates and genetic architecture of microglial activation in elderly human brain. *Nature Communications, 10*. doi:ARTN 409

10.1038/s41467-018-08279-3

Femminella, G. D., Dani, M., Wood, M., Fan, Z., Calsolaro, V., Atkinson, R., . . . Edison, P. (2019). Microglial activation in early Alzheimer trajectory is associated with higher gray matter volume. *Neurology, 92*(12), e1331-e1343. doi:10.1212/WNL.0000000000007133

Femminella, G. D., Ninan, S., Atkinson, R., Fan, Z., Brooks, D. J., & Edison, P. (2016). Does Microglial Activation Influence Hippocampal Volume and Neuronal Function in Alzheimer's Disease and Parkinson's Disease Dementia? *J Alzheimers Dis, 51*(4), 1275-1289. doi:10.3233/JAD-150827

Fischl, B., & Dale, A. M. (2000). Measuring the thickness of the human cerebral cortex from magnetic resonance images. *Proc Natl Acad Sci U S A, 97*(20), 11050-11055. doi:10.1073/pnas.200033797

Fischl, B., Liu, A., & Dale, A. M. (2001). Automated manifold surgery: constructing geometrically accurate and topologically correct models of the human cerebral cortex. *IEEE Trans Med Imaging, 20*(1), 70-80. doi:10.1109/42.906426

Fischl, B., van der Kouwe, A., Destrieux, C., Halgren, E., Segonne, F., Salat, D. H., . . . Dale, A. M. (2004). Automatically parcellating the human cerebral cortex. *Cereb Cortex, 14*(1), 11-22. doi:10.1093/cercor/bhg087

Floden, A. M., Li, S., & Combs, C. K. (2005). Beta-amyloid-stimulated microglia induce neuron death via synergistic stimulation of tumor necrosis factor alpha and NMDA receptors. *J Neurosci, 25*(10), 2566-2575. doi:10.1523/jneurosci.4998-04.2005

Fox, M. D., & Raichle, M. E. (2007). Spontaneous fluctuations in brain activity observed with functional magnetic resonance imaging. *Nat Rev Neurosci, 8*(9), 700-711. doi:10.1038/nrn2201

Franzmeier, N., Koutsouleris, N., Benzinger, T., Goate, A., Karch, C. M., Fagan, A. M., . . . Ewers, M. (2020). Predicting sporadic Alzheimer's disease progression via inherited Alzheimer's disease-informed machine-learning. *Alzheimers Dement, 16*(3), 501-511. doi:10.1002/alz.12032

Franzmeier, N., Suarez-Calvet, M., Frontzkowski, L., Moore, A., Hohman, T. J., Morenas-Rodriguez, E., . . . Alzheimer's Disease Neuroimaging, I. (2020). Higher CSF sTREM2 attenuates ApoE4-related risk for cognitive decline and neurodegeneration. *Mol Neurodegener, 15*(1), 57. doi:10.1186/s13024-020-00407-2

Friedman, B. A., Srinivasan, K., Ayalon, G., Meilandt, W. J., Lin, H., Huntley, M. A., . . . Hansen, D. V. (2018). Diverse Brain Myeloid Expression Profiles Reveal Distinct Microglial Activation States and Aspects of Alzheimer's Disease Not Evident in Mouse Models. *Cell Rep, 22*(3), 832-847. doi:10.1016/j.celrep.2017.12.066

Frost, B., & Diamond, M. I. (2010). Prion-like mechanisms in neurodegenerative diseases. *Nat Rev Neurosci, 11*(3), 155-159. doi:10.1038/nrn2786

Galatro, T. F., Holtman, I. R., Lerario, A. M., Vainchtein, I. D., Brouwer, N., Sola, P. R., . . . Eggen, B. J. L. (2017). Transcriptomic analysis of purified human cortical microglia reveals age-associated changes. *Nature Neuroscience, 20*(8), 1162-1171. doi:10.1038/nn.4597

Gavish, M., Bachman, I., Shoukrun, R., Katz, Y., Veenman, L., Weisinger, G., & Weizman, A. (1999). Enigma of the peripheral benzodiazepine receptor. *Pharmacol Rev, 51*(4), 629-650. Retrieved from https://www.ncbi.nlm.nih.gov/pubmed/10581326

Ginhoux, F., Greter, M., Leboeuf, M., Nandi, S., See, P., Gokhan, S., . . . Merad, M. (2010). Fate Mapping Analysis Reveals That Adult Microglia Derive from Primitive Macrophages. *Science, 330*(6005), 841-845. doi:10.1126/science.1194637

Girouard, H., & Iadecola, C. (2006). Neurovascular coupling in the normal brain and in hypertension, stroke, and Alzheimer disease. *J Appl Physiol (1985), 100*(1), 328-335. doi:10.1152/japplphysiol.00966.2005

Gold, B. T., Zhu, Z., Brown, C. A., Andersen, A. H., Ladu, M. J., Tai, L., . . . Smith, C. D. (2014). White matter integrity is associated with cerebrospinal fluid markers of Alzheimer's disease in normal adults. *Neurobiology of Aging, 35*(10), 2263-2271. doi:10.1016/j.neurobiolaging.2014.04.030

Gordon-Krajcer, W., Kozniewska, E., Lazarewicz, J. W., & Ksiezak-Reding, H. (2007). Differential changes in phosphorylation of tau at PHF-1 and 12E8 epitopes during brain ischemia and reperfusion in gerbils. *Neurochem Res, 32*(4-5), 729-737. doi:10.1007/s11064-006-9199-3

Gouw, A. A., Seewann, A., Vrenken, H., van der Flier, W. M., Rozemuller, J. M., Barkhof, F., . . . Geurts, J. J. (2008). Heterogeneity of white matter hyperintensities in Alzheimer's disease: post-mortem quantitative MRI and neuropathology. *Brain, 131*(Pt 12), 3286-3298. doi:10.1093/brain/awn265

Goveas, J., O'Dwyer, L., Mascalchi, M., Cosottini, M., Diciotti, S., De Santis, S., . . . Giannelli, M. (2015). Diffusion-MRI in neurodegenerative disorders. *Magn Reson Imaging, 33*(7), 853-876. doi:10.1016/j.mri.2015.04.006

Grade, M., Hernandez Tamames, J. A., Pizzini, F. B., Achten, E., Golay, X., & Smits, M. (2015). A neuroradiologist's guide to arterial spin labeling MRI in clinical practice. *Neuroradiology, 57*(12), 1181-1202. doi:10.1007/s00234-015-1571-z

Grammas, P. (2011). Neurovascular dysfunction, inflammation and endothelial activation: implications for the pathogenesis of Alzheimer's disease. *J Neuroinflammation, 8*, 26. doi:10.1186/1742-2094-8-26

Grammas, P., Moore, P., & Weigel, P. H. (1999). Microvessels from Alzheimer's disease brains kill neurons in vitro. *Am J Pathol, 154*(2), 337-342. doi:10.1016/S0002-9440(10)65280-7

Gratuze, M., Leyns, C. E. G., & Holtzman, D. M. (2018). New insights into the role of TREM2 in Alzheimer's disease. *Mol Neurodegener, 13*(1), 66. doi:10.1186/s13024-018-0298-9

Greicius, M. D., Srivastava, G., Reiss, A. L., & Menon, V. (2004). Default-mode network activity distinguishes Alzheimer's disease from healthy aging: evidence from functional MRI. *Proc Natl Acad Sci U S A, 101*(13), 4637-4642. doi:10.1073/pnas.0308627101

Griffanti, L., Douaud, G., Bijsterbosch, J., Evangelisti, S., Alfaro-Almagro, F., Glasser, M. F., . . . Smith, S. M. (2017). Hand classification of fMRI ICA noise components. *Neuroimage, 154*, 188-205. doi:10.1016/j.neuroimage.2016.12.036

Griffanti, L., Salimi-Khorshidi, G., Beckmann, C. F., Auerbach, E. J., Douaud, G., Sexton, C. E., . . . Smith, S. M. (2014). ICA-based artefact removal and accelerated fMRI acquisition for improved resting state network imaging. *Neuroimage, 95*, 232-247. doi:10.1016/j.neuroimage.2014.03.034

Guo, Q., Owen, D. R., Rabiner, E. A., Turkheimer, F. E., & Gunn, R. N. (2014). A graphical method to compare the in vivo binding potential of PET radioligands in the absence of a reference region: application to C-11 PBR28 and F-18 PBR111 for TSPO imaging. *Journal of Cerebral Blood Flow and Metabolism, 34*(7), 1162-1168. doi:10.1038/jcbfm.2014.65

Hahn, K., Myers, N., Prigarin, S., Rodenacker, K., Kurz, A., Forstl, H., . . . Sorg, C. (2013). Selectively and progressively disrupted structural connectivity of functional brain networks in Alzheimer's disease - revealed by a novel framework to analyze edge

distributions of networks detecting disruptions with strong statistical evidence. *Neuroimage, 81*, 96-109. doi:10.1016/j.neuroimage.2013.05.011

Hamelin, L., Lagarde, J., Dorothee, G., Leroy, C., Labit, M., Comley, R. A., . . . Clinical, I. t. (2016). Early and protective microglial activation in Alzheimer's disease: a prospective study using 18F-DPA-714 PET imaging. *Brain, 139*(Pt 4), 1252-1264. doi:10.1093/brain/aww017

Hamelin, L., Lagarde, J., Dorothee, G., Potier, M. C., Corlier, F., Kuhnast, B., . . . Sarazin, M. (2018). Distinct dynamic profiles of microglial activation are associated with progression of Alzheimer's disease. *Brain, 141*(6), 1855-1870. doi:10.1093/brain/awy079

Hamelin, L., Lagrade, J., Dorothee, G., Leroy, C., Labit, M., Comley, R. A., . . . Sarazin, M. (2016). Early and Protective microglial activation in Alzheimer's disease: a prospective study using 18F-DPA-714 PET imaging. *Brain, 139*, 1252-1264. Retrieved from https://watermark.silverchair.com/api/watermark?token=AQECAHi208BE49Ooan9kkhW_Ercy7Dm3ZL_9Cf3qfKAc485ysgAAAfgwggH0BgkqhkiG9w0BBwagggHlMIIB4QIBADCCAdoGCSqGSIb3DQEHATAeBglghkgBZQMEAS4wEQQMuyteIP-6p7d4vy6dAgEQgIIBq-MeJ_kLiXVic8Ox_IRprMwd4-INBCbriE4orlCPmpQ9TF4iYoyAJ7zjx3iU-rEm120yziMQkInQDrcc5oi778gP51O2nGt3dYspTx62dTKyIO61ciHlieoLBHRRaRWN_TXdWfUqnGGY4skBs0C3BcUgVG2wMWjDuxf7T0yRa25TWdoejWe5B_UUqlwHGGrurXJ4TblJrFJL4PvCG4kFazGw0PTEJeuSDX2j2wAJhlgDjYZFfdsVcnN7-JCyyFy_4mOWT7AHlAPaY1MZ6CmWhlSmjwXwvy-ciq3waRmp41dcP_0TO3D8FwNwGksTJej513VwYNBR2g2OMmE0YdIJ-X7y1l2mb_9gix-7F8w4zr-4qdtCm1WzN1pIzthHOY2vYapgSspgDLTG_ADq0SG2rgdqo8iqd3Kn7vkG9QUYCyA0g80fyjTLyQjOz6aqDyRQbD1w2m2sI1NNpf8EYSdfthhtIss1r2q-8x1DOcL2uqPm7xqCNWHe6xYIIVZ-dBMQeJa_UsgVd25OlEnrgiTc9y-0HYTfpBlCUbn-SN5YrlQIl3pDFw76eXHocX8

Hanisch, U. K. (2002). Microglia as a source and target of cytokines. *Glia, 40*(2), 140-155. doi:10.1002/glia.10161

Hardy, J., & Selkoe, D. J. (2002). Medicine - The amyloid hypothesis of Alzheimer's disease: Progress and problems on the road to therapeutics. *Science, 297*(5580), 353-356. doi:DOI 10.1126/science.1072994

Harsan, L. A., Poulet, P., Guignard, B., Steibel, J., Parizel, N., de Sousa, P. L., . . . Ghandour, M. S. (2006). Brain dysmyelination and recovery assessment by noninvasive in vivo diffusion tensor magnetic resonance imaging. *Journal of Neuroscience Research, 83*(3), 392-402. doi:10.1002/jnr.20742

Hawcroft, G., Gardner, S. H., & Hull, M. A. (2003). Activation of peroxisome proliferator-activated receptor gamma does not explain the antiproliferative activity of the nonsteroidal anti-inflammatory drug indomethacin on human colorectal cancer cells. *Journal of Pharmacology and Experimental Therapeutics, 305*(2), 632-637. doi:10.1124/jpet.103.048769

Hayes, A., Thaker, U., Iwatsubo, T., Pickering-Brown, S. M., & Mann, D. M. (2002). Pathological relationships between microglial cell activity and tau and amyloid beta protein in patients with Alzheimer's disease. *Neurosci Lett, 331*(3), 171-174. Retrieved from https://ac.els-cdn.com/S0304394002008881/1-s2.0-

S0304394002008881-main.pdf?_tid=55c3bf93-b378-429a-b19c-b57d141db33d&acdnat=1545041318_f1b2b5e1f32a27a429ba1e86d5b05151
Hedden, T., Van Dijk, K. R., Becker, J. A., Mehta, A., Sperling, R. A., Johnson, K. A., & Buckner, R. L. (2009). Disruption of functional connectivity in clinically normal older adults harboring amyloid burden. *J Neurosci, 29*(40), 12686-12694. doi:10.1523/JNEUROSCI.3189-09.2009
Heneka, M. T., Carson, M. J., El Khoury, J., Landreth, G. E., Brosseron, F., Feinstein, D. L., . . . Kummer, M. P. (2015). Neuroinflammation in Alzheimer's disease. *Lancet Neurol, 14*(4), 388-405. doi:10.1016/s1474-4422(15)70016-5
Heneka, M. T., Kummer, M. P., & Latz, E. (2014). Innate immune activation in neurodegenerative disease. *Nature Reviews Immunology, 14*(7), 463-477. doi:10.1038/nri3705
Heneka, M. T., Kummer, M. P., Stutz, A., Delekate, A., Schwartz, S., Vieira-Saecker, A., . . . Golenbock, D. T. (2013). NLRP3 is activated in Alzheimer's disease and contributes to pathology in APP/PS1 mice. *Nature, 493*(7434), 674-+. doi:10.1038/nature11729
Henjum, K., Almdahl, I. S., Arskog, V., Minthon, L., Hansson, O., Fladby, T., & Nilsson, L. N. (2016). Cerebrospinal fluid soluble TREM2 in aging and Alzheimer's disease. *Alzheimers Res Ther, 8*(1), 17. doi:10.1186/s13195-016-0182-1
Hollingworth, P., Harold, D., Sims, R., Gerrish, A., Lambert, J. C., Carrasquillo, M. M., . . . Consortium, E. (2011). Common variants at ABCA7, MS4A6A/MS4A4E, EPHA1, CD33 and CD2AP are associated with Alzheimer's disease. *Nature Genetics, 43*(5), 429-+. doi:10.1038/ng.803
Hong, S., Beja-Glasser, V. F., Nfonoyim, B. M., Frouin, A., Li, S. M., Ramakrishnan, S., . . . Stevens, B. (2016). Complement and microglia mediate early synapse loss in Alzheimer mouse models. *Science, 352*(6286), 712-716. doi:10.1126/science.aad8373
Hong, Y. J., Kim, C. M., Jang, E. H., Hwang, J., Roh, J. H., & Lee, J. H. (2016). White Matter Changes May Precede Gray Matter Loss in Elderly with Subjective Memory Impairment. *Dement Geriatr Cogn Disord, 42*(3-4), 227-235. doi:10.1159/000450749
Hopperton, K. E., Mohammad, D., Trepanier, M. O., Giuliano, V., & Bazinet, R. P. (2018). Markers of microglia in post-mortem brain samples from patients with Alzheimer's disease: a systematic review. *Mol Psychiatry, 23*(2), 177-198. doi:10.1038/mp.2017.246
Horwitz, B. (2003). The elusive concept of brain connectivity. *Neuroimage, 19*(2 Pt 1), 466-470. doi:10.1016/s1053-8119(03)00112-5
Humphries, M. D., & Gurney, K. (2008). Network 'small-world-ness': a quantitative method for determining canonical network equivalence. *PLoS One, 3*(4), e0002051. doi:10.1371/journal.pone.0002051
Hutton, C., Bork, A., Josephs, O., Deichmann, R., Ashburner, J., & Turner, R. (2002). Image distortion correction in fMRI: A quantitative evaluation. *Neuroimage, 16*(1), 217-240. doi:10.1006/nimg.2001.1054
Iadecola, C. (2004). Neurovascular regulation in the normal brain and in Alzheimer's disease. *Nat Rev Neurosci, 5*(5), 347-360. doi:10.1038/nrn1387
Iba, M., Guo, J. L., McBride, J. D., Zhang, B., Trojanowski, J. Q., & Lee, V. M. (2013). Synthetic tau fibrils mediate transmission of neurofibrillary tangles in a transgenic mouse model of Alzheimer's-like tauopathy. *J Neurosci, 33*(3), 1024-1037. doi:10.1523/JNEUROSCI.2642-12.2013

Iida, H., Higano, S., Tomura, N., Shishido, F., Kanno, I., Miura, S., . . . Uemura, K. (1988). Evaluation of regional differences of tracer appearance time in cerebral tissues using [15O] water and dynamic positron emission tomography. *J Cereb Blood Flow Metab, 8*(2), 285-288. doi:10.1038/jcbfm.1988.60

Ising, C., Venegas, C., Zhang, S., Scheiblich, H., Schmidt, S. V., Vieira-Saecker, A., . . . Heneka, M. T. (2019). NLRP3 inflammasome activation drives tau pathology. *Nature, 575*(7784), 669-673. doi:10.1038/s41586-019-1769-z

Ismail, R., Parbo, P., Madsen, L. S., Hansen, A. K., Hansen, K. V., Schaldemose, J. L., . . . Brooks, D. J. (2020). The relationships between neuroinflammation, beta-amyloid and tau deposition in Alzheimer's disease: a longitudinal PET study. *Journal of Neuroinflammation, 17*(1), 151. doi:10.1186/s12974-020-01820-6

Iturria-Medina, Y., Sotero, R. C., Toussaint, P. J., Evans, A. C., & Alzheimer's Disease Neuroimaging, I. (2014). Epidemic spreading model to characterize misfolded proteins propagation in aging and associated neurodegenerative disorders. *PLoS Comput Biol, 10*(11), e1003956. doi:10.1371/journal.pcbi.1003956

Jack, C. R., Jr., Bennett, D. A., Blennow, K., Carrillo, M. C., Dunn, B., Haeberlein, S. B., . . . Contributors. (2018). NIA-AA Research Framework: Toward a biological definition of Alzheimer's disease. *Alzheimers Dement, 14*(4), 535-562. doi:10.1016/j.jalz.2018.02.018

Jack, C. R., Jr., Knopman, D. S., Jagust, W. J., Petersen, R. C., Weiner, M. W., Aisen, P. S., . . . Trojanowski, J. Q. (2013). Tracking pathophysiological processes in Alzheimer's disease: an updated hypothetical model of dynamic biomarkers. *Lancet Neurol, 12*(2), 207-216. doi:10.1016/S1474-4422(12)70291-0

Jacobs, H. I. L., Hedden, T., Schultz, A. P., Sepulcre, J., Perea, R. D., Amariglio, R. E., . . . Johnson, K. A. (2018). Structural tract alterations predict downstream tau accumulation in amyloid-positive older individuals. *Nature Neuroscience, 21*(3), 424-431. doi:10.1038/s41593-018-0070-z

Jay, T. R., Miller, C. M., Cheng, P. J., Graham, L. C., Bemiller, S., Broihier, M. L., . . . Lamb, B. T. (2015). TREM2 deficiency eliminates TREM2(+) inflammatory macrophages and ameliorates pathology in Alzheimer's disease mouse models. *Journal of Experimental Medicine, 212*(3), 287-295. doi:10.1084/jem.20142322

Jay, T. R., von Saucken, V. E., & Landreth, G. E. (2017). TREM2 in Neurodegenerative Diseases. *Molecular Neurodegeneration, 12*. doi:10.1186/s13024-017-0197-5

Jenkinson, M., Bannister, P., Brady, M., & Smith, S. (2002). Improved optimization for the robust and accurate linear registration and motion correction of brain images. *Neuroimage, 17*(2), 825-841. doi:10.1016/s1053-8119(02)91132-8

Jenkinson, M., & Smith, S. (2001). A global optimisation method for robust affine registration of brain images. *Med Image Anal, 5*(2), 143-156. doi:10.1016/s1361-8415(01)00036-6

Jessen, N. A., Munk, A. S., Lundgaard, I., & Nedergaard, M. (2015). The Glymphatic System: A Beginner's Guide. *Neurochem Res, 40*(12), 2583-2599. doi:10.1007/s11064-015-1581-6

Jezzard, P., Barnett, A. S., & Pierpaoli, C. (1998). Characterization of and correction for eddy current artifacts in echo planar diffusion imaging. *Magn Reson Med, 39*(5), 801-812. doi:10.1002/mrm.1910390518

Ji, B., Maeda, J., Sawada, M., Ono, M., Okauchi, T., Inaji, M., . . . Suhara, T. (2008). Imaging of peripheral benzodiazepine receptor expression as biomarkers of detrimental versus

beneficial glial responses in mouse models of Alzheimer's and other CNS pathologies. *J Neurosci, 28*(47), 12255-12267. doi:10.1523/jneurosci.2312-08.2008

Jo, S., Yarishkin, O., Hwang, Y. J., Chun, Y. E., Park, M., Woo, D. H., . . . Lee, C. J. (2014). GABA from reactive astrocytes impairs memory in mouse models of Alzheimer's disease. *Nat Med, 20*(8), 886-896. doi:10.1038/nm.3639

Johnson, V. E., Stewart, J. E., Begbie, F. D., Trojanowski, J. Q., Smith, D. H., & Stewart, W. (2013). Inflammation and white matter degeneration persist for years after a single traumatic brain injury. *Brain, 136*(Pt 1), 28-42. doi:10.1093/brain/aws322

Jones, D. T., Knopman, D. S., Gunter, J. L., Graff-Radford, J., Vemuri, P., Boeve, B. F., . . . Alzheimer's Disease Neuroimaging, I. (2016). Cascading network failure across the Alzheimer's disease spectrum. *Brain, 139*(Pt 2), 547-562. doi:10.1093/brain/awv338

Jonsson, T., Stefansson, H., Steinberg, S., Jonsdottir, I., Jonsson, P. V., Snaedal, J., . . . Stefansson, K. (2013). Variant of TREM2 Associated with the Risk of Alzheimer's Disease. *New England Journal of Medicine, 368*(2), 107-116. doi:10.1056/NEJMoa1211103

Junck, L., Olson, J. M. M., Ciliax, B. J., Koeppe, R. A., Watkins, G. L., Jewett, D. M., . . . Young, A. B. (1989). Pet Imaging of Human Gliomas with Ligands for the Peripheral Benzodiazepine Binding-Site. *Annals of Neurology, 26*(6), 752-758. doi:DOI 10.1002/ana.410260611

Kamenetz, F., Tomita, T., Hsieh, H., Seabrook, G., Borchelt, D., Iwatsubo, T., . . . Malinow, R. (2003a). APP processing and synaptic function. *Neuron, 37*(6), 925-937. doi:10.1016/s0896-6273(03)00124-7

Kamenetz, F., Tomita, T., Hsieh, H., Seabrook, G., Borchelt, D., Iwatsubo, T., . . . Malinow, R. (2003b). APP processing and synaptic function. *Neuron, 37*(6), 925-937. doi:10.1016/s0896-6273(03)00124-7

Kantarci, K., Murray, M. E., Schwarz, C. G., Reid, R. I., Przybelski, S. A., Lesnick, T., . . . Dickson, D. W. (2017). White-matter integrity on DTI and the pathologic staging of Alzheimer's disease. *Neurobiol Aging, 56*, 172-179. doi:10.1016/j.neurobiolaging.2017.04.024

Kaufman, S. K., Del Tredici, K., Thomas, T. L., Braak, H., & Diamond, M. I. (2018). Tau seeding activity begins in the transentorhinal/entorhinal regions and anticipates phospho-tau pathology in Alzheimer's disease and PART. *Acta Neuropathol, 136*(1), 57-67. doi:10.1007/s00401-018-1855-6

Keren-Shaul, H., Spinrad, A., Weiner, A., Matcovitch-Natan, O., Dvir-Szternfeld, R., Ulland, T. K., . . . Amit, I. (2017). A Unique Microglia Type Associated with Restricting Development of Alzheimer's Disease. *Cell, 169*(7), 1276-1290 e1217. doi:10.1016/j.cell.2017.05.018

Khazaee, A., Ebrahimzadeh, A., & Babajani-Feremi, A. (2015). Identifying patients with Alzheimer's disease using resting-state fMRI and graph theory. *Clin Neurophysiol, 126*(11), 2132-2141. doi:10.1016/j.clinph.2015.02.060

Kierdorf, K., Erny, D., Goldmann, T., Sander, V., Schulz, C., Perdiguero, E. G., . . . Prinz, M. (2013). Microglia emerge from erythromyeloid precursors via Pu.1- and Irf8-dependent pathways. *Nature Neuroscience, 16*(3), 273-280. doi:10.1038/nn.3318

Kim, C. C., Nakamura, M. C., & Hsieh, C. L. (2016). Brain trauma elicits non-canonical macrophage activation states. *J Neuroinflammation, 13*(1), 117. doi:10.1186/s12974-016-0581-z

Kisler, K., Nelson, A. R., Montagne, A., & Zlokovic, B. V. (2017). Cerebral blood flow regulation and neurovascular dysfunction in Alzheimer disease. *Nat Rev Neurosci, 18*(7), 419-434. doi:10.1038/nrn.2017.48

Kitazawa, M., Yamasaki, T. R., & LaFerla, F. M. (2004). Microglia as a potential bridge between the amyloid beta-peptide and tau. *Ann N Y Acad Sci, 1035*, 85-103. doi:10.1196/annals.1332.006

Koenigsknecht, J., & Landreth, G. (2004). Microglial phagocytosis of fibrillar beta-amyloid through a beta1 integrin-dependent mechanism. *J Neurosci, 24*(44), 9838-9846. doi:10.1523/JNEUROSCI.2557-04.2004

Krasemann, S., Madore, C., Cialic, R., Baufeld, C., Calcagno, N., El Fatimy, R., . . . Butovsky, O. (2017). The TREM2-APOE Pathway Drives the Transcriptional Phenotype of Dysfunctional Microglia in Neurodegenerative Diseases. *Immunity, 47*(3), 566-+. doi:10.1016/j.immuni.2017.08.008

Kreisl, W. C., Henter, I. D., & Innis, R. B. (2018). Imaging Translocator Protein as a Biomarker of Neuroinflammation in Dementia. *Adv Pharmacol, 82*, 163-185. doi:10.1016/bs.apha.2017.08.004

Kreisl, W. C., Jenko, K. J., Hines, C. S., Lyoo, C. H., Corona, W., Morse, C. L., . . . Biomarkers Consortium, P. E. T. R. (2013). A genetic polymorphism for translocator protein 18 kDa affects both in vitro and in vivo radioligand binding in human brain to this putative biomarker of neuroinflammation. *Journal of Cerebral Blood Flow and Metabolism, 33*(1), 53-58. doi:10.1038/jcbfm.2012.131

Kreisl, W. C., Jenko, K. J., Hines, C. S., Lyoo, C. H., Corona, W., Morse, C. L., . . . Radiolig, B. C. P. (2013). A genetic polymorphism for translocator protein 18 kDa affects both in vitro and in vivo radioligand binding in human brain to this putative biomarker of neuroinflammation. *Journal of Cerebral Blood Flow and Metabolism, 33*(1), 53-58. doi:10.1038/jcbfm.2012.131

Kreisl, W. C., Lyoo, C. H., Liow, J. S., Snow, J., Page, E., Jenko, K. J., . . . Innis, R. B. (2017). Distinct patterns of increased translocator protein in posterior cortical atrophy and amnestic Alzheimer ' s disease. *Neurobiology of Aging, 51*, 132-140. doi:10.1016/j.neurobiolaging.2016.12.006

Kreisl, W. C., Lyoo, C. H., Liow, J. S., Wei, M., Snow, J., Page, E., . . . Innis, R. B. (2016a). (11)C-PBR28 binding to translocator protein increases with progression of Alzheimer's disease. *Neurobiol Aging, 44*, 53-61. doi:10.1016/j.neurobiolaging.2016.04.011

Kreisl, W. C., Lyoo, C. H., Liow, J. S., Wei, M., Snow, J., Page, E., . . . Innis, R. B. (2016b). C-11-PBR28 binding to translocator protein increases with progression of Alzheimer's disease. *Neurobiology of Aging, 44*, 53-61. doi:10.1016/j.neurobiolaging.2016.04.011

Kreisl, W. C., Lyoo, C. H., McGwier, M., Snow, J., Jenko, K. J., Kimura, N., . . . Biomarkers Consortium, P. E. T. R. P. T. (2013). In vivo radioligand binding to translocator protein correlates with severity of Alzheimer's disease. *Brain, 136*(Pt 7), 2228-2238. doi:10.1093/brain/awt145

La Joie, R., Visani, A. V., Baker, S. L., Brown, J. A., Bourakova, V., Cha, J., . . . Rabinovici, G. D. (2020). Prospective longitudinal atrophy in Alzheimer's disease correlates with the intensity and topography of baseline tau-PET. *Sci Transl Med, 12*(524). doi:10.1126/scitranslmed.aau5732

Lambert, J. C., Ibrahim-Verbaas, C. A., Harold, D., Naj, A. C., Sims, R., Bellenguez, C., . . . Charge. (2013). Meta-analysis of 74,046 individuals identifies 11 new susceptibility

loci for Alzheimer's disease. *Nature Genetics, 45*(12), 1452-U1206. doi:10.1038/ng.2802

Lannfelt, L., Relkin, N. R., & Siemers, E. R. (2014). Amyloid-ss-directed immunotherapy for Alzheimer's disease. *J Intern Med, 275*(3), 284-295. doi:10.1111/joim.12168

Latora, V., & Marchiori, M. (2001). Efficient behavior of small-world networks. *Phys Rev Lett, 87*(19), 198701. doi:10.1103/PhysRevLett.87.198701

Le Bihan, D., Mangin, J. F., Poupon, C., Clark, C. A., Pappata, S., Molko, N., & Chabriat, H. (2001). Diffusion tensor imaging: concepts and applications. *J Magn Reson Imaging, 13*(4), 534-546. doi:10.1002/jmri.1076

Lee, C. Y. D., Daggett, A., Gu, X. F., Jiang, L. L., Langfelder, P., Li, X. G., . . . Yang, X. W. (2018). Elevated TREM2 Gene Dosage Reprograms Microglia Responsivity and Ameliorates Pathological Phenotypes in Alzheimer's Disease Models. *Neuron, 97*(5), 1032-+. doi:10.1016/j.neuron.2018.02.002

Lee, S., Xu, G. X., Jay, T. R., Bhatta, S., Kim, K. W., Jung, S., . . . Lamb, B. T. (2014). Opposing Effects of Membrane-Anchored CX3CL1 on Amyloid and Tau Pathologies via the p38 MAPK Pathway. *Journal of Neuroscience, 34*(37), 12538-12546. doi:10.1523/jneurosci.0853-14.2014

Leng, F., & Edison, P. (2021). Neuroinflammation and microglial activation in Alzheimer disease: where do we go from here? *Nat Rev Neurol, 17*(3), 157-172. doi:10.1038/s41582-020-00435-y

Liddelow, S. A., & Barres, B. A. (2017). Reactive Astrocytes: Production, Function, and Therapeutic Potential. *Immunity, 46*(6), 957-967. doi:10.1016/j.immuni.2017.06.006

Liddelow, S. A., Guttenplan, K. A., Clarke, L. E., Bennett, F. C., Bohlen, C. J., Schirmer, L., . . . Barres, B. A. (2017). Neurotoxic reactive astrocytes are induced by activated microglia. *Nature, 541*(7638), 481-487. doi:10.1038/nature21029

Lim, S. H., Park, E., You, B., Jung, Y., Park, A. R., Park, S. G., & Lee, J. R. (2013). Neuronal Synapse Formation Induced by Microglia and Interleukin 10. *PLoS One, 8*(11). doi:UNSP e81218

10.1371/journal.pone.0081218

Liu, L., Drouet, V., Wu, J. W., Witter, M. P., Small, S. A., Clelland, C., & Duff, K. (2012). Trans-synaptic spread of tau pathology in vivo. *PLoS One, 7*(2), e31302. doi:10.1371/journal.pone.0031302

Liu, L. R., Liu, J. C., Bao, J. S., Bai, Q. Q., & Wang, G. Q. (2020). Interaction of Microglia and Astrocytes in the Neurovascular Unit. *Front Immunol, 11*, 1024. doi:10.3389/fimmu.2020.01024

Liu, S., Liu, Y., Hao, W., Wolf, L., Kiliaan, A. J., Penke, B., . . . Fassbender, K. (2012). TLR2 is a primary receptor for Alzheimer's amyloid beta peptide to trigger neuroinflammatory activation. *J Immunol, 188*(3), 1098-1107. doi:10.4049/jimmunol.1101121

Liu, Y., Yu, C., Zhang, X., Liu, J., Duan, Y., Alexander-Bloch, A. F., . . . Bullmore, E. (2014). Impaired long distance functional connectivity and weighted network architecture in Alzheimer's disease. *Cereb Cortex, 24*(6), 1422-1435. doi:10.1093/cercor/bhs410

Lo, C. Y., Wang, P. N., Chou, K. H., Wang, J., He, Y., & Lin, C. P. (2010). Diffusion tensor tractography reveals abnormal topological organization in structural cortical networks in Alzheimer's disease. *J Neurosci, 30*(50), 16876-16885. doi:10.1523/JNEUROSCI.4136-10.2010

Logan, J. (2000). Graphical analysis of PET data applied to reversible and irreversible tracers. *Nucl Med Biol, 27*(7), 661-670. doi:10.1016/s0969-8051(00)00137-2

Lope-Piedrafita, S. (2018). Diffusion Tensor Imaging (DTI). *Methods Mol Biol, 1718*, 103-116. doi:10.1007/978-1-4939-7531-0_7

Lui, H., Zhang, J., Makinson, S. R., Cahill, M. K., Kelley, K. W., Huang, H. Y., . . . Huang, E. J. (2016). Progranulin Deficiency Promotes Circuit-Specific Synaptic Pruning by Microglia via Complement Activation. *Cell, 165*(4), 921-935. doi:10.1016/j.cell.2016.04.001

Lustig, C., Snyder, A. Z., Bhakta, M., O'Brien, K. C., McAvoy, M., Raichle, M. E., . . . Buckner, R. L. (2003). Functional deactivations: Change with age and dementia of the Alzheimer type. *Proceedings of the National Academy of Sciences of the United States of America, 100*(24), 14504-14509. doi:10.1073/pnas.2235925100

Lyman, M., Lloyd, D. G., Ji, X., Vizcaychipi, M. P., & Ma, D. (2014). Neuroinflammation: the role and consequences. *Neurosci Res, 79*, 1-12. doi:10.1016/j.neures.2013.10.004

Lyoo, C. H., Ikawa, M., Liow, J. S., Zoghbi, S. S., Morse, C. L., Pike, V. W., . . . Kreisl, W. C. (2015a). Cerebellum Can Serve As a Pseudo-Reference Region in Alzheimer Disease to Detect Neuroinflammation Measured with PET Radioligand Binding to Translocator Protein. *J Nucl Med, 56*(5), 701-706. doi:10.2967/jnumed.114.146027

Lyoo, C. H., Ikawa, M., Liow, J. S., Zoghbi, S. S., Morse, C. L., Pike, V. W., . . . Kreisl, W. C. (2015b). Cerebellum Can Serve As a Pseudo-Reference Region in Alzheimer Disease to Detect Neuroinflammation Measured with PET Radioligand Binding to Translocator Protein. *Journal of Nuclear Medicine, 56*(5), 701-706. doi:10.2967/jnumed.114.146027

Maier, F. C., Wehrl, H. F., Schmid, A. M., Mannheim, J. G., Wiehr, S., Lerdkrai, C., . . . Pichler, B. J. (2014). Longitudinal PET-MRI reveals beta-amyloid deposition and rCBF dynamics and connects vascular amyloidosis to quantitative loss of perfusion. *Nat Med, 20*(12), 1485-1492. doi:10.1038/nm.3734

Malpetti, M., Kievit, R. A., Passamonti, L., Jones, P. S., Tsvetanov, K. A., Rittman, T., . . . Rowe, J. B. (2020). Microglial activation and tau burden predict cognitive decline in Alzheimer's disease. *Brain, 143*(5), 1588-1602. doi:10.1093/brain/awaa088

Marin, M. A., Ziburkus, J., Jankowsky, J., & Rasband, M. N. (2016). Amyloid-beta plaques disrupt axon initial segments. *Exp Neurol, 281*, 93-98. doi:10.1016/j.expneurol.2016.04.018

Martin, E., Boucher, C., Fontaine, B., & Delarasse, C. (2017). Distinct inflammatory phenotypes of microglia and monocyte-derived macrophages in Alzheimer's disease models: effects of aging and amyloid pathology. *Aging Cell, 16*(1), 27-38. doi:10.1111/acel.12522

Martinez, F. O., & Gordon, S. (2014). The M1 and M2 paradigm of macrophage activation: time for reassessment. *F1000Prime Rep, 6*, 13. doi:10.12703/P6-13

Mascali, D., DiNuzzo, M., Gili, T., Moraschi, M., Fratini, M., Maraviglia, B., . . . Giove, F. (2015). Intrinsic patterns of coupling between correlation and amplitude of low-frequency fMRI fluctuations are disrupted in degenerative dementia mainly due to functional disconnection. *PLoS One, 10*(4), e0120988. doi:10.1371/journal.pone.0120988

Masliah, E., Mallory, M., Hansen, L., Alford, M., Albright, T., Terry, R., . . . Saitoh, T. (1991). Immunoreactivity of Cd45, a Protein Phosphotyrosine Phosphatase, in Alzheimers-Disease. *Acta Neuropathologica, 83*(1), 12-20. doi:Doi 10.1007/Bf00294425

Masuda, T., Sankowski, R., Staszewski, O., Bottcher, C., Amann, L., Scheiwe, C., . . . Prinz, M. (2019). Spatial and temporal heterogeneity of mouse and human microglia at single-cell resolution. *Nature, 566*(7744), 388-392. doi:10.1038/s41586-019-0924-x

Matheson, G. J., Plaven-Sigray, P., Forsberg, A., Varrone, A., Farde, L., & Cervenka, S. (2017). Assessment of simplified ratio-based approaches for quantification of PET C-11 PBR28 data. *Ejnmmi Research, 7*. doi:10.1186/s13550-017-0304-1

Mathotaarachchi, S., Wang, S., Shin, M., Pascoal, T. A., Benedet, A. L., Kang, M. S., . . . Rosa-Neto, P. (2016). VoxelStats: A MATLAB Package for Multi-Modal Voxel-Wise Brain Image Analysis. *Front Neuroinform, 10*, 20. doi:10.3389/fninf.2016.00020

Mathys, H., Adaikkan, C., Gao, F., Young, J. Z., Manet, E., Hemberg, M., . . . Tsai, L. H. (2017). Temporal Tracking of Microglia Activation in Neurodegeneration at Single-Cell Resolution. *Cell Rep, 21*(2), 366-380. doi:10.1016/j.celrep.2017.09.039

Mattsson, N., Tosun, D., Insel, P. S., Simonson, A., Jack, C. R., Jr., Beckett, L. A., . . . Alzheimer's Disease Neuroimaging, I. (2014). Association of brain amyloid-beta with cerebral perfusion and structure in Alzheimer's disease and mild cognitive impairment. *Brain, 137*(Pt 5), 1550-1561. doi:10.1093/brain/awu043

Mcgeer, P. L., Itagaki, S., Tago, H., & Mcgeer, E. G. (1987). Reactive Microglia in Patients with Senile Dementia of Alzheimer Type Are Positive for the Histocompatibility Glycoprotein Hla-Dr. *Neuroscience Letters, 79*(1-2), 195-200. doi:Doi 10.1016/0304-3940(87)90696-3

McGeer, P. L., & McGeer, E. G. (2013). The amyloid cascade-inflammatory hypothesis of Alzheimer disease: implications for therapy. *Acta Neuropathol, 126*(4), 479-497. doi:10.1007/s00401-013-1177-7

McKeown, M. J., & Sejnowski, T. J. (1998). Independent component analysis of fMRI data: examining the assumptions. *Hum Brain Mapp, 6*(5-6), 368-372. Retrieved from https://www.ncbi.nlm.nih.gov/pubmed/9788074

McKhann, G., Drachman, D., Folstein, M., Katzman, R., Price, D., & Stadlan, E. M. (1984). Clinical diagnosis of Alzheimer's disease: report of the NINCDS-ADRDA Work Group under the auspices of Department of Health and Human Services Task Force on Alzheimer's Disease. *Neurology, 34*(7), 939-944. doi:10.1212/wnl.34.7.939

McKhann, G. M., Knopman, D. S., Chertkow, H., Hyman, B. T., Jack, C. R., Jr., Kawas, C. H., . . . Phelps, C. H. (2011). The diagnosis of dementia due to Alzheimer's disease: recommendations from the National Institute on Aging-Alzheimer's Association workgroups on diagnostic guidelines for Alzheimer's disease. *Alzheimers Dement, 7*(3), 263-269. doi:10.1016/j.jalz.2011.03.005

Melah, K. E., Lu, S. Y., Hoscheidt, S. M., Alexander, A. L., Adluru, N., Destiche, D. J., . . . Bendlin, B. B. (2016). Cerebrospinal Fluid Markers of Alzheimer's Disease Pathology and Microglial Activation are Associated with Altered White Matter Microstructure in Asymptomatic Adults at Risk for Alzheimer's Disease. *J Alzheimers Dis, 50*(3), 873-886. doi:10.3233/JAD-150897

Meyer-Luehmann, M., Spires-Jones, T. L., Prada, C., Garcia-Alloza, M., de Calignon, A., Rozkalne, A., . . . Hyman, B. T. (2008). Rapid appearance and local toxicity of amyloid-beta plaques in a mouse model of Alzheimer's disease. *Nature, 451*(7179), 720-724. doi:10.1038/nature06616

Micheau, O., & Tschopp, J. (2003). Induction of TNF receptor I-mediated apoptosis via two sequential signaling complexes. *Cell, 114*(2), 181-190. Retrieved from https://www.ncbi.nlm.nih.gov/pubmed/12887920

https://www.hal.inserm.fr/inserm-00527105/document
Michell-Robinson, M. A., Touil, H., Healy, L. M., Owen, D. R., Durafourt, B. A., Bar-Or, A., . . . Moore, C. S. (2015). Roles of microglia in brain development, tissue maintenance and repair. *Brain, 138*(Pt 5), 1138-1159. doi:10.1093/brain/awv066
Minett, T., Classey, J., Matthews, F. E., Fahrenhold, M., Taga, M., Brayne, C., . . . Mrc, C. (2016). Microglial immunophenotype in dementia with Alzheimer's pathology. *J Neuroinflammation, 13*(1), 135. doi:10.1186/s12974-016-0601-z
Mishra, A., Kim, H. J., Shin, A. H., & Thayer, S. A. (2012). Synapse loss induced by interleukin-1beta requires pre- and post-synaptic mechanisms. *J Neuroimmune Pharmacol, 7*(3), 571-578. doi:10.1007/s11481-012-9342-7
Mito, R., Raffelt, D., Dhollander, T., Vaughan, D. N., Tournier, J. D., Salvado, O., . . . Connelly, A. (2018). Fibre-specific white matter reductions in Alzheimer's disease and mild cognitive impairment. *Brain*. doi:10.1093/brain/awx355
Mittal, P., Singh, N., Chaturvedi, S., Jyoti, A., Mishra, A. K., & Hazari, P. P. (2021). Comprehensive review on design perspective of PET ligands based on beta-amyloids, tau and neuroinflammation for diagnostic intervention of Alzheimer's disease. *Clinical and Translational Imaging, 9*(2), 153-175. doi:10.1007/s40336-021-00410-7
Miyamoto, A., Wake, H., Ishikawa, A. W., Eto, K., Shibata, K., Murakoshi, H., . . . Nabekura, J. (2016). Microglia contact induces synapse formation in developing somatosensory cortex. *Nature Communications, 7*. doi:ARTN 12540

10.1038/ncomms12540
Morales, I., Jimenez, J. M., Mancilla, M., & Maccioni, R. B. (2013). Tau oligomers and fibrils induce activation of microglial cells. *J Alzheimers Dis, 37*(4), 849-856. doi:10.3233/jad-131843
Mori, S., Oishi, K., Jiang, H., Jiang, L., Li, X., Akhter, K., . . . Mazziotta, J. (2008). Stereotaxic white matter atlas based on diffusion tensor imaging in an ICBM template. *Neuroimage, 40*(2), 570-582. doi:10.1016/j.neuroimage.2007.12.035
Murgas, P., Godoy, B., & von Bernhardi, R. (2012). Abeta potentiates inflammatory activation of glial cells induced by scavenger receptor ligands and inflammatory mediators in culture. *Neurotox Res, 22*(1), 69-78. doi:10.1007/s12640-011-9306-3
Nair, A., Veronese, M., Xu, X. H., Curtis, C., Turkheimer, F., Howard, R., & Reeves, S. (2016). Test-retest analysis of a non-invasive method of quantifying C-11 -PBR28 binding in Alzheimer's disease. *Ejnmmi Research, 6*. doi:10.1186/s13550-016-0226-3
Navarro, V., Sanchez-Mejias, E., Jimenez, S., Munoz-Castro, C., Sanchez-Varo, R., Davila, J. C., . . . Vitorica, J. (2018). Microglia in Alzheimer's Disease: Activated, Dysfunctional or Degenerative. *Front Aging Neurosci, 10*, 140. doi:10.3389/fnagi.2018.00140
Nave, K. A., & Werner, H. B. (2014). Myelination of the nervous system: mechanisms and functions. *Annu Rev Cell Dev Biol, 30*, 503-533. doi:10.1146/annurev-cellbio-100913-013101
Neniskyte, U., Neher, J. J., & Brown, G. C. (2011). Neuronal death induced by nanomolar amyloid beta is mediated by primary phagocytosis of neurons by microglia. *J Biol Chem, 286*(46), 39904-39913. doi:10.1074/jbc.M111.267583
Nimmerjahn, A., Kirchhoff, F., & Helmchen, F. (2005). Resting microglial cells are highly dynamic surveillants of brain parenchyma in vivo. *Science, 308*(5726), 1314-1318. doi:10.1126/science.1110647

Nir, Y., Mukamel, R., Dinstein, I., Privman, E., Harel, M., Fisch, L., . . . Malach, R. (2008). Interhemispheric correlations of slow spontaneous neuronal fluctuations revealed in human sensory cortex. *Nature Neuroscience, 11*(9), 1100-1108. doi:10.1038/nn.2177

Nortley, R., Korte, N., Izquierdo, P., Hirunpattarasilp, C., Mishra, A., Jaunmuktane, Z., . . . Attwell, D. (2019). Amyloid beta oligomers constrict human capillaries in Alzheimer's disease via signaling to pericytes. *Science, 365*(6450). doi:10.1126/science.aav9518

Nuriel, T., Angulo, S. L., Khan, U., Ashok, A., Chen, Q., Figueroa, H. Y., . . . Duff, K. E. (2017). Neuronal hyperactivity due to loss of inhibitory tone in APOE4 mice lacking Alzheimer's disease-like pathology. *Nature Communications, 8*(1), 1464. doi:10.1038/s41467-017-01444-0

Ogawa, S., Lee, T. M., Nayak, A. S., & Glynn, P. (1990). Oxygenation-sensitive contrast in magnetic resonance image of rodent brain at high magnetic fields. *Magn Reson Med, 14*(1), 68-78. doi:10.1002/mrm.1910140108

Okello, A., Edison, P., Archer, H. A., Turkheimer, F. E., Kennedy, J., Bullock, R., . . . Brooks, D. J. (2009). Microglial activation and amyloid deposition in mild cognitive impairment A PET study. *Neurology, 72*(1), 56-62. doi:10.1212/01.wnl.0000338622.27876.0d

Olsson, B., Lautner, R., Andreasson, U., Ohrfelt, A., Portelius, E., Bjerke, M., . . . Zetterberg, H. (2016). CSF and blood biomarkers for the diagnosis of Alzheimer's disease: a systematic review and meta-analysis. *Lancet Neurol, 15*(7), 673-684. doi:10.1016/S1474-4422(16)00070-3

Ossenkoppele, R., Iaccarino, L., Schonhaut, D. R., Brown, J. A., La Joie, R., O'Neil, J. P., . . . Rabinovici, G. D. (2019). Tau covariance patterns in Alzheimer's disease patients match intrinsic connectivity networks in the healthy brain. *Neuroimage Clin, 23*, 101848. doi:10.1016/j.nicl.2019.101848

Ostergaard, L., Aamand, R., Gutierrez-Jimenez, E., Ho, Y. C., Blicher, J. U., Madsen, S. M., . . . West, M. J. (2013). The capillary dysfunction hypothesis of Alzheimer's disease. *Neurobiol Aging, 34*(4), 1018-1031. doi:10.1016/j.neurobiolaging.2012.09.011

Owen, D. R., Yeo, A. J., Gunn, R. N., Song, K., Wadsworth, G., Lewis, A., . . . Rubio, J. P. (2012). An 18-kDa Translocator Protein (TSPO) polymorphism explains differences in binding affinity of the PET radioligand PBR28. *Journal of Cerebral Blood Flow and Metabolism, 32*(1), 1-5. doi:10.1038/jcbfm.2011.147

Owen, D. R. J., Gunn, R. N., Rabiner, E. A., Bennacef, I., Fujita, M., Kreisl, W. C., . . . Parker, C. A. (2011). Mixed-Affinity Binding in Humans with 18-kDa Translocator Protein Ligands. *Journal of Nuclear Medicine, 52*(1), 24-32. doi:10.2967/jnumed.110.079459

Owens, T., Khorooshi, R., Wlodarczyk, A., & Asgari, N. (2014). Interferons in the Central Nervous System: A Few Instruments Play Many Tunes. *Glia, 62*(3), 339-355. doi:10.1002/glia.22608

Paganoni, S., Alshikho, M. J., Zurcher, N. R., Cernasov, P., Babu, S., Loggia, M. L., . . . Atassi, N. (2018). Imaging of glia activation in people with primary lateral sclerosis. *Neuroimage-Clinical, 17*, 347-353. doi:10.1016/j.nicl.2017.10.024

Palmqvist, S., Scholl, M., Strandberg, O., Mattsson, N., Stomrud, E., Zetterberg, H., . . . Hansson, O. (2017). Earliest accumulation of beta-amyloid occurs within the default-mode network and concurrently affects brain connectivity. *Nature Communications, 8*(1), 1214. doi:10.1038/s41467-017-01150-x

Palop, J. J., Chin, J., & Mucke, L. (2006). A network dysfunction perspective on neurodegenerative diseases. *Nature, 443*(7113), 768-773. doi:10.1038/nature05289

Palop, J. J., & Mucke, L. (2010). Amyloid-beta-induced neuronal dysfunction in Alzheimer's disease: from synapses toward neural networks. *Nature Neuroscience, 13*(7), 812-818. doi:10.1038/nn.2583

Pan, X. D., Zhu, Y. G., Lin, N., Zhang, J., Ye, Q. Y., Huang, H. P., & Chen, X. C. (2011). Microglial phagocytosis induced by fibrillar beta-amyloid is attenuated by oligomeric beta-amyloid: implications for Alzheimer's disease. *Molecular Neurodegeneration, 6*. doi:Artn 45

10.1186/1750-1326-6-45

Parbo, P., Ismail, R., Sommerauer, M., Stokholm, M. G., Hansen, A. K., Hansen, K. V., . . . Brooks, D. J. (2018). Does inflammation precede tau aggregation in early Alzheimer's disease? A PET study. *Neurobiol Dis, 117*, 211-216. doi:10.1016/j.nbd.2018.06.004

Paresce, D. M., Chung, H. Y., & Maxfield, F. R. (1997). Slow degradation of aggregates of the Alzheimer's disease amyloid beta-protein by microglial cells. *Journal of Biological Chemistry, 272*(46), 29390-29397. doi:DOI 10.1074/jbc.272.46.29390

Parkhurst, C. N., Yang, G., Ninan, I., Savas, J. N., Yates, J. R., Lafaille, J. J., . . . Gan, W. B. (2013). Microglia Promote Learning-Dependent Synapse Formation through Brain-Derived Neurotrophic Factor. *Cell, 155*(7), 1596-1609. doi:10.1016/j.cell.2013.11.030

Pascual, O., Ben Achour, S., Rostaing, P., Triller, A., & Bessis, A. (2012). Microglia activation triggers astrocyte-mediated modulation of excitatory neurotransmission. *Proceedings of the National Academy of Sciences of the United States of America, 109*(4), E197-E205. doi:10.1073/pnas.1111098109

Passamonti, L., Tsvetanov, K. A., Jones, P. S., Bevan-Jones, W. R., Arnold, R., Borchert, R. J., . . . Rowe, J. B. (2019). Neuroinflammation and Functional Connectivity in Alzheimer's Disease: Interactive Influences on Cognitive Performance. *J Neurosci, 39*(36), 7218-7226. doi:10.1523/JNEUROSCI.2574-18.2019

Peferoen, L., Kipp, M., van der Valk, P., van Noort, J. M., & Amor, S. (2014). Oligodendrocyte-microglia cross-talk in the central nervous system. *Immunology, 141*(3), 302-313. doi:10.1111/imm.12163

Pekny, M., Pekna, M., Messing, A., Steinhauser, C., Lee, J. M., Parpura, V., . . . Verkhratsky, A. (2016). Astrocytes: a central element in neurological diseases. *Acta Neuropathol, 131*(3), 323-345. doi:10.1007/s00401-015-1513-1

Pekny, M., Wilhelmsson, U., & Pekna, M. (2014). The dual role of astrocyte activation and reactive gliosis. *Neurosci Lett, 565*, 30-38. doi:10.1016/j.neulet.2013.12.071

Pfeiffer, T., Avignone, E., & Nagerl, U. V. (2016). Induction of hippocampal long-term potentiation increases the morphological dynamics of microglial processes and prolongs their contacts with dendritic spines. *Scientific Reports, 6*. doi:ARTN 32422

10.1038/srep32422

Philippens, I. H., Ormel, P. R., Baarends, G., Johansson, M., Remarque, E. J., & Doverskog, M. (2017). Acceleration of Amyloidosis by Inflammation in the Amyloid-Beta Marmoset Monkey Model of Alzheimer's Disease. *J Alzheimers Dis, 55*(1), 101-113. doi:10.3233/jad-160673

Plaza-Zabala, A., Sierra-Torre, V., & Sierra, A. (2017). Autophagy and Microglia: Novel Partners in Neurodegeneration and Aging. *International Journal of Molecular Sciences, 18*(3). doi:10.3390/ijms18030598

Plescher, M., Seifert, G., Hansen, J. N., Bedner, P., Steinhauser, C., & Halle, A. (2018). Plaque-dependent morphological and electrophysiological heterogeneity of microglia in an Alzheimer's disease mouse model. *Glia, 66*(7), 1464-1480. doi:10.1002/glia.23318

Posfai, B., Cserep, C., Orsolits, B., & Denes, A. (2019). New Insights into Microglia-Neuron Interactions: A Neuron's Perspective. *Neuroscience, 405*, 103-117. doi:10.1016/j.neuroscience.2018.04.046

Prokop, S., Miller, K. R., Labra, S. R., Pitkin, R. M., Hoxha, K., Narasimhan, S., . . . Trojanowski, J. Q. (2019). Impact of TREM2 risk variants on brain region-specific immune activation and plaque microenvironment in Alzheimer's disease patient brain samples. *Acta Neuropathol, 138*(4), 613-630. doi:10.1007/s00401-019-02048-2

Qi, Z., Wu, X., Wang, Z., Zhang, N., Dong, H., Yao, L., & Li, K. (2010). Impairment and compensation coexist in amnestic MCI default mode network. *Neuroimage, 50*(1), 48-55. doi:10.1016/j.neuroimage.2009.12.025

Racine, A. M., Adluru, N., Alexander, A. L., Christian, B. T., Okonkwo, O. C., Oh, J., . . . Johnson, S. C. (2014). Associations between white matter microstructure and amyloid burden in preclinical Alzheimer's disease: A multimodal imaging investigation. *Neuroimage-Clinical, 4*, 604-614. doi:10.1016/j.nicl.2014.02.001

Raha-Chowdhury, R., Henderson, J. W., Raha, A. A., Stott, S. R. W., Vuono, R., Foscarin, S., . . . Zaman, S. H. (2018). Erythromyeloid-Derived TREM2: A Major Determinant of Alzheimer's Disease Pathology in Down Syndrome. *Journal of Alzheimers Disease, 61*(3), 1143-1162. doi:10.3233/jad-170814

Raichle, M. E. (2015). The brain's default mode network. *Annu Rev Neurosci, 38*, 433-447. doi:10.1146/annurev-neuro-071013-014030

Raichle, M. E., MacLeod, A. M., Snyder, A. Z., Powers, W. J., Gusnard, D. A., & Shulman, G. L. (2001). A default mode of brain function. *Proceedings of the National Academy of Sciences, 98*(2), 676-682.

Raj, A., Kuceyeski, A., & Weiner, M. (2012). A network diffusion model of disease progression in dementia. *Neuron, 73*(6), 1204-1215. doi:10.1016/j.neuron.2011.12.040

Ransohoff, R. M. (2016). A polarizing question: do M1 and M2 microglia exist? *Nature Neuroscience, 19*(8), 987-991. doi:10.1038/nn.4338

Rasmussen, J. M., Lakatos, A., van Erp, T. G., Kruggel, F., Keator, D. B., Fallon, J. T., . . . Alzheimer's Disease Neuroimaging, I. (2012). Empirical derivation of the reference region for computing diagnostic sensitive (1)(8)fluorodeoxyglucose ratios in Alzheimer's disease based on the ADNI sample. *Biochim Biophys Acta, 1822*(3), 457-466. doi:10.1016/j.bbadis.2011.09.008

Rasmussen, M. K., Mestre, H., & Nedergaard, M. (2018). The glymphatic pathway in neurological disorders. *Lancet Neurol, 17*(11), 1016-1024. doi:10.1016/S1474-4422(18)30318-1

Raz, L., Bhaskar, K., Weaver, J., Marini, S., Zhang, Q., Thompson, J. F., . . . Rosenberg, G. A. (2019). Hypoxia promotes tau hyperphosphorylation with associated neuropathology in vascular dysfunction. *Neurobiol Dis, 126*, 124-136. doi:10.1016/j.nbd.2018.07.009

Raz, L., Knoefel, J., & Bhaskar, K. (2016). The neuropathology and cerebrovascular mechanisms of dementia. *J Cereb Blood Flow Metab, 36*(1), 172-186. doi:10.1038/jcbfm.2015.164

Reijmer, Y. D., Leemans, A., Caeyenberghs, K., Heringa, S. M., Koek, H. L., Biessels, G. J., & Utrecht Vascular Cognitive Impairment Study, G. (2013). Disruption of cerebral

networks and cognitive impairment in Alzheimer disease. *Neurology, 80*(15), 1370-1377. doi:10.1212/WNL.0b013e31828c2ee5

Reisberg, B., Franssen, E. H., Souren, L. E., Auer, S. R., Akram, I., & Kenowsky, S. (2002). Evidence and mechanisms of retrogenesis in Alzheimer's and other dementias: management and treatment import. *Am J Alzheimers Dis Other Demen, 17*(4), 202-212. doi:10.1177/153331750201700411

Risk, B. B., Matteson, D. S., Ruppert, D., Eloyan, A., & Caffo, B. S. (2014). An evaluation of independent component analyses with an application to resting-state fMRI. *Biometrics, 70*(1), 224-236. doi:10.1111/biom.12111

Rizzo, G., Veronese, M., Tonietto, M., Zanotti-Fregonara, P., Turkheimer, F. E., & Bertoldo, A. (2014). Kinetic modeling without accounting for the vascular component impairs the quantification of C-11 PBR28 brain PET data. *Journal of Cerebral Blood Flow and Metabolism, 34*(6), 1060-1069. doi:10.1038/jcbfm.2014.55

Rojas, S., Martin, A., Arranz, M. J., Pareto, D., Purroy, J., Verdaguer, E., . . . Planas, A. M. (2007). Imaging brain inflammation with [(11)C]PK11195 by PET and induction of the peripheral-type benzodiazepine receptor after transient focal ischemia in rats. *J Cereb Blood Flow Metab, 27*(12), 1975-1986. doi:10.1038/sj.jcbfm.9600500

Rubinov, M., & Sporns, O. (2010). Complex network measures of brain connectivity: uses and interpretations. *Neuroimage, 52*(3), 1059-1069. doi:10.1016/j.neuroimage.2009.10.003

Rueckert, D., Sonoda, L. I., Hayes, C., Hill, D. L., Leach, M. O., & Hawkes, D. J. (1999). Nonrigid registration using free-form deformations: application to breast MR images. *IEEE Trans Med Imaging, 18*(8), 712-721. doi:10.1109/42.796284

Ruitenberg, A., den Heijer, T., Bakker, S. L., van Swieten, J. C., Koudstaal, P. J., Hofman, A., & Breteler, M. M. (2005). Cerebral hypoperfusion and clinical onset of dementia: the Rotterdam Study. *Annals of Neurology, 57*(6), 789-794. doi:10.1002/ana.20493

Salimi-Khorshidi, G., Douaud, G., Beckmann, C. F., Glasser, M. F., Griffanti, L., & Smith, S. M. (2014). Automatic denoising of functional MRI data: combining independent component analysis and hierarchical fusion of classifiers. *Neuroimage, 90*, 449-468. doi:10.1016/j.neuroimage.2013.11.046

Sanchez-Mejias, E., Navarro, V., Jimenez, S., Sanchez-Mico, M., Sanchez-Varo, R., Nunez-Diaz, C., . . . Vitorica, J. (2016). Soluble phospho-tau from Alzheimer's disease hippocampus drives microglial degeneration. *Acta Neuropathol, 132*(6), 897-916. doi:10.1007/s00401-016-1630-5

Schain, M., Zanderigo, F., Ogden, R. T., & Kreisl, W. C. (2018). Non-invasive estimation of C-11 PBR28 binding potential. *Neuroimage, 169*, 278-285. doi:10.1016/j.neuroimage.2017.12.002

Scheltens, P., Barkhof, F., Leys, D., Wolters, E. C., Ravid, R., & Kamphorst, W. (1995). Histopathologic correlates of white matter changes on MRI in Alzheimer's disease and normal aging. *Neurology, 45*(5), 883-888. doi:10.1212/wnl.45.5.883

Scholvinck, M. L., Maier, A., Ye, F. Q., Duyn, J. H., & Leopold, D. A. (2010). Neural basis of global resting-state fMRI activity. *Proc Natl Acad Sci U S A, 107*(22), 10238-10243. doi:10.1073/pnas.0913110107

Schroeter, M. L., Stein, T., Maslowski, N., & Neumann, J. (2009). Neural correlates of Alzheimer's disease and mild cognitive impairment: a systematic and quantitative meta-analysis involving 1351 patients. *Neuroimage, 47*(4), 1196-1206. doi:10.1016/j.neuroimage.2009.05.037

Seeley, W. W., Crawford, R. K., Zhou, J., Miller, B. L., & Greicius, M. D. (2009). Neurodegenerative diseases target large-scale human brain networks. *Neuron, 62*(1), 42-52. doi:10.1016/j.neuron.2009.03.024

Segonne, F., Dale, A. M., Busa, E., Glessner, M., Salat, D., Hahn, H. K., & Fischl, B. (2004). A hybrid approach to the skull stripping problem in MRI. *Neuroimage, 22*(3), 1060-1075. doi:10.1016/j.neuroimage.2004.03.032

Segonne, F., Pacheco, J., & Fischl, B. (2007). Geometrically accurate topology-correction of cortical surfaces using nonseparating loops. *IEEE Trans Med Imaging, 26*(4), 518-529. doi:10.1109/TMI.2006.887364

Sekiya, M., Wang, M. H., Fujisaki, N., Sakakibara, Y., Quan, X. M., Ehrlich, M. E., . . . Iijima, K. M. (2018). Integrated biology approach reveals molecular and pathological interactions among Alzheimer's A beta 42, Tau, TREM2, and TYROBP in Drosophila models. *Genome Medicine, 10*. doi:10.1186/s13073-018-0530-9

Shah, P., Lal, N., Leung, E., Traul, D. E., Gonzalo-Ruiz, A., & Geula, C. (2010). Neuronal and axonal loss are selectively linked to fibrillar amyloid-{beta} within plaques of the aged primate cerebral cortex. *Am J Pathol, 177*(1), 325-333. doi:10.2353/ajpath.2010.090937

Sheline, Y. I., Raichle, M. E., Snyder, A. Z., Morris, J. C., Head, D., Wang, S., & Mintun, M. A. (2010). Amyloid plaques disrupt resting state default mode network connectivity in cognitively normal elderly. *Biol Psychiatry, 67*(6), 584-587. doi:10.1016/j.biopsych.2009.08.024

Shi, Q. Q., Chowdhury, S., Ma, R., Le, K. X., Hong, S., Caldarone, B. J., . . . Lemere, C. A. (2017). Complement C3 deficiency protects against neurodegeneration in aged plaque-rich APP/PS1 mice. *Science Translational Medicine, 9*(392). doi:10.1126/scitranslmed.aaf6295

Shmuel, A., & Leopold, D. A. (2008). Neuronal correlates of spontaneous fluctuations in fMRI signals in monkey visual cortex: Implications for functional connectivity at rest. *Hum Brain Mapp, 29*(7), 751-761. doi:10.1002/hbm.20580

Shu, N., Liang, Y., Li, H., Zhang, J., Li, X., Wang, L., . . . Zhang, Z. (2012). Disrupted topological organization in white matter structural networks in amnestic mild cognitive impairment: relationship to subtype. *Radiology, 265*(2), 518-527. doi:10.1148/radiol.12112361

Singhal, T., O'Connor, K., Dubey, S., Belanger, A. P., Hurwitz, S., Chu, R. X., . . . Bakshi, R. (2018). 18F-PBR06 Versus 11C-PBR28 PET for Assessing White Matter Translocator Protein Binding in Multiple Sclerosis. *Clinical Nuclear Medicine, 43*(9), E289-E295. doi:10.1097/rlu.0000000000002179

Sipe, G. O., Lowery, R. L., Tremblay, M. E., Kelly, E. A., Lamantia, C. E., & Majewska, A. K. (2016). Microglial P2Y12 is necessary for synaptic plasticity in mouse visual cortex. *Nature Communications, 7*. doi:ARTN 10905

10.1038/ncomms10905

Sjobeck, M., Haglund, M., & Englund, E. (2006a). White matter mapping in Alzheimer's disease: A neuropathological study. *Neurobiology of Aging, 27*(5), 673-680. doi:10.1016/j.neurobiolagang.2005.03.007

Sjobeck, M., Haglund, M., & Englund, E. (2006b). White matter mapping in Alzheimer's disease: A neuropathological study. *Neurobiol Aging, 27*(5), 673-680. doi:10.1016/j.neurobiolaging.2005.03.007

Slifstein, M., & Laruelle, M. (2000). Effects of statistical noise on graphic analysis of PET neuroreceptor studies. *J Nucl Med, 41*(12), 2083-2088. Retrieved from https://www.ncbi.nlm.nih.gov/pubmed/11138696

Slifstein, M., & Laruelle, M. (2001). Models and methods for derivation of in vivo neuroreceptor parameters with PET and SPECT reversible radiotracers. *Nuclear Medicine and Biology, 28*(5), 595-608. doi:10.1016/s0969-8051(01)00214-1

Small, S. A., & Duff, K. (2008). Linking A beta and Tau in Late-Onset Alzheimer's Disease: A Dual Pathway Hypothesis. *Neuron, 60*(4), 534-542. doi:10.1016/j.neuron.2008.11.007

Smith, S. M., Jenkinson, M., Johansen-Berg, H., Rueckert, D., Nichols, T. E., Mackay, C. E., . . . Behrens, T. E. (2006). Tract-based spatial statistics: voxelwise analysis of multi-subject diffusion data. *Neuroimage, 31*(4), 1487-1505. doi:10.1016/j.neuroimage.2006.02.024

Smith, S. M., Jenkinson, M., Woolrich, M. W., Beckmann, C. F., Behrens, T. E., Johansen-Berg, H., . . . Matthews, P. M. (2004). Advances in functional and structural MR image analysis and implementation as FSL. *Neuroimage, 23 Suppl 1*, S208-219. doi:10.1016/j.neuroimage.2004.07.051

Smith, S. M., & Nichols, T. E. (2009). Threshold-free cluster enhancement: addressing problems of smoothing, threshold dependence and localisation in cluster inference. *Neuroimage, 44*(1), 83-98. doi:10.1016/j.neuroimage.2008.03.061

Soares, J. M., Marques, P., Alves, V., & Sousa, N. (2013). A hitchhiker's guide to diffusion tensor imaging. *Front Neurosci, 7*, 31. doi:10.3389/fnins.2013.00031

Sole-Domenech, S., Cruz, D. L., Capetillo-Zarate, E., & Maxfield, F. R. (2016). The endocytic pathway in microglia during health, aging and Alzheimer's disease. *Ageing Research Reviews, 32*, 89-103. doi:10.1016/j.arr.2016.07.002

Sorg, C., Riedl, V., Muhlau, M., Calhoun, V. D., Eichele, T., Laer, L., . . . Wohlschlager, A. M. (2007). Selective changes of resting-state networks in individuals at risk for Alzheimer's disease. *Proceedings of the National Academy of Sciences of the United States of America, 104*(47), 18760-18765. doi:10.1073/pnas.0708803104

Spangenberg, E. E., & Green, K. N. (2017). Inflammation in Alzheimer's disease: Lessons learned from microglia-depletion models. *Brain Behav Immun, 61*, 1-11. doi:10.1016/j.bbi.2016.07.003

Spees, W. M., Buhl, N., Sun, P., Ackerman, J. J., Neil, J. J., & Garbow, J. R. (2011). Quantification and compensation of eddy-current-induced magnetic-field gradients. *J Magn Reson, 212*(1), 116-123. doi:10.1016/j.jmr.2011.06.016

Sperling, R. A., Aisen, P. S., Beckett, L. A., Bennett, D. A., Craft, S., Fagan, A. M., . . . Phelps, C. H. (2011). Toward defining the preclinical stages of Alzheimer's disease: recommendations from the National Institute on Aging-Alzheimer's Association workgroups on diagnostic guidelines for Alzheimer's disease. *Alzheimers Dement, 7*(3), 280-292. doi:10.1016/j.jalz.2011.03.003

Spittau, B. (2017). Aging Microglia-Phenotypes, Functions and Implications for Age-Related Neurodegenerative Diseases. *Frontiers in Aging Neuroscience, 9*. doi:10.3389/fnagi.2017.00194

Squarzoni, P., Oller, G., Hoeffel, G., Pont-Lezica, L., Rostaing, P., Low, D., . . . Garel, S. (2014). Microglia Modulate Wiring of the Embryonic Forebrain. *Cell Reports, 8*(5), 1271-1279. doi:10.1016/j.celrep.2014.07.042

Strain, J. F., Smith, R. X., Beaumont, H., Roe, C. M., Gordon, B. A., Mishra, S., . . . Ances, B. M. (2018). Loss of white matter integrity reflects tau accumulation in Alzheimer disease defined regions. *Neurology, 91*(4), e313-e318. doi:10.1212/WNL.0000000000005864

Streit, W. J. (2006). Microglial senescence: does the brain's immune system have an expiration date? *Trends Neurosci, 29*(9), 506-510. doi:10.1016/j.tins.2006.07.001

Streit, W. J., Braak, H., Del Tredici, K., Leyh, J., Lier, J., Khoshbouei, H., . . . Bechmann, I. (2018). Microglial activation occurs late during preclinical Alzheimer's disease. *Glia, 66*(12), 2550-2562. doi:10.1002/glia.23510

Streit, W. J., Braak, H., Xue, Q. S., & Bechmann, I. (2009). Dystrophic (senescent) rather than activated microglial cells are associated with tau pathology and likely precede neurodegeneration in Alzheimer's disease. *Acta Neuropathologica, 118*(4), 475-485. doi:10.1007/s00401-009-0556-6

Streit, W. J., Sammons, N. W., Kuhns, A. J., & Sparks, D. L. (2004). Dystrophic microglia in the aging human brain. *Glia, 45*(2), 208-212. doi:10.1002/glia.10319

Stricker, N. H., Schweinsburg, B. C., Delano-Wood, L., Wierenga, C. E., Bangen, K. J., Haaland, K. Y., . . . Bondi, M. W. (2009). Decreased white matter integrity in late-myelinating fiber pathways in Alzheimer's disease supports retrogenesis. *Neuroimage, 45*(1), 10-16. doi:10.1016/j.neuroimage.2008.11.027

Strowig, T., Henao-Mejia, J., Elinav, E., & Flavell, R. (2012). Inflammasomes in health and disease. *Nature, 481*(7381), 278-286. doi:10.1038/nature10759

Suarez-Calvet, M., Kleinberger, G., Araque Caballero, M. A., Brendel, M., Rominger, A., Alcolea, D., . . . Haass, C. (2016). sTREM2 cerebrospinal fluid levels are a potential biomarker for microglia activity in early-stage Alzheimer's disease and associate with neuronal injury markers. *EMBO Mol Med, 8*(5), 466-476. doi:10.15252/emmm.201506123

Suarez-Calvet, M., Morenas-Rodriguez, E., Kleinberger, G., Schlepckow, K., Araque Caballero, M. A., Franzmeier, N., . . . Alzheimer's Disease Neuroimaging, I. (2019). Early increase of CSF sTREM2 in Alzheimer's disease is associated with tau related-neurodegeneration but not with amyloid-beta pathology. *Mol Neurodegener, 14*(1), 1. doi:10.1186/s13024-018-0301-5

Sun, S. W., Liang, H. F., Trinkaus, K., Cross, A. H., Armstrong, R. C., & Song, S. K. (2006). Noninvasive detection of cuprizone induced axonal damage and demyelination in the mouse corpus callosum. *Magn Reson Med, 55*(2), 302-308. doi:10.1002/mrm.20774

Sun, X., He, G., Qing, H., Zhou, W., Dobie, F., Cai, F., . . . Song, W. (2006). Hypoxia facilitates Alzheimer's disease pathogenesis by up-regulating BACE1 gene expression. *Proc Natl Acad Sci U S A, 103*(49), 18727-18732. doi:10.1073/pnas.0606298103

Sun, Y., Bi, Q., Wang, X., Hu, X., Li, H., Li, X., . . . Han, Y. (2018). Prediction of Conversion From Amnestic Mild Cognitive Impairment to Alzheimer's Disease Based on the Brain Structural Connectome. *Front Neurol, 9*, 1178. doi:10.3389/fneur.2018.01178

Supekar, K., Menon, V., Rubin, D., Musen, M., & Greicius, M. D. (2008). Network analysis of intrinsic functional brain connectivity in Alzheimer's disease. *PLoS Comput Biol, 4*(6), e1000100. doi:10.1371/journal.pcbi.1000100

Sutphen, C. L., Jasielec, M. S., Shah, A. R., Macy, E. M., Xiong, C., Vlassenko, A. G., . . . Fagan, A. M. (2015). Longitudinal Cerebrospinal Fluid Biomarker Changes in Preclinical Alzheimer Disease During Middle Age. *JAMA Neurol, 72*(9), 1029-1042. doi:10.1001/jamaneurol.2015.1285

Swardfager, W., Lanctot, K., Rothenburg, L., Wong, A., Cappell, J., & Herrmann, N. (2010). A meta-analysis of cytokines in Alzheimer's disease. *Biol Psychiatry, 68*(10), 930-941. doi:10.1016/j.biopsych.2010.06.012

Sweeney, M. D., Sagare, A. P., & Zlokovic, B. V. (2018). Blood-brain barrier breakdown in Alzheimer disease and other neurodegenerative disorders. *Nat Rev Neurol, 14*(3), 133-150. doi:10.1038/nrneurol.2017.188

Takahashi, H., Klein, Z. A., Bhagat, S. M., Kaufman, A. C., Kostylev, M. A., Ikezu, T., . . . Alzheimer's Dis, N. (2017). Opposing effects of progranulin deficiency on amyloid and tau pathologies via microglial TYROBP network. *Acta Neuropathologica, 133*(5), 785-807. doi:10.1007/s00401-017-1668-z

Takano, T., Han, X., Deane, R., Zlokovic, B., & Nedergaard, M. (2007). Two-photon imaging of astrocytic Ca2+ signaling and the microvasculature in experimental mice models of Alzheimer's disease. *Ann N Y Acad Sci, 1097*, 40-50. doi:10.1196/annals.1379.004

Takeuchi, H., Mizuno, T., Zhang, G., Wang, J., Kawanokuchi, J., Kuno, R., & Suzumura, A. (2005). Neuritic beading induced by activated microglia is an early feature of neuronal dysfunction toward neuronal death by inhibition of mitochondrial respiration and axonal transport. *J Biol Chem, 280*(11), 10444-10454. doi:10.1074/jbc.M413863200

Tarantini, S., Tran, C. H. T., Gordon, G. R., Ungvari, Z., & Csiszar, A. (2017). Impaired neurovascular coupling in aging and Alzheimer's disease: Contribution of astrocyte dysfunction and endothelial impairment to cognitive decline. *Exp Gerontol, 94*, 52-58. doi:10.1016/j.exger.2016.11.004

Tarasoff-Conway, J. M., Carare, R. O., Osorio, R. S., Glodzik, L., Butler, T., Fieremans, E., . . . de Leon, M. J. (2015). Clearance systems in the brain-implications for Alzheimer disease. *Nat Rev Neurol, 11*(8), 457-470. doi:10.1038/nrneurol.2015.119

Thal, D. R., Rub, U., Orantes, M., & Braak, H. (2002). Phases of A beta-deposition in the human brain and its relevance for the development of AD. *Neurology, 58*(12), 1791-1800. doi:10.1212/wnl.58.12.1791

Thal, D. R., Schultz, C., Dehghani, F., Yamaguchi, H., Braak, H., & Braak, E. (2000). Amyloid beta-protein (Abeta)-containing astrocytes are located preferentially near N-terminal-truncated Abeta deposits in the human entorhinal cortex. *Acta Neuropathol, 100*(6), 608-617. Retrieved from https://www.ncbi.nlm.nih.gov/pubmed/11078212

Thurfjell, L., Lilja, J., Lundqvist, R., Buckley, C., Smith, A., Vandenberghe, R., & Sherwin, P. (2014). Automated quantification of 18F-flutemetamol PET activity for categorizing scans as negative or positive for brain amyloid: concordance with visual image reads. *J Nucl Med, 55*(10), 1623-1628. doi:10.2967/jnumed.114.142109

Tibshirani, R. (1996). Regression shrinkage and selection via the Lasso. *Journal of the Royal Statistical Society Series B-Methodological, 58*(1), 267-288. doi:10.1111/j.2517-6161.1996.tb02080.x

Tischer, J., Krueger, M., Mueller, W., Staszewski, O., Prinz, M., Streit, W. J., & Bechmann, I. (2016). Inhomogeneous Distribution of Iba-1 Characterizes Microglial Pathology in Alzheimer's Disease. *Glia, 64*(9), 1562-1572. doi:10.1002/glia.23024

Tooyama, I., Kimura, H., Akiyama, H., & Mcgeer, P. L. (1990). Reactive Microglia Express Class-I and Class-Ii Major Histocompatibility Complex Antigens in Alzheimers-Disease. *Brain Research, 523*(2), 273-280. doi:Doi 10.1016/0006-8993(90)91496-4

Toth, P., Tarantini, S., Csiszar, A., & Ungvari, Z. (2017). Functional vascular contributions to cognitive impairment and dementia: mechanisms and consequences of cerebral autoregulatory dysfunction, endothelial impairment, and neurovascular uncoupling in aging. *Am J Physiol Heart Circ Physiol, 312*(1), H1-H20. doi:10.1152/ajpheart.00581.2016

Tournier, J. D., Mori, S., & Leemans, A. (2011). Diffusion tensor imaging and beyond. *Magn Reson Med, 65*(6), 1532-1556. doi:10.1002/mrm.22924

Tucholka, A., Grau-Rivera, O., Falcon, C., Rami, L., Sanchez-Valle, R., Llado, A., . . . Alzheimer's Disease Neuroimaging, I. (2018). Structural Connectivity Alterations Along the Alzheimer's Disease Continuum: Reproducibility Across Two Independent Samples and Correlation with Cerebrospinal Fluid Amyloid-beta and Tau. *J Alzheimers Dis, 61*(4), 1575-1587. doi:10.3233/JAD-170553

Tuisku, J., Plaven-Sigray, P., Gaiser, E. C., Airas, L., Al-Abdulrasul, H., Bruck, A., . . . Grp, H. C. P. S. (2019). Effects of age, BMI and sex on the glial cell marker TSPO - a multicentre C-11 PBR28 HRRT PET study. *Eur J Nucl Med Mol Imaging, 46*(11), 2329-2338. doi:10.1007/s00259-019-04403-7

Turkheimer, F., Sokoloff, L., Bertoldo, A., Lucignani, G., Reivich, M., Jaggi, J. L., & Schmidt, K. (1998). Estimation of component and parameter distributions in spectral analysis. *J Cereb Blood Flow Metab, 18*(11), 1211-1222. doi:10.1097/00004647-199811000-00007

Turkheimer, F. E., Edison, P., Pavese, N., Roncaroli, F., Anderson, A. N., Hammers, A., . . . Brooks, D. J. (2007). Reference and target region modeling of [11C]-(R)-PK11195 brain studies. *J Nucl Med, 48*(1), 158-167. Retrieved from https://www.ncbi.nlm.nih.gov/pubmed/17204713

van den Heuvel, M. P., & Hulshoff Pol, H. E. (2010). Exploring the brain network: a review on resting-state fMRI functional connectivity. *Eur Neuropsychopharmacol, 20*(8), 519-534. doi:10.1016/j.euroneuro.2010.03.008

Varnum, M. M., & Ikezu, T. (2012). The Classification of Microglial Activation Phenotypes on Neurodegeneration and Regeneration in Alzheimer's Disease Brain. *Archivum Immunologiae Et Therapiae Experimentalis, 60*(4), 251-266. doi:10.1007/s00005-012-0181-2

Varrone, A., & Nordberg, A. (2015). Molecular imaging of neuroinflammation in Alzheimer's disease. *Clinical and Translational Imaging, 3*(6), 437-447. doi:10.1007/s40336-015-0137-8

Venegas, C., & Heneka, M. T. (2017). Danger-associated molecular patterns in Alzheimer's disease. *Journal of Leukocyte Biology, 101*(1), 87-98. doi:10.1189/jlb.3MR0416-204R

Venegas, C., Kumar, S., Franklin, B. S., Dierkes, T., Brinkschulte, R., Tejera, D., . . . Heneka, M. T. (2017). Microglia-derived ASC specks cross-seed amyloid-beta in Alzheimer's disease. *Nature, 552*(7685), 355-361. doi:10.1038/nature25158

Venneti, S., Lopresti, B. J., & Wiley, C. A. (2006). The peripheral benzodiazepine receptor (Translocator protein 18kDa) in microglia: from pathology to imaging. *Prog Neurobiol, 80*(6), 308-322. doi:10.1016/j.pneurobio.2006.10.002

Venneti, S., Wang, G., Nguyen, J., & Wiley, C. A. (2008). The positron emission tomography ligand DAA1106 binds with high affinity to activated microglia in human neurological disorders. *J Neuropathol Exp Neurol, 67*(10), 1001-1010. doi:10.1097/NEN.0b013e318188b204

Verfaillie, S. C. J., Pichet Binette, A., Vachon-Presseau, E., Tabrizi, S., Savard, M., Bellec, P., . . . Group, P.-A. R. (2018). Subjective Cognitive Decline Is Associated With Altered Default Mode Network Connectivity in Individuals With a Family History of Alzheimer's Disease. *Biol Psychiatry Cogn Neurosci Neuroimaging, 3*(5), 463-472. doi:10.1016/j.bpsc.2017.11.012

Veronese, M., Marques, T. R., Bloomfield, P. S., Rizzo, G., Singh, N., Jones, D., . . . Turkheimer, F. E. (2018). Kinetic modelling of C-11 PBR28 for 18kDa translocator protein PET data: A validation study of vascular modelling in the brain using XBD173 and tissue analysis. *Journal of Cerebral Blood Flow and Metabolism, 38*(7), 1227-1242. doi:10.1177/0271678x17712388

Veronese, M., Rizzo, G., Bertoldo, A., & Turkheimer, F. E. (2016). Spectral Analysis of Dynamic PET Studies: A Review of 20 Years of Method Developments and Applications. *Comput Math Methods Med, 2016*, 7187541. doi:10.1155/2016/7187541

Verret, L., Mann, E. O., Hang, G. B., Barth, A. M., Cobos, I., Ho, K., . . . Palop, J. J. (2012). Inhibitory interneuron deficit links altered network activity and cognitive dysfunction in Alzheimer model. *Cell, 149*(3), 708-721. doi:10.1016/j.cell.2012.02.046

Vezzani, A., & Viviani, B. (2015). Neuromodulatory properties of inflammatory cytokines and their impact on neuronal excitability. *Neuropharmacology, 96*(Pt A), 70-82. doi:10.1016/j.neuropharm.2014.10.027

Vogel, J. W., Iturria-Medina, Y., Strandberg, O. T., Smith, R., Levitis, E., Evans, A. C., . . . Swedish BioFinder, S. (2020). Spread of pathological tau proteins through communicating neurons in human Alzheimer's disease. *Nature Communications, 11*(1), 2612. doi:10.1038/s41467-020-15701-2

Wai, Y. Y., Hsu, W. C., Fung, H. C., Lee, J. D., Chan, H. L., Tsai, M. L., . . . Wang, J. J. (2014). Tract-based spatial statistics: application to mild cognitive impairment. *Biomed Res Int, 2014*, 713079. doi:10.1155/2014/713079

Walker, D. G., & Lue, L. F. (2015). Immune phenotypes of microglia in human neurodegenerative disease: challenges to detecting microglial polarization in human brains. *Alzheimers Res Ther, 7*(1), 56. doi:10.1186/s13195-015-0139-9

Wang, J., Wang, X., Xia, M., Liao, X., Evans, A., & He, Y. (2015). GRETNA: a graph theoretical network analysis toolbox for imaging connectomics. *Front Hum Neurosci, 9*, 386. doi:10.3389/fnhum.2015.00386

Wang, K., Liang, M., Wang, L., Tian, L., Zhang, X., Li, K., & Jiang, T. (2007). Altered functional connectivity in early Alzheimer's disease: a resting-state fMRI study. *Hum Brain Mapp, 28*(10), 967-978. doi:10.1002/hbm.20324

Wang, L., Zang, Y., He, Y., Liang, M., Zhang, X., Tian, L., . . . Li, K. (2006). Changes in hippocampal connectivity in the early stages of Alzheimer's disease: evidence from resting state fMRI. *Neuroimage, 31*(2), 496-504. doi:10.1016/j.neuroimage.2005.12.033

Wang, Y., Risacher, S. L., West, J. D., McDonald, B. C., Magee, T. R., Farlow, M. R., . . . Saykin, A. J. (2013). Altered default mode network connectivity in older adults with cognitive complaints and amnestic mild cognitive impairment. *J Alzheimers Dis, 35*(4), 751-760. doi:10.3233/JAD-130080

Wang, Y., Ulland, T. K., Ulrich, J. D., Song, W., Tzaferis, J. A., Hole, J. T., . . . Colonna, M. (2016). TREM2-mediated early microglial response limits diffusion and toxicity of amyloid plaques. *J Exp Med, 213*(5), 667-675. doi:10.1084/jem.20151948

Wang, Z., Yang, D., Zhang, X., Li, T., Li, J., Tang, Y., & Le, W. (2011). Hypoxia-induced down-regulation of neprilysin by histone modification in mouse primary cortical and hippocampal neurons. *PLoS One, 6*(4), e19229. doi:10.1371/journal.pone.0019229

Watts, D. J., & Strogatz, S. H. (1998). Collective dynamics of 'small-world' networks. *Nature, 393*(6684), 440-442. doi:10.1038/30918

Wes, P. D., Easton, A., Corradi, J., Barten, D. M., Devidze, N., DeCarr, L. B., . . . Cacace, A. M. (2014). Tau overexpression impacts a neuroinflammation gene expression network perturbed in Alzheimer's disease. *PLoS One, 9*(8), e106050. doi:10.1371/journal.pone.0106050

Whitfield-Gabrieli, S., & Nieto-Castanon, A. (2012). Conn: a functional connectivity toolbox for correlated and anticorrelated brain networks. *Brain Connect, 2*(3), 125-141. doi:10.1089/brain.2012.0073

Winkler, A. M., Ridgway, G. R., Webster, M. A., Smith, S. M., & Nichols, T. E. (2014). Permutation inference for the general linear model. *Neuroimage, 92*, 381-397. doi:10.1016/j.neuroimage.2014.01.060

Winkler, E. A., Nishida, Y., Sagare, A. P., Rege, S. V., Bell, R. D., Perlmutter, D., . . . Zlokovic, B. V. (2015). GLUT1 reductions exacerbate Alzheimer's disease vasculo-neuronal dysfunction and degeneration. *Nature Neuroscience, 18*(4), 521-530. doi:10.1038/nn.3966

Witten, D. M., Tibshirani, R., & Hastie, T. (2009). A penalized matrix decomposition, with applications to sparse principal components and canonical correlation analysis. *Biostatistics, 10*(3), 515-534. doi:10.1093/biostatistics/kxp008

Woolrich, M. W., Jbabdi, S., Patenaude, B., Chappell, M., Makni, S., Behrens, T., . . . Smith, S. M. (2009). Bayesian analysis of neuroimaging data in FSL. *Neuroimage, 45*(1 Suppl), S173-186. doi:10.1016/j.neuroimage.2008.10.055

Wunderlich, P., Glebov, K., Kemmerling, N., Tien, N. T., Neumann, H., & Walter, J. (2013). Sequential proteolytic processing of the triggering receptor expressed on myeloid cells-2 (TREM2) protein by ectodomain shedding and gamma-secretase-dependent intramembranous cleavage. *J Biol Chem, 288*(46), 33027-33036. doi:10.1074/jbc.M113.517540

Wyss-Coray, T., Loike, J. D., Brionne, T. C., Lu, E., Anankov, R., Yan, F., . . . Husemann, J. (2003). Adult mouse astrocytes degrade amyloid-beta in vitro and in situ. *Nat Med, 9*(4), 453-457. doi:10.1038/nm838

Yin, X., Wright, J., Wall, T., & Grammas, P. (2010). Brain endothelial cells synthesize neurotoxic thrombin in Alzheimer's disease. *Am J Pathol, 176*(4), 1600-1606. doi:10.2353/ajpath.2010.090406

Yin, Z. R., Raj, D., Saiepour, N., Van Damd, D., Brouwer, N., Holtman, I. R., . . . Boddeke, E. (2017). Immune hyperreactivity of Ab plaque-associated microglia in Alzheimer's disease. *Neurobiology of Aging, 55*, 115-122. doi:10.1016/j.neurobiolaging.2017.03.021

Yokoi, T., Watanabe, H., Yamaguchi, H., Bagarinao, E., Masuda, M., Imai, K., . . . Sobue, G. (2018). Involvement of the Precuneus/Posterior Cingulate Cortex Is Significant for the Development of Alzheimer's Disease: A PET (THK5351, PiB) and Resting fMRI Study. *Front Aging Neurosci, 10*, 304. doi:10.3389/fnagi.2018.00304

Yokokura, M., Mori, N., Yagi, S., Yoshikawa, E., Kikuchi, M., Yoshihara, Y., . . . Ouchi, Y. (2011). In vivo changes in microglial activation and amyloid deposits in brain regions

with hypometabolism in Alzheimer's disease. *Eur J Nucl Med Mol Imaging, 38*(2), 343-351. doi:10.1007/s00259-010-1612-0

Zanderigo, F., Ogden, R. T., & Parsey, R. V. (2013). Reference region approaches in PET: a comparative study on multiple radioligands. *J Cereb Blood Flow Metab, 33*(6), 888-897. doi:10.1038/jcbfm.2013.26

Zanotti-Fregonara, P., Kreisl, W. C., Innis, R. B., & Lyoo, C. H. (2019). Automatic Extraction of a Reference Region for the Noninvasive Quantification of Translocator Protein in Brain Using C-11-PBR28. *Journal of Nuclear Medicine, 60*(7), 978-984. doi:10.2967/jnumed.118.222927

Zhao, Z., Nelson, A. R., Betsholtz, C., & Zlokovic, B. V. (2015). Establishment and Dysfunction of the Blood-Brain Barrier. *Cell, 163*(5), 1064-1078. doi:10.1016/j.cell.2015.10.067

Zhuang, L., Liu, X., Xu, X., Yue, C., Shu, H., Bai, F., . . . Zhang, Z. (2012). Association of the interleukin 1 beta gene and brain spontaneous activity in amnestic mild cognitive impairment. *J Neuroinflammation, 9*, 263. doi:10.1186/1742-2094-9-263

Zlokovic, B. V. (2011a). Neurovascular pathways to neurodegeneration in Alzheimer's disease and other disorders. *Nature Reviews Neuroscience, 12*(12), 723-738. doi:10.1038/nrn3114

Zlokovic, B. V. (2011b). Neurovascular pathways to neurodegeneration in Alzheimer's disease and other disorders. *Nat Rev Neurosci, 12*(12), 723-738. doi:10.1038/nrn3114

Zott, B., Simon, M. M., Hong, W., Unger, F., Chen-Engerer, H. J., Frosch, M. P., . . . Konnerth, A. (2019). A vicious cycle of beta amyloid-dependent neuronal hyperactivation. *Science, 365*(6453), 559-565. doi:10.1126/science.aay0198

Zou, J., Tao, S., Johnson, A., Tomljanovic, Z., Polly, K., Klein, J., . . . Kreisl, W. C. (2020). Microglial activation, but not tau pathology, is independently associated with amyloid positivity and memory impairment. *Neurobiology of Aging, 85*, 11-21. doi:10.1016/j.neurobiolaging.2019.09.019

Appendix 1. MRI Acquisition Parameters

SIEMENS MAGNETOM Verio syngo MR B17

\\USER\HEAD\ELAD/AMYLOID/DELIRIUM (Paul Edison)\Visit 1\localizer

TA: 0:13 PAT: Off Voxel size: 1.1×1.0×7.0 mm Rel. SNR: 1.00 SIEMENS: gre

Properties	
Prio Recon	Off
Before measurement	
After measurement	
Load to viewer	On
Inline movie	Off
Auto store images	On
Load to stamp segments	Off
Load images to graphic segments	Off
Auto open inline display	Off
Start measurement without further preparation	Off
Wait for user to start	Off
Start measurements	single

Routine	
Slice group 1	
Slices	1
Dist. factor	20 %
Position	Isocenter
Orientation	Sagittal
Phase enc. dir.	A >> P
Rotation	0.00 deg
Slice group 2	
Slices	1
Dist. factor	20 %
Position	Isocenter
Orientation	Transversal
Phase enc. dir.	A >> P
Rotation	0.00 deg
Slice group 3	
Slices	1
Dist. factor	20 %
Position	Isocenter
Orientation	Coronal
Phase enc. dir.	R >> L
Rotation	0.00 deg
Phase oversampling	0 %
FoV read	250 mm
FoV phase	100.0 %
Slice thickness	7.0 mm
TR	8.6 ms
TE	4.00 ms
Averages	2
Concatenations	3
Filter	Prescan Normalize, Elliptical filter
Coil elements	HEA;HEP

Contrast	
TD	0 ms
MTC	Off
Magn. preparation	None
Flip angle	20 deg
Fat suppr.	None
Water suppr.	None
SWI	Off
Averaging mode	Short term
Reconstruction	Magnitude
Measurements	1
Multiple series	Each measurement

Resolution	
Base resolution	256
Phase resolution	90 %
Phase partial Fourier	Off
Interpolation	On
PAT mode	None
Matrix Coil Mode	Auto (CP)
Image Filter	Off
Distortion Corr.	Off
Unfiltered images	Off
Prescan Normalize	On
Normalize	Off
B1 filter	Off
Raw filter	Off
Elliptical filter	On
Mode	Inplane

Geometry	
Multi-slice mode	Sequential
Series	Interleaved
Saturation mode	Standard
Special sat.	None
Set-n-Go Protocol	Off
Table position	H
Table position	0 mm
Inline Composing	Off

System	
Body	Off
HEP	On
HEA	On
Positioning mode	REF
MSMA	S - C - T
Sagittal	R >> L
Coronal	A >> P
Transversal	F >> H
Coil Combine Mode	Adaptive Combine
Auto Coil Select	Default
Shim mode	Tune up
Adjust with body coil	Off
Confirm freq. adjustment	Off
Assume Silicone	Off
? Ref. amplitude 1H	0.000 V
Adjustment Tolerance	Auto
Adjust volume	
Position	Isocenter
Orientation	Transversal
Rotation	0.00 deg
R >> L	350 mm
A >> P	263 mm
F >> H	350 mm

Physio	
1st Signal/Mode	None
Segments	1
Tagging	None
Dark blood	Off
Resp. control	Off

Inline	
Subtract	Off
Liver registration	Off
Std-Dev-Sag	Off

Std-Dev-Cor	Off
Std-Dev-Tra	Off
Std-Dev-Time	Off
MIP-Sag	Off
MIP-Cor	Off
MIP-Tra	Off
MIP-Time	Off
Save original images	On
Wash - In	Off
Wash - Out	Off
TTP	Off
PEI	Off
MIP - time	Off

Sequence

Introduction	On
Dimension	2D
Phase stabilisation	Off
Asymmetric echo	Allowed
Contrasts	1
Bandwidth	320 Hz/Px
Flow comp.	No
Allowed delay	0 s
RF pulse type	Normal
Gradient mode	Normal
Excitation	Slice-sel.
RF spoiling	On

SIEMENS MAGNETOM Verio syngo MR B17

\\USER\HEAD\ELAD/AMYLOID/DELIRIUM (Paul Edison)\Visit 1\MPRAGE_ADNI_P2

TA: 5:03 PAT: 2 Voxel size: 1.0×1.0×1.0 mm Rel. SNR: 1.00 SIEMENS: tfl

Properties

Prio Recon	Off
Before measurement	
After measurement	
Load to viewer	On
Inline movie	Off
Auto store images	On
Load to stamp segments	Off
Load images to graphic segments	Off
Auto open inline display	Off
Start measurement without further preparation	On
Wait for user to start	Off
Start measurements	single

Routine

Slab group 1	
Slabs	1
Dist. factor	50 %
Position	R2.4 A28.2 H1.9
Orientation	Sagittal
Phase enc. dir.	A >> P
Rotation	0.00 deg
Phase oversampling	0 %
Slice oversampling	10.0 %
Slices per slab	160
FoV read	256 mm
FoV phase	93.8 %
Slice thickness	1.00 mm
TR	2300 ms
TE	2.98 ms
Averages	1
Concatenations	1
Filter	Distortion Corr.(2D), Prescan Normalize
Coil elements	HEA;HEP

Contrast

Magn. preparation	Non-sel. IR
TI	900 ms
Flip angle	9 deg
Fat suppr.	None
Water suppr.	None
Averaging mode	Long term
Reconstruction	Magnitude
Measurements	1
Multiple series	Off

Resolution

Base resolution	256
Phase resolution	100 %
Slice resolution	100 %
Phase partial Fourier	Off
Slice partial Fourier	Off
Interpolation	Off
PAT mode	GRAPPA
Accel. factor PE	2
Ref. lines PE	24
Accel. factor 3D	1
Matrix Coil Mode	Auto (Triple)
Reference scan mode	Integrated
Image Filter	Off
Distortion Corr.	On
Mode	2D
Unfiltered images	On
Unfiltered images	Off
Prescan Normalize	On
Normalize	Off
B1 filter	Off
Raw filter	Off
Elliptical filter	Off

Geometry

Multi-slice mode	Single shot
Series	Interleaved
Set-n-Go Protocol	Off
Table position	H
Table position	0 mm
Inline Composing	Off

System

Body	Off
HEP	On
HEA	On
Positioning mode	REF
MSMA	S - C - T
Sagittal	R >> L
Coronal	A >> P
Transversal	F >> H
Save uncombined	Off
Coil Combine Mode	Adaptive Combine
Auto Coil Select	Default
Shim mode	Standard
Adjust with body coil	Off
Confirm freq. adjustment	Off
Assume Silicone	Off
? Ref. amplitude 1H	0.000 V
Adjustment Tolerance	Auto
Adjust volume	
Position	R2.4 A28.2 H1.9
Orientation	Sagittal
Rotation	0.00 deg
F >> H	256 mm
A >> P	240 mm
R >> L	160 mm

Physio

1st Signal/Mode	None
Dark blood	Off
Resp. control	Off

Inline

Subtract	Off
Std-Dev-Sag	Off
Std-Dev-Cor	Off
Std-Dev-Tra	Off
Std-Dev-Time	Off
MIP-Sag	Off
MIP-Cor	Off
MIP-Tra	Off
MIP-Time	Off
Save original images	On

Sequence

Introduction	On
Dimension	3D
Elliptical scanning	Off
Asymmetric echo	Off
Bandwidth	240 Hz/Px
Flow comp.	No
Echo spacing	7.1 ms
RF pulse type	Fast
Gradient mode	Normal
Excitation	Non-sel.
RF spoiling	On

SIEMENS MAGNETOM Verio syngo MR B17

\\USER\HEAD\ELAD/AMYLOID/DELIRIUM (Paul Edison)\Visit 1\pd+t2_tse_Tra

TA: 2:36 PAT: 2 Voxel size: 1.0×1.0×3.5 mm Rel. SNR: 1.00 SIEMENS: tse

Properties	
Prio Recon	Off
Before measurement	
After measurement	
Load to viewer	On
Inline movie	Off
Auto store images	On
Load to stamp segments	On
Load images to graphic segments	Off
Auto open inline display	Off
Start measurement without further preparation	On
Wait for user to start	On
Start measurements	single

Routine	
Slice group 1	
Slices	40
Dist. factor	10 %
Position	R5.5 P24.3 H6.5
Orientation	Transversal
Phase enc. dir.	R >> L
Rotation	89.70 deg
Phase oversampling	30 %
FoV read	256 mm
FoV phase	75.0 %
Slice thickness	3.5 mm
TR	7370 ms
TE 1	8.7 ms
TE 2	78 ms
Averages	1
Concatenations	1
Filter	Distortion Corr.(2D), Prescan Normalize, Elliptical filter
Coil elements	HEA;HEP

Contrast	
MTC	Off
Magn. preparation	None
Flip angle	150 deg
Fat suppr.	None
Water suppr.	None
Restore magn.	Off
Averaging mode	Long term
Reconstruction	Magnitude
Measurements	1
Multiple series	Each measurement

Resolution	
Base resolution	256
Phase resolution	100 %
Phase partial Fourier	Off
Trajectory	Cartesian
Interpolation	Off
PAT mode	GRAPPA
Accel. factor PE	2
Ref. lines PE	30
Matrix Coil Mode	Auto (Triple)
Reference scan mode	Integrated
Image Filter	Off
Distortion Corr.	On
Mode	2D
Unfiltered images	Off
Unfiltered images	Off
Prescan Normalize	On
Normalize	Off
B1 filter	Off
Raw filter	Off
Elliptical filter	On
Mode	Inplane

Geometry	
Multi-slice mode	Interleaved
Series	Interleaved
Special sat.	None
Set-n-Go Protocol	Off
Table position	H
Table position	0 mm
Inline Composing	Off

System	
Body	Off
HEP	On
HEA	On
Positioning mode	FIX
MSMA	S - C - T
Sagittal	R >> L
Coronal	A >> P
Transversal	F >> H
Coil Combine Mode	Sum of Squares
Auto Coil Select	Default
Shim mode	Standard
Adjust with body coil	Off
Confirm freq. adjustment	Off
Assume Silicone	Off
? Ref. amplitude 1H	0.000 V
Adjustment Tolerance	Auto
Adjust volume	
Position	R5.5 P24.3 H6.5
Orientation	Transversal
Rotation	89.70 deg
A >> P	256 mm
R >> L	192 mm
F >> H	154 mm

Physio	
1st Signal/Mode	None
Dark blood	Off
Resp. control	Off

Inline	
Subtract	Off
Std-Dev-Sag	Off
Std-Dev-Cor	Off
Std-Dev-Tra	Off
Std-Dev-Time	Off
MIP-Sag	Off
MIP-Cor	Off
MIP-Tra	Off
MIP-Time	Off
Save original images	On

Sequence	
Introduction	On

5/+

Dimension	2D
Compensate T2 decay	Off
Reduce Motion Sens.	Off
Contrasts	2
Bandwidth	203 Hz/Px
Flow comp.	No
Allowed delay	60 s
Echo spacing	8.71 ms
Define	Turbo factor
Turbo factor	7
Echo trains per slice	20
RF pulse type	Fast
Gradient mode	Fast

SIEMENS MAGNETOM Verio syngo MR B17

\\USER\HEAD\ELAD/AMYLOID/DELIRIUM (Paul Edison)\Visit 1\t2_tirm_tra_dark-fluid

TA: 2:44 PAT: 2 Voxel size: 0.9×0.9×4.0 mm Rel. SNR: 1.00 SIEMENS: tse

Properties

Prio Recon	Off
Before measurement	
After measurement	
Load to viewer	On
Inline movie	Off
Auto store images	On
Load to stamp segments	Off
Load images to graphic segments	Off
Auto open inline display	Off
Start measurement without further preparation	On
Wait for user to start	Off
Start measurements	single

Routine

Slice group 1	
Slices	30
Dist. factor	30 %
Position	R5.5 P24.3 H6.5
Orientation	Transversal
Phase enc. dir.	R >> L
Rotation	89.70 deg
Phase oversampling	0 %
FoV read	220 mm
FoV phase	90.6 %
Slice thickness	4.0 mm
TR	9000 ms
TE	95.0 ms
Averages	1
Concatenations	2
Filter	Distortion Corr.(2D), Prescan Normalize
Coil elements	HEA;HEP

Contrast

TD	0.0 ms
MTC	Off
Magn. preparation	Slice-sel. IR
TI	2500 ms
Freeze suppressed tissue	On
Flip angle	130 deg
Fat suppr.	Fat sat.
Fat sat. mode	Strong
Water suppr.	None
Restore magn.	Off
Averaging mode	Long term
Reconstruction	Magnitude
Measurements	1
Multiple series	Each measurement

Resolution

Base resolution	256
Phase resolution	100 %
Phase partial Fourier	Off
Trajectory	Cartesian
Interpolation	On
PAT mode	GRAPPA
Accel. factor PE	2
Ref. lines PE	24
Matrix Coil Mode	Auto (Triple)
Reference scan mode	Integrated
Image Filter	Off
Distortion Corr.	On
Mode	2D
Unfiltered images	Off
Unfiltered images	Off
Prescan Normalize	On
Normalize	Off
B1 filter	Off
Raw filter	Off
Elliptical filter	Off

Geometry

Multi-slice mode	Interleaved
Series	Interleaved
Special sat.	None
Set-n-Go Protocol	Off
Table position	H
Table position	0 mm
Inline Composing	Off

System

Body	Off
HEP	On
HEA	On
Positioning mode	FIX
MSMA	S - C - T
Sagittal	R >> L
Coronal	A >> P
Transversal	F >> H
Coil Combine Mode	Adaptive Combine
Auto Coil Select	Default
Shim mode	Standard
Adjust with body coil	Off
Confirm freq. adjustment	Off
Assume Silicone	Off
? Ref. amplitude 1H	0.000 V
Adjustment Tolerance	Auto
Adjust volume	
Position	R5.5 P24.3 H6.5
Orientation	Transversal
Rotation	89.70 deg
A >> P	220 mm
R >> L	200 mm
F >> H	155 mm

Physio

1st Signal/Mode	None
Dark blood	Off
Resp. control	Off

Inline

Subtract	Off
Std-Dev-Sag	Off
Std-Dev-Cor	Off
Std-Dev-Tra	Off
Std-Dev-Time	Off
MIP-Sag	Off
MIP-Cor	Off
MIP-Tra	Off
MIP-Time	Off
Save original images	On

SIEMENS MAGNETOM Verio syngo MR B17

Sequence	
Introduction	On
Dimension	2D
Compensate T2 decay	Off
Reduce Motion Sens.	On
Contrasts	1
Bandwidth	287 Hz/Px
Flow comp.	No
Allowed delay	60 s
Echo spacing	7.29 ms
Define	Turbo factor
Turbo factor	16
Echo trains per slice	8
RF pulse type	Fast
Gradient mode	Fast

SIEMENS MAGNETOM Verio syngo MR B17

\\USER\HEAD\ELAD/AMYLOID/DELIRIUM (Paul Edison)\Visit 1\gre_field_mapping

TA: 1:18 Voxel size: 3.0×3.0×3.0 mm Rel. SNR: 1.00 SIEMENS: gre_field_mapping

Properties	
Prio Recon	Off
Before measurement	
After measurement	
Load to viewer	On
Inline movie	Off
Auto store images	On
Load to stamp segments	Off
Load images to graphic segments	Off
Auto open inline display	Off
Start measurement without further preparation	On
Wait for user to start	On
Start measurements	single

Routine	
Slice group 1	
Slices	35
Dist. factor	0 %
Position	R2.0 A1.0 H15.6
Orientation	T > C-31.5 > S0.9
Phase enc. dir.	A >> P
Rotation	0.00 deg
Phase oversampling	0 %
FoV read	192 mm
FoV phase	100.0 %
Slice thickness	3.0 mm
TR	599 ms
TE 1	5.19 ms
TE 2	7.65 ms
Averages	1
Concatenations	1
Filter	Prescan Normalize
Coil elements	HEA;HEP

Contrast	
MTC	Off
Flip angle	60 deg
Fat suppr.	None
Averaging mode	Long term
Reconstruction	Magn./Phase
Measurements	1
Multiple series	Off

Resolution	
Base resolution	64
Phase resolution	100 %
Phase partial Fourier	Off
Interpolation	Off
Matrix Coil Mode	Auto (CP)
Image Filter	Off
Distortion Corr.	Off
Unfiltered images	Off
Prescan Normalize	On
Normalize	Off
B1 filter	Off
Raw filter	Off
Elliptical filter	Off

Geometry	
Multi-slice mode	Interleaved
Series	Interleaved

Special sat.	None
Set-n-Go Protocol	Off
Table position	H
Table position	0 mm
Inline Composing	Off

System	
Body	Off
HEP	On
HEA	On
Positioning mode	FIX
MSMA	S - C - T
Sagittal	R >> L
Coronal	A >> P
Transversal	F >> H
Save uncombined	Off
Coil Combine Mode	Sum of Squares
Auto Coil Select	Default
Shim mode	Standard
Adjust with body coil	Off
Confirm freq. adjustment	Off
Assume Silicone	Off
? Ref. amplitude 1H	0.000 V
Adjustment Tolerance	Auto
Adjust volume	
Position	R2.0 A1.0 H15.6
Orientation	T > C-31.5 > S0.9
Rotation	0.00 deg
R >> L	192 mm
A >> P	192 mm
F >> H	105 mm

Composing	

Sequence	
Introduction	Off
Dimension	2D
Asymmetric echo	Off
Contrasts	2
Bandwidth	260 Hz/Px
Flow comp.	Yes
RF pulse type	Normal
Gradient mode	Normal
RF spoiling	On

SIEMENS MAGNETOM Verio syngo MR B17

\\USER\HEAD\ELAD/AMYLOID/DELIRIUM (Paul Edison)\Visit 1\RestingState fMRI

TA: 10:06 PAT: 2 Voxel size: 3.0×3.0×3.0 mm Rel. SNR: 1.00 SIEMENS: ep2d_bold

Properties	
Prio Recon	Off
Before measurement	
After measurement	
Load to viewer	On
Inline movie	Off
Auto store images	On
Load to stamp segments	Off
Load images to graphic segments	Off
Auto open inline display	Off
Start measurement without further preparation	On
Wait for user to start	On
Start measurements	single

Routine	
Slice group 1	
Slices	35
Dist. factor	0 %
Position	R2.0 A1.0 H15.6
Orientation	T > C-31.5 > S0.9
Phase enc. dir.	A >> P
Rotation	0.00 deg
Phase oversampling	0 %
FoV read	192 mm
FoV phase	100.0 %
Slice thickness	3.0 mm
TR	2000 ms
TE	30 ms
Averages	1
Concatenations	1
Filter	Prescan Normalize
Coil elements	HEA;HEP

Contrast	
MTC	Off
Flip angle	80 deg
Fat suppr.	Fat sat.
Averaging mode	Long term
Reconstruction	Magnitude
Measurements	300
Delay in TR	0 ms
Multiple series	Off

Resolution	
Base resolution	64
Phase resolution	100 %
Phase partial Fourier	Off
Interpolation	Off
PAT mode	GRAPPA
Accel. factor PE	2
Ref. lines PE	24
Matrix Coil Mode	Auto (Triple)
Reference scan mode	Separate
Distortion Corr.	Off
Unfiltered images	Off
Prescan Normalize	On
Raw filter	On
Elliptical filter	Off
Hamming	Off

Geometry	
Multi-slice mode	Interleaved
Series	Interleaved
Special sat.	None
Set-n-Go Protocol	Off
Table position	H
Table position	0 mm
Inline Composing	Off

System	
Body	Off
HEP	On
HEA	On
Positioning mode	FIX
MSMA	S - C - T
Sagittal	R >> L
Coronal	A >> P
Transversal	F >> H
Coil Combine Mode	Sum of Squares
Auto Coil Select	Default
Shim mode	Standard
Adjust with body coil	Off
Confirm freq. adjustment	Off
Assume Silicone	Off
? Ref. amplitude 1H	0.000 V
Adjustment Tolerance	Auto
Adjust volume	
Position	R2.0 A1.0 H15.6
Orientation	T > C-31.5 > S0.9
Rotation	0.00 deg
R >> L	192 mm
A >> P	192 mm
F >> H	105 mm

Physio	
1st Signal/Mode	None

BOLD	
GLM Statistics	Off
Dynamic t-maps	Off
Starting ignore meas	0
Ignore after transition	0
Model transition states	On
Temp. highpass filter	On
Threshold	4.00
Paradigm size	20
Meas[1]	Baseline
Meas[2]	Baseline
Meas[3]	Baseline
Meas[4]	Baseline
Meas[5]	Baseline
Meas[6]	Baseline
Meas[7]	Baseline
Meas[8]	Baseline
Meas[9]	Baseline
Meas[10]	Baseline
Meas[11]	Active
Meas[12]	Active
Meas[13]	Active
Meas[14]	Active
Meas[15]	Active
Meas[16]	Active
Meas[17]	Active
Meas[18]	Active
Meas[19]	Active

Meas[20]	Active
Motion correction	Off
Spatial filter	Off

Sequence

Introduction	Off
Bandwidth	1906 Hz/Px
Free echo spacing	Off
Echo spacing	0.61 ms
EPI factor	64
RF pulse type	Normal
Gradient mode	Fast

SIEMENS MAGNETOM Verio syngo MR B17

\\USER\HEAD\ELAD/AMYLOID/DELIRIUM (Paul Edison)\Visit 1\ep2d_tra_pasl_p2

TA: 4:20 PAT: 2 Voxel size: 3.0×3.0×6.0 mm Rel. SNR: 1.00 SIEMENS: ep2d_pasl

Properties

Prio Recon	Off
Before measurement	
After measurement	
Load to viewer	On
Inline movie	Off
Auto store images	On
Load to stamp segments	Off
Load images to graphic segments	Off
Auto open inline display	Off
Start measurement without further preparation	On
Wait for user to start	Off
Start measurements	single

Routine

Slice group 1	
Slices	14
Dist. factor	25 %
Position	R0.2 P10.8 H13.0
Orientation	Transversal
Phase enc. dir.	A >> P
Rotation	0.00 deg
Phase oversampling	10 %
FoV read	192 mm
FoV phase	100.0 %
Slice thickness	6.0 mm
TR	2500.0 ms
TE	11 ms
Averages	1
Concatenations	1
Filter	Prescan Normalize
Coil elements	HEA;HEP

Contrast

Inversion time 2	1800.0 ms
Inversion time 1	700 ms
Saturation stop time	1600 ms
Flip angle	90 deg
Fat suppr.	Fat sat.
Fat sat. mode	Strong
Averaging mode	Long term
Reconstruction	Magnitude
Measurements	101
Delay in TR	0 ms
Multiple series	Off
Perfusion mode	PICORE Q2T
Inversion time 1	700 ms
Saturation stop time	1600 ms
Inversion time 2	1800.0 ms
Flow limit	100.0 cm/s

Resolution

Base resolution	64
Phase resolution	100 %
Phase partial Fourier	7/8
Interpolation	Off
PAT mode	GRAPPA
Accel. factor PE	2
Ref. lines PE	24
Matrix Coil Mode	Auto (Triple)
Reference scan mode	Separate

Prescan Normalize	On
Raw filter	Off
Elliptical filter	Off
Hamming	Off

Geometry

Multi-slice mode	Interleaved
Series	Ascending
Special sat.	Parallel F
Gap	29.5 mm
Thickness	100 mm
Set-n-Go Protocol	Off
Table position	H
Table position	0 mm
Inline Composing	Off

System

Body	Off
HEP	On
HEA	On
SP4	Off
SP2	Off
SP8	Off
SP6	Off
SP3	Off
SP1	Off
SP7	Off
SP5	Off
Positioning mode	REF
MSMA	S - C - T
Sagittal	R >> L
Coronal	A >> P
Transversal	F >> H
Save uncombined	Off
Coil Combine Mode	Sum of Squares
Auto Coil Select	Default
Shim mode	Standard
Adjust with body coil	Off
Confirm freq. adjustment	Off
Assume Silicone	Off
? Ref. amplitude 1H	0.000 V
Adjustment Tolerance	Auto
Adjust volume	
Position	R0.2 P10.8 H13.0
Orientation	Transversal
Rotation	0.00 deg
R >> L	192 mm
A >> P	192 mm
F >> H	104 mm

Physio

1st Signal/Mode	None

BOLD

GLM Statistics	Off
Dynamic t-maps	Off
Starting ignore meas	1
Ignore after transition	0
Model transition states	Off
Temp. highpass filter	On
Threshold	4.00
Paradigm size	4
Meas[1]	Baseline
Meas[2]	Active

Meas[3]	Baseline
Meas[4]	Active
Motion correction	On
Interpolation	3D-K-space
Spatial filter	On
Filter setting	2.0

Sequence

Introduction	Off
Bandwidth	2232 Hz/Px
Free echo spacing	Off
Echo spacing	0.53 ms
EPI factor	64
RF pulse type	Normal
Gradient mode	Fast

SIEMENS MAGNETOM Verio syngo MR B17

\\USER\HEAD\ELAD/AMYLOID/DELIRIUM (Paul Edison)\Visit 1\t1_tse_rs_tra

TA: 2:36 PAT: Off Voxel size: 0.7×0.7×2.5 mm Rel. SNR: 1.00 SIEMENS: tse

Properties	
Prio Recon	Off
Before measurement	
After measurement	
Load to viewer	On
Inline movie	Off
Auto store images	On
Load to stamp segments	Off
Load images to graphic segments	Off
Auto open inline display	Off
Start measurement without further preparation	On
Wait for user to start	Off
Start measurements	single

Routine	
Slice group 1	
Slices	11
Dist. factor	30 %
Position	L0.3 P8.8 F19.2
Orientation	T > S-0.8
Phase enc. dir.	R >> L
Rotation	90.60 deg
Phase oversampling	30 %
FoV read	220 mm
FoV phase	85.0 %
Slice thickness	2.5 mm
TR	650 ms
TE	13 ms
Averages	2
Concatenations	1
Filter	Prescan Normalize, Elliptical filter
Coil elements	HEA;HEP

Contrast	
MTC	Off
Magn. preparation	None
Flip angle	120 deg
Fat suppr.	None
Water suppr.	None
Restore magn.	Off
Averaging mode	Long term
Reconstruction	Magnitude
Measurements	1
Multiple series	Each measurement

Resolution	
Base resolution	320
Phase resolution	100 %
Phase partial Fourier	Off
Trajectory	Cartesian
Interpolation	On
PAT mode	None
Matrix Coil Mode	Auto (CP)
Image Filter	Off
Distortion Corr.	Off
Unfiltered images	Off
Prescan Normalize	On
Normalize	Off
B1 filter	Off
Raw filter	Off
Elliptical filter	On
Mode	Inplane

Geometry	
Multi-slice mode	Interleaved
Series	Interleaved
Special sat.	None
Set-n-Go Protocol	Off
Table position	H
Table position	0 mm
Inline Composing	Off

System	
Body	Off
HEP	On
HEA	On
Positioning mode	FIX
MSMA	S - C - T
Sagittal	R >> L
Coronal	A >> P
Transversal	F >> H
Coil Combine Mode	Adaptive Combine
Auto Coil Select	Default
Shim mode	Tune up
Adjust with body coil	Off
Confirm freq. adjustment	Off
Assume Silicone	Off
? Ref. amplitude 1H	0.000 V
Adjustment Tolerance	Auto
Adjust volume	
Position	Isocenter
Orientation	Transversal
Rotation	0.00 deg
R >> L	350 mm
A >> P	263 mm
F >> H	350 mm

Physio	
1st Signal/Mode	None
Dark blood	Off
Resp. control	Off

Inline	
Subtract	Off
Std-Dev-Sag	Off
Std-Dev-Cor	Off
Std-Dev-Tra	Off
Std-Dev-Time	Off
MIP-Sag	Off
MIP-Cor	Off
MIP-Tra	Off
MIP-Time	Off
Save original images	On

Sequence	
Introduction	On
Dimension	2D
Compensate T2 decay	Off
Reduce Motion Sens.	On
Contrasts	1
Bandwidth	220 Hz/Px
Flow comp.	Slice

Allowed delay	60 s
Echo spacing	12.9 ms
Define	Turbo factor
Turbo factor	3
Echo trains per slice	118
RF pulse type	Fast
Gradient mode	Normal

SIEMENS MAGNETOM Verio syngo MR B17

\\USER\HEAD\ELAD/AMYLOID/DELIRIUM (Paul Edison)\Visit 1\DTI_64dir_2x2x2

TA: 10:12 PAT: 2 Voxel size: 2.0×2.0×2.0 mm Rel. SNR: 1.00 SIEMENS: ep2d_diff

Properties

Prio Recon	Off
Before measurement	
After measurement	
Load to viewer	On
Inline movie	Off
Auto store images	On
Load to stamp segments	Off
Load images to graphic segments	Off
Auto open inline display	Off
Start measurement without further preparation	On
Wait for user to start	Off
Start measurements	single

Routine

Slice group 1	
Slices	62
Dist. factor	0 %
Position	R7.3 P3.6 H21.8
Orientation	Transversal
Phase enc. dir.	A >> P
Rotation	0.00 deg
Phase oversampling	0 %
FoV read	256 mm
FoV phase	100.0 %
Slice thickness	2.0 mm
TR	9000 ms
TE	99 ms
Averages	1
Concatenations	1
Filter	Raw filter, Prescan Normalize
Coil elements	HEA;HEP

Contrast

MTC	Off
Magn. preparation	None
Fat suppr.	Fat sat.
Averaging mode	Long term
Reconstruction	Magnitude
Delay in TR	0 ms
Multiple series	Off

Resolution

Base resolution	128
Phase resolution	100 %
Phase partial Fourier	6/8
Interpolation	Off
PAT mode	GRAPPA
Accel. factor PE	2
Ref. lines PE	24
Matrix Coil Mode	Auto (Triple)
Reference scan mode	Separate
Distortion Corr.	Off
Prescan Normalize	On
Raw filter	On
Intensity	Medium
Slope	48
Elliptical filter	Off
Hamming	Off

Geometry

Multi-slice mode	Interleaved
Series	Interleaved
Special sat.	None
Set-n-Go Protocol	Off
Table position	H
Table position	0 mm
Inline Composing	Off

System

Body	Off
HEP	On
HEA	On
Positioning mode	REF
MSMA	S - C - T
Sagittal	R >> L
Coronal	A >> P
Transversal	F >> H
Coil Combine Mode	Adaptive Combine
Auto Coil Select	Default
Shim mode	Standard
Adjust with body coil	Off
Confirm freq. adjustment	Off
Assume Silicone	Off
? Ref. amplitude 1H	0.000 V
Adjustment Tolerance	Auto
Adjust volume	
Position	R7.3 P3.6 H21.8
Orientation	Transversal
Rotation	0.00 deg
R >> L	256 mm
A >> P	256 mm
F >> H	124 mm

Physio

1st Signal/Mode	None
Resp. control	Off

Diff

Diffusion mode	MDDW
Diff. weightings	2
b-value 1	0 s/mm²
b-value 2	1000 s/mm²
Diff. weighted images	On
Trace weighted images	On
Average ADC maps	On
Individual ADC maps	Off
FA maps	On
Mosaic	On
Tensor	On
Noise level	30
Diff. directions	64

Sequence

Introduction	Off
Bandwidth	1562 Hz/Px
Free echo spacing	Off
Echo spacing	0.72 ms
EPI factor	128
RF pulse type	Normal
Gradient mode	Fast

SIEMENS MAGNETOM Verio syngo MR B17

\\USER\HEAD\ELAD/AMYLOID/DELIRIUM (Paul Edison)\Visit 1\svs_pcc_water

TA: 0:18 Vol: 20 ×20 ×20 mm Rel. SNR: 1.00 SIEMENS: svs_se

Properties	
Prio Recon	Off
Before measurement	
After measurement	
Load to viewer	On
Inline movie	Off
Auto store images	On
Load to stamp segments	Off
Load images to graphic segments	Off
Auto open inline display	Off
Start measurement without further preparation	On
Wait for user to start	On
Start measurements	single

Routine	
Position	L31.0 A46.9 H41.7
Orientation	Transversal
Rotation	0.00 deg
Vol A >> P	20 mm
Vol R >> L	20 mm
Vol F >> H	20 mm
TR	3000 ms
TE	30 ms
Averages	4
Filter	Prescan Normalize
Coil elements	HEA;HEP

Contrast	
Flip angle	90 deg
Water suppr.	None
Spectral suppr.	None
Measurements	1

Resolution	
Prescan Normalize	On
Vector size	2048
Matrix Coil Mode	CP
Unfiltered images	Off

Geometry	
Set-n-Go Protocol	Off
Table position	H
Table position	0 mm
Inline Composing	Off

System	
Body	Off
HEP	On
HEA	On
Positioning mode	REF
MSMA	S - C - T
Sagittal	R >> L
Coronal	A >> P
Transversal	F >> H
Save uncombined	Off
Auto Coil Select	Default
Shim mode	Advanced
Adj. water suppr.	On
Adjust with body coil	Off
Confirm freq. adjustment	Off
Assume Silicone	Off

? Ref. amplitude 1H	0.000 V
Adjustment Tolerance	Auto
Adjust volume	
Position	L31.0 A46.9 H41.7
Orientation	Transversal
Rotation	0.00 deg
R >> L	20 mm
A >> P	20 mm
F >> H	20 mm

Physio	
1st Signal/Mode	None

Composing

Sequence	
Preparation scans	2
Delta frequency	-2.3 ppm
Phase cycling	Auto
Bandwidth	2000 Hz
Acquisition duration	1024 ms
Remove oversampling	On

SIEMENS MAGNETOM Verio syngo MR B17

\\USER\HEAD\ELAD/AMYLOID/DELIRIUM (Paul Edison)\Visit 1\csi_se_30

TA: 6:53 Voxel size: 10.0×10.0×15.0 mm Rel. SNR: 1.00 SIEMENS: csi_se

Properties	
Prio Recon	Off
Before measurement	
After measurement	
Load to viewer	On
Inline movie	Off
Auto store images	On
Load to stamp segments	Off
Load images to graphic segments	Off
Auto open inline display	Off
Start measurement without further preparation	On
Wait for user to start	Off
Start measurements	single

Routine	
Position	L0.0 P13.3 H8.0
Orientation	T > C-1.3 > S0.1
Rotation	44 deg
FoV R >> L	160 mm
FoV A >> P	160 mm
Thickness F >> H	15 mm
Vol R >> L	80 mm
Vol A >> P	80 mm
Slices	1
TR	1700 ms
TE	30 ms
Averages	3
Filter	Prescan Normalize, Hamming
Coil elements	HEA;HEP

Contrast	
Averaging mode	Long term
Flip angle	90 deg
Water suppr.	Weak water suppr.
Water suppr. BW	50 Hz
Spectral suppr.	None
Measurements	1

Resolution	
Scan res. R >> L	16
Scan res. A >> P	16
Interpol. res. R >> L	16
Interpol. res. A >> P	16
Hamming	On
Width	50
Prescan Normalize	On
Vector size	1024
Matrix Coil Mode	Auto (CP)
Unfiltered images	Off

Geometry	
Fully excited Vol	On
Sat. region 1	
Thickness	40 mm
Position	R81.9 P1.0 H0.0
Orientation	S > C0.7
Sat. delta frequ.	-3.60 ppm
Sat. region 2	
Thickness	40 mm
Position	L81.7 A1.0 H0.0
Orientation	S > C0.7
Sat. delta frequ.	-3.60 ppm
Sat. region 3	
Thickness	50 mm
Position	L1.2 P98.9 H12.1
Orientation	C > T-7.0 > S-0.7
Sat. delta frequ.	-3.60 ppm
Sat. region 4	
Thickness	50 mm
Position	R0.8 A72.0 F11.2
Orientation	C > T-8.9 > S-0.7
Sat. delta frequ.	-3.60 ppm
Set-n-Go Protocol	Off
Table position	H
Table position	0 mm
Inline Composing	Off

System	
Body	Off
HEP	On
HEA	On
SP4	Off
SP2	Off
SP8	Off
SP6	Off
SP3	Off
SP1	Off
SP7	Off
SP5	Off
Positioning mode	FIX
MSMA	S - C - T
Sagittal	R >> L
Coronal	A >> P
Transversal	F >> H
Save uncombined	Off
Auto Coil Select	Default
Shim mode	Advanced
Adj. water suppr.	On
Adjust with body coil	Off
Confirm freq. adjustment	Off
Assume Silicone	Off
? Ref. amplitude 1H	0.000 V
Adjustment Tolerance	Auto
Adjust volume	
Position	L0.0 P13.3 H8.0
Orientation	T > C-1.3 > S0.1
Rotation	44.00 deg
R >> L	80 mm
A >> P	80 mm
F >> H	15 mm

Composing	

Sequence	
Preparation scans	4
Dimension	2D
Delta frequency	-2.7 ppm
Phase encoding	Weighted
Bandwidth	1200 Hz
Acquisition duration	853 ms
Remove oversampling	On

Appendix 2. Cortical Parcellation for Graph Theory Analysis

Label	Anatomical	Label	Anatomical	Label	Anatomical
1	L. Amygdala	31	R. Sup. Frontal Med.	61	L. Sup. Parietal Gyrus
2	R. Amygdala	32	L. Sup. Frontal Orbital	62	R. Sup. Parietal Gyrus
3	L. Angular Gyrus	33	R. Sup. Frontal Orbital	63	L. Postcentral Gyrus
4	R. Angular Gyrus	34	R. Superior Frontal	64	R. Postcentral Gyrus
5	L. Calcarine Fissure	35	L. Fusiform Gyrus	65	L. Precentral Gyrus
6	R. Calcarine Fissure	36	R. Fusiform Gyrus	66	R. Precentral Gyrus
7	L. Caudate Nucleus	37	L. Heschl Gyrus	67	L. Precuneus
8	R. Caudate Nucleus	38	R. Heschl Gyrus	68	R. Precuneus
9	L. Ant. Cingulate Cort.	39	L. Hippocampus	69	L. Putamen
10	R. Ant. Cingulate Cort.	40	R. Hippocampus	70	R. Putamen
11	L. Mid. Cingulate Cort.	41	L. Insula	71	L. Rectus gyrus
12	R. Mid. Cingulate Cort.	42	R. Insula	72	R. Rectus gyrus
13	L. Pos. Cingulate Cort.	43	L. Lingual Gyrus	73	L. Rolandic Operculum
14	R. Pos. Cingulate Cort.	44	R. Lingual Gyrus	74	R. Rolandic Operculum
15	L. Cuneus	45	L. Inf. Occipital Gyrus	75	L. Supplementary Motor Area
16	R. Cuneus	46	R. Inf. Occipital Gyrus	76	R. Supplementary Motor Area
17	L. Inf. Frontal Oper.	47	L. Mid. Occipital Gyrus	77	L. Supramarginal Gyrus
18	R. Inf. Frontal Oper.	48	R. Mid. Occipital Gyrus	78	R. Supramarginal Gyrus
19	L. Inf. Frontal Orbital	49	L. Sup. Occipital Gyrus	79	L. Inf. Temporal Gyrus
20	R. Inf. Frontal Orbital	50	R. Sup. Occipital Gyrus	80	R. Inf. Temporal Gyrus
21	L. Inf. Frontal Triang.	51	L. Olfactory Cortex	81	L. Mid. Temporal Gyrus
22	R. Inf. Frontal Triang.	52	R. Olfactory Cortex	82	R. Mid. Temporal Gyrus
23	L. Med. Frontal Orbital	53	L. Pallidum	83	L. Mid. Temporal Pole Gyrus
24	R. Med. Frontal Orbital	54	R. Pallidum	84	R. Mid. Temporal Pole Gyrus
25	L. Frontal Middle	55	L. Paracentral Lobule	85	L. Sup. Temporal Pole Gyrus
26	L. Frontal Mid. Orbital	56	R. Paracentral Lobule	86	R. Sup. Temporal Pole Gyrus
27	R. Mid Frontal Orbital	57	L. Parahippocampal	87	L. Sup. Temporal Gyrus
28	R. Middle Frontal	58	R. Parahippocampal	88	R. Sup. Temporal Gyrus
29	L. Superior Frontal	59	L. Inf. Parietal Gyrus	89	L. Thalamus
30	L. Frontal Sup. Med.	60	R. Inf. Parietal Gyrus	90	R. Thalamus

Appendix 3. Brief demographics and scan availability for each participant

ID	Gender	MMSE	Age	Amyloid_status	AV1451	PBR
AD01	Male	22	76	Positive	Negative	Y
AD02	Female	20	74	Positive	Positive	Y
AD03	Male	18	65	Negative	NA	N
AD04	Female	23	77	NA	NA	Y
AD05	Male	28	77	Positive	NA	Y
AD06	Male	22	80	Positive	Positive	Y
AD07	Female	26	77	Positive	Positive	N
AD08	Female	27	55	Negative	NA	Y
AD09	Female	24	65	Positive	Positive	Y
AD10	Female	25	79	Positive	Positive	Y
AD11	Male	10	80	NA	NA	N
AD12	Male	25	76	Positive	Negative	Y
AD13	Male	22	73	Positive	Positive	Y
AD14	Male	19	78	Negative	Negative	Y
AD15	Female	22	78	Positive	Positive	Y
AD16	Male	16	85	Positive	Negative	Y
AD17	Male	18	76	Positive	Positive	Y
AD18	Male	30	73	Positive	Positive	Y
AD19	Female	22	54	Positive	Positive	Y
AD20	Male	24	75	NA	Positive	Y
AD21	Female	24	66	Positive	Positive	Y
AD22	Male	29	68	NA	Negative	Y
HC01	Female	25	67	Negative	Positive	Y
HC02	Female	25	74	Negative	NA	Y
HC03	Female	28	57	Negative	NA	Y
HC04	Female	30	72	Negative	NA	N
HC05	Female	30	70	Positive	Negative	Y
HC06	Female	30	60	Positive	NA	Y
HC07	Male	30	60	Negative	NA	Y
HC08	Female	30	51	Negative	Negative	Y
HC09	Male	29	74	Negative	NA	Y

HC10	Male	30	64	Negative	NA	Y
HC11	Male	30	55	Negative	NA	Y
HC12	Female	28	54	Negative	Negative	Y
HC13	Male	30	57	Negative	NA	Y
HC14	Female	30	59	Negative	NA	Y
HC15	Male	30	68	Negative	NA	N
HC16	Male	30	70	Negative	Negative	N
HC17	Male	29	58	Negative	NA	Y
HC18	Male	30	74	Negative	Positive	Y
HC19	Female	30	76	Negative	Negative	Y
HC20	Female	30	77	NA	NA	Y
HC21	Male	29	84	Positive	Negative	Y
MCI01	Female	27	75	Positive	NA	Y
MCI02	Female	26	56	Positive	NA	Y
MCI03	Female	29	72	Positive	NA	Y
MCI04	Female	28	72	Negative	NA	N
MCI05	Female	30	78	Negative	NA	Y
MCI06	Male	29	63	Negative	NA	Y
MCI07	Male	26	71	NA	NA	Y
MCI08	Female	26	77	Positive	NA	Y
MCI09	Male	27	74	Negative	Negative	Y
MCI10	Female	25	62	Negative	Negative	N
MCI11	Male	29	79	Positive	Positive	Y
MCI12	Male	30	65	Negative	NA	N
MCI13	Male	28	79	Positive	Positive	Y
MCI14	Male	27	63	Negative	Positive	Y
MCI15	Male	30	68	Negative	NA	Y
MCI16	Female	30	53	Negative	NA	N
MCI17	Male	29	81	Positive	Positive	N
MCI18	Female	28	79	Negative	NA	Y
MCI19	Male	30	77	Positive	Positive	Y
MCI20	Male	29	70	Negative	NA	N
MCI21	Female	29	58	Negative	NA	Y
MCI22	Male	30	55	Negative	NA	N
MCI23	Female	23	64	Negative	NA	Y

MCI24	Female	30	74	Positive	NA	Y
MCI25	Male	24	78	Negative	Negative	Y
MCI26	Male	29	66	Negative	Negative	Y
MCI27	Male	27	80	Negative	NA	N
MCI28	Female	24	58	Negative	Negative	Y
MCI29	Female	28	79	NA	Positive	Y
MCI30	Male	30	55	Negative	NA	Y
MCI31	Female	28	73	Negative	NA	Y
MCI32	Female	29	86	Positive	NA	N
MCI33	Male	26	85	Positive	Positive	Y
MCI34	Male	25	69	Negative	NA	N
MCI35	Female	26	71	Positive	Positive	Y
MCI36	Male	29	84	Positive	Positive	Y
MCI37	Male	27	75	Negative	Negative	Y
MCI38	Male	27	59	Negative	NA	N
MCI39	Male	29	78	Positive	Negative	N
MCI40	Male	26	72	NA	Negative	Y
MCI41	Male	27	79	Positive	NA	N
MCI42	Male	26	67	Positive	Positive	N
MCI43	Male	28	72	Positive	Positive	Y
MCI44	Male	28	69	Negative	NA	Y
MCI45	Male	28	77	Negative	Positive	Y

NA: scan not available to determine; Y: participant has the scan available; N: scan not available for the participant.

Appendix 4. Publication

Leng, F., Edison, P. Neuroinflammation and microglial activation in Alzheimer disease: where do we go from here?. *Nat Rev Neurol* **17,** 157–172 (2021). https://doi.org/10.1038/s41582-020-00435-y